DISS. ETH NO. 25345

Experimental and Techno-Economic Assessment of Catalytic Methanation of Biogas for Power-to-Gas Processes

A thesis submitted to attain the degree of

DOCTOR OF SCIENCES of ETH ZURICH

(Dr. sc. ETH Zurich)

presented by

JULIA WITTE
Master of Science, Technische Universität Berlin
born on 08.08.1985
citizen of Germany

accepted on the recommendation of

Prof. Dr. Alexander Wokaun, examiner
Prof. Dr. Konrad Hungerbühler, co-examiner
Dr. Tilman J. Schildhauer, co-examiner
Dr. Serge M.A. Biollaz, co-examiner

2018

Wir sind das,
was wir denken.
Alles was wir sind,
Ensteht mit unseren Gedanken.
Mit unseren Gedanken,
Erschaffen wir die Welt.

- Siddhartha Gautama, 560 - 480 v. Chr.

Acknowledgements

I would like to express my sincerest thank to Prof. Alexander Wokaun who directed my PhD thesis and provided me with his clear scientific insights frequently. For the acceptance of the position as co-examiner, I want to thank Prof. Konrad Hungerbühler.

I thank the group leader Dr. Serge Biollaz for giving me the opportunity to conduct my PhD in the group of Thermo-Chemical Processes. I want to express a very big thank you to Dr. Tilman Schildhauer for being a great supervisor, for his support over the entire time of my PhD and for the very good relationship.

I thank Dr. Sinan Teske for the warm welcome in the group and for the introduction into my research topic. I thank Frank Schillinger as PhD-colleague until the last hour who supported and helped me where it was possible and Dr. Adelaide Calbry-Muzyka for always having an open ear. I thank Agnieszka Hamburger-Nowakowska for her continuous and warm support and I want to thank the operators Tanja Wieseler, Sergio Rodriguez and the analyst Alwin Frei for their commitment during so many hours of experiments. A very big thank you goes to the whole TCP group with a great working environment not only regarding the professionalism but also for the friendly atmosphere: Daniel Wuillemin, Hansjörg Wagenbach, Jörg Schneebeli, Claudia Saretzki, Philipp Riechmann, Daniel Meyer, Martin Künstle, Peter Hottinger, Marcel Hottiger, Janez Javornik and Andreas Gantenbein. Thank you very much for the inspiring talks and performances during the coffee breaks of my dear colleagues: Gerald Bauer, Saŝa Bjelić, Thibault Fovanna, Christopher Hunston, Timon Käser, Frank Pilger, Dennis Palagin, Thomas Rohrbach, Daniel Steitz, Vitaly Sushkevich, Michael Szostak, Mohamed Tarik and Patrik Zimmermann.

A big thank you goes to my partner and daughter for supporting me unconditionally through my whole PhD and for enriching my life.

Villigen, November 20, 2018 JULIA WITTE

Abstract

The energy systems of various countries in Europe are currently in transition. In order to face the consequences of climate change caused by additional carbon dioxide emissions from fossil sources, and to restrict the hazardous waste from nuclear power plants, alternative sources for power generation are required at large scale. Renewable energy resources like wind and sun are targeted to solve the power generation problem with carbon-free electricity. However, the energy flows in nature are subjected to hourly, daily and seasonal fluctuations which the current electricity grid cannot balance out. Storable energy carriers must be produced so that electricity and heat can be provided on demand.

The Power-to-Gas (PtG) system is one approach which may contribute to solve the storage problem caused by using renewable energies at large scale. The concept envisages the conversion of electrical energy to chemical energy in the form of hydrogen or methane. These gases can be stored in existing gas grids. However, the injection of hydrogen into the European gas grid is generally restricted to two percent, so that a further conversion step from hydrogen to synthetic natural gas (SNG) is required. In order to produce methane from hydrogen, a carbon source is needed such as CO_2 from exhaust gas, wood gasification or anaerobic digestion of bio-waste. Biogas from anaerobic digestion is a particularly attractive carbon dioxide source, since the carbon dioxide content is relatively high with up to 45 %. Furthermore, no prior carbon dioxide separation is required because the only bulk component present besides CO_2, is methane which can be fed to the methanation unit as a quasi-inert component. Additionally, the SNG production from biogas can be increased up to 80 % by converting the otherwise emitted carbon dioxide to methane.

The whole process chain of direct methanation from the biogas to unrestrictedly injectable biomethane (SNG from renewable sources) was investigated with the target of implementation into industry. For this, experiments of the key units, the methanation and the gas separation membrane, were conducted to prove the technical feasibility and to validate established mathematical models. In a next step, technical process models for several possible process designs were established including different methanation technologies and subsequent upgrading units. Here, the technical feasibility at a process level

should be demonstrated, which is defined by the achievement of the required product gas quality given by the gas grid requirements. For implementation into industry, the economic performance of the process is as important as the technical feasibility. For all designed and simulated processes, cost - optimisation as well as an economic assessment was conducted considering key factors like capital and operation costs, feasible electricity prices and achievable profits.

The stable operation of the bubbling fluidised bed methanation over more than 1100 hours was demonstrated in experiments with real biogas as the feed stream. An average methane - yield of 96 % was reached in the pilot-scale reactor, with dry molar concentrations in the methanation gas for methane, hydrogen and carbon dioxide of 87 %, 11 % and 1 % respectively. The produced biomethane was continuously injected into the gas grid. The slow progress of deactivation over time was monitored and evaluated. Sulphur compounds could be identified as the main source of deactivation. Finally, the sulphur species could be removed almost completely by a gas cleaning unit upstream of the reactor, so that almost no further deactivation was observed. Additionally, the kinetics of the model could be evaluated with experimental data. To obtain a methanation product gas which fulfils the gas grid requirements, a gas separation membrane was tested experimentally downstream of the methanation reactor. The requirements for unrestricted injection into the gas grid could be reached with a hydrogen concentration below 2 %, which resulted in a permeate flow of one fifth of the feed flow. Counter-current flow appeared to be the more effective operation mode of the membrane for the given separation task. The permeability factors of the membrane were investigated and found to be significantly lower for penetrants in realistic gas mixtures than for pure components. However, in literature permeability factors from pure components often are applied and set constant for membrane module simulations, which can overestimate the membrane performance. The influence of pressure and concentrations on the permeability was described mathematically for a more realistic simulation of the membrane performance.

With the technical process simulations combined with economic assessments for several possible methanation reactors and subsequent upgrading technologies, the most beneficial process for the direct methanation of biogas could be identified. The process containing bubbling fluidised bed methanation and a gas separation membrane characterised by high permeabilities and medium selectivities showed the best technical and economic performance. By comparing a fixed bed as main reactor with a fluidised bed methanation reactor, it could be pointed out that a fixed bed reactor requires about three times the catalyst mass of a fluidised bed reactor for achieving the same chemical performance. As consequence, the fixed bed is two times more expensive than a fluidised bed. However, both reactor types are limited by kinetic and thermodynamic effects, so

that no complete conversion is possible. An additional upgrading unit is required which separates the excess hydrogen from the methane. Here, the gas separation membrane is favoured due to its beneficial influence on the process robustness. In terms of capital and operation costs, the electrolysis clearly dominates the overall process costs with a share of 70 %. For an electricity price of 6 $Ct_€/kWh_{el}$ and an assumed biogas price of 6 $Ct_€/kWh_{biogas}$, the production costs of the optimum process are 11 $Ct_€/kWh_{SNG}$, which is the limit of profitability. If extra revenues from heat and oxygen are considered and a 10 %-points higher methane concentration in the raw biogas is assumed, the maximum feasible electricity price increases by 3 $Ct_€/kWh_{el}$.

The technical feasibility of the direct methanation of biogas was demonstrated by experiments and by detailed process simulations. The economic profitability of the Power-to-Gas process depends on site conditions like the costs of purchased electricity, biogas composition and the possibility of selling the by-products (process heat and oxygen). For a biogas plant which can make use of the process heat from the methanation and has access to electricity without paying grid-use fees, it is realistic that the presented process is profitable. These results are an important step towards the implementation of Power-to-Gas processes into industry with biogas as carbon source, so that the potential fluctuating electricity generation by the usage of renewables to a large extent can be compensated.

Zusammenfassung

Die Energiesysteme befinden sich in einigen Ländern im Wandel. Alternative Resourcen für die Strom- und Wärmeproduktion werden im großen Maßstab benötigt, um dem Klimawandel zu begegen, welcher durch zusätzliche Kohlenstoffdioxid-Emissionen verursacht wurde und um nuklearen Sondermüll zu vermeiden. Erneuerbare Energiequellen, wie Wind und Sonne, sollen das Problem der Energieversorgung mit einer kohlenstofffreien Stromproduktion lösen. Die Energieflüsse in der Natur sind jedoch stündlichen, täglichen bis hin zu saisonalen Fluktuationen unterworfen, welche das derzeitige Stromnetz nicht ausbalancieren kann. Ein speicherbarer Energieträger wird benötigt, so dass Strom und Wärme auf Nachfrage zur Verfügung gestellt werden kann.

Das Power-to-Gas (PtG) System ist ein Ansatz, mit dem das Speicherproblem durch die Verwendung erneuerbarer Energien im großen Maßstab gelöst werden kann. Dieser Ansatz sieht die Umwandlung von elektrischer zu chemischer Energie vor in Form von Wasserstoff oder Methan. Diese Gase können im Erdgasnetz gespeichert und bei Bedarf verwendet werden. Die Einspeisung von Wasserstoff in das europäische Gasnetz ist jedoch im Allgemeinen auf zwei Prozent beschränkt, sodass ein weiterer Umwandlungsschritt von Wasserstoff zu Methan berücksichtigt wird. Um Methan aus Wasserstoff herzustellen, wird eine Kohlenstoffquelle benötigt wie z.B. Kohlenstoffdioxid aus Abgasen, Holzvergasung oder aus der anaerobe Vergärung von biologischen Abfällen. Das produzierte Biogas aus der anaerobe Vergärung ist eine besonders attraktive Kohenstoffquelle, da der Kohlenstoffdioxidgehalt mit bis zu 45 % relativ hoch ist und keine zusätzliche CO_2-Abtrennung nötig ist. Neben dem CO_2 liegt nur noch Methan als Hauptkomponente im Biogas vor, welches als quasi-inert direkt in die Methanisierung mit eingeleitet werden kann. Zusätzlich kann die Erdgasproduktion aus Biogas um bis zu 80 % gesteigert werden durch die Umwandlung des sonst emittierten Kohlenstoffdioxids zu Methan.

Die gesamte Prozesskette der Direkt-Methanisierung, vom Biogas bis hin zum uneingeschränkt einspeisefähigem Biomethan (Erdgas aus erneuerbaren Quellen) wurde mit dem Ziel untersucht, den Prozess in der Industrie implementieren zu können. Dafür wurden Experimente für die Schlüsseleinheiten Methanisierung und Gasseperations-Membran durchgeführt, um die technische Machbarkeit zu demonstrieren und um die erzeugten mathematischen Modelle zu evaluieren. In einem nächsten Schritt wurden Prozess-

Modelle von unterschiedlichen Prozessvariationen zur Direkt-Methanisierung von Biogas erstellt, welche verschiedene Methanisierungstechnologien und nachfolgende Aufreinigungsstufen beinhalten. Die technische Machbarkeit auf Prozessebene soll gezeigt werden, welche durch das Erreichen der geforderten Prouktqualität definiert ist, sodass die Richtlinien des Erdgasnetzes für eine uneingeschränkte Einspeisung eingehalten werden können. Für die Einführung neuer Technologien in die Industrie ist die Wirtschaftlichkeit genauso wichtig wie die technische Machbarkeit. Für alle entwickelten und simulierten Prozesse wurde eine Kosten-Optimierung sowie eine Wirtschaftlichkeitsanalyse durchgeführt, welche Schlüsselfaktoren wie Kapital- und Betriebskosten, wirtschaftlich machbare Strompreise und erwirtschaftete Profite beinhaltet.

Für die Wirbelschicht Methanisierung konnte in einem Langzeitversuch von über 1100 Stunden ein stabiler Betrieb demonstriert werden bei dem echtes Biogas als Zustrom diente. Eine durchschnittliche Methan-Ausbeute von 96 % wurde in der Wirbelschicht im Pilot-Maßstab errreicht mit einer Produktgaszusammensetzung für Methan, Wasserstoff und Kohlenstoffdioxid von $87\,\mathrm{vol}-\%$, $11\,\mathrm{vol}-\%$ and $1\,\mathrm{vol}-\%$. Das produzierte Biomethan wurde kontinuirlich in das benachbarte Erdgasnetz eingeleitet. Der langsame Verlauf der Katalysator-Deaktivierung wurde überwacht und ausgewertet. Organische Schwefelverbindungen konnten als Hauptursache der aufgetretenden Deaktivierung indentifiziert werden. Diese konnten aus dem Zustrom bis zur Nachweisgrenze entfernt werden, sodass fast keine weitere Deaktivierung beobachtet werden konnte. Zusätzlich konnten die im Model verwendeten Kinetiken und hydrodynamischen Gleichungen mit experimentellen Daten evaluiert werden. Um nach der Methanisierung uneingeschränkt einspeisefähiges Biomethan zu erhalten, ist eine weitere Aufreinigungsstufe nötig. Dafür wurde eine Gasseperations-Membran experimentell untersucht. Die Richtlinien vom Erdgasnetz für eine uneingeschränkte Einspeisung mit einer Wasserstoffkonzentration im Produktstrom unter $2\,\mathrm{vol}-\%$ konnten damit eingehalten werden. Der Betrieb im Gegenstrom erwies sich als die effektivere Einstellung in der Membran für die gegebene Trennaufgabe. Die Permeabilitäten der Membran wurden untersucht. Dabei stellte sich heraus, dass die Permeabilitäten von hoch-penetrierenden Komponenten in einer realistische Gasmischung deutlich niedriger waren als für Reinstoffe. In der Literatur sind jedoch meist nur Reinstoff-Permeabilitäten bestimmt, welche dann in Modellen verwendet werden und als konstant angesehen werden, welches zur Überbewertung der Trennleistung einer Membran in den Modellen führt. Eigene Experimente zeigten, dass die Permeabilität deutlich von Druck, Temperatur und der Gaszusammensetzung abhängt. Die Permeabilität konnte mathematisch beschrieben werden.

Der bestmögliche Prozess für die Direkt-Methanisierung von Biogas konnte identifiziert werden mit Hilfe der technischen Prozess-Simulationen und der wirtschaftlichen Bewertung der verschiedenen Methanisierungsreaktoren und der nachfolgenden Aufreinigungsstufe. Der Prozess mit der technisch und wirtschaftlich besten Performance beinhaltet eine Wirbelschichtmethanisierung und eine nachfolgende Gasseparations-Membran mit hohen Permeabilitäten und mittleren Selektivitäten. Im Vergleich zwischen einer Festbett- und Wirbelschicht-Methanisierung konnte gezeigt werden, dass ein Festbett drei mal mehr Katalysatormenge benötigt um den gleichen Umsatz wie eine Wirbelschicht zu erreichen. Daraus resultieren zweifach höhere Kosten für ein Festbett. Beide Reaktortypen sind jedoch durch kinetische und thermodynamische Effekte limitiert, sodass kein vollständiger Umsatz möglich ist. Eine zusätzliche Aufreinigugsstufe ist nötig, welche den überschüssigen Wasserstoff vom Methan trennt. Wie bereits erwähnt, erwies sich die Gasseperations-Membran als besonders günstig, da sie die Robutsheit des Prozesses unterstützt. Bezüglich der Kapital- und Betriebskosten dominiert die Elektrolyse mit einem Anteil von 70 % klar die gesamten Prozesskosten. Für einen Strompeis von 6 $Ct_{€}/kWh_{el}$ liegen die Produktionskosten des optimalen Prozesses bei 11 $Ct_{€}/kWh_{biomethan}$, welches als Profitabilitätsgrenze gesehen wird da es dem Verkaufspreis von Biomethan entspricht. Die Profitabilität hängt stark von Standortfaktoren ab. So könnte ein Strompreis von 9 $Ct_{€}/kWh_{el}$ noch wirtschaftlich sein, falls Nebeneinkünfte von Prozesswärme und Sauerstoffproduktion berücksichtigt werden könnten, sowie ein 10 % höherer Methananteil im Biogas vorhanden wäre.

Die technische Machbarkeit der Direkt-Methanisierung von Biogas konnte demonstriert werden, einerseits im Experiment andererseits mit detaillierten Prozess-Simulationen. Ob der vorgestellte Power-to-Gas Prozess profitabel ist, hängt von den Standortbedingungen ab wie den Strombezugskosten, der Biogas-Zusammensetzung und der Möglichkeit Nebenprodukte verkaufen zu können. Die Biogasanlage, welche wirtschaftlichen Nutzen von der Prozesswärme aus der Methanisierung ziehen kann und Zugang zu Strom hat ohne Netznutzungsgebühren zahlen zu müssen, hat eine realistische Chance, dass die vorgestellten Prozesse profitabel sind. Diese Ergebnisse sind ein wichtiger Schritt zur Implementierung von Power-to-Gas Prozessen in der Industrie mit Biogas als Kohlenstoffquelle. Dadurch könnte ein Teil der fluktuierenden Elektrizitätserzeugung durch erneuerbare Energien im großen Maßstab ausgeglichen werden.

Contents

Nomenclature

Roman Symbols

ΔG_R^0	gibbs free enthalpy	$kJ\ mol^{-1}$
ΔH	heat of adsorption	$kJ\ mol^{-1}$
ΔH_r^0	standard heat of reaction	$kJ\ mol^{-1}$
ΔS_R^0	standard entropy	$kJ\ mol^{-1}\ K^{-1}$
$\dot{n}$	molar flow	$mol\ s^{-1}$
$\dot{N}_{VC}$	bulk flow from bubble to dense phase	$mol\ s^{-1}$
$\dot{Q}$	heat flow	kW
$\dot{V}$	standard volume flow	$Nm^3\ h^{-1}$
A	surface area	m^2
a	life time	yr
a	specific mass transfer area	$m^2\ m^{-3}$
A_c	cross sectional area	m^2
B	langmuir affinity factor	Pa^{-1}
C	costs	€
c	concentration	$mol\ m^{-3}$
C_i	permeability constant of component i	$Barrer$
c_p	specific heat capacity	$kJ\ mol^{-1}\ K^{-1}$
d, D	diameter	m
D_i	diffusivity of component i	$m^2\ s^{-1}$
dC	delta costs	%

E_A	activation energy	$kJ\ mol^{-1}$
f	fugacity	bar
F_D	drag force	$kg\ m\ s^{-2}$
F_G	gravitational force	$kg\ m\ s^{-2}$
F_{PC}	plant costs factor	-
G	mass flow	$kg\ s^{-1}$
g	gravitational constant	$m\ s^{-2}$
$GHSV$	gas hourly space velocity	$Nm^3_{Feed}\ h^{-1}\ m^{-3}_{reactor}$
H	height	m
H_i	solubility constant of component i, Henry's Law	$mol\ m^{-3}Pa^{-1}$
I	current	A
i	interest	%
K	adsorption constant	differ
k	reaction constant	differ
K_G	mass transfer coefficient	$m\ s^{-1}$
K_p	equilibrium constant	-
K_{ab}	parameter of permeability polynomial	$mol\ m^{-3}Pa^{-1}$
$k_{T_{ref}}$	pre-exponential factor	differ
L	length	m
L_{cap}	langmuir capacity factor	$mol\ m^{-3}$
m	mass	kg
N	quantity	-
Nu	nusselt number	-
p	pressure	bar
p_i	partial pressure of component i	bar
Pr	prandtl number	-

Q	capacity	kW
R	ideal gas constant	$J\ mol^{-1}\ K^{-1}$
R	resistance	Ω
r	radius	m
R_i	rate of formation	$mol\ s^{-1}\ kg_{cat}^{-1}$
Re	reynolds number	-
Rev	revenues	$€\ yr^{-1}$
s	effective thickness of membrane	m
S_i	solubility of component i	Pa^{-1}
T	temperature	$°C$
t	time	differ
U	thermal transmittance	$W\ m^{-2}\ K^{-1}$
U	voltage	V
u	superficial velocity	$m\ s^{-1}$
u_{mf}	minimum fluidisation velocity	$m\ s^{-1}$
v_b	visible bubble velocity	$m\ s^{-1}$
V_m	molar volume	$Nm^3\ mol^{-1}$
w	scale factor	–
x	molar fraction	- or %
Y	yield	- or %

Greek Symbols

α	heat transfer coefficient	$W\ m^{-2}\ K^{-1}$
$\alpha_{i/j}$	ideal selectivity of component i over component j	$W\ m^{-2}\ K^{-1}$
η	dynamic viscosity	$Pa\ s$
λ	thermal conductivity	$W\ m^{-1}\ K^{-1}$
ν	correction factor of visible bubble velocity	-

ν_i	stoichiometric factor of component i	-
ψ	correction factor of visible bubble velocity	-
ρ	density	$kg\ m^{-3}$
ε	void fraction	-
φ	fugacity coefficient	-

Subscripts

b	bubble or bubble phase
$base$	base case
BM	bare module
cat	catalyst
e	emulsion/dense phase
el	electricity
$fibre$	fibres of a gas separation membrane
i	component index
j	integral step in length or time
k	equipment index
lim	limit
m	reaction index; 1... methanation, 2... WGS
mem	membrane
mf	minimum fluidisation
mix	mixture
p	particle or pressure
per	permeate
$proc$	process
$prod$	production
red	reduction

ref reference conditions

ret retentate

tot total

$Trans$ transfer

Superscripts

0 at standard conditions

inv investment

Acronyms

AEL alkaline electrolysis

BFB bubbling fluidised bed

CA cellulose acetate

CAPEX capital expenditure

CEPCI chemical engineering plant cost index

CHP combined heat and power

COSYMA container based system for methanation

CSTR continuously stirred tank reactor

FB fixed bed

FCS feed channel spacer

FFV fractional free volume

HX heat exchanger

IAS intermodulation analysis system

IDLH immediately dangerous to life or health

in input

MEDEA measurement data evaluation

Meth methanation reaction

mGC micro gas chromatography

MOF	metal organic framework
MS	mass spectroscopy
NDIR	non-dispersive infrared
OPEX	operation expenditure
out	output
PC	permeate collection
PPO	poly(2,6-dimethylphenylene oxide)
PSA	pressure swing adsorption
PSF	polysulfone
PtG	power-to-gas
SNG	synthetic natural gas
SR	steam reforming
toe	tonne of oil equivalent
TPO	temperature programmed oxidation
TSA	temperature swing adsorption
WGS	water-gas-shift reaction

1 General Introduction

1.1 Motivation

1.1.1 Conventional Energy Systems and its Effect to the Environment

The conventional energy system is based to a large extent on fossil fuels such as petroleum, coal and natural gas. These hydrocarbons were formed in natural processes over million of years [1] and contain energy originally obtained from photosynthesis [2]. Because the depletion of fossil fuels by humans is much faster than the production of the fuels by nature, those fuels are not considered as renewable reresources. With the combustion of the fuels for the global production of heat and electricity, large amounts of additional carbon dioxide are released into atmosphere which are supposed to be responsible for the general increase of temperature at global scale (global warming). Consequences of the global warming are increasing extreme weather events, ice melting of glaciers and sea ice as well as increasing human migration due deteriorated living conditions caused by droughts, severe weather, lower groundwater tables and a loss of arable land [3].

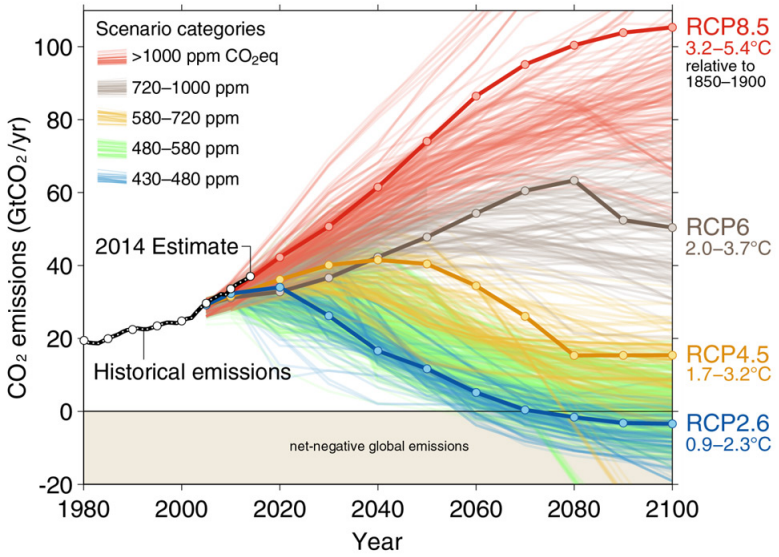

Figure 1.1: Global carbon dioxide emission pathways from fossil fuel combustion; historic values (black), and future emissions scenarios [4]

In 2017, the global emission of CO_2 from fossil fuels was 37 billion metric tons [5] with a corresponding atmospheric CO_2 concentration of 407 ppm [6]. This is almost the double amount of CO_2 emissions in comparison to the year 1980. They are assumed to grow further as it is illustrated in figure 1.1. Here, carbon dioxide emission pathways from fossil fuel combustion are shown as historic values (black) and for different future scenarios (color). Additionally, the corresponding CO_2 concentrations in the atmosphere and the expected global temperature increase are illustrated. If no measures of carbon dioxide savings are implemented in the conventional energy system, the scenarios with the red color are probable. Here, the equivalent CO_2 concentrations will increase above 1000 ppm until 2100 with a corresponding temperature increase between 3.2 °C and 5.4 °C. This high temperature increase would lead to severe changes of the weather conditions with the already mentioned consequences at global scale. In order to moderate the consequences of global warming, carbon dioxide emissions from fossil fuels must be reduced strongly. Politicians from more than 195 nations who participated in the United Nations Climate Change Conference 2015 in Paris decided to limit the global warming to 2 °C. This requires a reduction of CO_2 emissions to zero until the next century and no further increase of emissions after that time [7]. The required global transition in the energy systems to limit the global warming is challenging and unprecedented.

Besides the usage of fossil fuels, also nuclear power plants became a target for criticism. First, because of severe safety issues regarding accidents of nuclear power plants. In March 2011, an earthquake and a subsequent tsunami damaged the cooling system of the nuclear power plant Fukushima Daiichi in Japan, which caused a core meltdown in three reactors, hydrogen explosions, and radioactive releases. Additionally, radioactive contamination from the Fukushima plant forced the evacuation of communities up to 25 miles away and affected up to 100,000 residents. Contaminated water from the plant was discharged into the sea, creating international controversy [8]. And second, because of the ongoing disposal problem of nuclear waste. Due to radioactive material with long half-life, long-term storage of many thousand years is required after the end of usage. This is typically done with deep geologic repositories. However, those storages are very expensive and have to face unpredictable uncertainties due to the enormous period of time the geological disposals have to keep the hazardous waste safely [9].

In order to figure out the challenges of the energy system transition, it is helpful to understand the principles of the conventional energy systems. The production of heat and electricity is determined by the demand of energy from the costumers. The electricity grid cannot store electricity, hence the production must follow the consumption intermediately. In figure 1.2, a typical 24h-curve of the electricity demand in summer is illustrated. The maximum demand during the day is significantly higher than the mini-

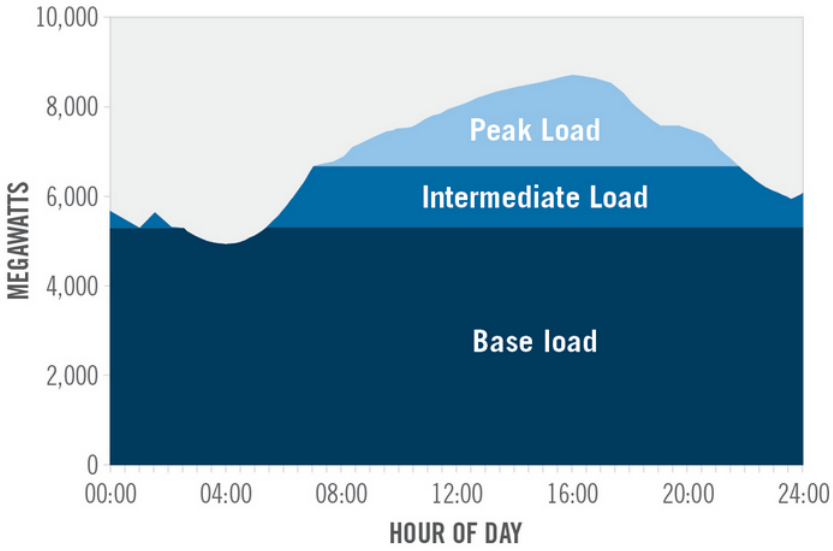

Figure 1.2: Typical demand of electricity over 24 hours in summer and it's classification in base load, intermediate load and peak load [10]

mum demand during the night. In order to balance the different loads, a combination of conventional energy plants is required. The load cycle can be subdivided into the base load, intermediate load and peak load. The base load is a continuous electricity load, which is conventionally produced by lignite, nuclear power plants and run-of-river hydro power plants. Lignite and nuclear power plants have a start-up time of weeks and are most efficient in continuous production. The intermediate load is served by hard coal plants and natural gas combined cycle plants, where a gas turbine and a subsequent steam turbine produce electricity from the same heat source. Those power plants are appropriate to run for several hours to provide the grid with electricity typically during the day. The last category, the peak load, is assigned to peak times of electricity demand usually in the order of minutes. Natural gas turbines and dam hydro power plants are able to switch on and off during that time and can produce electricity very flexibly. In general, electricity from continuous production has the lowest production costs, whereas peak load electricity is the most expensive one.

1.1.2 Energy Systems Based on Renewable Resources

In order to avoid additional emissions of carbon dioxide from fossil resources, renewable energy resources can be used based on wind, sun, water and biomass. With these renewable resources, electricity is produced. For the heat production mainly biomass is used which provides also hydrocarbons for the biofuel production such as biodiesel. The electricity production from renewable resources is typically realised via solar panels, wind and hydro power turbines in combination with a generator as well as via wood chip

or wood pellet plants. The heat production includes mainly the combustion of biogenic solid and gaseous fuels (mainly wood, biogas and biomethane), and to a smaller extent the usage of solar-thermal and geothermal systems.

All over the world, countries increase their efforts to reach higher shares of renewable energy productions. The three nations with the highest modern renewable power capacities in 2016 are China, the United States of America and Germany [11]. The term 'modern renewable energies' excludes hydro power. The distinction is made, because hydro-power remains the largest single element by far of renewable power capacity and has been installed since decades, and thus can mask developments in other renewable energy technologies if included. In all three nations, the usage of modern renewables increased significantly over the past 10 years, however the share of energy from modern renewable resources to the global total final energy consumption was only about 6 % [11].

In Germany, this share is significantly higher with about 15 % (389 TWh) in 2016 with main contributions from wind turbines (26 %) and biogenic fuels (47 %, mainly ligneous) [12]. The avoided CO_2 equivalent emissions were 159 Mio tons. The biggest share of the avoided CO_2 emissions coming from the renewable electricity production, which replaced mainly electricity from hard coal and natural gas. In contrast to Germany, Switzerland produces more than half of the electricity from hydro power (56 % in 2016) since decades [13] so that the share of all renewables of the total final energy consumption was 22 % in 2016. However, modern renewables produce only 2 % of the total energy demand in Switzerland [14]. The political objectives regarding the energy system in Germany and Switzerland contain phasing out nuclear power besides the increase of the renewable energy supply [15] [16]. In Switzerland, a share of 38 % of electricity produced from nuclear power plants in 2014 is targeted to be compensated by renewable resources in 2050 [15] [17].

An increased share of renewable resources in the energy supply chain has effects on the energy system. Because of daily and seasonaly changing conditions of wind, sun and water, renewable electricity production is subjected to fluctuations which have to be compensated. In the case of renewable electricity, the production is not executed on demand like from fossil resources, but on occasion. In order to maintain energy security, storage possibilities of renewable electricity have to be applied. A storage system should not only balance the electricity fluctuations between hours and days, but also between summer and winter. Therefore, storage possibilities at large scale will be required in future with a further increase of renewable electricity shares. Until now, those storage possibilities are not available at large scale, so that e.g. in Germany parts of the renewable electricity production had to shut-down temporarily to avoid an overload

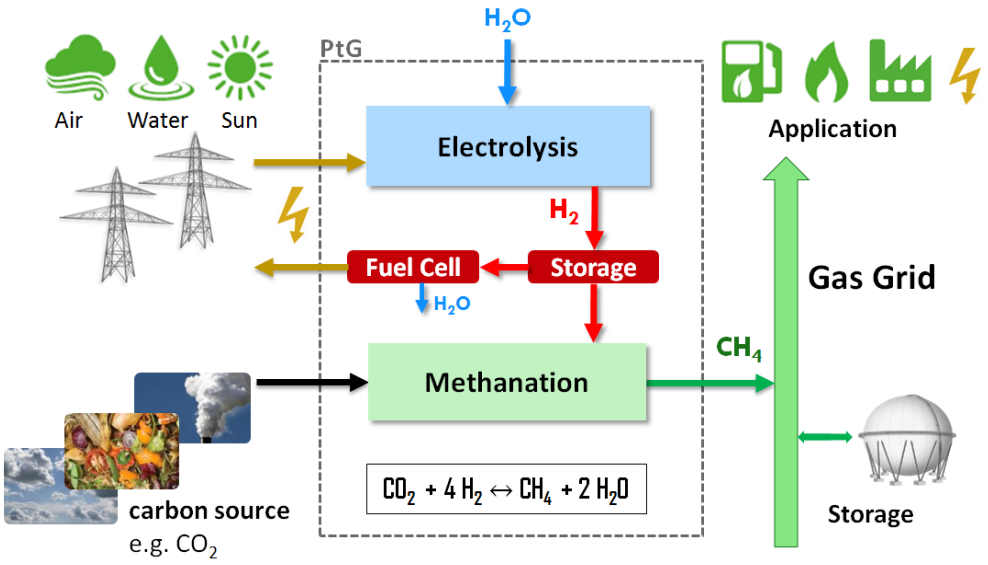

Figure 1.3: Scheme of a Power-to-Gas (PtG) system based on the carbon source carbon dioxide

of the electricity grid. This curtailment energy was 3.7 TWh in 2016 which is about 1 % of the energy supply from renewable resources in Germany [18]. Another negative effect of excess electricity, which cannot be stored, concerns the electricity prices at the European spot market. At several times over the last years, electricity prices became negative. That means, that the costumer earns money by consuming electricity. In Germany, electricity prices at the spot market were negative for 97 hours in the year 2016 with a market value of 68 Mio € [19].

The Power-to-Gas (PtG) system is one approach which may contribute to solve the storage problem caused by using renewable energies to a large extent. In figure 1.3, a PtG system based on carbon dioxide is illustrated. Here, excess electricity from renewable energy resources like wind, flowing water and solar radiation is used in an electrolysis to produce hydrogen from water. The hydrogen can be stored e.g. in salt caverns as it is done in Germany, France and USA until electricity is needed again. Then hydrogen is converted back to electricity via a fuel cell. However, a storage infrastructure and a delivery system of hydrogen at large scale is not present today, therefore an additional conversion step is taken into account. In this methanation step, hydrogen is converted further to methane with a carbon dioxide source. The CO_2 can be obtained from exhaust gas, directly from air or from biogas. For methane, a large storage infrastructure already exists in form of the gas grids. In the gas grid, methane can be stored long-term or can be used in other applications e.g. for the transport sector, for heat production or for the chemical industry.

The PtG approach combines the electricity grid with the gas grid to balance the fluctuating electricity production caused by an increased exploitation of renewable energy resources. However, also for new processes based on renewable resources, the ecological impact has to be considered, since those processes are not automatically more environmentally friendly than processes based on fossil resources [20].

1.2 Cooperation with Industry

In order to explore the feasibility of the PtG-upgrade process in industry, a cooperation was started between the research group *Thermal Process Engineering* of the Paul Scherrer Institute and the largest natural gas supplier of Switzerland, *Energie360°*. For this, a bubbling fluidised bed methanation reactor was applied under real conditions in the biogas industry. It is essential for the technology transfer from research to industry that realistic operation conditions are investigated, so that phenomena are not missed which occur in complex mixtures including e.g. trace components or during long-term operation. This way, industry partners can gain confidence to apply the new technology. The mentioned cooperation concerns investigations regarding the technical and economic feasibility of the PtG-upgrade process, which is described in chapter 3, 4, 5 and 6. The key units of the PtG-upgrade process are an electrolysis for the hydrogen production, a methanation unit for the methane production from carbon dioxide and a gas separation membrane for the final purification of the product gas. Two of the three key units of the PtG-upgrade process, methanation and membrane, are investigated in detail to evaluate their performance and their impact on the whole process chain.

1.3 Objectives and General Methods

The overall objective of this thesis is to present the feasibility of processes for the direct methanation of biogas which are completely based on renewable resources. For the evaluation of feasibility, a holistic approach was chosen including technical and economic assessments of single units and whole process chains. A process is defined as technically feasible, if the produced biomethane fulfils the general gas grid requirements in Switzerland or Germany for an unrestricted injection. A process is defined as economically feasible, if the product biomethane can be produced under profitable conditions.

For the technical evaluations, experiments under real conditions were conducted regarding the key units bubbling fluidised bed methanation and gas separation membrane in order to investigate their performance on a unit level. Furthermore, rigorous models of the key units were established and evaluated with the experimental results. The experiments of the bubbling fluidised bed and the gas separation membrane are described

in chapter 5 and chapter 6. In a next step, the direct methanation of biogas was investigated on a process level via simulations which is described in chapter 3. First, several complete processes were designed. For this, two catalytic methanation reactor types were combined with further upgrading units and supporting units in simulations. Second, various operation conditions were tested in the process simulations to understand the behaviour of the single units in the whole process and to evaluate the technical feasibility which corresponds to the compliance of biomethane with the gas grid requirements for unrestricted injection.

Regarding the economic evaluations, which are described in chapter 4, first cost optimisations were done for each process considered in the technical part. For this, operation conditions were varied to determine the impact of process parameters on the costs under the constraint that only process condition combinations are permissible which result in biomethane unrestrictedly injectable into the gas grid. The level of detail for the economic assessments refers to the 'equipment factored estimate' which results in an accuracy of $+30\,\%$ and $-20\,\%$ regarding the total plant costs. The data required for this kind of economic assessment like sizing of equipment, utilities and raw material consumption were available from the simulations. After the economically optimised process parameters were identified, an absolute cost assessment was carried out for each optimised process at the same level of accuracy so that the processes can be economically compared with each other. Furthermore, sensitivity analyses were done regarding site factors like the costs of purchased electricity and the biogas composition.

2 Theoretical Background for the Methanation of Biogas

2.1 Biogas, Biomethane and Power-to-Gas Systems

2.1.1 Biogas and Conventional Biomethane Production

Biogas is a possible carbon source for the PtG process which can be produced continuously. Therefore it can serve as base load source (see section 1.1.1). It consists of methane and carbon dioxide as bulk components and varies in its methane composition between 53 % - 86 % [21] depending on the kind of digested biomass. Low methane contents are obtained with green bio-waste as raw material, whereas digested carcasses produce the highest content of methane. Other raw materials are domestic waste, manure and sewage sludge, which produce biogas with medium methane content. Typical trace components are nitrogen (0 - 5 %), hydrogen (0 - 1 %), sulphur compounds (0.01 - 1 %), ammonia (0.02 - 0.5 %) and oxygen (0 - 0.5 %) [22].

Due to the usage of renewable carbon sources, the CO_2 content in the atmosphere does not increase with the combustion of the produced gas. It stays constant, because the carbon atoms released during combustion were captured before by plants, animals etc. Hence, a natural carbon cycle is established with no further increase of the CO_2 concentration in the atmosphere if biomass is harvested sustainably. The biggest part of biogas is combusted in combined heat and power (CHP) plants for electricity production. A smaller part is purified further so that it can be injected into the gas grid. In Europe, the biogas production reached 15.6 mio tonnes of oil equivalent (toe) in 2015 with Germany as leading country (7.9 mio toe) followed by the UK (2.3 mio toe) and Italy (1.9 mio toe) [24] with an increasing trend.

The four main steps in the biogas production (hydrolysis, acidogenesis, acetogenesis and methanogenesis) are illustrated in figure 2.1. In the first step (hydrolysis), large molecules such as carbohydrates, fats and proteins are hydrolysed by anaerobic hydrolytic bacteria to smaller molecules such as sugars, fatty acids and amino acids. In the next step (acidogenesis), the sugars, fatty acids and amino acids are fermented by anaerobic acedogenic bacteria to volatile fatty acids (VFA) like propionic and butyric

acids (organic acid) and to some extent to hydrogen and carbon dioxide. In the step acetogenesis, VFAs are completely degraded to acetic acids, hydrogen and carbon dioxide. In the last step (methanogenesis), hydrogen and acetic acids are converted to methane together with carbon dioxide by methanogenic bacteria according:

$$4\ H_2 + CO_2 \rightleftharpoons CH_4 + 2\ H_2O \tag{2.1}$$

$$CH_3COOH \rightarrow CH_4 + CO_2 \tag{2.2}$$

Anaerobic digestion can be performed at different temperature levels from 10 to 65 °C, for which different kind of mesophilic and thermophilic bacteria are necessary [22]. Bacteria suitable for ambient temperatures (10 - 25 °C) have slower conversion rates, but do not need extra heating. Bacteria which are performing at elevated temperatures (50 - 65 °C) show faster conversion rates, but require a constant heat source.

As already mentioned, the produced biogas consists of about 40 % carbon dioxide and 60 % methane as bulk components, water vapour and sulphur components. For the production of biomethane, further processing is needed to increase the heating value of the gas and to remove water and sulphur components from the gas. For this, carbon dioxide and sulphides are conventionally separated from the methane flow which is dried afterwards, so that the product gas fulfils general gas grid requirements for an unrestricted injection into the gas grid. This purified methane stream is referred to

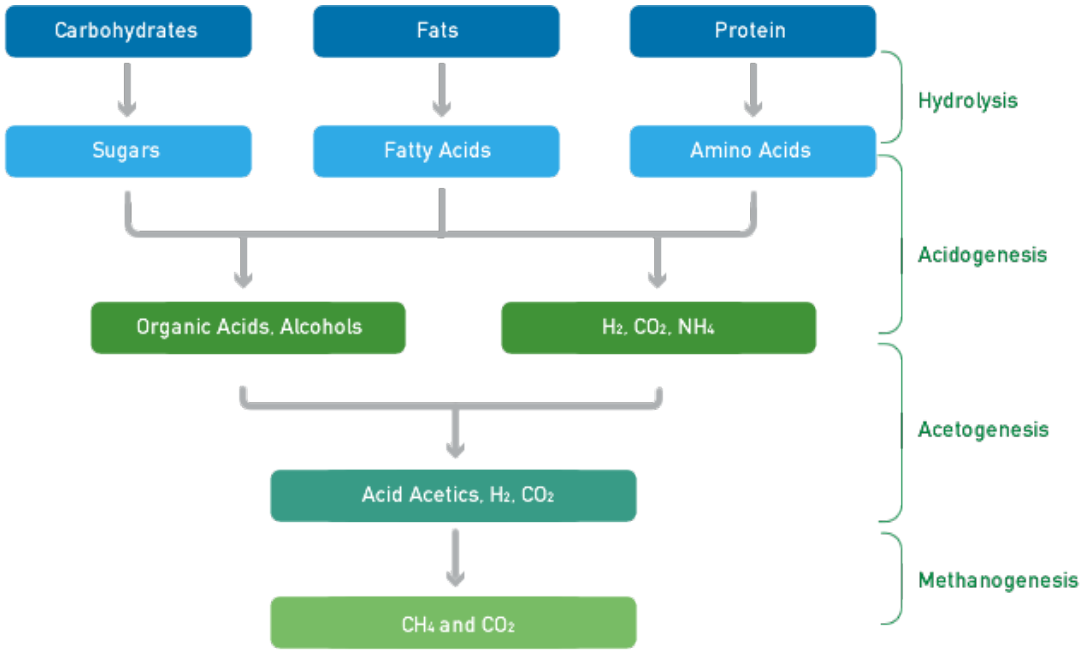

Figure 2.1: Processing steps in the biogas production [23]

as biomethane. Water scrubbing, gas separation membranes, pressure swing adsorption (PSA), and chemical scrubbing using amines are commercially applied as CO_2-separation technology [25]. From all mentioned technologies, the amine based scrubber has the highest selectivity towards carbon dioxide, whereas methane is mostly unaffected [26]. As a result, the methane content in the separated carbon dioxide stream is minimal. However, the regeneration of amine solutions requires thermal energy which is not needed in the case of gas membranes and PSA. Those technologies, in turn, require electricity for the compression to elevated pressures and are less selective so that more methane is in the separated flow. The separated carbon dioxide then is released into atmosphere where too high methane concentrations as contaminents are problematic since methane has a 34 times higher global warming potential than carbon dioxide over a 100-year time horizon [27]. The drying process is typically realised via a temperature swing adsorption (TSA) process containing desiccants which also need to be regenerated thermally. If a membrane is applied, a drying unit is not necessary, since the membrane also separates water from methane. An additional gas cleaning unit is necessary to remove trace components like H_2S and other organic sulphur compounds which otherwise would interfere with the CO_2 removal unit, other downstream equipment or the gas grid.

2.1.2 Direct Methanation of Biogas within a Power-to-Gas System

The Power-to-Gas (PtG) process replaces the conventional gas upgrade unit (gas cleaning, CO_2 separation and drying) downstream of the anaerobic digestion. In figure 2.2, the scheme of the Biogas-PtG upgrade process is illustrated. Hydrogen is produced via electrolysis operated with renewable electricity. Biomass is converted in an anaerobic digestion step mainly to methane and carbon dioxide. The biogas contains trace components like hydrogen sulphide, organic sulphur and siloxanes, which have to be removed in a gas cleaning unit before the biogas enters the catalytic methanation in order to prevent deactivation of the methanation catalyst. Combined with hydrogen, carbon dioxide from

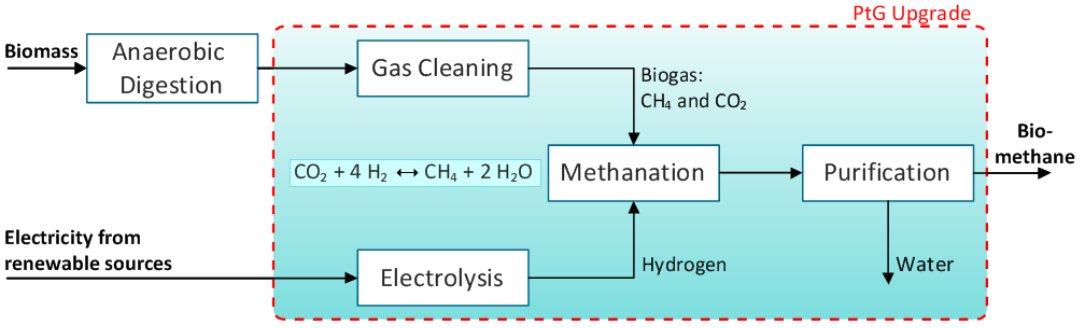

Figure 2.2: Scheme of a PtG system integrated in a biogas process

biogas is converted to methane in the methanation reactor. Further upgrading of the gas is necessary in a subsequent purification unit to reach gas grid requirements. Thanks to the integration of the PtG process into the biogas plant, synergies are created. With the integration of the PtG system, no cost intensive CO_2 separation is needed; instead the whole raw biogas stream enters the PtG system. Here, carbon dioxide is considered as a valuable raw material within the PtG process and is converted to additional methane. Due to this procedure, the product stream increases by 40 % - 80 % depending on the carbon dioxide content of the raw biogas. Thus, biomethane production can be increased significantly with the same amount of biomass used, which results in a higher raw material efficiency. Further, the catalytic methanation unit generates process heat which can be used for heat integration in the biogas plant or can be sold.

2.1.3 Potential of Biomethane in Switzerland

By far the biggest part of the natural gas in Switzerland is imported and fossil-based. The share of the nationally produced biomethane is only less than 1 %. However, the Swiss Association of Gas Industry (Verband der Schweizer Gaswirtschaft, VSG) is comitted to increase the biomethane share in the swiss gas grid to 30 % until 2030 [28]. In order to reach the challenging aim, not only more biomass (e.g. manure) must be used for the biomethane production, also the efficiency regarding the raw materials must be increased, which is possible by applying the PtG upgrade process. In figure 2.3, an energy flow diagram of the biogas and biomethane potential in Switzerland 2015 is shown. There are two applications of biogas in Switzerland. In the upper

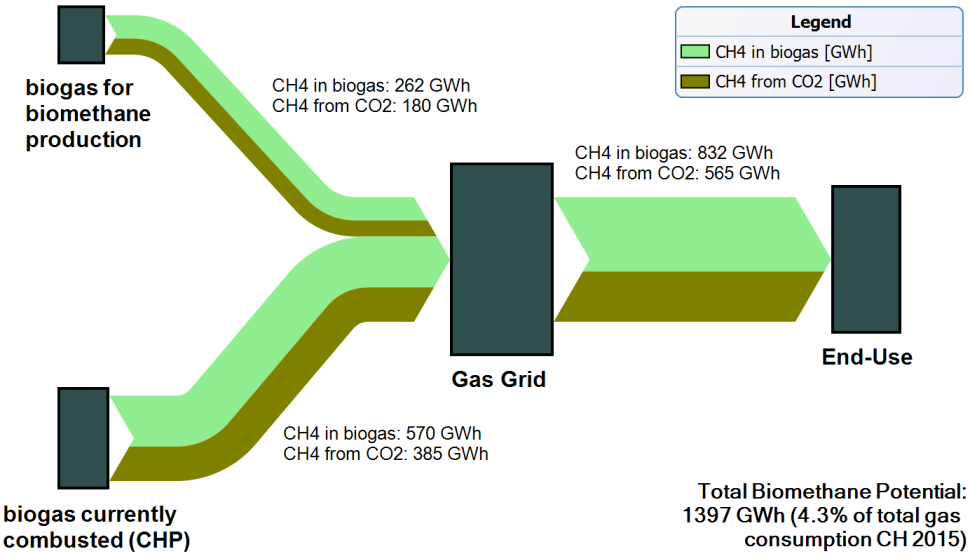

Figure 2.3: Energy flow diagram of the biogas and biomethane production in Switzerland, 2015 (Data from [29])

application (biogas for biomethane production), biogas is purified to obtain biomethane which is injected into the gas grid. The second application is the combustion of biogas to produce electricity in a CHP plant (biogas currently combusted). Two methane flows are indicated, the light-green flows refer to methane which is already in the biogas. The dark-green flows refer to methane which can be produced from carbon dioxide in the biogas with the application of the PtG-upgrade process. Currently, 262 GWh of biomethane are produced in Switzerland which is 0.8 % of the total gas sector. In combination with the PtG-upgrade, the biomethane production could be increased by additional 180 GWh due to the conversion of carbon dioxide to further methane. However as already mentioned, only a small part of the biogas is processes further to biomethane currently. If the biogas, which is currently combusted, would be conventionally upgraded to biomethane again 570 GWh of additional biomethane could be produced, and further 385 GWh with the PtG upgrade. This sums up to a five times higher biomethane production than today. Hence, the total biomethane potential in Switzerland is 1.4 TWh with no further biomass exploitation which represents 4.3 % of the total gas sector.

2.2 Methanation Technologies

2.2.1 Catalytic Methanation Reaction System

The reactions in a methanation reactor are conventionally catalysed by a nickel catalyst. The nickel catalyst material is industrial available and is characterised by low costs and medium activity. However, other materials exist which show a better catalytic performance. In figure 2.4, the costs and the interpolated descriptor for methanation activity ΔE_{diss} for different catalyst materials are shown. The descriptor of activity was put into relation with the actual activity of the catalyst materials (volcano plot) and was identified to be optimal at a value of $E_{diss,opt} = 0.06\,\text{eV}$ [30]. For higher E_{diss} - values, adsorption of C and O on the catalyst surface is weak and limits the reaction rate. Whereas, lower E_{diss} - values are referred to strong adsorption and must lead to low rates of removal of adsorbed C and O from the surface in order to form the reaction products. Figure 2.4 illustrates that ruthenium and cobalt based catalysts are more active than the nickel catalyst but their are also more expensive. A lower activity can be compensated by a larger amount of catalyst material. Hence, catalyst costs and activity together form an optimum. In the diagram, also a Ni_3Fe alloy is presented, which shows a better performance than nickel in both ways (costs and activity). The calculated performance of Ni-Fe alloys was experimentally tested and showed promising results regarding the activity in comparison to nickel catalysts [31].

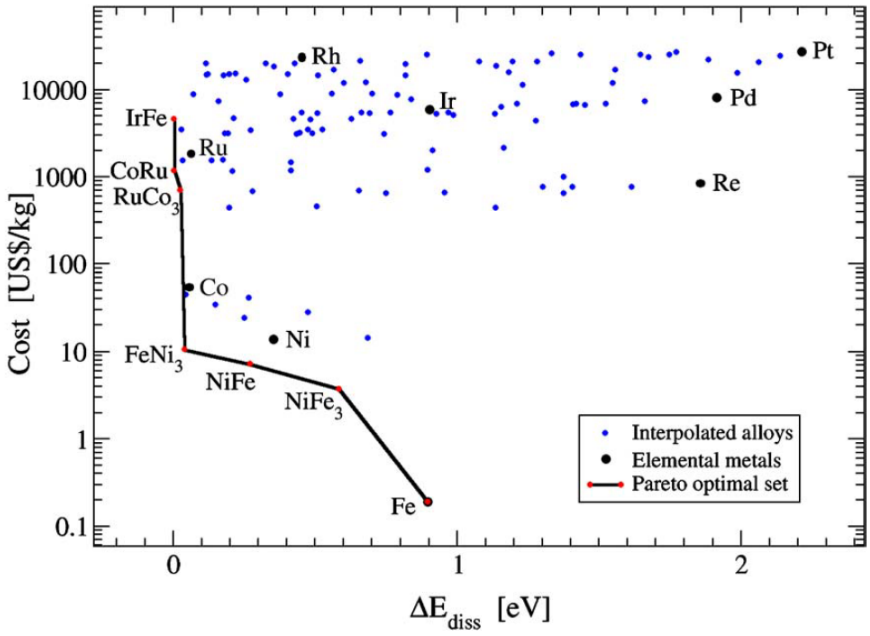

Figure 2.4: Pareto plot of activity measure $\Delta E_{diss} = E_{diss} - E_{diss,opt}$ and the cost of more than one hundred elemental metals and bimetallic alloys. Each blue point corresponds to a particular alloy. The elemental metals are shown (black), and the Pareto optimal set is also indicated (red) [30]

The methanation reaction system can be described by two chemical netto reactions:

$$CO + H_2O \rightleftharpoons CO_2 + H_2 \qquad , \Delta H_R^0 = \text{-41.16 kJ/mol} \tag{2.3}$$

$$3H_2 + CO \rightleftharpoons CH_4 + H_2O \qquad , \Delta H_R^0 = \text{-206.28 kJ/mol} \tag{2.4}$$

which are known as water gas shift (WGS) and methanation reaction. Both reactions are influenced by the chemical equilibrium, hence they can react forward and backwards depending on pressure, temperature and gas composition. Both reactions are exothermic, therefore the heat produced during the reaction has to be considered. The chemical equation for the CO_2 methanation is given by:

$$4H_2 + CO_2 \rightleftharpoons CH_4 + 2H_2O \qquad , \Delta H_R^0 = \text{-165.12 kJ/mol} \tag{2.5}$$

and is a linear combination of equations 2.3 and 2.4. In this case, the water gas shift reaction runs backwards, so that carbon dioxide together with hydrogen react to carbon monoxide and water, and further to methane. Due to this reason, the heat of reaction or standard reaction enthalpy from the methanation reaction is reduced by the now endothermic part of the WGS reaction.

The relationship between the equilibrium constant K_p and the standard reaction enthalpy $\Delta H_R^0(T)$ is laid down within the Van't Hoff equation:

$$\frac{\partial ln(K_p)}{\partial T} = \frac{\Delta H_R^0(T)}{R\,T^2} \tag{2.6}$$

The standard reaction enthalpy is standardised to the pressure of 1 atm but depends on the temperature and is determined in the following way:

$$\Delta H_R^0(T) = \sum_i \nu_i H_{f,i}^0(T) \quad \text{with } H_{f,i}^0(T) = H_{f,i}^0(T^0) + \int_{T^0}^{T} c_{p,i}(T)dT \tag{2.7}$$

as the sum of the standard reaction enthalpy multiplied by the corresponding stoichiometric factor ν_i per component i of the reaction. The standard reaction enthalpy at reference temperature T^0 is listed in thermodynamic data banks. The heat capacities $c_{p,i}$ are given by correlations and are also obtained from thermodynamic data banks. The reaction constant K can be determined with the mathematical relationship:

$$ln(K) = -\frac{\Delta G_R^0(T)}{R\,T} \tag{2.8}$$

And the mathematical expressions for the Gibbs free enthalpy $\Delta G_R^0(T)$ with:

$$\Delta G_R^0(T) = \Delta H_R^0(T) - T \cdot \Delta S_R^0(T) \tag{2.9}$$

The standard entropy $\Delta S_R^0(T)$ is calculated similarly to the enthalpy with:

$$\Delta S_R^0(T) = \sum_i \nu_i S_i^0(T) \quad \text{with } S_i^0(T) = S_i^0(T^0) + \int_{T^0}^{T} \frac{c_{p,i}(T)}{T} dT \tag{2.10}$$

The reaction constant K equals the equilibrium constant K_p if the reaction reached its equilibrium state. The equilibrium constant is calculated with:

$$K_p = \prod_i p_i^{\nu_i} \tag{2.11}$$

with $\nu_i > 0$ for products and $\nu_i < 0$ for reactants. Hence, the reactions depend on pressure, temperature and composition which is illustrated in figure 2.5 and figure 2.6 for the CO_2 methanation. The inlet composition is a binary mixture of hydrogen and carbon dioxide in a relation of 4:1. The equilibrium concentrations are calculated with the method of minimising Gibbs enthalpy via the simulation software *Aspen*. The reaction is mole reducing, therefore it is evident that the conversion to methane increases with the pressure. Correspondingly, the concentrations of the reactants hydrogen and carbon

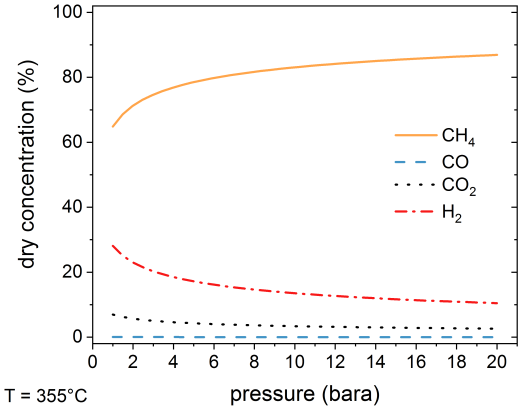

Figure 2.5: Dry equilibrium concentrations of CO_2 methanation as a function of the pressure of the components methane, carbon monoxide, carbon dioxide and hydrogen at 355°C for an input composition of hydrogen and carbon dioxide in a relation of 4:1

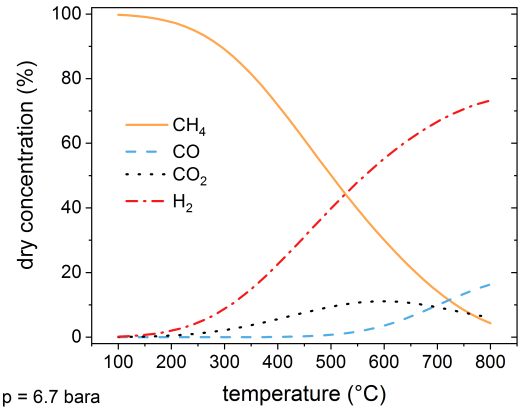

Figure 2.6: Dry equilibrium concentrations of CO_2 methanation as a function of the temperature of the components methane, carbon monoxide, carbon dioxide and hydrogen at 6.5 bara for an input composition of hydrogen and carbon dioxide in a relation of 4:1

dioxide decrease with the pressure as shown in figure 2.5. The reaction from carbon monoxide to methane is favoured by the thermodynamic equilibrium, so that almost no carbon monoxide stays unconverted in this case. The gradient of methane concentrations becomes smaller with the pressure, so that at elevated pressures no large improvements can be achieved regarding the conversion with a further pressure increase. In figure 2.6, the equilibrium concentrations as a function of the temperature is illustrated with same inlet composition as described in the figure before. The methanation reaction is favoured by low temperatures due to its exothermic nature so that at 100°C, the conversion from carbon dioxide to methane is close to 100%. However, it must be considered, that below 200 - 250 °C, the nickel in the catalyst may form, together with carbon monoxide, nickel tetracarbonyl [32] which is generally considered to be one of the most toxic industrial chemicals [33].

$$Ni(s) + 4\ CO \rightarrow Ni(CO)_4(g) \tag{2.12}$$

The US health exposure limit IDLH (immediately dangerous to life or health) for the gaseous nickel tetracarbonyl is set to 2 ppm which is 600 times lower than the IDHL for carbon monoxide. Therefore, reactor temperatures below 200 - 250 °C should be avoided. Corresponding to figure 2.6, the methane concentration decreases with further increasing temperature and vice versa, the reactant concentrations (CO_2, H_2) increase. The carbon dioxide concentration shows a maximum at 600 °C together with an increasing share of carbon monoxide. From this point on, the reversed WGS shift reaction

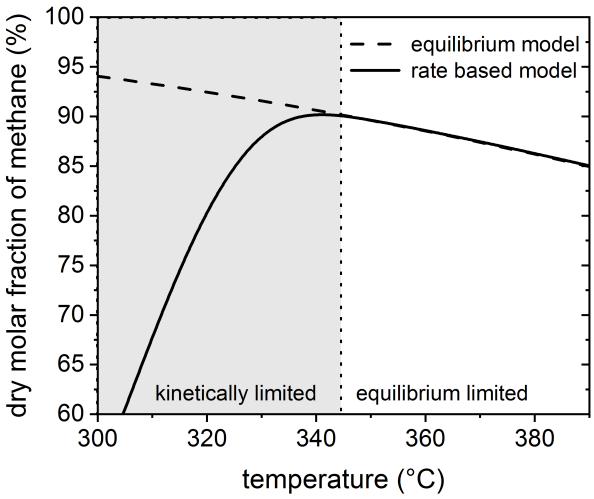

Figure 2.7: Methane concentration as a function of the temperature for the equilibrium model and the rate based model; feed: biogas with 62 vol-% methane and 38 vol-% carbon dioxide, $H_2/CO_2 = 4.0$, $H_2O/CO_2 = 0.5$; p = 6.7 bara

and the reversed methanation reaction are thermodynamically favoured, so that carbon monoxide from methane and carbon dioxide are mainly produced. The hydrogen concentration increases with the temperature, because less hydrogen is converted to methane and the hydrogen amount required for converting carbon dioxide to carbon monoxide is three times smaller (WGS reaction).

However, the discussed reactions do not only depend on thermodynamics. They are also influenced by kinetic effects. In figure 2.6, almost 100% conversion to methane was reached at 100 °C in the equilibrium state. However, the catalyst is not fully active at those low temperatures so that clearly lower conversion rates are obtained in experiments. In order to consider this behaviour, kinetics of the catalyst for the given chemical equations have to be applied which was done with the Langmuir-Hinshelwood approach in the form of:

$$k = \frac{(\text{kinetic term})(\text{driving force})}{(\text{adsorption term})} \tag{2.13}$$

The Langmuir-Hinshelwood approach considers besides a kinetic term a driving force term and an adsorption term. The adsorption term takes the surface coverage of the relevant components into account which slows down the reaction progress. The driving force term is expressed via partial pressures of considered gas components. Additionally, the thermodynamic equilibrium term was included to the rate expressions, which are listed in chapter 3 as equation 3.8 and 3.9 for the fluidised bed and as equations

3.19 and 3.20 for the fixed bed methanation. The effect of the implemented kinetics on the conversion to methane is illustrated in figure 2.7. Here, the methane concentration downstream of CO_2-methanation is shown as a function of the reactor temperature for the simple equilibrium model and the rate-based model. As already discussed, the conversion to methane increases with lower temperatures considering only the thermodynamic equilibrium. The rate-based model shows at lower temperatures only low methane concentrations. Here, the reaction is limited by kinetic effects. With increasing temperature, the catalyst becomes more active and the methane concentration of the rate based model reaches the equilibrium concentration so that a maximum is formed. With further increasing temperature, the reaction now is limited by thermodynamic effects which results again in lower methane concentrations.

2.2.2 Fixed Bed

The properties of methanation reactors are governed by the dissipation of heat which is produced extensively during the exothermic methanation reaction. Fixed bed reactors for methanation can be distinguished between adiabatic and cooled reactors. A schematic illustration is given in figures 2.8 and 2.9. Adiabatic fixed bed reactors (figure 2.8) are built regularly in a multi-stage process with intermediate cooling. In the first stage, temperatures increase up to 650 °C (with product gas recirculation) or 800 °C (without product gas recirculation) [34]. At those elevated temperatures, the reaction is strongly limited by the thermodynamic equilibrium which results in low conversion rates. The qualitative temperature profile as a function of the obtained methane concentration is given in figure 2.10 with the limiting equilibrium course for a three-stage adiabatic reactor and for a cooled fixed bed. To overcome this restriction, the product gas from the first stage is cooled to a minimum temperature where the catalyst is still active and is injected into a second stage. Here, the remaining reactants are supposed to convert further. The heat production is smaller due the smaller amounts of reactants left, so that the temperature increase is less pronounced and with that, a more beneficial equilibrium state is obtained which allows further conversion. This procedure is repeated until the desired conversion is obtained, which results typically in three to five stages, followed by condenser and trim reactor. In order to dampen the temperature peak at

Figure 2.8: Adiabatic fixed bed reactors with intermediate cooling

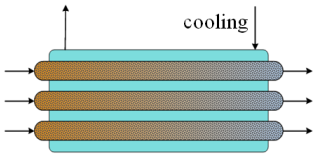

Figure 2.9: Cooled fixed bed as multi-tubular reactor

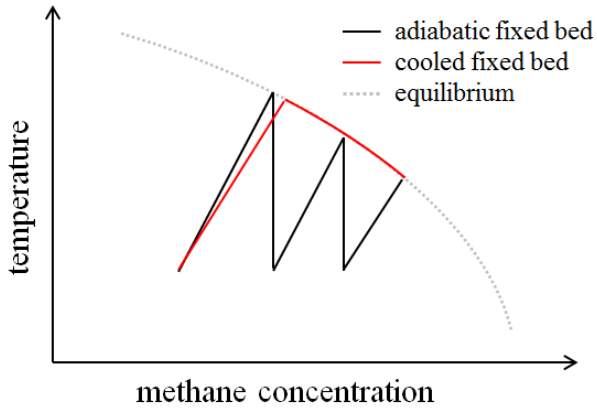

Figure 2.10: Qualitative temperature profiles of adiabatic multi-stage fixed bed reactors and a cooled fixed bed reactor

the beginning of the first reactor, a recycle flow of a part of the cooled outlet gas can be redirected to the first reactor. With this procedure, the reactive gas flow is diluted with cooler and quasi-inert gas.

A cooled fixed bed reactor is typically built as a multi-tubular reactor as illustrated in figure 2.9. The catalyst is present inside the tubes and the cooling medium flows on the shell side. As cooling fluid, molten salts are typically used with operation temperatures between 220 °C and 600 °C for different salt types [35]. The main disadvantage of this salts is the high melting point, so that the salt freezes and block the heat exchanger tubes if it is not permanently heated. Despite the cooling, a large temperature increase at the beginning of the reactor is obtained (figure 2.10) due to the small heat exchange area in comparison to the volume where the heat is produced. Again, the thermodynamic equilibrium limit is reached at high temperatures which restricts the conversion and the corresponding heat production. Due to decreased heat production, the cooling system is able to reduce the gas temperature for the rest of the reactor length. The conversion follows the equilibrium concentration and is therefore heat transfer limited. The temperature is decreased as long as the catalyst is not significantly restricted by kinetic effects.

2.2.3 Bubbling Fluidised Bed

A bubbling fluidised bed reactor consists of a vessel with internal heat exchanger tubes (see figure 2.11). From below, the feed gas is injected with a specific velocity which moves the catalyst particles inside the vessel. The minimum fluidisation velocity u_{mf} is an important parameter to describe a bubbling fluidised bed. At the minimum fluidisation velocity, the hydrodynamic drag force F_D and the gravitational force F_G are in balance

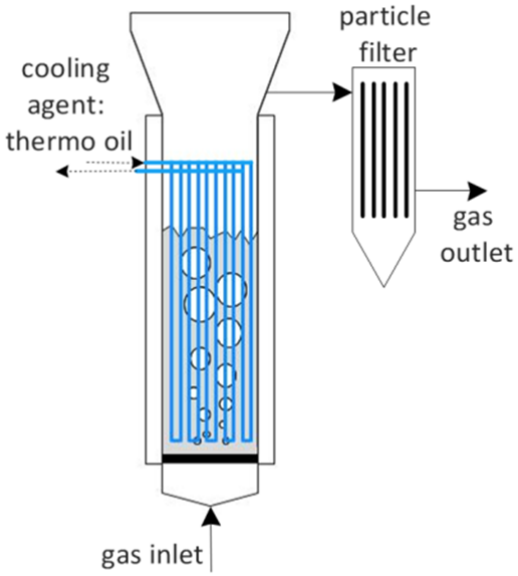

Figure 2.11: Scheme of a bubbling fluidised bed reactor

so that the particles are in suspension. With further increasing gas velocity, bubbles are established between the particles which creates two phases: the bubble phase and the dense phase. In the bubble phase, the amount of catalyst particles is minimum, hence the major part of the reaction is assumed to be in the dense phase. The gas flow is divided into the mentioned dense phase flow and the bubble phase flow, which is expressed via the equation for the visible bubble velocity v_b:

$$v_b = u - u_{mf} \tag{2.14}$$

Here, the part of the gas flow which exceeds the flow required for minimum fluidisation velocity ends up in the bubble phase. However, experiments in literature have shown that this expression overestimates the bubble velocity [36] and a correction factor $\psi \leqq 1$ was proposed so that:

$$v_b = \psi(u - u_{mf}) \tag{2.15}$$

The exact value for ψ depends on the particle size and on the ratio of the height of the bubbles to the reactor diameter H_b/d_{reac}. For large heights and small diameters, the ψ factor is close to one so that more gas is present in the bubble phase. Current research has shown that also with heat exchanger internals, the coalescence of the bubbles progresses over the reactor height and the measured chord length of the bubbles increases until a u/u_{mf} - value of six [37]. Also for higher u/u_{mf} - values, it cannot be excluded that the bubble size is increasing over the height, since only the chord length was measured

and wider bubbles are not represented by this method. Additionally, coalescence of the bubbles was also observed for increased fluidisation numbers. With sufficient fluidisation of the catalyst particles, the produced heat of reaction is distributed equally over the total height of the reactor. The heat exchanger area of the whole reactor is used to dissipate the heat so that close to isothermal conditions are obtained. Hence, for the bubbling fluidised bed, the reaction can be operated over the whole reactor length at optimum temperature like indicated in figure 2.7 which results in a smaller reactor volume for a specified conversion rate in comparison with a cooled fixed bed reactor. An increased fluidisation is also beneficial for the regeneration of the catalyst material which is circulating over the whole reactor height. Catalyst particles in a reactor zone with high catalyst stress (region close to inlet) are transported to zones with less catalyst stress (upper region), so that the catalyst can regenerate from carbon atoms adsorbed on its surface. Due to this property, it is also possible to convert alkenes such as ethylene to methane. Between the dense and the bubble phase, mass transport $\dot{n}_T$ is established due to (1) concentration differences between the phases caused by the reaction in the dense phase and (2) the gas volume differences, since the methanation reaction is mole reducing.

$$\dot{n}_{T,i} = K_{G,i} \cdot A_T \cdot (c_{b,i} - c_{d,i}) + \dot{n}_{bulk} \cdot x_{b,i} \tag{2.16}$$

The mass transport of the reactants from the bubble to the dense phase is essential for high conversion rates in the reactor. The mass transport is influenced by the interface mass transport area A_T which corresponds to the surface area of the bubbles. On the one hand, large gas flows for the fluidisation ensure an even heat distribution over the reactor height for a sufficient heat dissipation. On the other hand, large gas flows result in increased bubble diameters, which decreases the bubble surface area in proportion to the gas volume in the bubble phase. As consequence, the interface mass transport is reduced. Hence, a trade-off has to be found between fluidisation and interface mass transfer, so that the inlet gas flow is large enough for a sufficient fluidisation, but still ensures good mass transfer properties.

In summary, the fixed bed reactors are limited by heat transfer whereas the bubbling fluidised bed reactors are limited by interface mass transfer between the bubble and the dense phase. However, the effect of the corresponding limitation is more pronounced for a fixed bed reactor which results in larger reactor volumes required in comparison with a fluidised bed reactor. A more detailed mathematically description of both reactor types can be found in chapter 3.3.2.

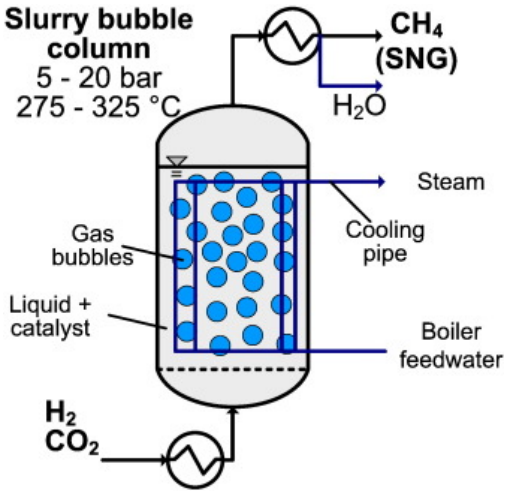

Figure 2.12: Scheme of a slurry bubble column reactor [38]

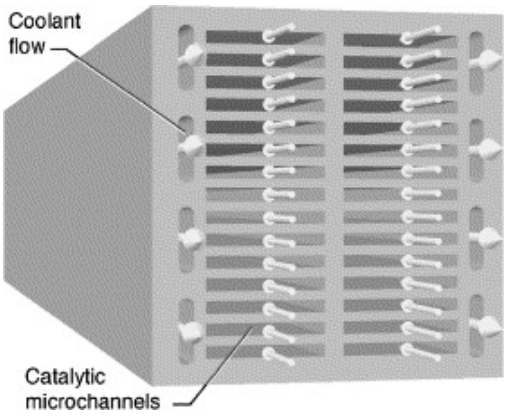

Figure 2.13: Scheme of a section of microchannel reactor [39]

2.2.4 Other Catalytic Reactor Types

Other catalytic methanation reactor types, inter alia, are bubble column reactors, micro channel reactors and monolithic reactors. Like for the fixed and the fluidised bed, the characteristic parameters for the reactor performance are the mass and heat transfer, as well as flow conditions, temperature and pressure.

A slurry bubble column is illustrated in figure 2.12. The reactor vessel contains a heat transfer liquid in a mixture with the catalyst particles, typically a nickel catalyst. From below, the gaseous reactants are injected via a distributor plate for a small bubble size in the liquid. The gaseous reactants have to be transported through three phases to be converted from gas to liquid and from liquid to solid (catalyst particles). The internal heat exchanger dissipates the reaction heat which is transported efficiently by the heat transfer liquid. Similarly to the fluidised bed, the effective heat transport allows isothermal conditions in the bubble column for an optimal reactor temperature. Also catalyst replacements can be done during operation and the bubble column shows a good dynamic behaviour [40]. However, with the additional liquid phase, the reaction in this reactor type is mainly limited by the gas-liquid mass transfer [38]. Another issue of combining the heat transfer liquid with the catalyst is the maximum allowable temperature of the liquid which can be in the range where the catalyst is still kinetically limited. As a result, the reactor temperature is below the optimal point so that conversion rates are below the therodynamic limit. For higher temperatures, the heat transfer liquid starts to evaporate or to decompose [38].

In a monolithic packed bed reactor, two phases are present: the reactive gases and the solid catalyst material coated on a monolith support which can be arranged in a "honeycomb" structure or as foams or fibres [41], [42]. Due to this structure, the pressure drop can be lower and the heat transfer is improved in comparison to a fixed bed with spherical particles or pellets [43]. The monolithic support materials typically are Al_2O_3 and SiO_2 and cement $CaCO_3$ [43] or from corrugated metal sheets which are rolled up. The active catalytic material in a monolithic catalyst is located near the exterior surface of each channel, rather than distributed throughout the bulk of the support, providing a high effectiveness [44] and a higher activity compared to pellet nickel. Also smaller pore diffusional resistance and high mass transfer rates in monolithic catalysts are beneficial for the reactor performance [45]. However, when the catalyst material must be exchanged due to deactivation, the whole monolithic structure has to be replaced which is more expensive than the catalyst replacement in the other presented reactor types.

Another option for improving heat and mass transfer in a methanation reactor is a micro-channel design as shown in figure 2.13. The reactive gases flow through the rectangular channels. Similarly to the monolithic structures, the catalyst is directly applied to the channel walls. The micro-reactor is cooled from the side walls with heat transfer liquid. Due to the micro-structure, those reactor types can deliver high heat- and mass transfer between the reactive gas flow and the channel walls [39]. Hence, a precise temperature control and a compact design is possible. As a consequence, medium temperature profiles can be established over the reactor length which can increase the conversion further by using kinetic and thermodynamic effects. The exchange of the catalyst in this kind of micro channel reactor is not possible. The whole reactor structure has to be replaced, which is associated with high costs.

2.2.5 Biological Methanation

The biological methanation is catalysed by the micro organisms methanogenic archaea [49]. This anaerobic specie carries out the last step of the anaerobic digestion of biogas, the methanogenesis (see section 2.1.1). Mainly hydrogen and carbon dioxide are converted to methane by these microbes which belong to the thermophilic organisms with operation temperatures at about 60 °C [50]. Typically, continuously stirred and pressurised reactor tanks are applied for the biological methanation. In the tank, the nutrient medium is present containing the microbes, and from below the feed gas is inserted which consists of hydrogen and the carbon dioxide source (biogas or pure carbon dioxide). For this technology, the following operation parameters are essential: (1) Increased temperatures up to 65 °C are beneficial for a higher productivity of the mircrobes [50] due to increased reaction rates. (2) High mechanical mixing rates increase the mass transport of hydrogen from the gas phase to the liquid phase. The limiting effect in the

methanation type	reactor type	vol. spec. performance ($kW_{SNG}/l_{reactor}$) $\sim$ 90% methane	$>$ 95% methane	source
biologic	CSTR	0.04	0.02	[46]
biologic	CSTR	-	0.002	[47]
biologic	CSTR		0.03	[48][1]
catalytic	FB	0.5[2]	-	this work
catalytic	BFB	2.3[3]	-	this work

Table 2.1: Volume specific reactor performances for different methanation technologies and methane concentrations (dry) in the product gas with biogas as feed; SNG: synthetic natural gas, CSTR: continuous stirred tank reactor, FB: fixed bed reactor, BFB: bubbling fluidised bed reactor

biological methanation is the dissolution of hydrogen [48]. However, stirring rates at high speed are energy intensive with an electricity consumption of 0.2 kW_{el}/kW_{newCH_4} which is about three quarters of the total electricity consumption of the methanation process (without electrolysis) [48]. (3) The residence time or correspondingly the reactor volume in relation to the feed flow, influences the conversion rates to methane which results in large reactor sizes in comparison to the feed volume flow to obtain methane concentrations higher than 95 vol-%. In table 2.1, the volume specific performance for different methanation technologies is listed for the application of biogas upgrading. Here, it is distinguished between the obtained methane concentration in the product gas. For the catalytic methanation, concentrations of methane above 95 vol-% after one stage are not possible due to the equilibrium restrictions at elevated temperatures. Methane concentrations in the biological methanation can exceed 95 vol-% due to the lower temperatures, but require a clearly larger reactor volume. In comparison to the catalytic methanation, the reactor size of the biological tank is about one order of magnitude larger for 90 vol-% methane in the product gas. If the biological reactor is designed for producing SNG (synthetic natural gas) which fulfils the gas grid requirements for unrestricted injection, the reactor size can be two orders of magnitude larger in comparison to a catalytic methanation. The differences in the volume specific performance between the fixed bed and fluidised bed reactors are caused by the heat transfer properties of the reactors.

For improving the mass transfer from the gas to the liquid phase in the biological methanation reactor without energy-intensive stirring, other reactor types are investigated recently. One option is a trickled bed with packings with a large contact area

[1] MicrobEnergy
[2] Reactor volume includes the shell side cooling
[3] Reactor volume includes the internal tubes for cooling

between the gas and liquid phase for an enhanced mass transfer [51]. Another option are hollow-fibre membrane reactors, where the feed is injected into the tank with the microbes via hollow fibres. The gas permeating through the membrane forms very small bubbles in the tank, which again increases the contact area between gas and liquid phase [52].

2.3 Gas Separation Membrane Technologies

2.3.1 Separation Process

The separation process in a gas separation membrane is characterised by (1) partial pressure differences as driving force between the high (retentate) and low pressure side (permeate) ($p_{i,ret} - p_{i,per}$) and by (2) a permeability parameter (C_i) specific for each component i and the membrane material. The permeability describes the ability of permeation for each component through the membrane wall which differs corresponding to the properties of the components. The components can be distinguished between high-permeable and low-permeable species. The unit of the permeability is typically expressed in Barrer with:

$$1 \text{ Barrer} = \frac{10^{-10}\ cm^3(STP)\ cm}{cm^2\ s\ cmHg} \tag{2.17}$$

which is rewritten in SI-units:

$$1 \text{ Barrer} = 7.5 \cdot 10^{-13} \frac{m^3(STP)}{s\ m\ bar} \tag{2.18}$$

The permeating volume flow $\dot{V}_i$ can be described by Fick's law:

$$\dot{V}_i = \frac{C_i \cdot A\ (p_{i,ret} - p_{i,per})}{s} \tag{2.19}$$

Additionally to the partial pressure differences and the permeability factor, the membrane area A and the effective thickness of the membrane s characterise the permeation. The effective thickness corresponds only to the membrane layer which represents a resistance for the gas components to pass. This layer typically sits on top of a thicker porous layer which serves a supporting material. Besides the permeability factors, a common parameter to describe the performance of a membrane is the ideal selectivity $\alpha_{i/j}$ given by:

$$\alpha_{i/j} = \frac{C_i}{C_j} \tag{2.20}$$

This expression reflects the ability of a membrane to separate two gases from each other where the permeability of a highly permeable gas i is put into relation to the permeability of a low-permeable gas j.

The permeability factor C_i is commonly described by a 'diffusion-solution' model or a 'resistance' model. The permeability is expressed for the 'diffusion-solution' model with:

$$C_i = S_i \; D_i \tag{2.21}$$

where the components first dissolve on the membrane surface at the high pressure side. Then, the gas components diffuse through the membrane to the low pressure side. The diffusion depends on the temperature, whereas the solution is influenced by the partial pressures of the components. A more detailed description regarding the determination of the two parameters is given in section 6.2.2. The other model refers to the resistance R in a electrical circuit for the determination of the permeability [53]. The current I is described as the ration of voltage U and resistance R:

$$I = \frac{U}{R} \tag{2.22}$$

which is applied to the equation 2.19 for each component i so that:

$$V_i = \frac{\Delta p_i}{R_i} \tag{2.23}$$

with the expression for R_i given by:

$$R_i = \frac{s}{C_i \; A} \tag{2.24}$$

The total resistance is described analogously to an electrical circuit including parallel and serial connections. For this, the membrane thickness is divided into different zones of resistance with parallel or/and serial elements e.g. in the effective layer R_{zone1}, pores or defects in the effective layer R_{zone2}, porous supporting layer R_{zone3}, coating R_{zone4} etc. The two different resistances in the effective layer are seen as parallel connection, the rest is a serial connection so that the total resistance is expressed by:

$$R_{tot,i} = \frac{R_{zone1,i} \; R_{zone2,i}}{R_{zone1,i} + R_{zone2,i}} + R_{zone3,i} + R_{zone4,i} \tag{2.25}$$

Each resistance $R_{zoneX,i}$ has to be determined separately according to 2.24 by:

$$R_{zoneX,i} = \frac{s_{zoneX}}{C_{zoneX,i} \; A_{zoneX}} \tag{2.26}$$

	H_2	CO_2	CH_4	CO
T_{crit}, °C	- 269.8	31.1	- 82.6	- 139.2
p_{crit}, bara	13.0	73.8	46.0	35.1

Table 2.2: Critical data [54]

However in this approach, the permeability $C_{zoneX,i}$ is set constant and cannot reflect the influence of the partial pressure of each component and the temperature on the permeability, whereas the 'diffusion-solution' model includes this relationship.

An option for improving the mathematical description of the transport processes in the membrane is the consideration of non-ideal behaviour of the gas species. For low pressures and high temperatures in adequate distance to the critical point of the considered components (table 2.2), ideal behaviour of the gas components can be assumed. For this, the following assumptions are made: (1) no intermolecular forces between gas molecules exist, (2) the molecules occupy no volume or the volume is negligibly small in comparison to the space around them and (3) collisions of molecules are perfectly elastic, so that no kinetic energy is lost. The membrane usually is operated at medium pressures and temperatures, so that non-ideal gas behaviour can be expected to some extent. In order to describe the deviation of the non-ideal behaviour to the ideal gas, the fugacity f_i can be applied which is defined by:

$$f_i = \varphi_i \cdot p_i \tag{2.27}$$

The fugacity coefficient φ_i equals one for ideal gas, so that the fugacity f_i corresponds to the partial pressure p_i of a component i and the ideal gas law can be applied. For non-ideal behaviour of the gas, the fugacity coefficient can become greater one or smaller one which has the following physical meaning:

- $\varphi > 1$: repulsion forces are present between the molecules
- $\varphi < 1$: attraction forces are present between the molecules

In figure 2.14, the fugacity coefficients are illustrated for the components hydrogen, methane and carbon dioxide as a function of the temperature at the pressure levels of 2 bar and 10 bar. The value one is marked as ideal gas. As mentioned earlier, for increased temperature and low pressure, the fugacity coefficients are close to the ideal-gas line. With decreasing temperature, and at elevated pressure the effect of the non-ideal behaviour of the gases become larger. For carbon dioxide and methane, the fugacity coefficients are smaller one so that attraction forces are predominant. For hydrogen, repulsion forces are prevalent with a fugacity coefficient greater than one. At a pressure

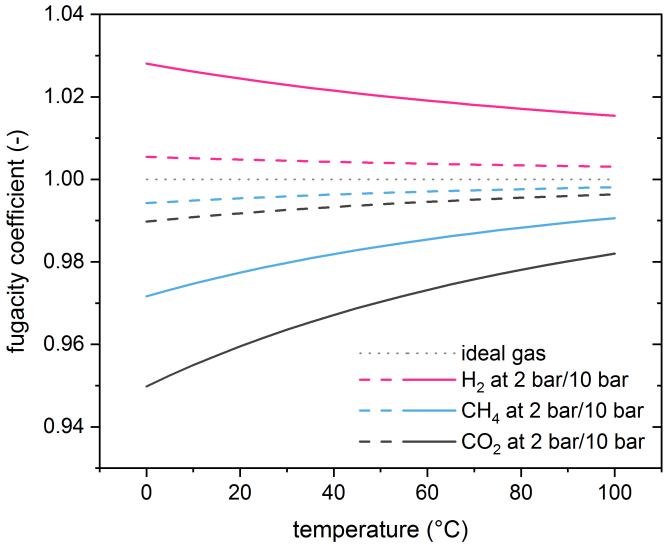

Figure 2.14: Fugacity coefficients φ_i for the gases hydrogen, methane and carbon dioxide as a function of the temperature for two different pressures calculated with the simulation software *Aspen* for the gas mixture: CH_4 85%, H_2 13%, CO_2 2%

of two bar, the non-ideal behaviour of the gas components is negligible. However, at elevated pressure, the non-ideal effect becomes larger, so that at 10 bar for a temperature relevant for a membrane (app. 40 °C), the consideration of non-ideal gas behaviour is justified. The concentration of the components in the gas mixture has an influence on the fugacity coefficient. In general, a low concentration of the presented components results in a larger deviation from ideal gas and vice versa due to the increased interactions between different types of molecules. However, the effect of the concentration is not as pronounced as of temperature and pressure. For the implementation of real gas behaviour, equation 2.19 has to be adapted so that the partial pressures are exchanged with the fugacity for each component.

2.3.2 Membrane Material Types

During the last decades, gas separation membranes became industrially relevant as purification technology. In general, polymeric membranes are mainly used in industrial applications due to the low costs, ease of processing and high packing density [55]. A large number of polymers has been developed over the last decades. However, this section will focus on different types of polymers which are actually applied in industry.

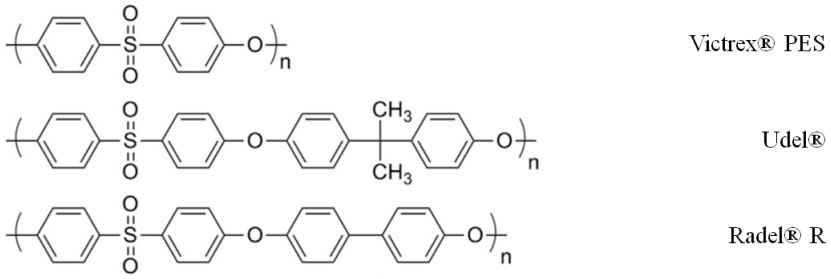

Figure 2.15: Chemical structure of selected polysulfones, adapted from [58]

Polysulfones

Polysulfones (PSF) consist of aromatic diphenylene sulfone repeated units (-Ar-SO_2-Ar-) and are considered to be one of the most chemically and thermally stable thermoplastic polymers available [56]. They are applied for hydrogen and air separation, inter alia, due to their high selectivites [57]. There are several commercially applied polysulfones such as Victrex ® PES, Udel® and Radel® R illustrated in figure 2.15. Polysulfones are characterised by excellent mechanical properties, a wide operating temperature range, good chemical resistance and easy production of membranes in a variety of configurations for establishing the required properties [56]. For this, the gas transport properties of polysulfones have been broadly studied [59–67]. Symmetric bulky substitutions, like methyl groups, on the phenyl rings increase the permeability whereas asymmetric substitutions of the same groups reduce the permeability [68]. However, the adaptation towards large permeabilities can cause higher affinity of plasticisation by gases like carbon dioxide [67] which results in swelling of the polymer and with that the permeability increases of all components. As consequence, selectivities are decreasing.

Cellulose acetates

The first generation of commercial membranes applied for natural gas separations were based on cellulose acetates (CA) [57, 69–71]. Besides high selectivities, the improved permeability rates were important for the commercialisation of the CA membranes which results in a decrease of the required membrane area for the separation task. Initially, this membrane type was applied to desalination processes [72]. CA membrane modules have low costs in their production due to inexpensive raw material (cellulose) and a relatively high grade of industrial maturity of the production process [73]. Also this type of membrane material tends to plasticises in the presence of carbon dioxide which results in a decrease of CO_2/CH_4 selectivity on one hand, but in an increase of CO_2 permeability on the other hand [74] which might compensate the worsened selectivity by an increased mass transport (see section 4.4.1).

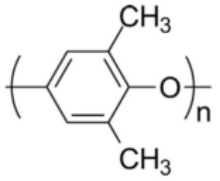

Figure 2.16: Chemical structure of poly(phenylene oxide) (PPO)

Poly(2,6-dimethyl-1,4-phenylene oxide)

Poly(2,6-dimethyl-1,4-phenylene oxide) (PPO) was industrially implemented first by General Electrics and AKZO [75]. Due to the good mechanical properties and the thermo-oxidative stability, PPO was the first commercialised aromatic polyether and is still used in many industrial applications such as gas separations [76]. The PPO material shows high permeabilities together with medium selectivities so that less membrane material is required for the separation task if no high purity on the permeate side is needed. For this kind of separation, PPO membranes are cost effective. The high permeabilities result from the kinked ether linkage and the absence of polar groups which suppress efficient chain packing and densification so that a large fractional free volume (FFV) is established [58]. Unfortunately, large fractional free volumes (FFV) tend to have higher aging rates (aging: decrease of FFV over time), than polymers with low FFV [58]. The moderate selectivities are caused partially by the absence of polar moieties on the polymer backbone [77]. As consequence, most research was done by adding several functional groups to improve selectivity [65, 78–84].

Polyimides

Aromatic polyimides are characterised by high selectivities and mechanical stability. These materials are widely applied in industry e.g. by Air Liquide, Praxair, Parker-Hannifin and Ube [57]. Matrimid® is an industrial available aromatic polyimide which consists of the groups BTDA (3,3'-4,4'-benzophenone tetracarboxylic dianhydride) and DAPI (diaminophenylindane) [85, 86]. Additionally, bulky groups stretch out of the plane (e.g. methyl and phenyl groups) so that the polymer backbone becomes stiff which

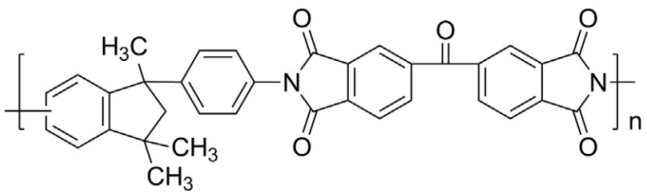

Figure 2.17: Chemical structure of the polyimide Matrimid®

Polymer	H_2	CO_2	O_2	N_2	CH_4
Matrimid®[4]	17.5	7.29	1.46	0.22	0.21
CA-2.45[5]	12	4.8	0.82	0.15	0.15
PSF[6]	14	5.6	1.4	0.25	0.25
PPO[7]	61	61	16.8	4.1	4.3

Table 2.3: Permeability of pure components of commercially relevant polymers

results in a high thermal stability of the material up to 300 °C [58]. The chemical structure of Matrimid is illustrated in figure 2.17. Matrimid has one of the highest H_2/CH_4 selectivities among the presented polymers so that this membrane is interesting for the separation of hydrogen from SNG after a methanation unit. However, permeability rates are small to medium which results in a larger required membrane area. Additionally, this membrane type is significantly more expensive than many other commercial polymers, such as polysulfone [58].

Comparison of the Presented Polymers regarding Hydrogen Separation from Methane

The permeabilities of the presented polymers are listed in table 2.3. The corresponding ideal selectivities can be calculated with equation 2.20. The PPO polymer shows by far the highest permeability for all listed compounds. The other polymers have a similar range of permeability. As already mentioned, higher permeability rates result in a smaller required membrane area due to the larger permeation flow so that the costs decrease. Hence, the PPO membrane has a potential to save costs in comparison to the other polymers. However, the trade-off between permeability and selectivity has to be considered, so that for the PPO membrane the selectivities are generally lower than for the other polymers. In figure 2.18, the mentioned trade-off is illustrated with the H_2/CH_4 selectivity as a function of H_2 permeability for the presented polymers. High permeabilities come at costs of the selectivity, so that the upper right corner of the diagram contains no data points. In literaure, it has been recogniced that the selectivity for gas pairs varies inversely with the permeability of the more permeable gas of the specific pair [90]. An upper bond for this relationship could be identified for various gas pairs. Above the upper bond, no values existed at that time (1990) [90]. Corresponding to the trade-off, the Matrimid membrane shows the best performance because it is the closest to the upper bond. Nevertheless, that does not necessarily mean, that this membrane is the most feasible polymer for the separation of hydrogen from methane since also

[4] at 35 °C and 4 bar, from [87]
[5] Cellulose acetate, at 1 bar and 35 °C, from [88]
[6] Polysulfone, CO_2 and CH_4 at 10 bar and 35 °C, O_2 and N_2 at 1bar and 35 °C, from [61]
[7] Poly(2,6-dimethylphenylene oxide), from [89]

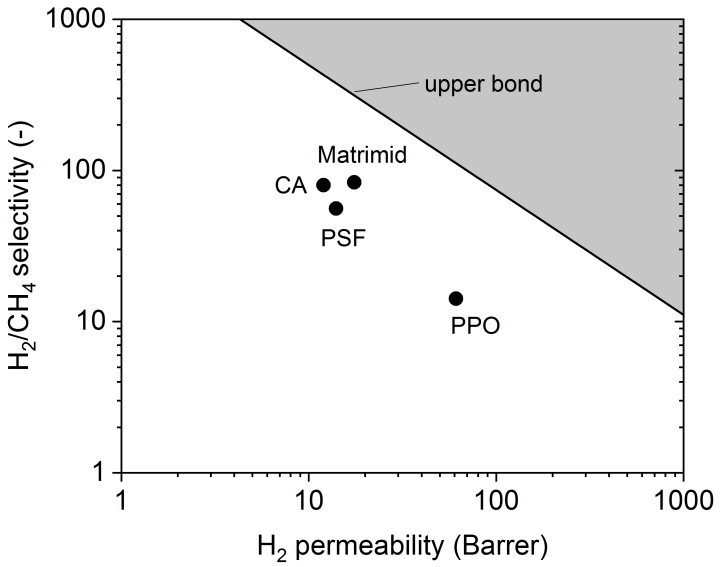

Figure 2.18: H_2/CH_4 selectivity as a function of the H_2 permeability for the presented polymers with the upper bond introduced by [90]

economic considerations have to be taken into account. In general, polymers with high permeabilities are economically favoured as long as they can fulfil the separation task despite their lower selectivities.

2.3.3 Membrane Modules

Two types of gas separation membrane modules are predominant in industrial applications. (1) The hollow-fibre module and (2) the spiral-wound module. The hollow-fibre module, shown in figure 2.19, contains usually ten thousands of hollow fibres in one module. The feed gas can be introduced either on the shell side or on the fibre or 'tube' side. The feed gas side represents the high pressure side of the membrane and is referred to as retentate. Over the length of the module, part of the gases permeates selectively through the membrane to the low pressure side where at the end, the permeate is leaving the module. Depending on which side (shell or 'tube') the feed is entering the module, the effective layer of the membrane is either on the outside surface of the fibre (shell-side feed) or on the inside surface of the hollow fibre (tube-side feed) [93]. The module can be operated in co-current or counter-current mode. The counter-current mode is in general more effective. Typically, the membrane modules are operated between 5 and 15 bar retentate pressure for biogas upgrade. However, higher pressures up to 40 bar are possible in special modules [94]. The spiral-wound module consist of three flat layers of different materials, wrapped around a central tube. The three layers are the feed channel spacer layer (FCS), the membrane layer (M) and the permeate collection layer (PC) ordered

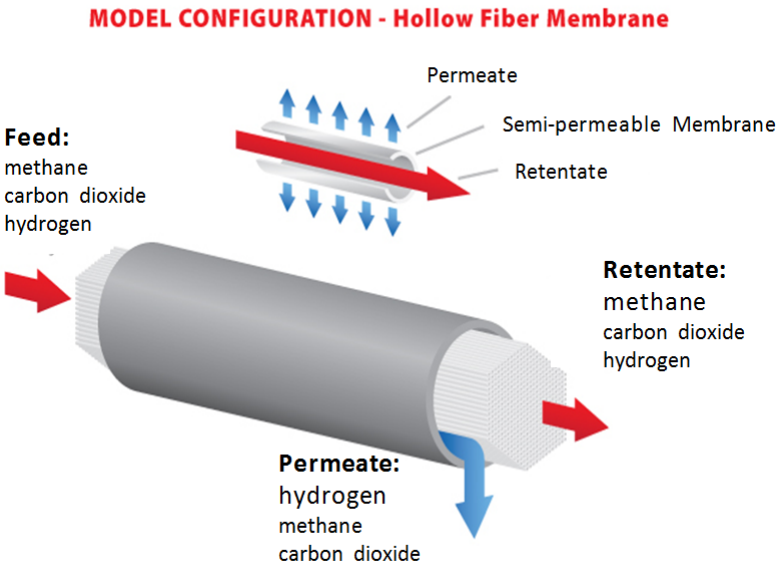

Figure 2.19: Hollow fibre membrane module in co-current operation for the separation of methanation gas; permeate on the shell side, adapted from [91]

in the following repeated sequence: (-FCS-M-PC-M-)$_n$. The feed is introduced into the membrane module from the flat side, where it enters the channel spacer layer. From here, part of the gases permeate selectively through the neighbouring membrane and is collected in the permeate collection layer. The permeate flows in cross-flow to the retentate flow into the inside of the wounded tube until it reaches the perforated permeate collection pipe. From this tube, the permeate leaves the module. Regarding the production costs per square meter of membrane area, the hollow fibre modules are supposed to be less expensive than the spiral-wound version [55]. In addition, the packing density (ratio of membrane area to module volume) is larger for the hollow fibre module, so that the surrounding pressurised vessel can be designed smaller in comparison to spiral wound membranes with the same area size. This again saves production costs.

The modules can be arranged in one or multi-stages with or without recycle flows. The working principle of those arrangements shall be explained with the example of carbon dioxide separation from biogas illustrated in figure 2.21. The feed is biogas which contains roughly one half carbon dioxide and one half methane. In this example, the performance of the first stage shall be not sufficient to obtain a biomethane flow with a high purity so that stream 6 contains a significant amount of carbon dioxide. As a consequence, a second stage in serial mode is arranged to purify stream 6 further in order to obtain a methane rich stream 8. The permeate of stage I (stream 3) is entering a recycle stage, so that also the stream 3 is enriched with carbon dioxide as permeate

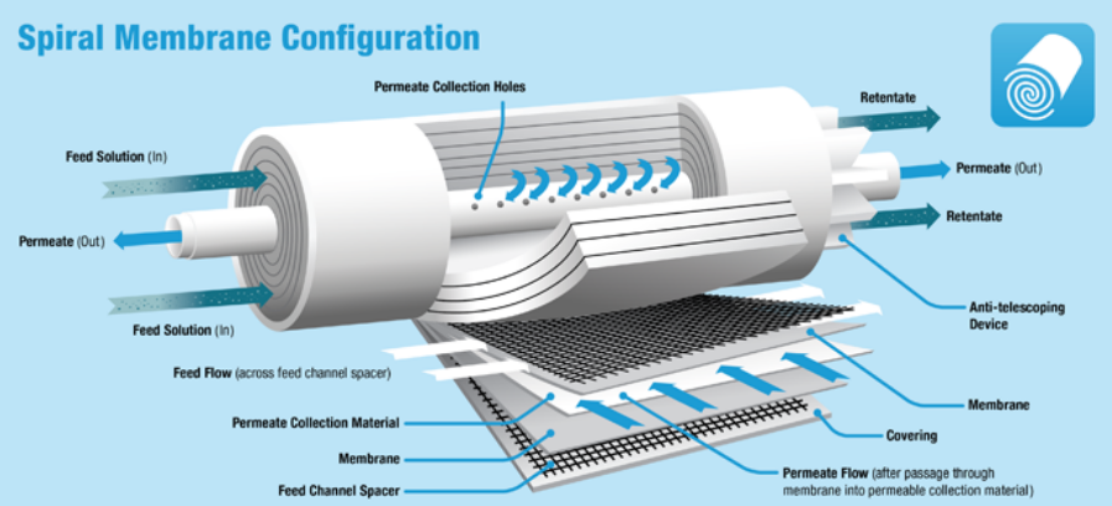

Figure 2.20: Spiral-wound membrane module [92]

(stream 4). With this procedure, less methane is lost and almost only carbon dioxide is released. The bigger share of methane from stream 3 stays in the retentate (stream 5). In order to avoid the loss of methane, stream 5 is recycled back to stream 1. The same goes for stream 7 which is recycled as well.

In summary, serial connected stages purify the retentate, whereas parallel connected stages (like stage I and recycle stage) purify the permeate. With recycle flows, it is avoided to lose valuable compounds which were not separated properly by the previous stages.

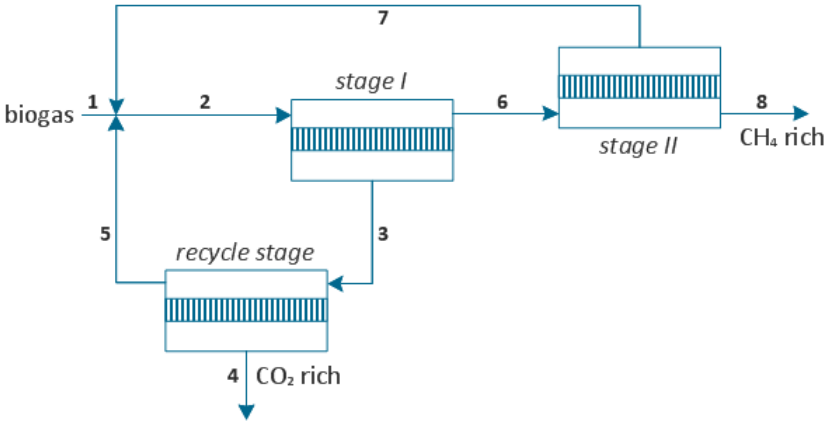

Figure 2.21: Exemplary multi-stage membrane process for carbon dioxide separation from SNG

3 Direct Methanation of Biogas: Process Design and Process Modelling[1]

3.1 Abstract

Direct methanation of biogas is a promising application of the Power-to-Gas concept, since up to 80 % more methane can be produced in comparison to conventional biogas upgrading methods. Six different processes, in which a bubbling fluidized bed or a fixed bed technology serves as the main reactor, were designed, simulated in detail and evaluated in terms of technical feasibility and product gas quality. Both reactor types showed the same chemical performance, since they are both restricted by kinetic and thermodynamic effects. However, the cooled fixed bed reactor requires about three times more reactor volume than the bubbling fluidized bed. Both methanation technologies did not reach Swiss or German high calorific gas grid requirements in one step, so that further upgrading units are necessary which were often not considered in previous literature. Hence, the technological effort for biogas upgrading is higher than often stated in literature. With a subsequent second-stage fixed bed or a gas separation membrane, every process considered reaches the required product gas quality. It is more challenging to fall below the maximum limit of hydrogen (2 vol-%) than to reach the mandatory methane content for grid injection. The electrolysis clearly dominates the power consumption in all processes.

3.2 Introduction

Previous publications investigated PtG applications with biogas as the carbon source via simplified process models [95–99] which led to the neglect of important process units after the main reactor, i.e. the upgrading to fulfil the gas grid requirements. Often, only equilibrium models are applied for the catalytic methanation, which result in reaction rates close to complete conversion for lower temperatures ($< 300\,°C$). However,

[1] This chapter is based on the following publication: J. Witte, J. Settino, S.M.A. Biollaz, T.J. Schildhauer. "Direct Catalytic Methanation of Biogas – Part I: New Insights into Biomethane Production using Rate-Based Modelling and Detailed Process Analysis". In: *Energy Conversion and Management* 171 (2018), pp. 750-768. DOI: 10.1016/j.enconman.2018.05.056. Julia Witte established the process designs and performed the simulations (incl. heat integration) and the modelling of the membrane module, evaluated the simulation data, created all diagrams and wrote the text.

conventional nickel catalysts are not fully active at those temperatures so that the thermodynamic equilibrium cannot be reached and the conversion rates are clearly below equilibrium. Only at higher temperatures above 320 °C, the catalyst is active enough to reach equilibrium, but those temperatures are thermodynamically less beneficial so that methane yields above 95 % are not possible for a hydrogen addition close to stoichiometry. Methane yields of 95 % and below result in a methane concentration of less than 96 vol − % after the reactor, so that those gas flows are not fulfilling general gas grid requirements in Germany or Switzerland [21, 100, 101].

However, in this work the bases for the process analysis are detailed process designs with underlying rigorous modelling for the main units. Crucial aspects for the technical analysis were the kinetic data for the methanation reactors, the hydrodynamic behaviour of the fluidised bed technology, the choice of purification methods and the sizing of the equipment. In order to explore the feasibility of this concept in detail, six different process designs for direct catalytic methanation of biogas were established, simulated and evaluated in terms of product gas quality and technical feasibility. For this, two different methanation technologies, Bubbling Fluidized Bed (BFB) and Fixed Bed (FB), are compared with each other. In the purification step, different gas separation membranes (Mem) or a second stage fixed bed (FB) are investigated. The flowsheeting calculations in this work are the basis for an economic evaluation of these processes in chapter 4.

Additionally, in the context of the storage of fluctuating renewable electricity flows, the processes in general should be able to operate in a dynamic mode. Polymer electrolyte membrane (PEM) electrolysers are able to start-up in the range of few minutes. The methanation reactors have start-up times of about 15 minutes from a stand-by mode. Both units are able to operate in full and partial load, so that it would be possible to compensate fluctuating energy flows by operating in flexible modes.

3.3 Methods

3.3.1 Process Design

The target of the biogas upgrading processes considered is the production of biomethane which is injectable into the existing gas grid in Germany or Switzerland. Hence, the produced biomethane must fulfil the gas grid requirements listed in 3.1, which define the product gas quality for all process models. Rigorous process models were developed for gas upgrading of biogas from anaerobic digestion to biomethane within the PtG concept based on the scheme described in Figure 2.2. The software products Athena Visual Studio© and Matlab® were used for the implementation. Six different processes were developed in which different methanation technologies and further upgrade units are

Components	Requirements
Methane	$\geq$ 96 vol-%
Hydrogen	$\leq$ 2 vol-%
Carbon Dioxide	$\leq$ 4 vol-%
Water	dew point at -8 °C at pressure level of injection point of the gas grid

Table 3.1: Gas grid requirements of Switzerland and Germany for main components issued for the simulation [21, 100, 101].

included. For the methanation, a fixed bed and bubbling fluidized bed were considered as the main reactor, while a hydrogen separation membrane or a second-stage fixed bed methanation reactor were considered as the subsequent upgrade unit. An overview of the processes can be found in Table 3.2. In all models, the state-of-the-art gas cleaning

Model description of biogas upgrade processes	Abbreviation
Bubbling fluidised bed methanation (BFB) and fixed bed methanation (FB)	BFB-FB
Two-stage fixed bed methanation technology	FB-FB
BFB methanation and H_2-membrane with intermediate compression	BFB-Mem
FB methanation and H_2-membrane with intermediate compression	FB-Mem
BFB methanation and H_2-membrane without intermediate compression	BFB-MemS
FB methanation and H_2-membrane without intermediate compression	FB-MemS

Table 3.2: Overview of the process models for upgrading biogas from fermentation

unit is not included, because it removes only trace components which have no thermodynamic influence on the reactor and are not physically relevant for the overall process. The processes are assumed to operate in steady-state mode.

The inlet volume stream is fixed at 200 Nm^3/h, which represents a medium size biogas plant in Switzerland. The inlet composition of biogas is set to 45 vol-% carbon dioxide and 55 vol-% methane, which represents the maximum amount of carbon dioxide in the biogas from green waste [21] and is technically the most challenging composition.

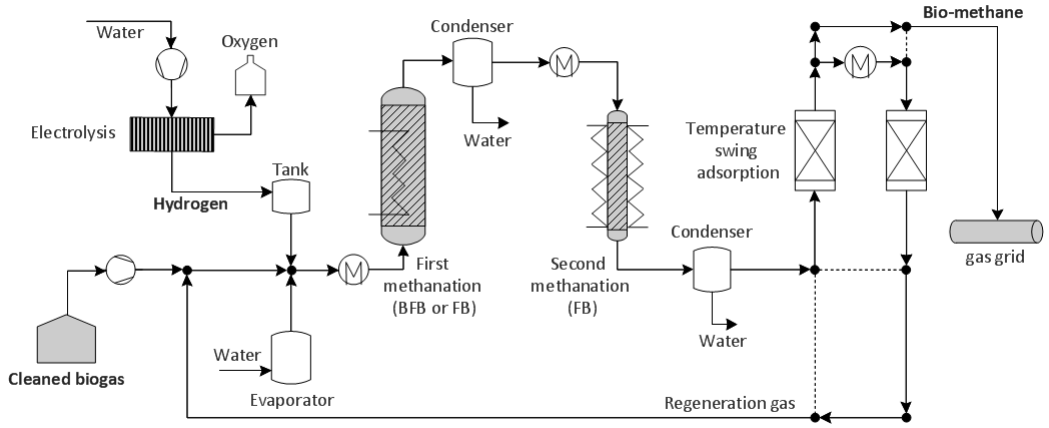

Figure 3.1: Flowsheet for the biogas upgrading process via two-stage methanation according to model BFB-FB and FB-FB

Upgrading process via two-stage methanation (BFB-FB, FB-FB)

The corresponding flowsheet is illustrated in Figure 3.1. Cleaned biogas is compressed to operational pressure. Then, steam provided by an evaporator in a ratio $H_2O/CO_{2,in}$ of 0.5 along with hydrogen is mixed with the raw biogas at operational pressure. The added steam prevents the catalyst from deactivation in the next step. Hydrogen and oxygen are produced via electrolysis from water at 30 bar. Hydrogen is held by a tank for further processing, and oxygen is stored in bottles to be sold. For the processes without membrane, hydrogen is added in a slightly over-stoichiometric ratio $H_2/CO_{2,in}$ of 4.03. After a preheating step, the gas mixture enters a bubbling fluidized bed methanation (process BFB-FB) or a fixed bed methanation (process FB-FB) where carbon dioxide and hydrogen are converted to methane and water by a nickel catalyst. Two independent chemical equations for the catalysed hydrogenation are considered for the overall reaction: the water gas shift (WGS) (Equation 3.1) and the methanation reaction (Equation 3.2):

$$CO_2 + H_2 \leftrightarrow CO + H_2O \qquad \triangle H_r^0 = 41.16\ kJ/mol \tag{3.1}$$

$$3H_2 + CO \leftrightarrow CH_4 + H_2O \qquad \triangle H_r^0 = -206.28\ kJ/mol \tag{3.2}$$

Both reactions are influenced by thermodynamic equilibrium. For the FB and the BFB model, a rate-based model was implemented with kinetic data from literature [102–104]. Both reactors are cooled to maintain thermodynamically beneficial temperatures. The overall reaction is highly exothermic ($\triangle H_{reac}^0 = -165.12\ kJ/mol$), which results in high requirements for the heat exchange performance of the reactor. After leaving the main reactor, the gas stream is cooled to 20 °C in a condenser unit, where water which is formed during the reaction is separated from the gas until saturation concentration.

Because the gas stream does not fulfil the gas grid requirements after the first stage of methanation, further upgrading is needed. Due to the water separation, the thermodynamic equilibrium is shifted towards the products side. Therefore, a second stage methanation was implemented, where the remaining carbon dioxide and the remaining hydrogen are converted to methane (Equation 3.1 and Equation 3.2) in a fixed bed reactor until the required product gas quality is reached. Again, water is produced during the reaction. It is separated in a subsequent second condenser unit, reaching saturation concentration at 20 °C and operational pressure. For injection into the gas grid the gas stream must be technically free of water, which is expressed by a dew point of -8 °C at injection pressure (Table 3.1). For this reason, a dryer unit is necessary, which is achieved via temperature swing adsorption (TSA) technology. Silica gel is used as drying agent. The adsorption vessel operates at ambient temperature, whereas desorption takes place at 110 °C [105]. Approximately 10 % of the product gas is used as regeneration gas to ensure product purity [105]. It is not possible to use air as the regeneration gas because of the contamination of the product gas with oxygen and nitrogen while switching desorption and adsorption vessels. In order not to lose 10 % of the product gas and to avoid emissions of methane, the saturated regeneration gas is redirected to the biogas stream as a recycle loop. The dried product gas stream is expanded to the pressure level of the injection point of the gas grid, which depends on the site and varies between 5 barg (transportation grid at low pressure) and 0.02 – 0.1 barg (distribution grid) [106].

Upgrading process via methanation and hydrogen membrane with intermediate compression (BFB-Mem, FB-Mem)

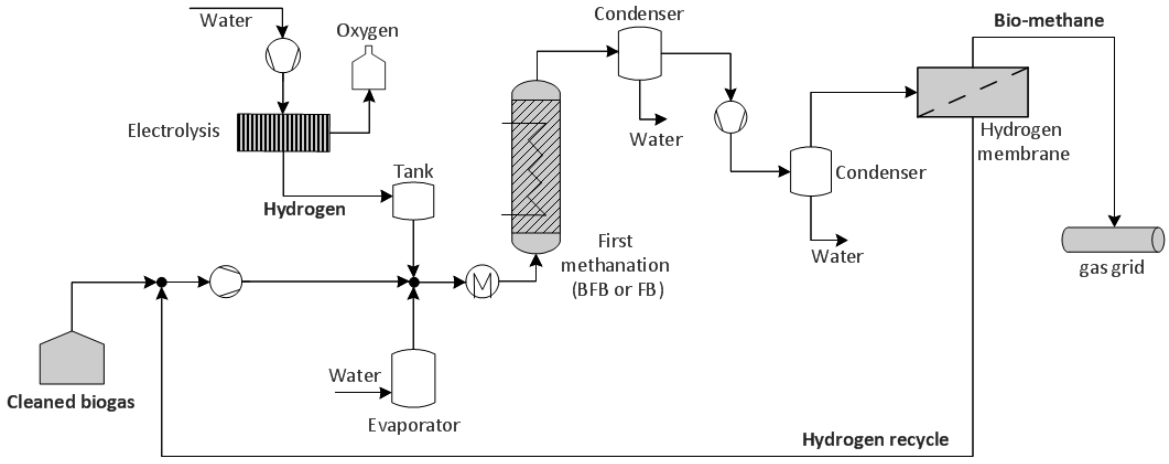

Figure 3.2: Flowsheet for the biogas upgrading via methanation and hydrogen membrane according to models BFB-Mem and FB-Mem

The first part of the process until the first condenser is similar to the flowsheet described before, except for the amount of hydrogen added to the reactor. The corresponding flowsheet is illustrated in Figure 3.2. Thanks to the H_2-membrane, it is possible to vary the input ratio $H_2/CO_{2,in}$ between 3.9 and 4.0. The amount of hydrogen in the recycle stream can increase the ratio H_2/CO_2 inside the reactor so that conditions in the reactor are at least stoichiometric. The models BFB-Mem and FB-Mem differ from models of the previous section with respect to the processing of the remaining hydrogen after the main methanation unit and the subsequent condenser. Here, the remaining hydrogen is separated from the product gas stream by a gas separation membrane and is recycled to the methanation unit. The pressure in the membrane on the retentate side is increased with a second compressor in order to reach higher partial pressure differences between retentate and permeate sides, which increases the separation performance of the membrane for the same membrane area. After the membrane's compressor, a second condenser is implemented. Remaining water in the gas stream is condensed at 20 °C and membrane pressure. The gas stream enters the hydrogen membrane, where hydrogen and water, as well as some methane and carbon dioxide are separated from the biomethane product stream. The biomethane stream is technically free of water and does not need further drying. The recycled hydrogen stream is mixed with the biogas stream and compressed again to the operational pressure in order to be fed into the methanation reactor. The pressure of the product gas stream is adjusted to the gas grid pressure level. For the evaluation, BFB-reactor pressures from 3 bara to 12 bara and FB-reactor pressures from 6 bara to 45 bara are considered, which is a medium pressure range for fixed bed applications [107]. It is assumed that the subsequent membrane module can resist pressures up to 40 bara [108], which restricts the maximum operation pressure.

Upgrading process via methanation and hydrogen membrane without intermediate compression (BFB-MemS, FB-MemS)

The processes BFB-MemS and FB-MemS (Figure 3.3) represent simplified versions of the processes BFB-Mem and FB-Mem. Only one pressure level is considered, therefore the second compressor and the second condenser were removed. Hence, the pressure in the methanation reactor and the membrane are the same, neglecting pressure losses. As a result, the pressure in the membrane will be smaller for most cases than for the processes BFB/FB-Mem, which results in a larger required membrane area to compensate for the performance loss due to smaller partial pressure differences inside the membrane modules. All processes with a fluidised bed are evaluated until a maximum pressure of 12 bara. Until this pressure level, is assumed that the heat dissipation properties of the fluidised bed reactor are still sufficient to maintain isothermal conditions. An overview of the range of operation conditions which were evaluated for each process can be found

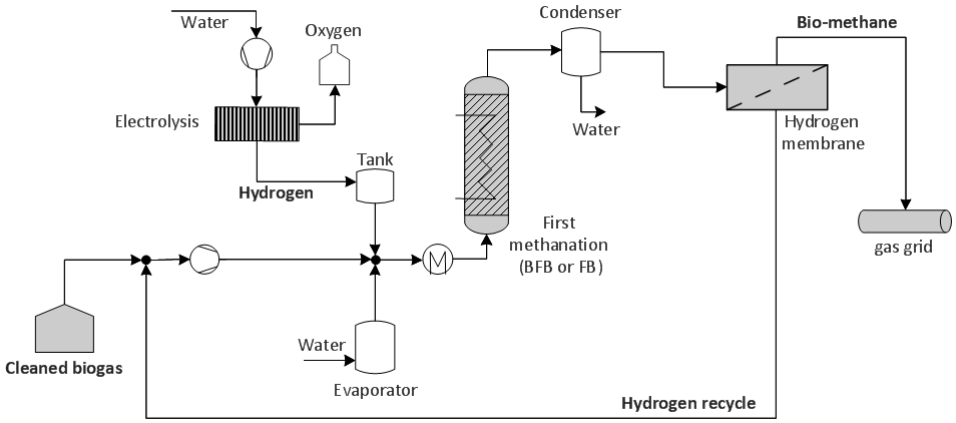

Figure 3.3: Flowsheet for the biogas upgrading via methanation and simplified hydrogen membrane according to models BFB-MemS and FB-MemS

in table 3.3. For processes with a second fixed bed, only the system pressure can be changed. All other parameters such as temperatures, bed length etc. depend on the pressure needed to reach gas grid requirements. The input ratio of hydrogen to CO_2 is fixed at 4.03. With a higher ratio, more than 2 vol-% of hydrogen would remain in the product gas. A lower ratio causes risks of catalyst deactivation. For processes with a membrane, the H_2/CO_2 input ratio is varied also. In this case, H_2/CO_2 ratios inside the reactor can be adjusted independently of the input ratio within certain ranges. As a result, despite sub-stoichiometric input ratios, the H_2/CO_2 ratios inside the reactor can be stoichiometric at minimum.

3.3.2 Modelling

Isothermal bubbling fluidised bed reactor

The internally cooled fluidised bed reactor is modelled according to the pseudo-homogeneous two phase approach of Kopyscinski et al. [110] where hydrodynamic correlations for

process	$H_2/CO_{2,input}$,-	$p_{sys}, bara$	$p_{mem}, bara$	**membrane type**
BFB-FB	4.03	6 - 12	-	-
BFB-Mem	3.9 - 4.0	3 - 9	19, 19, 40	PPO, Matr-PPO, Matrimid
BFB-MemS	4.0	9 - 12	9 - 12	PPO
FB-FB	4.03	6 - 45	-	-
FB-Mem	3.9 - 4.0	6 - 9	19, 19, 40	PPO,Matr-PPO, Matrimid
FB-MemS	3.9 – 4.0	9 - 40	9 - 40	PPO, Matr-PPO, Matrimid

Table 3.3: Evaluated conditions for the different processes

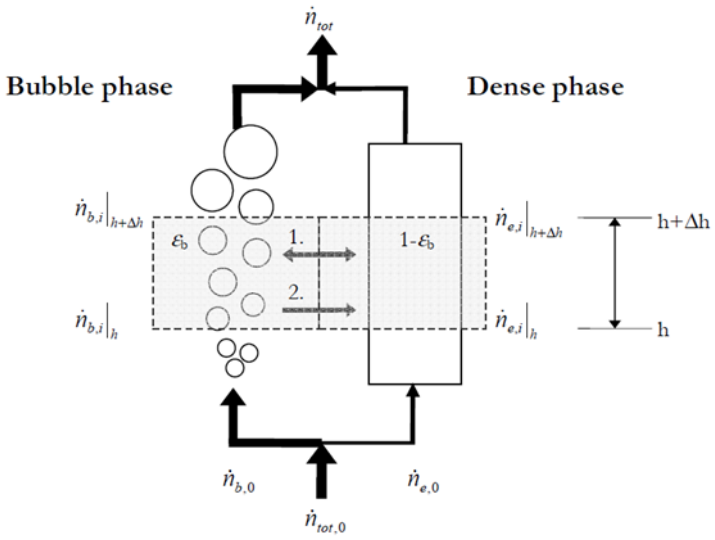

Figure 3.4: Two phase model used for the bubbling fluidised bed model [109]

freely bubbling fluidized beds are applied. According to Figure 3.4, the total inlet gas flow $\dot{n}_{tot,0}$ is divided into the bubble $\dot{n}_{b,0}$ and the dense phase $\dot{n}_{e,0}$ gas flow, corresponding to the volumetric fraction of the bubble phase ε_b and of the dense phase $\varepsilon_e = 1-\varepsilon_b$. The volumetric fraction of the bubble phase is determined by the following equation from Hilligart et al. [111] via superficial velocities u and bubble diameters d_b derived from bubble size correlations :

$$u_b = \psi\ (u - u_{mf}) + 0.711\ \nu\ \sqrt{g\ d_b} \tag{3.3}$$

$$\varepsilon_b = \psi\ \frac{(u - u_{mf})}{u_b} \tag{3.4}$$

The parameters ψ and ν consider the different types of Geldart particles and depend on reactor height and diameter. The molar balances for the bubble and dense phase are shown in Equation 3.5 and 3.6, respectively.

$$\frac{d\dot{n}_{b,i}}{dh} = -K_{G,i} \cdot a \cdot A_c \cdot (c_{b,i} - c_{e,i}) - \dot{N}_{vc} \cdot x_{b,i} \tag{3.5}$$

$$\frac{d\dot{n}_{e,i}}{dh} = K_{G,i} \cdot a \cdot A_c \cdot (c_{b,i} - c_{e,i}) + \dot{N}_{vc} \cdot x_{b,i} + (1-\varepsilon_b) \cdot (1-\varepsilon_{mf}) \cdot \rho_p \cdot A_c \cdot R_i \tag{3.6}$$

Here, $(1-\varepsilon_b)$ represents the volume fraction of the dense phase, $(1-\varepsilon_{mf})$ express the volume fraction of the particles assuming minimal fluidisation conditions in the dense phase and $R_i = \sum \nu_{i,m} r_m$ describes the overall reaction, where m represents the WGS and methanation reactions for each component i.

Between the two phases, mass transfer occurs due to concentration differences but also due to the mole reducing reaction. The inter-phase mass transfer is described as the sum of the two phenomena, see Equation 3.7:

$$\dot{N}_{vc} = \frac{d\dot{n}_{vc}}{dh} = \sum K_{G,i} \cdot a \cdot A_{cross} \cdot (c_{b,i} - c_{e,i}) + (1-\varepsilon_b) \cdot (1-\varepsilon_{mf}) \cdot \rho_p \cdot A_{cross} \cdot R_i \quad (3.7)$$

The following assumptions for the differential equations applied in the bubbling fluidised bed model were made:

- Steady state conditions and ideal gas behaviour
- No reaction in the bubble phase
- Laminar boundary layers around the catalyst particles as well as pore diffusion are neglected; hence gas concentrations in the dense phase and on the catalyst particles are equal
- Radial gas concentration differences are neglected
- Deactivation mechanisms of the catalyst are neglected

Deactivation mechanisms on the catalyst are not considered in the fluidised bed model. However, in the economic analysis in chapter 4 the catalyst material will be exchanged every year due to deactivation. Experimental results from [112] and [29] showed only minor signs of deactivation due to coke forming. In combination with a sufficient gas cleaning unit for sulphur removal, the minor deactivation effects can be compensated by the yearly replacement of the catalyst material.

Two main aspects influence the performance of the reactor: the reaction kinetics and the hydrodynamics caused by the bubbles inside of the reactor. For the kinetics, a Langmuir-Hinshelwood approach was implemented with rate equations for the water gas shift reaction:

$$r_{WGS}^{BFB} = \frac{k_{WGS}(K_\alpha p_{CO} p_{H_2O} - (\frac{p_{CO_2}\ p_{H_2}}{K_{eq,WGS}}))}{p_{H_2}^{0.5}(1 + K_C\ p_{CO}^d\ p_{H_2}^e + K_{OH}\ p_{H_2O}\ p_{H_2}^{-0.5})^2} \quad (3.8)$$

and for the methanation reaction:

$$r_{Meth}^{BFB} = \frac{k_{meth}\ K_C\ p_{CO}^a\ p_{H_2}^b\ (1 - (\frac{p_{CH_4}\ p_{H_2O}}{K_{eq,meth}\ p_{CO}\ p_{H_2}^3}))^c}{(1 + K_C\ p_{CO}^d\ p_{H_2}^e + K_{OH}\ p_{H_2O}\ p_{H_2}^{-0.5})^2} \quad (3.9)$$

parameter	unit	value
$k^{BFB}_{WGS,ref}$	-	8.4
$k^{BFB}_{Meth,ref}$	-	1.08
$E^{BFB}_{A,WGS}$	kJ/mol	155.7
$E^{BFB}_{A,Meth}$	kJ/mol	63.1
$K_{\alpha,ref}$	bar^{-2}	0.36
$K_{C,ref}$	$bar^{-1.5}$	2.53
$K_{OH,ref}$	$bar^{-0.5}$	0.67
ΔH_α	kJ/mol	-1.7
ΔH_C	kJ/mol	-50.7
ΔH_{OH}	kJ/mol	-87.5
a	-	0.5
b	-	1
c	-	1
d	-	0.5
e	-	0.5
T_{ref}	K	598.15

Table 3.4: Kinetic and adsorption constants of the methanation and water-gas-shift rate expressions for the bubbling fluidized bed methanation [102]

Rate and adsorption constants are based on the Arrhenius and Van't Hoff approach:

$$k_i = k_{i,T_{ref}} \ \exp\left(\frac{E_{A,i}}{R\ T_{ref}}\left(1 - \frac{T_{ref}}{T}\right)\right) \qquad , i = WGS, Meth \tag{3.10}$$

$$K_j = K_{j,T_{ref}} \ \exp\left(\frac{\Delta H_j}{R\ T_{ref}}\left(1 - \frac{T_{ref}}{T}\right)\right) \qquad , j = \alpha, C, OH \ldots \tag{3.11}$$

The values of the kinetic parameters are given in Table 3.4.

The hydrodynamics of the reactor are expressed through bubble size correlations, with which bubble rise velocities and the bubble holdup ε_b are determined in a next step. This procedure allows the determination of the total surface area of the bubbles and then the inter-phase mass transport from the bubble into the dense phase. Then, the kinetic expressions are applied, which result in new molar flows of the components due to the reactions in the dense phase at a specific reactor height. Different bubble size correlations for fluidised beds exist in the literature [113–120], but only at non-reactive conditions and without heat exchanger internals. Another study has shown that bubble growth is

inhibited by the presence of internals [121], therefore the bubble size correlation with the smallest overall bubble size was chosen, as given by Werther [113]:

$$d_B = 0.835\ (1 + 0.272\ (u - u_{mf}))^{\frac{1}{3}}(1 + 0.0684\ h)^{1.21} \tag{3.12}$$

Since the bubble diameter influences the gas composition in the dense phase via the mass transfer area and therefore the reaction performance, a precise correlation is essential for the accuracy of the model.

Fixed bed reactor

The fixed bed (FB) methanation model is also based on kinetic expressions and considers the same chemical equations 3.1 and 3.2 as the bubbling fluidized bed (BFB) model. The shell-side cooled reactor includes internal tubes with an inner diameter of 2.5 cm each, which contain the catalyst. The description of the applied pseudo-homogeneous first order model can be found from [103]. The following assumptions are made for the fixed bed model:

- Steady state conditions and ideal gas behaviour
- Laminar boundary layers around the catalyst particles as well as pore diffusion are neglected; hence gas concentrations in the dense phase and on the catalyst particles are equal
- Radial gas concentration differences are neglected
- Deactivation mechanisms of the catalyst are neglected

Results from literature have shown that a homogeneous reactor model without considering intra particle transport processes is sufficient to describe the overall trend of the reaction [103] which is needed for the evaluation of process conditions. Only for cases like large catalyst pellet sizes or small Reynold numbers, a heterogeneous model would be more accurate. In this work however, no such cases are applied. Again, deactivation mechanisms are neglected in the physical model, but a yearly exchange of the catalyst material in the economic analysis (chapter 4) considers deactivation effects. Deactivation rates for a fixed bed might be higher than for a bubbling fluidised bed due to more challenging conditions in the fixed bed like high peak temperatures and a permanently high catalyst stress for the catalyst particle at the beginning of the reactor vessel. However, no directly comparable studies for fixed and fluidised beds under the same conditions are carried out addressing deactivation mechanisms. Therefore, the same deactivation rates in the economic model for both reactor types are assumed. The applied axial molar

balance and the energy balance for the fixed bed reactor are given by [122]:

$$\frac{d\dot{n}_i}{dz} = \sum_m \nu_{i,m}\ r_m \cdot A_{cross} \cdot \rho_{cat} \tag{3.13}$$

$$G \cdot c_p \cdot \frac{dT}{dz} = \sum_m r_m \cdot \Delta H_{reac,m} \cdot \rho_{cat} + \frac{4\ U}{d_{tube}} \cdot (T(z) - T_{cool}) \tag{3.14}$$

The overall thermal transmittance U is calculated at each step based on the actual gas composition according to the correlation for a particle bed for spherical particles of 1.8 mm diameter [123]:

$$Nu = 0.223 \cdot Re_p^{0.6109} \cdot Pr^{0.333} \tag{3.15}$$

And the corresponding expressions for the Nusselt, Reynolds and Prandtl numbers:

$$Nu = \frac{\alpha_{internal} \cdot d_p}{\lambda_{fluid}} \tag{3.16}$$

$$Pr = \frac{c_p \cdot \eta}{\lambda_{fluid}} \tag{3.17}$$

$$Re_p = \frac{G \cdot d_p}{\eta} \tag{3.18}$$

The main thermal resistance is assumed to be in the internal gas phase between the catalyst particle and the inner reactor wall, hence the thermal transmittance is expressed through $1/U = 1/\alpha_{internal}$, where the thermal resistance in the wall and outside the tube is neglected.

Two different sets of kinetic parameters were applied due to the different conditions in the main and the second fixed bed reactor. In the main reactor, high temperature peaks until 700 °C are present, which requires a catalyst which is thermally stable at those conditions. In the second fixed bed, temperatures are comparable to a fluidised bed reactor since only a small amount of reactants are left. Here, the same catalyst type like for a fluidised bed can be applied, which is more active at lower temperatures than the catalyst for the main fixed bed. For the main fixed bed reactor, kinetic data were taken from [104]. The catalyst described is thermally stable at high temperatures, but is less active at lower temperatures. The kinetics for the methanation reaction in equation 3.20 are originally retrieved from the perspective of steam reforming, where the methanation reaction from CO to methane was defined as reversed reaction. Hence, the parameter K_{SR} in equation 3.20 represents the equilibrium constant of steam reforming.

$$r_{WGS}^{FB} = \frac{k_{WGS}\ (p_{CO}\ p_{H_2O} - p_{CO_2}\ p_{H_2}/K_{WGS})}{p_{H_2}\ (1 + K_{CO}\ p_{CO} + K_{H_2}\ p_{H_2} + K_{CH_4}\ p_{CH_4} + K_{H_2O}\ p_{H_2O}\ p_{H_2}^{-1})^2} \tag{3.19}$$

$$r_{Meth}^{FB} = \frac{k_{Meth}\ (p_{CO}\ p_{H_2}^3/K_{SR} - p_{CH_4}\ p_{H_2O})}{p_{H_2}^{2.5}\ (1 + K_{CO}\ p_{CO} + K_{H_2}\ p_{H_2} + K_{CH_4}\ p_{CH_4} + K_{H_2O}\ p_{H_2O}\ p_{H_2}^{-1})^2} \quad (3.20)$$

Rate and adsorption constants are determined analogously by the Arrhenius and Van't Hoff approach.

For the second stage fixed bed model, the same kinetic parameters as for the bubbling fluidised bed are applied (see table 3.4). In comparison to the main reactor, the kinetic values applied here describe a more thermodynamically beneficial catalyst, because it is more active at lower temperatures. But the thermal stability is not as high as for the first catalyst bed. However, in the second stage fixed bed only medium temperatures are reached, because the reaction extent and therefore the reaction heat produced are low due to the small amount of remaining carbon dioxide in the inlet gas to the second stage reactor.

Gas separation membrane

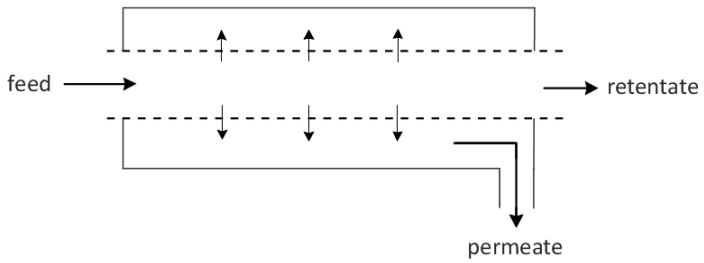

Figure 3.5: Simplified scheme of a hollow-fibre module of a membrane

Figure 3.5 shows a scheme of a membrane module with one fibre in co-current flow. The feed enters the module on the fibre-side. Over the length of the module, gas components permeate through the membrane wall to the shell side. The following assumptions are made:

- Ideal gas behaviour
- Axial dispersion is neglected
- Pressure drop inside the fibre is neglected
- Influence of the pressure and of other components in the gas mixture to the permeability parameter of one component is neglected; hence permeability parameter is set constant

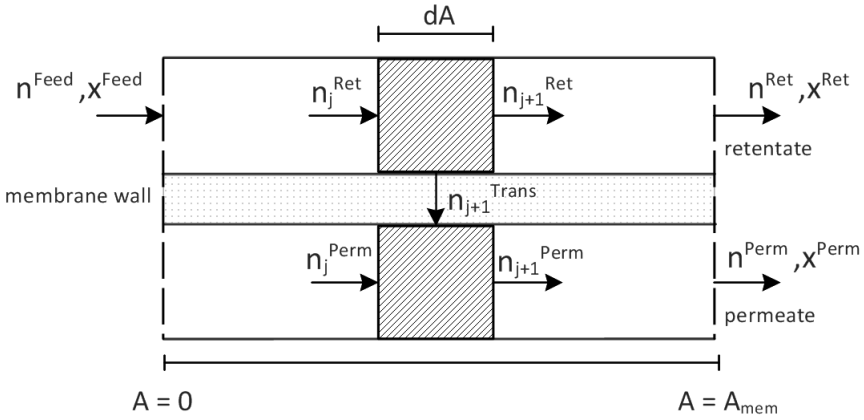

Figure 3.6: Cross-sectional element of the membrane area with mass balance

The local volume flow of gas through a non-porous membrane can be described by an adapted Fick's law [124]:

$$dV_i^{Perm} = \frac{C_i \ (p_i^{Ret} - p_i^{Perm}) \ dA}{s} \tag{3.21}$$

It is assumed that the permeability of a pure component C_i does not change in a mixture or with varying module pressure. In Figure 3.6, a cross-sectional element of the membrane module is shown with its mass balance. The integration problem for the j-th differential element dA is solved numerically for one component with the following equations:

$$\dot{n}_{j+1}^{Ret} = \dot{n}_j^{Ret} - \dot{n}_{j+1}^{Trans} \tag{3.22}$$

$$\dot{n}_{j+1}^{Perm} = \dot{n}_j^{Perm} + \dot{n}_{j+1}^{Trans} \tag{3.23}$$

The boundary conditions for the retentate are: $\dot{n}_0^{Ret} = \dot{n}^{Feed}$,$x_0^{Ret} = x^{Feed}$; and for the permeate: $\dot{n}_0^{Perm} = 0$ and $x_0^{Perm} = 0$. The transport term $\dot{n}_{j+1}^{Trans}$ represents the permeation and is described by Equation 3.21. The numerical expression for one component is as follows:

$$\dot{n}_{j+1}^{Trans} = \frac{C \ (x_j^{Ret} \ p^{Feed} - x_j^{Perm} \ p^{Perm}) \ dA}{s \cdot V_m} \tag{3.24}$$

Three different polymer membranes were investigated which differ from each other in terms of selectivity and permeability, as listed in table 3.5. The ideal selectivity is defined as the ratio of the permeability of the compound to be separated relative to the permeability of other gas compounds. In general,a trade off between permeability

membrane type	permeability, barrer			ideal selectivity, -		ref
	H_2	CH_4	CO_2	H_2/CH_4	H_2/CO_2	
Matrimid	17.5	0.21	7.29	83.3	2.4	[126]
PPO[2]	61	4.3	61	14.2	1	[127]
Matr-PPO	61	4.3	7.29	14.2	8.4	-

Table 3.5: Permeabilities of common gases for polymere based membranes

and selectivity has been recognised [125], so that membranes with high selectivities show smaller permeabilities and vice versa. Matrimid membranes are characterised by high selectivity rates of hydrogen towards methane, but in general low permeation rates. PPO membranes show inverse properties with high permeation rates and lower selectivity. In order to understand the impact of the membrane properties on the process, a hypothetical membrane Matr-PPO was also evaluated. This membrane combines the properties of the two membranes Matrimid and PPO. For this, the permeability of H_2 is taken from PPO membrane and the permeability of CO_2 is taken from Matrimid membrane in order to establish a more beneficial membrane for the given separation task. This approach leads to smaller membrane areas due to the high permeability and a beneficial separation performance especially for the components hydrogen and carbon dioxide. The effective thickness s of a membrane, which is the part of the thickness that effects the separation, influences the permeation rate strongly. The effective thickness of typical membranes is less than 500 nm and often below 100nm [57]. In this work, the effective thickness was set to 100 nm.

Electrolysis,dryer and supporting modules

The shortcut electrolyser model is based on the specific electricity consumption of 4.6 $kWh/Nm^3_{H_2}$ [128], which is an average value for alkaline and PEM electrolysers. The drying is realized via temperature swing adsorption (TSA). The underlying shortcut model is based on the specific adsorption amount of water on silica gel of 0.3 kg_{water}/kg_{silica} for commercially available desiccants [129]. Condensers, evaporators, heat exchangers and compressors serve as supporting units, which are based on thermodynamic models applied with thermo-physical property data from the NIST (National Institute of Standards and Technology) database.

3.4 Results and Discussion

The processes were investigated in terms of the behaviour of single units as well as the interplay of units in the whole process. The technical target is the fulfilment of the gas

[2] Poly(2,6-dimethylphenylene oxide)

grid requirements mentioned in table 3.1, which can be reached for every process in a range of corresponding operational conditions.

3.4.1 Fixed Bed

Representative results of the fixed bed model are shown for one case of the FB-FB process. In Figure 3.7 and Figure 3.8, concentration profiles of the main components H_2, CH_4 and CO_2 are illustrated for different pressures over the length of the main fixed bed reactor (first FB, Figure 3.7) and the subsequent second fixed bed (Figure 3.8). The gas hourly space velocity (GHSV) is defined as follows:

$$GHSV = \frac{\dot{V}_{Feed}^{std}}{V_{reactor}} \ . \tag{3.25}$$

where the total inlet volume flow $\dot{V}_{Feed}^{std}$ is put into relation with the free reactor volume of the bed $V_{reactor}$ excluding the space required for the heat exchange. The simulated fixed bed has a GHSV of 2950 $Nm_{Feed}^3\ h^{-1}\ m_r^{-3}$. Increased pressure in the reactor results in a steeper increase of methane concentration over the reactor length and thus a faster conversion of carbon dioxide to methane. The end concentration of methane is also slightly higher for increased pressure, which is expected based on thermodynamics and Chatelier's principle because the reaction is mole reducing. The increased reaction rate due to increased pressure is also reflected in the corresponding temperature profiles (Figure 3.7). Here, temperature peaks are formed in the area with the highest reaction extent. Then, over the length, the temperature falls again due to cooling. The maximum peak-temperature increases with the pressure. Temperature differences of 300 K are obtained in a fixed bed reactor, which is in agreement with literature [103, 122]. Before the temperature peak in the reactor, the reaction is determined by kinetic effects. After the peak, thermodynamic equilibrium sets a limit for the conversion of carbon dioxide to methane. The concentrations of the components follow the equilibrium composition at the corresponding temperature. This means that the length of the reactor is determined by the cooling performance in order to reach thermodynamically beneficial temperatures inside the reactor. Avoiding temperature peaks would allow a shorter reactor length, but the heat transfer performance of the fixed bed reactor is not sufficient without further measures to sufficiently dissipate the produced reaction heat.

The pressure also influences the heat transfer properties of the reactor, as reflected in the thermal transmittance shown in Figure 3.7. The thermal transmittance is calculated via Nusselt, Prandtl and Reynolds numbers (see sub section 3.3.2). Therefore, it depends on the viscosity, density, heat capacity and velocity of the gas mixture, which are all influenced by temperature and pressure. The thermal transmittance is positively influenced by the conversion of reactants to products. Figure 3.7 shows that increased

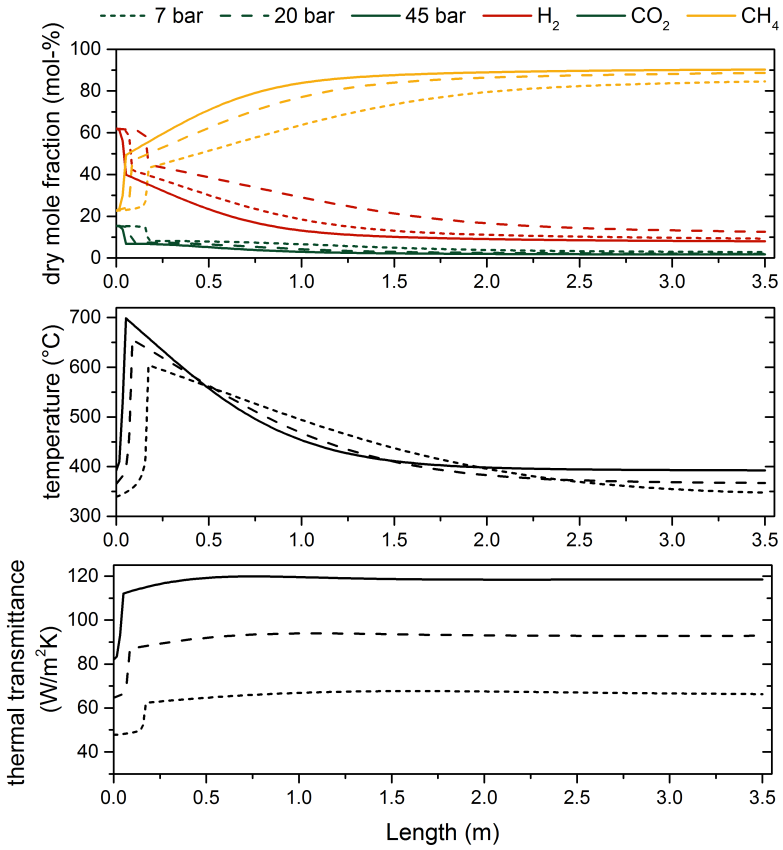

Figure 3.7: Concentration profiles of the main components and the corresponding temperature and thermal transmittance profiles over the length of the main fixed bed reactor in FB-FB process for different pressures ($T_{cool} = T_{in,FB}$, $V_{biogas} = 200\ Nm^3/h$, $H_2/CO_2 = 4.03$, $H_2O/CO_2 = 0.5$, main reactor: $A_{cross} = 0.06\ m^3$, catalyst stress $= 0.5\ Nm^3_{CO_2}\ h^{-1}\ kg^{-1}_{cat}$, $GHSV_{tot} = 2950\ Nm^3_{Feed}\ h^{-1}\ m^{-3}_{reactor}$)

pressures result in an improved heat transfer, expressed through an increased thermal transmittance. Higher temperatures also result in larger coefficients, but with a smaller effect than pressure.

Despite cooling and high pressures, the reaction extent of the first stage fixed bed reactor is not sufficient to reach the hydrogen and methane concentrations required by the gas grid (Table 3.1). Hence, after the first condenser, a second fixed bed is installed to convert the remaining CO_2 and the remaining hydrogen such that the gas grid requirements are met. In Figure 3.8, the concentration profiles of the main components and the temperature profiles for the second-stage fixed bed are illustrated at different pressure levels. After the second fixed bed, the gas grid requirements can be reached at different pressures. The lower limit of methane concentration is reached with less

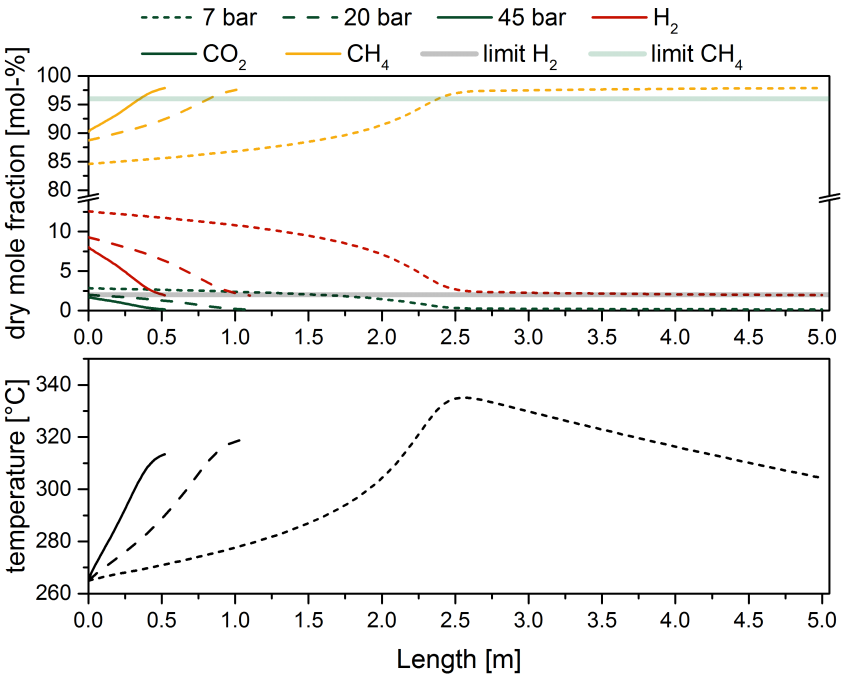

Figure 3.8: Concentration profiles of main the components and corresponding temperature profiles over the length of the subsequent fixed bed reactor in FB-FB process for different pressures ($T_{cool} = T_{in,FB} - 30\ K$, $V_{biogas} = 200\ Nm^3/h$, $H_2/CO_2 = 4.03$, $H_2O/CO_2 = 0.5$, second reactor: $A_{cross} = 0.025\ m^2$, catalyst stress varies between 0.06 $Nm^3_{CO_2} h^{-1} kg^{-1}_{cat}$ at 7 bara and 0.62 $Nm^3_{CO_2} h^{-1} kg^{-1}_{cat}$ at 45 bara)

reactor length than the upper limit of hydrogen. Hence, it is more demanding to fulfil the maximal hydrogen limit of 2 vol-% than the other concentration requirements. At a pressure of 7 bara, the reactor needed to reach the concentration limits of methane and hydrogen is ten times longer than for a pressure of 45 bara. The temperature profiles correspond to the concentration profiles. Here, no such significant temperature peak is formed. In comparison with the first-stage fixed bed, only a small temperature increase of 75 K can be observed, since only a small amount of remaining CO_2 and hydrogen are left as reactants. The heat dissipation performance of the second fixed bed is sufficient to avoid large temperature differences in the reactor. The inlet composition of the second-stage fixed bed varies with different pressures, because the reaction extents in the first-stage fixed are higher at increased pressures. This also results in a smaller maximum temperature at higher pressures in the second-stage fixed bed.

3.4.2 Isothermal Bubbling Fluidised Bed

In Figure 3.9, concentration profiles of the dense and bubble phases over the length of the BFB reactor are shown for the main components H_2, CO_2 and CH_4 and freeboard concentrations. The GHSV of the BFB reactor is larger than for a fixed bed by a factor

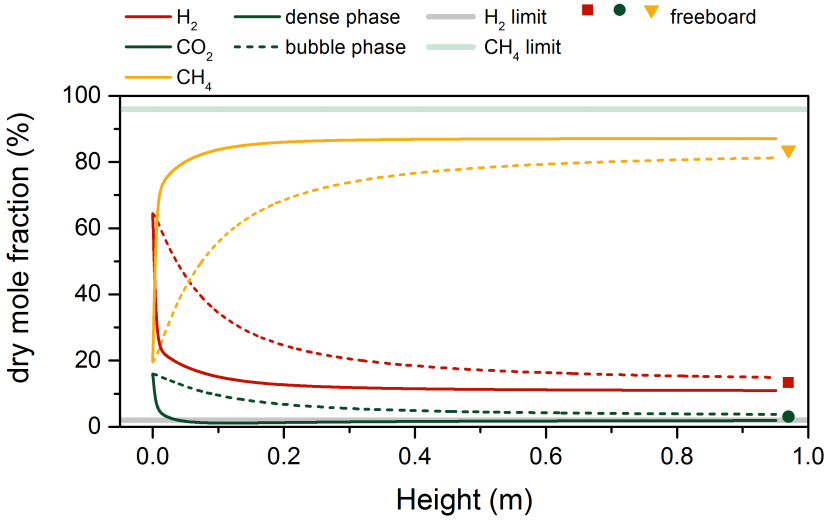

Figure 3.9: Concentration profiles over the length of the BFB reactor at 12 bara for the bubble and dense phase ($T_{reac} = 385\ °C$, $V_{biogas} = 200\ Nm^3/h$, $H_2/CO_2 = 4.03$, $H_2O/CO_2 = 0.5$, $A^{free}_{reactor} = 0.025\ m^2$, catalyst stress $= 1.5\ Nm^3_{CO_2} h^{-1} kg^{-1}_{cat}$, $GHSV_{tot} = 4810\ Nm^3_{Feed}\ h^{-1}\ m^{-3}_{reactor}$)

of 1.6 with an absolute value of 4810 $Nm^3_{Feed}\ h^{-1}\ m_r^{-3}$. Most of the CO_2 and hydrogen is converted in the first 10 cm of the reactor length. After this, mass transfer from the bubble to the dense phase determines the reaction rates. The decrease of hydrogen and CO_2 concentrations in the bubble phase is only caused by mass transfer, since it is assumed that no reaction takes place in the bubbles. Sufficient heat transfer to ensure isothermal conditions allows the operation at the optimal temperature. In contrast to fixed bed reactors, the reaction takes place at the optimal temperature over the entire reactor, so that the BFB reactor can be designed with three times less catalyst material in comparison to the FB reactor for the same reaction performance. As for the fixed bed reactor, the BFB reactor also does not reach the required gas concentrations of methane and hydrogen due to thermodynamic limitations. Hence, further gas upgrade is also needed.

Adapting the geometry of the BFB reactor for changing operational conditions like temperature, pressure or input flow rate is crucial to ensure proper fluidisation inside the reactor. In Figure 3.10, the influence of pressure and temperature in the reactor on the reactor geometry is illustrated for a fixed input flow rate. The reactor diameter decreases with increasing pressure in order to assure a fixed fluidisation velocity. For sufficient particle movement, the ratio of gas velocity to minimal fluidisation velocity u/u_{mf} is set in all cases to 6.0 at the outlet of the reactor. The particle movement ensures near-isothermal conditions over the height of the reactor, as well as a regeneration of catalyst particles from coking, which are transported from areas with high catalyst

stress and heat generation (lower part of reactor) to areas with low catalyst stress and respectively low heat generation (upper part of reactor). The temperature has a smaller effect on the diameter, but for higher temperatures slightly larger diameters are required to compensate the gas expansion. The maximum pressure in the BFB reactor is assumed to be 12 bara. Until to this point, the volume flow of inlet gas can cause sufficient fluidisation for isothermal conditions, while the catalyst stress (Nm^3/h of CO_2 per kg of catalyst) at the lower part of the reactor is still in a reasonable range.

In order to operate the reactor isothermally, the heat of reaction must be dissipated. For this, the required internal heat exchange area of the tubes is determined by the maximum occurring reaction heat assuming 100 % conversion, the given average temperature difference between the reactor temperature and the cooling agent, as well as the thermal transmittance. The thermal transmittance is assumed to be constant at 150 W/m^2K. With increasing pressures, the maximum heat production remains constant because of the constant inlet flow rate. Hence the required heat transfer area is also constant. This means that higher pressure causes a smaller diameter, but a larger height. The required heat transfer area decreases with higher temperatures due to the increasing temperature difference between the reactor and the cooling agent. The volume of the reactor is determined by heat transfer properties and fluidisation of the reactor and not by the course of the reaction. The necessary heat transfer area (internal tubes) requires more catalyst material than the reaction itself.

In Figure 3.11, the performance of the BFB reactor over the temperature is shown for different pressures. As the performance indicator the yield of methane was chosen and is defined as follows:

$$Y_{CH_4} = \frac{\dot{n}^{out}_{CH_4} - \dot{n}^{in}_{CH_4}}{\dot{n}^{in}_{CO_2}} \tag{3.26}$$

For every set of operational conditions in Figure 3.11, the required adaptations to the reactor geometry are made. At lower temperatures, the reaction cannot reach thermodynamic equilibrium because of the low activity of the catalyst, and only small yields are reached. With increasing temperatures, the catalyst becomes more active until thermodynamic equilibrium is reached at the corresponding temperature. This point forms a maximum. With increasing temperatures, the yield decreases following the thermodynamic limit of the reaction. Hence, for every pressure and given input flow rates, an optimal temperature exists where the yield of methane is at maximum. From 2 bara to 6 bara, the maximum yield increases and shifts towards lower temperatures, but with further increased pressure, the reaction performance no longer improves. The necessary adaptations to the reactor geometry towards smaller diameters and a larger height

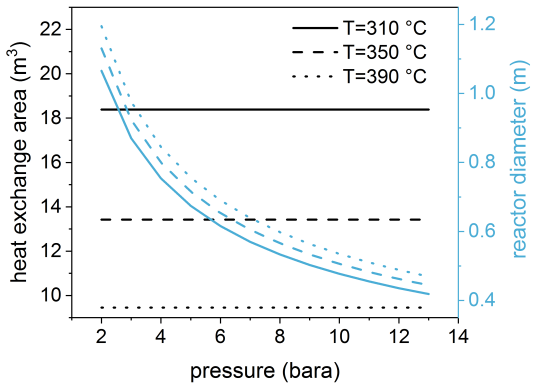

Figure 3.10: Influence of temperature and pressure on the reactor geometry of the fluidised bed reactor; $T_{cool,in} = 240\ °C$, $\alpha = 150\ W/(m^2\ K)$

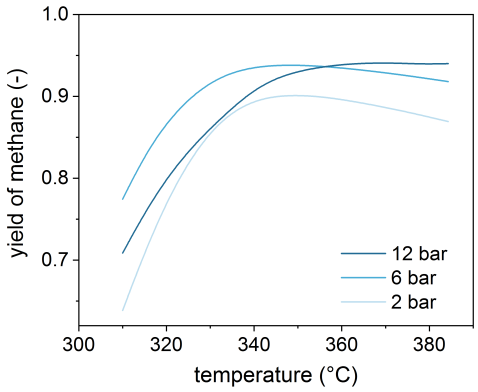

Figure 3.11: Performance of the fluidised bed reactor over temperature and pressure; $V_{biogas} = 200\ Nm^3/h$, in reactor: $H_2/CO_2 = 4.03$, $H_2O/CO_2 = 0.5$

for increased pressures, change the hydrodynamic behaviour and cause a reaction more strongly limited by mass transfer. The equation applied in the model for the visible bubble velocity taken from [111] is:

$$v_b = \psi \cdot (u - u_{mf}) \tag{3.27}$$

The parameter ψ describes the deviation of the visible bubble velocity from the two-phase theory. With slimmer reactor geometry, the parameter ψ increases as does the visible bubble velocity. More gas stays in the bubble phase, which increases the bubble hold-up. The reaction becomes more restricted by mass transfer from the bubble to the dense phase. The two effects of high pressure, which is thermodynamically more beneficial, and the more strongly mass transfer restricted reaction compensate for each other, so that no higher yield is reached with further pressure increases.

For the BFB-FB process, the yield in the fluidised bed is maximised to ensure low heat production in the subsequent FB reactor. Figure 3.11 showed that this target does not determine the operational conditions in the bubbling fluidised bed reactor, because the same maximum yield was reached for different pressures. Economic considerations in chapter 4 lead to a clearly defined optimal pressure for the BFB-FB process and other processes, where not only the reactor performance, but also other cost deciding factors are evaluated.

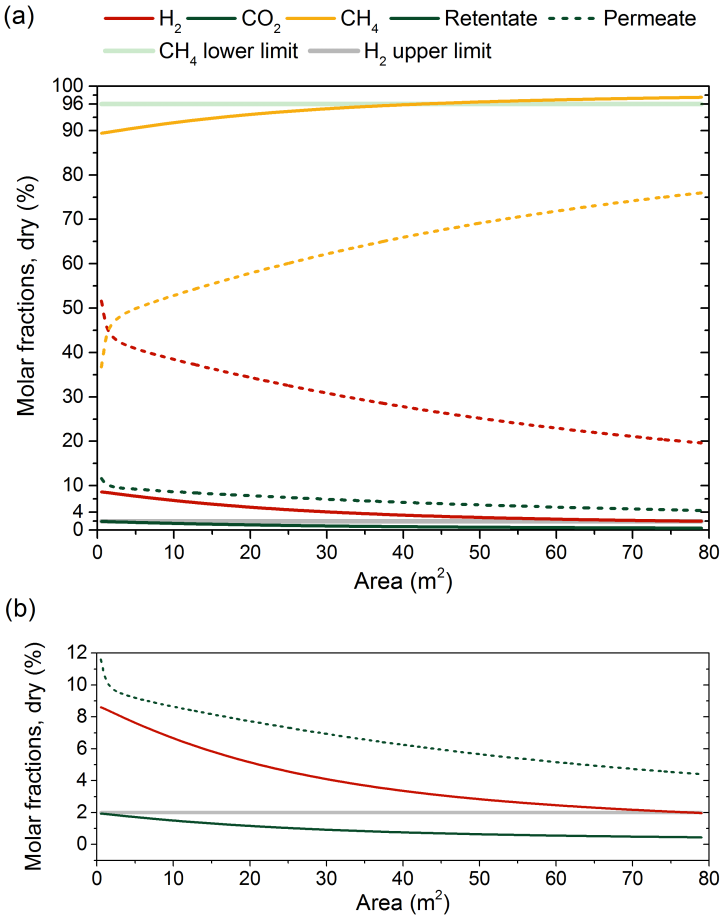

Figure 3.12: (a) Concentration profile of the main components on the retentate and permeate side for the PPO membrane as a function of the membrane area; (b) enlarged section of (a) for the molar fractions of CO_2 and hydrogen between zero and twelve percent; $p_{mem} = 12\ bara$, $p_{meth} = 12\ bara$, $H_2/CO_{2,in} = 4.0$, Process BFB-MemS

3.4.3 Gas Separation Membrane

The technical behaviour of the membrane influences the composition and the flow rate of the recycle stream. Consequently, it changes the concentration of components inside the reactor, as well as the total volume flow through the process inside the loop. Hence, the performance of the membrane influences the whole process significantly. The membrane module was therefore investigated in detail. Figure 3.12 (a) and (b) show concentration profiles of the main components hydrogen, methane and carbon dioxide for the permeate (recycle flow) and the retentate (biomethane flow) as a function of the PPO membrane area. The concentration of methane in the retentate increases with the area. At the same time, the methane fraction of the permeate side also increases. This means that methane permeates through the membrane to a greater extent than

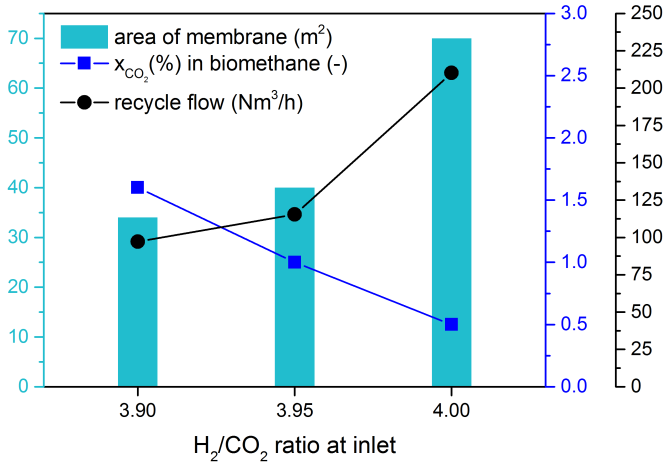

Figure 3.13: Effect of hydrogen saving to the process (membrane: Matr-PPO, $p_{mem} = 19\ bara$, fractions in biomethane: $x_{H_2} \sim 1.97\ vol-\%$, $96.1\ vol-\% < x_{CH_4} < 97.5\ vol-\%$; $p_{meth} = 9\ bara$, process: BFB-Mem)

hydrogen does. Due to the fact that hydrogen permeates more selectively through the membrane than methane, the fraction of hydrogen in the retentate is brought to 2 vol-%. In Figure 3.12 (b), an enlarged version of Figure 3.12 (a) is shown for carbon dioxide and hydrogen concentrations over the membrane area. It is shown that with a membrane area of almost 80 m^2, the hydrogen concentration in the retentate reaches the maximum allowable limit of 2 vol-%, whereas the methane limit (96 vol-%) was reached with half of this membrane area. As for the second fixed bed, it is more demanding to reach the hydrogen requirements of the gas grid than the methane requirements. Almost all of the CO_2 ends up in the permeate due to the high permeability of CO_2 through PPO membranes, which is illustrated in Figure 3.12 (b), where the CO_2 concentration in the retentate reaches almost zero.

A sub-stoichiometric addition ($H_2/CO_{2,in} < 4.0$) of hydrogen would create overall cost benefits for the operational and capital costs. Therefore, it is useful to investigate how hydrogen can be saved. For this, significantly more hydrogen than carbon dioxide must be separated by the membrane and recycled back to the reactor, so that the conditions inside the reactor are always slightly over-stoichiometric. Hence, a PPO membrane is not appropriate for saving hydrogen due to hydrogen and CO_2 having similar permeabilities in this membrane. The permeability of carbon dioxide must be sufficiently lower than that of hydrogen, which is the case for the hypothetical membrane Matr-PPO. In Figure 3.13, the effect of hydrogen saving on the process is explained for the Matr-PPO membrane. Here, the total membrane area required, the obtained recycle flow and the fraction of carbon dioxide in the biomethane stream are represented as a

function of the input ratio H_2/CO_2. The input ratio is defined as follows:

$$\left.\frac{H_2}{CO_2}\right|_{input} = \frac{\dot{n}_{H_2}^{Electrol}}{\dot{n}_{CO_2}^{biogas}} \tag{3.28}$$

The H_2/CO_2-ratio inside the reactor changes between 4.03 and 4.6 with the corresponding H_2/CO_2 input ratios. The hydrogen fraction in the product gas reaches about 2 vol-% for every input ratio; the methane fraction varies between 96.1 vol-% and 97.5 vol-% depending on the remaining CO_2 content. With decreasing hydrogen input from $H_2/CO_{2,in}$ = 4.0 to 3.90, the total membrane area required decreases as does the recycle flow rate obtained. In the recycle stream, the largest share belongs to methane despite the high selectivity of hydrogen compared to that of methane, because in the membrane feed, the methane content is already very high at about 90 vol-%. With smaller membrane areas, less methane permeates through the membrane together with hydrogen and CO_2, which reduces the total recycle volume flow. At the same time, the conversion of CO_2 decreases as well because there is less hydrogen present in the reactor, which reduces the H_2/CO_2 ratio inside the reactor. The resulting non-converted CO_2 is reflected in the increased content of CO_2 in the product gas, which reaches 1.6 vol-% for $H_2/CO_{2,in}$ = 3.9. A significant further decrease of the input ratio $H_2/CO_{2,in}$ is not possible, because then the concentration of methane would fall below 96 vol-%. In summary, with the approach of saving hydrogen, the grid injection requirements of 96 vol-% $_{min}$ for CH_4 and 2 vol-%$_{max}$ for H_2 can be met by filling the balance of 2 vol-% with CO_2 so that the concentration of methane in the product gas would be about 96 vol-% and about 2 vol-% for each hydrogen and CO_2.

In Figure 3.14, the three different membranes Matrimid, PPO and Matr-PPO are compared with each other, when used in the same process. Their total membrane area required to fulfil gas grid requirements and the corresponding recycle stream obtained are illustrated for the process FB-MemS. The input ratio of $H_2/CO_{2,in}$ is either set to a stoichiometric value of four for the membranes Matrimid, PPO and Matr-PPO/4.0 or is set to a ratio of 3.9 for the membrane Matr-PPO/3.9 (hydrogen saving approach). Matrimid membrane has the lowest permeability rates, followed by Matr-PPO and PPO membranes. The smaller the permeability and the permeating mass flow through the membrane, the larger is the membrane area required to reach a hydrogen concentration of below 2 vol-% in the retentate. Therefore, Matrimid membrane requires about ten times more area than the PPO membrane. On the other hand, the resulting permeate flow of Matrimid contains mainly hydrogen, which results in a smaller recycle flow. For the membranes PPO and Matr-PPO, the largest part of the recycle flow is methane due to lower selectivity of hydrogen over methane. In order to separate the required amount of hydrogen, the recycle flow rates for PPO and Matr-PPO/3.9 membranes are about 1.6

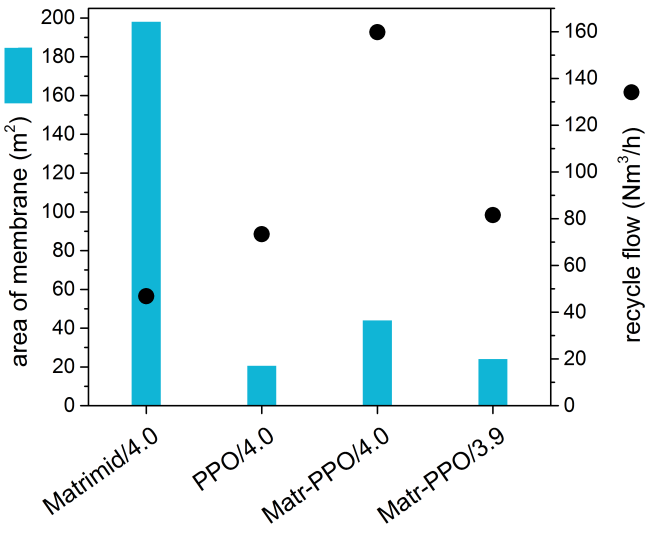

Figure 3.14: Total membrane area required to reach gas grid requirements in the retentate for different membrane materials, and the corresponding recycle flow rates (process FB-MemS, $p_{mem} = p_{meth} = 22\ bara$, $H_2/CO_2 = 4.0$ or 3.9)

times larger than for Matrimid. In comparison with the PPO membrane, Matr-PPO/4.0 membrane generates a significantly larger recycle stream. Less CO_2 permeates through the membrane because of the smaller permeability of CO_2 and a higher H_2/CO_2 selectivity ratio than in PPO membranes. As a result, less CO_2 is recycled to the reactor, and thus less hydrogen reacts with CO_2. The consequently increased amount of hydrogen in the outlet flow of the reactor requires a larger membrane area to meet the gas quality target and generates a larger recycle flow. Here, the established H_2/CO_2 ratio in the reactor is 4.6. A sub-stoichiometric $H_2/CO_{2,in}$ input ratio of 3.9 (Matr-PPO/3.9) is more beneficial for this membrane, which results in a similar required membrane area and a similar recycle flow as for the PPO membrane.

In literature, accurate information regarding the effective thickness s of a specific membrane is often not available. The assumption of 100 nm for every membrane is chosen from a range taken from [57], where 500 nm was stated as maximum. The effective thickness influences the required membrane area for the given separation task. In the model a direct proportional relationship exists between effective thickness and membrane area. Hence, for the maximum effective thickness of 500 nm, the required membrane area would be five times larger. Flow rates and compositions of retentate and permeate are the same with the corresponding membrane area.

In general, a trade-off exists between a high permeability, which saves membrane area and a high selectivity, which decreases the recycle flow rate. Nevertheless, a Matrimid

membrane would require such a high membrane area that it is unlikely that lower compression costs for the recycle stream could compensate for the increased costs of the membrane.

3.4.4 Process Flow Diagrams

Every process considered was illustrated as a flow diagram with the software e!Sankey® at operation conditions with which each process fulfils gas grid requirements. The shown operating conditions are already economical optimised and are a result of chapter 4. The corresponding technical data for these optimised processes can be found in the same chapter 4 (Table 6). Differences between the processes with a bubbling fluidised bed or a fixed bed as main reactor are only minor from an energy flow point view; therefore flow diagrams are shown representatively for the processes FB-FB, BFB-MemS, BFB-Mem and BFB-Mem3.9. The other flow diagrams, where in each instance the other main reactor is shown (BFB-FB, FB-MemS, FB-Mem), are included in the appendix.

The flow diagrams of the processes, shown in Figure 3.15 to Figure 3.18, correspond to the flowsheets in Figure 3.1 to Figure 3.3. All processes except BFB-Mem3.9 achieve product gas compositions of about 98 vol-% methane and 2 vol-% hydrogen. The BFB-Mem3.9 process with sub-stoichiometric hydrogen addition produces higher carbon dioxide concentrations at cost of the share of methane, but is still in the range of the gas grid requirements.

For every process, heat integration was done. All processes can provide themselves with heat produced within the process. After heat integration, excess heat is obtained at different temperature levels. Excess heat from the main reactor is present at a temperature between 350 °C and 380 °C depending on operational requirements. Excess heat from the condensers is obtained at the boiling point temperature for corresponding pressure, which is between 170 °C and 210 °C. The dissipated heat to cool the biomethane to the boiling point temperature of the first condenser is used to pre-heat the feed going to reactor. The electrolysis also provides heat, but only at relatively low temperatures of 60 °C - 80 °C. Heat integration for fixed bed reactors is more complex than for fluidised beds, see Figure 3.15. For fixed beds, the input temperature of the feed gas must be at least at operational temperature, otherwise the reaction will not start in the reactor. Because the fixed bed reactor is cooled to achieve thermodynamically beneficial temperatures, the outlet temperature of the reactor is too low to heat the feed gas to operational temperature. Here, it is necessary to use a part of the reaction heat along with heat from the subsequent condenser to heat up the feed gas in two steps, which requires a more complex heat exchanger system. For bubbling fluidised beds, it is sufficient only to use heat from the subsequent condenser to pre-heat the feed gas. In these

beds, reactor inlet temperatures can be lower than the operational reactor temperature due to good heat dispersion inside the BFB reactor. Heat for water evaporation is taken partly from the reaction heat and partly from the first condenser in all processes.

For the processes with a second-stage fixed bed (see e.g. Figure 3.15), more than 99.6 % conversion of carbon dioxide is necessary over the entire process in order to reach below 2 vol-% hydrogen concentration with a H_2/CO_2 input ratio of 4.03. Especially with the tendency of fixed bed reactors to deactivate due to coking, this is a challenging target for a long-duration operation. In terms of process control, two stage methanation processes are more demanding since the H_2 feed must be permanently adjusted to the carbon dioxide content in the biogas, which is subjected to fluctuations. On the other hand, processes with a membrane generally allow a higher H_2 addition corresponding with the maximum amount of carbon dioxide in the biogas over the year, which can be compensated by a bigger membrane area or higher pressure level. In this case, no strict control of the hydrogen feed is necessary.

In Figure 3.16 and Figure 3.17, the processes with a BFB reactor and a separation membrane are illustrated: one process with two pressure levels (BFB-Mem) and the other process with one pressure level (BFB-MemS). Process BFB-MemS is simpler than BFB-Mem because one compressor and one condenser less are used. On the other hand, larger recycle flows are achieved due to the lower pressure differences inside the membrane, which worsen the membrane performance. A larger membrane area is needed to reach 2 vol-% of hydrogen in the retentate flow and thus more methane permeates through the membrane. Larger recycle flows generally require larger components within the loop and cause higher power consumption of the compressor in particular. Hence, by removing the second compressor and condenser, investment cost savings can be made, but as a consequence, higher costs are incurred for the first compression and for larger equipment in general and for the membrane in particular.

Regarding energy consumption (heat and electricity) of the individual units within the processes, the electrolysis dominates the processes with an energy consumption two orders of magnitude higher than for the other units. Therefore, savings in hydrogen production will have a noticeable effect on the power consumption of the process as well as on the costs. Figure 3.18 shows the flow diagram of process BFB-Mem3.9, where less hydrogen is added to the biogas stream than in the other processes. This is possible due to the hypothetical membrane Matr-PPO with its high selectivity of hydrogen over methane, as well as its sufficient high selectivity of hydrogen compared to that of carbon dioxide. The required membrane area and the obtained recycle flow are similar to the corresponding parameters of process BFB-Mem, except for the smaller amount of carbon

dioxide in the recycle flow. Hence, parameters of process BFB-MemS are in a reasonable range, despite sub-stoichiometric addition of hydrogen to the system.

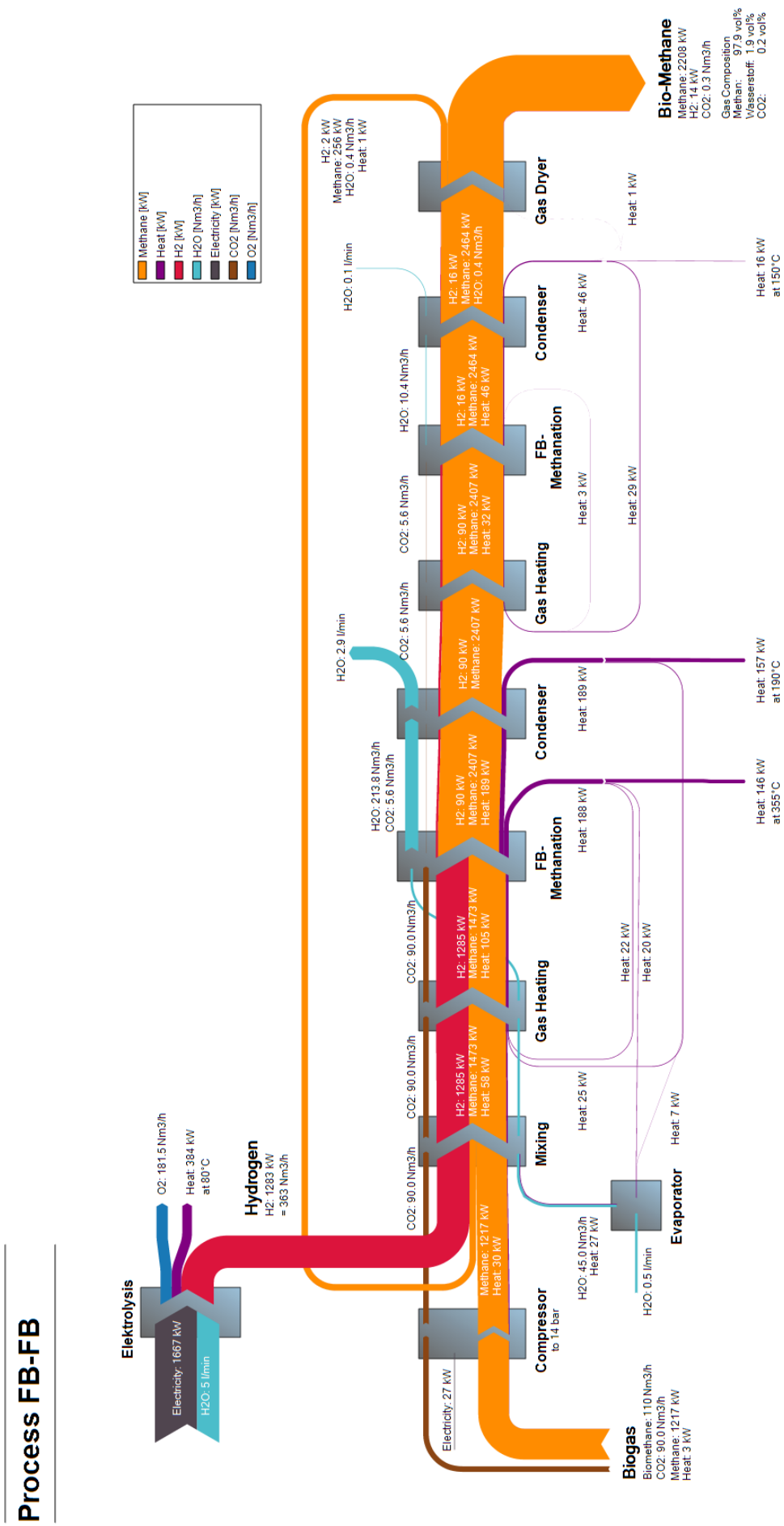

Figure 3.15: Flow diagram of process FB-FB; $p_{sys} = 14\ bara$, $H_2/CO_{2,input} = 4.03$

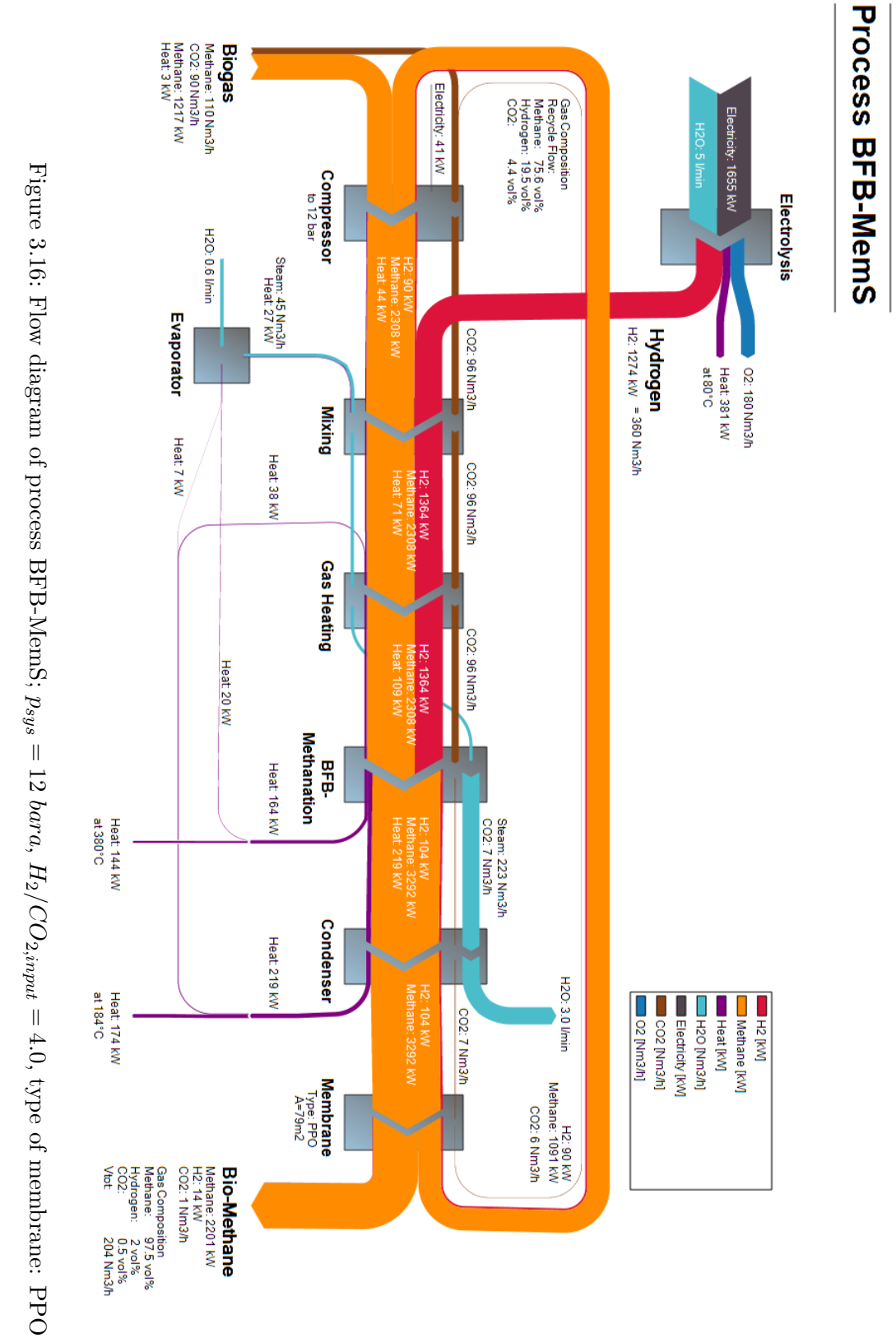

Figure 3.16: Flow diagram of process BFB-MemS; $p_{sys} = 12\ bara$, $H_2/CO_{2,input} = 4.0$, type of membrane: PPO

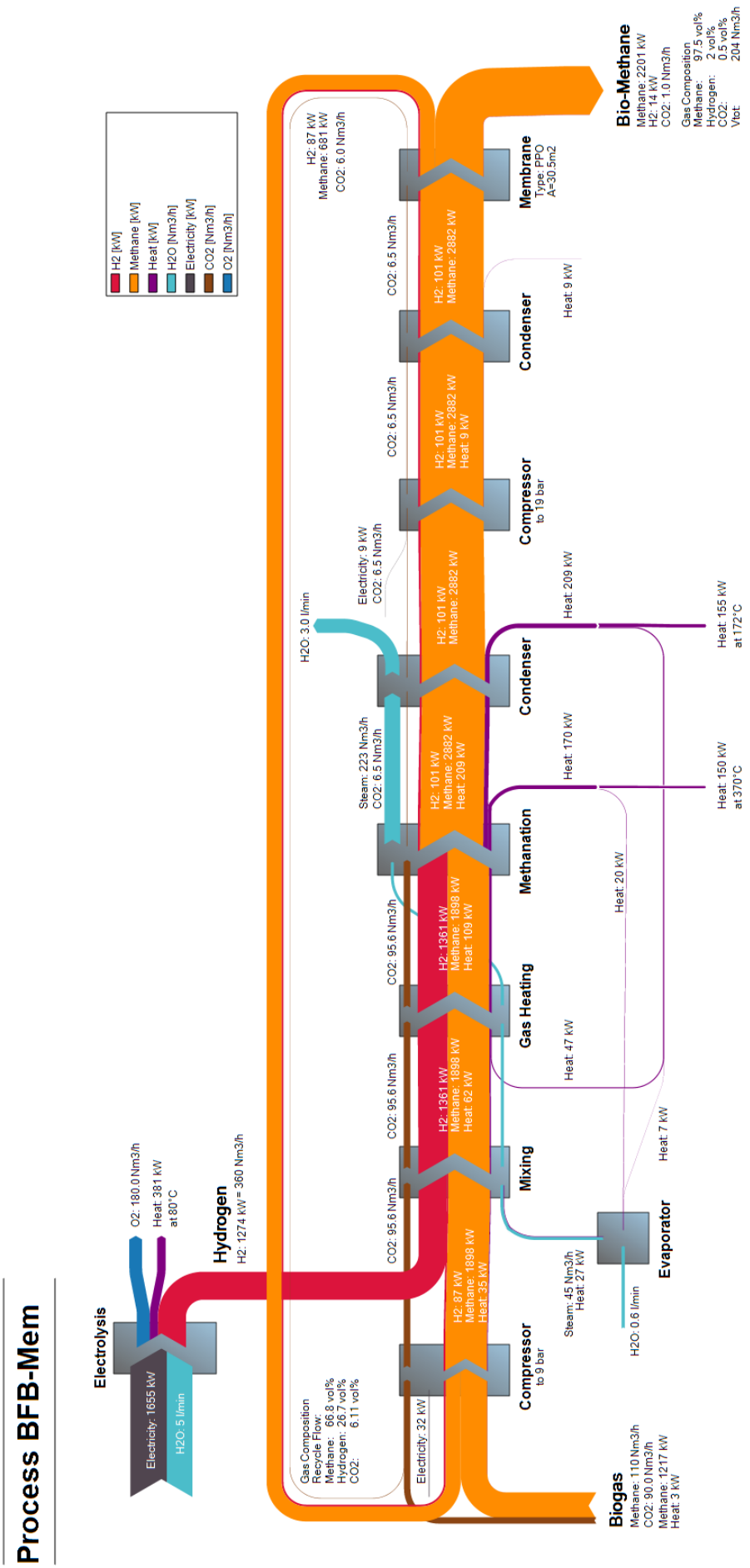

Figure 3.17: Flow diagram of process BFB-Mem; $p_{meth} = 9\ bara, p_{mem} = 19\ bara$, $H_2/CO_{2,input} = 4.0$, type of membrane: PPO

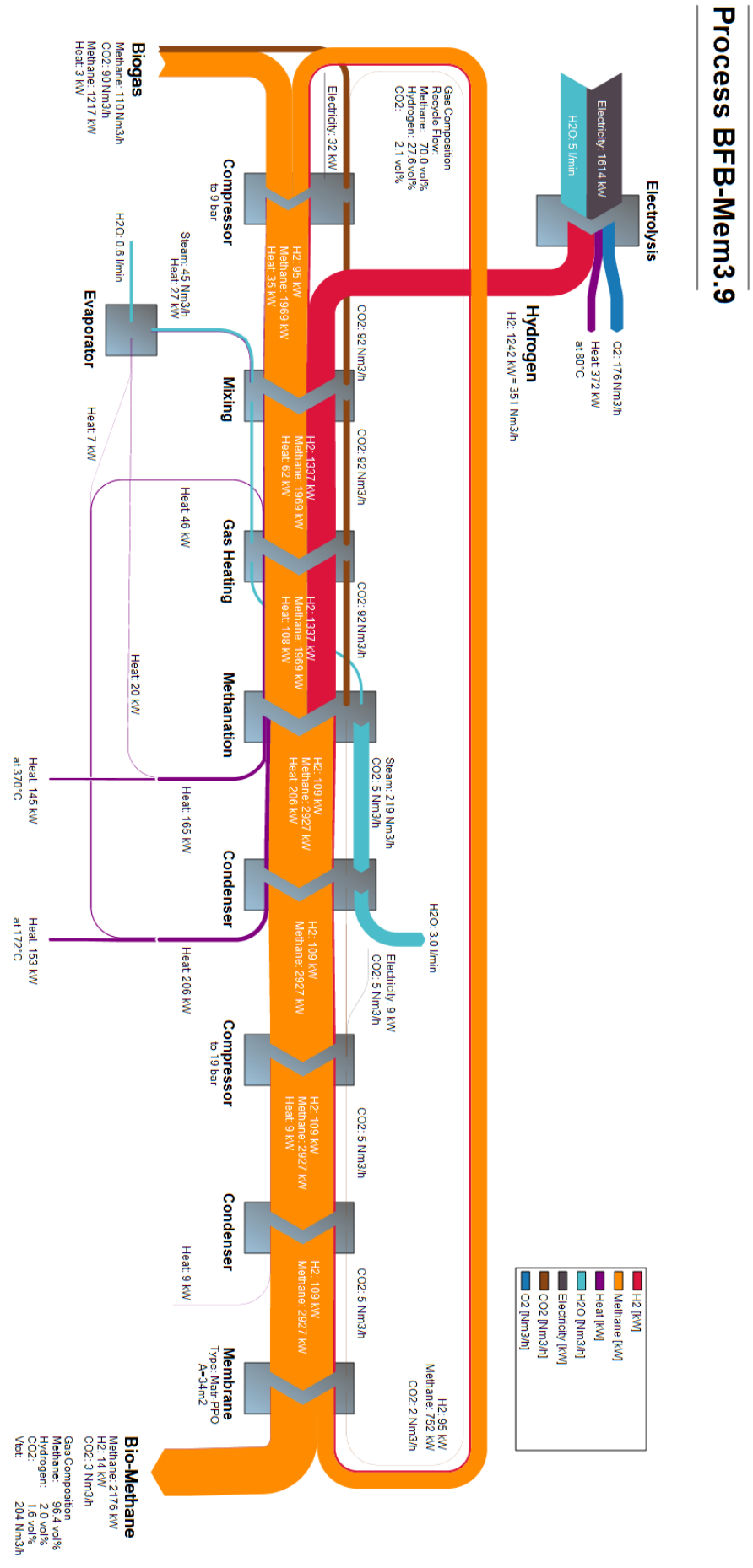

Figure 3.18: Flow diagram of process BFB-Mem3.9; $p_{meth} = 9\ bara$, $p_{mem} = 19\ bara$, $H_2/CO_{2,input} = 4.0$, type of membrane: Matr-PPO

3.5 Conclusions

Process modelling and simulations were done for direct methanation of biogas in order to produce unrestrictedly injectable biomethane for the Swiss or German natural gas grid. For this, two different methanation reactors (fixed bed and bubbling fluidised bed) and further upgrading technologies were evaluated using detailed rate-based models. It was shown that all processes produce biomethane which fulfils gas grid requirements for unrestricted injection ($>$ 96 vol-% CH_4, $<$ 2 vol-% H_2). The performance of either methanation reactors is not sufficient to reach gas grid requirements in one step, due to thermodynamic and kinetic limitations. Further upgrading after the main reactor is needed, for which a second (fixed bed) methanation or a hydrogen separation membrane was considered. This step as well as supporting units like condensers, evaporators etc. seem often to be neglected in previous literature [95]-[99] although the effort and corresponding costs to reach gas grid requirements are not marginal. In general, the reactor volume of a fixed bed is about three times larger than of a fluidised bed for processing the same biogas flow. A constant fluidisation and a sufficient heat transfer area for all operational conditions are required for fluidised bed reactors. On the other hand, more elaborated heat exchanger systems are needed for fixed bed reactors.

All processes show excess heat production at approximately 350 °C (main reactor) and 150 °C (condenser) after heat integration was completed. The removal of a second compressor and condenser in the simpler process versions BFB/FB-MemS does not necessarily achieve technical advantages in comparison with the corresponding process with two pressure levels, due to the larger recycle streams and larger membrane areas required. A second compressor has the advantage of a wider operating window for the process, because the reactor and the membrane can be controlled independently from each other regarding the pressure. The different membrane types Matrimid, PPO and the hypothetical membrane Matr-PPO were investigated. The membrane type PPO seems more favourable for the purification than Matrimid membranes despite their high selectivity of hydrogen over methane. The low permeability rates of Matrimid result in membrane areas required, which are one order of magnitude higher than for the other investigated membranes. For the hypothetical membrane Matr-PPO, reduced hydrogen needs would be possible. The recycle flow containing low amounts of carbon dioxide in comparison to hydrogen allows a sub-stoichiometric addition of hydrogen until an input ratio of $H_2/CO_{2,in} = 3.9$, while stoichiometric conditions are still achieved inside the reactor and gas grid requirements are fulfilled. Since the energy consumption of the electrolyser clearly dominates every considered process, saving hydrogen creates benefits for the processes.

Nevertheless, technical aspects alone cannot decide which the most appropriate process is for upgrading biogas via direct methanation, since all considered processes and a variety of process parameters together can meet the product specifications of the gas grid. In the end, an economic analysis of the different processes and of different operation conditions can give an answer to the question, which is the most beneficial approach.

4 Direct Methanation of Biogas: Techno-Economic Assessment[1]

4.1 Abstract

Six different processes for the direct methanation of biogas for biomethane production were evaluated regarding their economically optimised operating conditions, their absolute costs and profitability. Detailed process simulations turned out to be important to obtain a solid process design with which a realistic cost estimate is possible. Costs data for the methanation from literature are often under-estimated due to the lack of a required second upgrading step (post-upgrading) to reach the demanded gas grid specifications and of additional process equipment. A fixed bed methanation reactor is two times more expensive than a bubbling fluidised bed reactor but due to the dominant share of costs of the electrolysis, costs differences between the whole processes of 5 % are less pronounced. It turned out that a gas separation membrane and a second fixed bed, as a post-upgrading step, are equally expensive. However, a gas separation membrane seems to be technically more robust. Biomethane production costs of 22.7 $Ct_{€}/kWh_{new}$ for processes containing a fluidised bed and of 23.9 $Ct_{€}/kWh_{new}$ for processes containing a main fixed bed are obtained. As a consequence, the corresponding processes are profitable until an electricity price of 6.0 $Ct_{€}/kWh_{el}$ and 5.3 $Ct_{€}/kWh_{el}$ without considering the extra revenues from process heat and oxygen. Furthermore, the profitability of the processes increases with the methane content in the biogas. Considering extra revenues and a concentration increase of 10 % for methane in the biogas, the maximum electricity price for a profitable process increases by 3 $Ct_{€}/kWh_{el}$.

[1]This chapter is based on the following publication: J. Witte , A. Kunz , S.M.A. Biollaz, T.J. Schildhauer. "Direct Catalytic Methanation of Biogas – Part II: Techno-Economic Process Assessment and Feasibility Reflections". In: *Energy Conversion and Management* 178 (2018), pp. 26-43. https://doi.org/10.1016/j.enconman.2018.09.079. Julia Witte performed the cost optimisation via delta-costs method and carried out the absolute costs assessment, determined detailed costs of the reactor types and the production costs of the whole processes considering different site conditions via sensitivity analyses, created all diagrams and wrote the text.

4.2 Introduction

In chapter 3, possible processes for the direct methanation of biogas were designed with the application of detailed models describing the main process units: fluidised bed and fixed bed as methanation reactor and the gas separation membrane. For the methanation reactor, rate-based models were implemented which consider not only the thermodynamic equilibrium but also the kinetic properties of the catalyst for a specific reaction. The models are described in the section 3.3.2. The designed and technically evaluated processes are illustrated schematically in Figure 3.1 to Figure 3.3. For the economic analysis the seven presented processes of chapter 3 are considered.

Biogas is defined as the raw gas produced via digestion. It contains methane and carbon dioxide as bulk chemicals. Biomethane is considered to be the end-product ($>$ 96 vol-% of methane) after the upgrade of the biogas via methanation and is unrestricted injectable into the gas grid. All processes start with a biogas flow of 200 Nm^3/h, which contains 55 vol-% methane and 45 vol-% carbon dioxide. This CO_2 concentration is the maximum amount expected in biogas and represent technically and economically the most challenging conditions, which is illustrated in the economic results. The end-product of all processes is biomethane, fulfilling general gas grid requirements in Germany and Switzerland (i.e. $CH_4 \geq 96$ vol-%, $H_2 \leq 2$ vol-% [100, 101]). The main parts of the processes are the electrolysis providing hydrogen, the main methanation reactor converting CO_2 with hydrogen into methane, and a further upgrading step which is either a second fixed bed methanation or a gas separation membrane (Mem). Regarding the main reactor, the two technologies are considered for economic analysis: the fixed bed (FB) and the bubbling fluidized bed (BFB). For the membrane three different membrane types were technically investigated in chapter 3 and are considered for the economical analysis as well.

All processes are self-sufficient in terms of process heat after measures of heat-integration and produce further excess heat on two temperature levels. One heat flow is produced in the main reactor due to the reaction heat at a temperature of approximately 360 °C. The other heat flow is established during the first condensation. Here, the condensation enthalpy mainly of the water produced during reaction at specific pressure and corresponding temperature is causing excess heat at approximately 180 °C. In chapter 3, it could be shown, that all presented processes can reach the mentioned gas grid requirements with corresponding operating conditions. However, the optimum process conditions and the most beneficial process for the direct methanation of biogas could not be identified from a technical perspective since various combinations of operating conditions and all presented processes were technically feasible.

In this chapter, these processes are evaluated economically in order to identify in a first step the most profitable operating conditions for each process while the product gas is still fulfilling the gas grid requirements. In a second step, the most profitable process is determined. Here, an economic comparison is conducted between the fixed bed and bubbling fluidized bed reactor, as well as between the further upgrading technologies, the second fixed bed methanation and the gas separation membrane.

4.3 Methods

The objective of the economic analysis is the comparison of the six processes regarding their profitability for an input biogas flow of 200 Nm^3/h containing 45 vol-% carbon dioxide and 55 vol-% methane. Capital and operating costs are considered. A lifetime of 15 years and an interest rate of 5% are assumed. A biogas price of 6 $Ct_€/kWh_{biogas}$ is considered. This price is a result of the feed-in tariffs for electricity from biogas. Hence, the biogas costs can be seen as opportunity costs. The actual production costs of biogas may be significantly lower. But in order to compete with the conversion of biogas into electricity, the opportunity costs of biogas are chosen for the assessment. Further economic data can be found in Table 4.1. The economic assessment was done in two steps. First, a Difference-in-Costs method was applied to identify the most profitable operating conditions for each process so that gas grid requirements are fulfilled. Second, a detailed absolute economic analysis on the base of the cost optimised processes from step one was done for every process. The processes are compared with each other regarding costs and profitability.

For both steps, capital and operation costs were determined. For the capital cost, cost functions for the modules of the process units were developed with data from literature [132]. These cost functions have the following structure:

$$C_{BM} = C_{Pur} \cdot F_{BM}, \quad \text{with } F_{BM} = f(F_M, F_P) \tag{4.1}$$

The costs of the bare modules C_{BM} consist of the purchased equipment costs C_{pur} multiplied by a bare module factor F_{BM}, which considers additional costs for the material and if necessary for the pressure in the component. The material and pressure factors F_M and F_P are taken from literature [132]. The purchased equipment costs depend typically on the size of the unit, which can be given by dimensions of the unit (e.g. reactor vessel: height and diameter) or the necessary capacity (e.g. compressor: power). The required data is obtained from the detailed simulation study in chapter 3. The accuracy

[2] piping, electricals and instruments incl.

economic factors	value	units	source
electricity	0.05	€/kWh$_{el}$	[95]
heat revenues	0.04	€/kWh	[95]
biogas price	0.06	€/kWh$_{biogas}$	[130, 131]
biomethane selling price	0.11	€/kWh$_{total}$	[130]
operation hours	8322	h/a	[130]
gas separation membrane	900	€/m^2	[132]
electrolysis, AEL[2]	930	€/kW$_{el}$	[128]
catalyst	90	€/kg	[133]
desiccant, silica gel	20	€/kg	[134]
gas cleaning adsorbents	320	€/Nm$^3_{biogas}$/h	[135]
hydrogen tank	50	€/Nm^3	[136]
biogas tank	80	€/Nm^3	[137]
interest rate	5	%	[130]
lifetime	15	yr	[130]

Table 4.1: Economic values

of this equipment factored cost estimates is within ± 20% [132]. Higher accuracies would require more detailed process flow sheets, pre-final equipment design, and piping and instrumentation diagrams which is out of scope for this work.

4.3.1 Delta-Costs Method

The aim of the difference-in-costs method (referred to as dC-method) is the identification of cost optimal operating conditions ensuring that the concentration limits of hydrogen, CO_2 and methane in the product gas are reached. From a technical point of view, various combinations of operating conditions can be applied in the processes to produce biomethane with the required product quality. The investigated ranges of operating conditions for each process are listed in Table 3.3. The operating ranges used in chapter 3 are applied for the dC-method. The operating conditions are evaluated regarding their economic outcome. For this, a base case is defined for every process with fixed operating values, for which the annual operating and capital costs C_{Base} are obtained. Now, operating conditions are varied and compared with respect to economics to the base case for each process. It depends on the process which conditions can be varied independently. For processes with a second fixed bed or with a PPO membrane type, only the process pressure can be varied. The other process parameters, like reactor temperature or H_2/CO_2 input ratio etc., are given in order to produce the required biomethane gas quality. For processes, which contain a membrane type with appropri-

cost factors F_{PC}	value
piping	0.4
instruments	0.1
electricals	0.2
buildings and foundations	0.13
engineering and approval	0.3

Table 4.2: Considered plant cost factors F_{PC} [139] for absolute economic analysis

ate selectivity properties (Matrimid and Matr-PPO) also the H_2/CO_2 inlet ratio can be varied independently from the reactor pressure. This procedure is described in chapter 3.

For every set of operating conditions for one process, capital and operating costs are calculated (CAPEX and OPEX). For the dC-method, the investment costs are directly obtained from the total bare module costs CB_M. Then the capital expenditures (annuity) are calculated based on the mentioned assumed lifetime a and the interests rate i:

$$C_{CAPEX} = C_{tot}^{inv} \cdot \frac{(1+i)^a \cdot i}{(1+i)^a - 1} \tag{4.2}$$

Plant costs factors and the plant costs index are not included in the difference-in-costs method, but will be in the absolute economic analysis. The operating costs correspond to the operating expenditures. Here, yearly electricity costs for compressors and the electrolysis are considered along with the material costs for the yearly catalyst renewal as well as for the gas cleaning and drying adsorbents. The cost values for this are listed in Table 4.1. For the yearly operation and maintenance (O & M) costs, 5 % of the total investment costs are considered [138]. For the dC-method, only the parts of the costs are considered, which are changing due to different operating conditions. This is valid since only the difference between the costs shall be monitored. For the same reason, the constant cost factors are not considered, which are used in the absolute economic analysis in a next step. Exceptions are the electrolyser-costs, which are always included in the evaluation. Oxygen revenues from the electrolysis are not considered, because selling prices can become zero, if locally there is an excess of oxygen production.

The costs difference dC is determined in the following way:

$$dC = \left(\left(\frac{C}{C_{base}}\right) - 1\right) \cdot 100\ \% \tag{4.3}$$

The total yearly costs C include operating and capital costs, which are changing due to the varied operating conditions. The most profitable case can be found were dC is at minimum.

4.3.2 Absolute Economic Assessment

Once cost-optimal operating conditions are found for every process, a detailed absolute economic analysis of each process is conducted. For the total investment costs C_{tot}^{inv} (equation 4.4), the bare module costs C_{BM} (equation 4.1) of each unit k is considered along with a chemical engineering plant cost index CEPCI (Equation 4.5) and plant cost factors F_{PC} in the following way:

$$C_{tot}^{inv} = \sum_{k} C_{BM,k} \cdot CEPCI \cdot \left(1 + \sum F_{PC}\right) \tag{4.4}$$

$$CEPCI = \frac{CEPCI_{current}}{CEPCI_{ref}} = 1.4 \tag{4.5}$$

The plant cost index adjusts the costs to the inflation rate. The reference value $CEPCI_{ref}$ is set to 400 and refers to January 2004, for which the cost functions are obtained [132]. The current CEPCI value (March 2017) is 562. In addition to the bare module costs with inflation adjustment, indirect plant costs like e.g. engineering and approval costs are considered in a next step. For this, plant cost estimating factors F_{PC} are used, which are listed in Table 3. The sum of these factors is multiplied with the inflation adjusted bare module costs to receive the total investment costs for the process. In a last step, the yearly capital expenditures (CAPEX) are calculated from the total investment costs with equation 4.2 considering lifetime and interest rate listed in Table 4.1.

For the absolute economic evaluation, a detailed cost assessment was done. In particular for the main methanation reactor, a rigorous equipment analysis was carried out. In Figure 4.1, a scheme of the main reactor is shown with its required components for the reactor vessel, the cooling cycle and for the activation of the catalyst. The reactor vessel is either a multi-tubular fixed bed with shell-side cooling (a) or a fluidised bed with internal cooling tubes and a subsequent particle filter (b) corresponding to the evaluated process. For the cooling cycle of the cooling agent, two heat exchangers (one for cooling, the other for heating at the start-up) and one pump is considered. Further, equipment and vessels for catalyst pre-treatment and catalyst filling/removal are considered.

The relevant data for the economic evaluation like sizing of the equipment, electricity consumptions, excess heat etc. are obtained from the simulation results in in chapter 3.

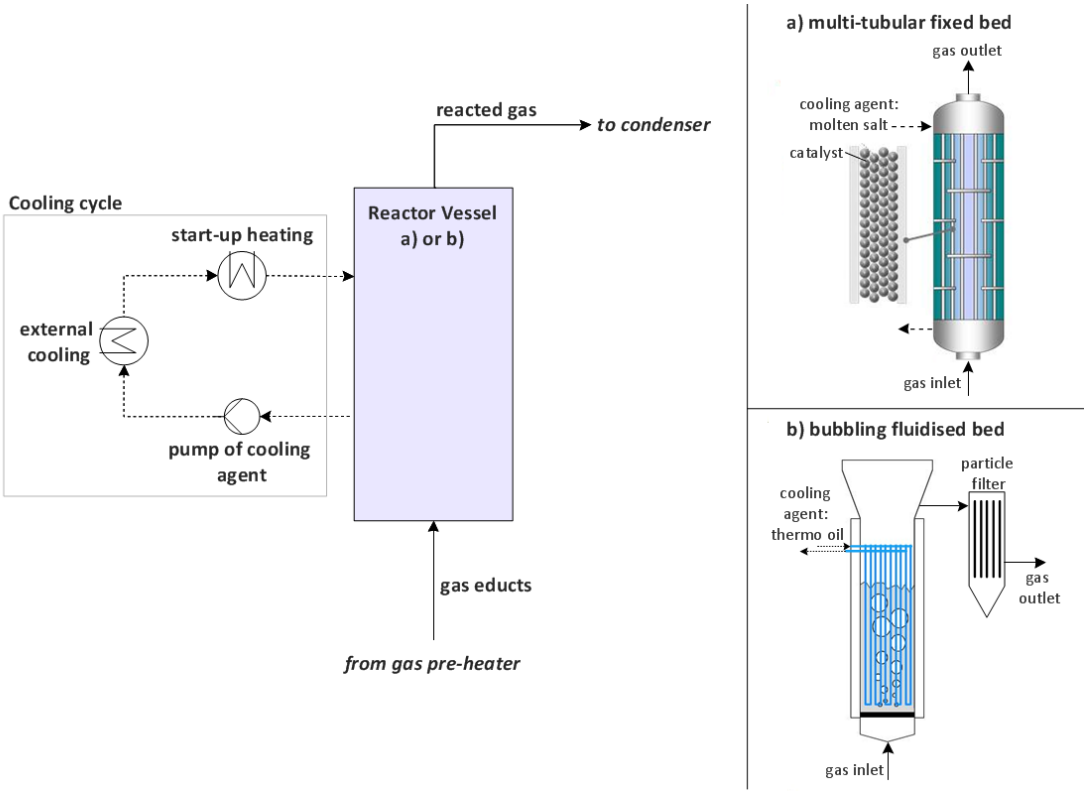

Figure 4.1: Components of the main reactor considered in the economic analysis for a) a multi-tubular fixed bed [140] and b) a bubbling fluidised bed

4.4 Results and Discussion

A variety of possible operating conditions and corresponding equipment sizing was identified along with different membrane types, which can produce biomethane fulfilling the gas grid requirements for unrestricted injection. To find out which possible combinations of the process modules and operating conditions are the most economical ones, a cost difference method (referred to as Delta-Costs or dC-method) is carried out. With the economically optimised process conditions retrieved from the dC-method, the absolute economic assessment will be conducted in a next step.

4.4.1 Delta-Costs

All cases shown in this section produce biomethane which fulfils the gas grid requirements. With the dC-method the different processes cannot be compared with each other, but within a process the cost optimal conditions can be found. For the processes with a membrane (except type PPO), the reactor pressure and the hydrogen input can be varied independently. The optimum membrane pressure for each membrane was identified with 19 bara for PPO and Matr-PPO membranes and 40 bara for Matrimid membranes. At

these pressure levels, the combined costs of membrane compression (CAPEX+OPEX) and membrane area are at minimum. The low permeability rates of the Matrimid membrane result in higher pressure differences required than for the PPO membrane to produce the required biomethane-retentate. Lower pressure differences would cause an exponential increase of the membrane area required, which is not economical. All processes provide an excess of heat after heat integration. Hereinafter, the results of the difference-in-costs method are shown for the different processes.

Process BFB-FB

In Figure 4.2, the delta-costs of the process BFB-FB are illustrated as a function of the pressure. The process pressure was varied between 7 bara to 12 bara. The base case was set to 6 bara. The geometry of the BFB reactor was adapted to the different pressures and temperatures according to chapter 3. For higher pressures, the BFB reactor becomes slimmer, but longer, so that the volume and the catalyst mass remains the same, which results in about the same capital and catalyst costs. Also the temperature inside the reactor influences the volume of reactor because with higher temperature, heat dissipation becomes more effective which allows a decrease of heat exchanger area and reduces therefore the necessary volume of reactor, but these changes are marginal due to required temperature changes between 365 °C and 375 °C in the main reactor. Hence, changes in capital and catalyst costs for the fluidised bed were minor. Therefore, they can be neglected for the dC-analysis for the BFB-FB process. The considered costs for the dC-analysis are the capital and operating costs of compression, the capital costs of the fixed bed reactor, the material costs of the annual fixed bed-catalyst replacement and the heat revenues. In comparison to the base case (BFB-FB at 6 bar) capital and operating costs of the compression are increasing while the costs of the fixed bed reactor and of the catalyst are decreasing. The FB reactor becomes shorter with increasing pressures thanks to an improved performance (see section 3.4). The heat revenues are handled as savings, therefore, they appear as negative delta costs. They are increasing with higher pressures, due to a smaller heat flow required for gas preheating since the inlet temperature of the heat exchanger is higher due to increased compression. The total delta-costs are obtained by summation of the individual delta-costs of the considered equipment. They are decreasing with the pressure and are minimal between 10 and 12 bara, which correspond to the highest saving potential. If no heat revenues are considered, the minimum delta costs would be obtained at 10 bara. However, the delta costs difference between 10 and 12 bara is minor and heat revenues shall be considered for the dC-method. Therefore, the optimum operating pressure is set to 12 bara for the BFB-FB process in terms of costs. The other process parameters are determined by the pressure to reach the required gas quality at the end of the process.

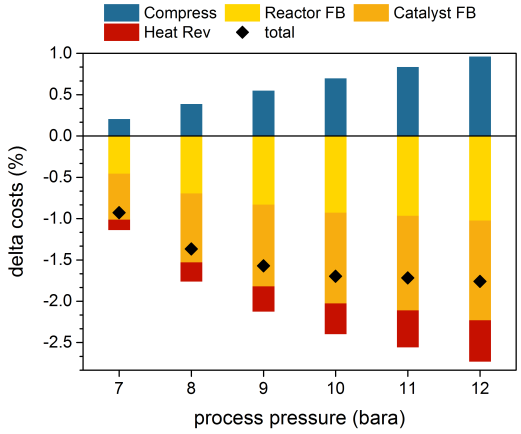

Figure 4.2: Delta costs of process BFB-FB over the process pressure with $H_2/CO_{2,input}$ = 4.03 in comparison to the base case of 6 bara for BFB-FB

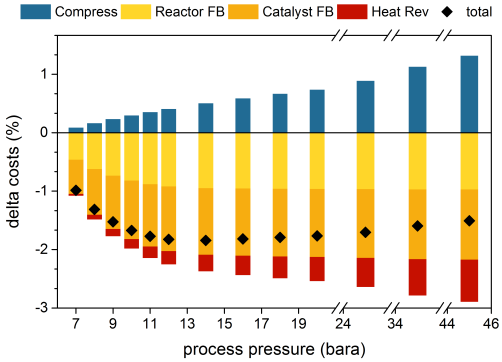

Figure 4.3: Delta costs of process FB-FB over the process pressure with $H_2/CO_{2,input}$ = 4.03 in comparison to the base case of 6bara for FB-FB

Process FB-FB

In Figure 4.3, delta costs and recycle flow rates of the process FB-FB are illustrated as a function of the process pressure. Cooled FB reactors are assumed to operate until 45 bara [107]. The main reactor has a fixed size of 3.5 m and 120 internal tubes a 2.5 cm with catalyst inside. The length of the second fixed bed is adapted to the pressure in order to produce biomethane with gas grid quality. The process pressure was varied between 7 and 45 bara. Again, the base case was set to 6 bara. The result is comparable with process BFB-FB until 12 bara. Here, savings of costs for the second fixed bed due to increased pressure and heat revenues exceed the increased compression costs. A minimum of delta costs is formed between 11 and 14 bara. Again, heat revenues decide at which pressure exactly the minimum delta costs are obtained. Then the total delta costs are increasing again, because the savings for the second fixed bed and the heat revenues cannot compensate the further increasing costs of compression any more. Hence, the economically optimal operating conditions with heat revenues considered were set at 14 bara for the FB-FB process. Without taking the costs of the electrolysis into account, the maximum cost difference between the optimised case and the base case is around -30 % for both processes (BFB-FB and FB-FB).

Process BFB-Mem

In Figure 4.4, the delta-costs of the process BFB-Mem for different membrane types are shown with a base case at 3 bara process pressure and $H_2/CO_{2,input}$ = 4.0 for a PPO membrane. The input ratio of hydrogen to carbon dioxide is defined in equation 3.28. The base case for the diagrams (a)–(c) is the same. The different membrane types PPO,

Matrimid and Matr-PPO corresponding to the diagrams (a)-(c) are discussed more into detail in chapter 3. The BFB reactor is adapted to the different operating conditions but again, differences in capital costs for the reactor are marginal and hence not included in the dC-analysis. The catalyst costs in this case must be included because the reactor temperature changes between 350 °C and 380 °C. For higher reactor temperatures the required heat exchange area inside the BFB reactor decreases due to the bigger temperature difference between the reactor and the cooling agent. Since the reactor diameter is fixed with the fluidisation conditions, the height of the reactor can be decreased for a smaller heat exchange area. Changing the height of the reactor causes only marginal capital cost differences, but influences the catalyst costs noticeably. Therefore, for the BFB-Mem process, the following components are considered for the dC-analysis: capital and operating costs of both compressors and of the electrolysis, capital costs of the membrane, material costs of the annually replaced catalyst and the heat revenues. In the diagrams (a) and (b) of Figure 4.4, the process pressure which includes the evaporator, the main reactor and the first condenser was varied between 4 bara and 9 bara. The pressure on the retenate side in the membrane is fixed with 19 bara for PPO and Matr-PPO membranes and 40 bara for Matrimid. Here, the delta costs are shown for (a) the PPO membrane and (b) the Matrimid membrane.

In diagram (a), higher conversion rates due to increased pressure lead to a smaller membrane area required because less hydrogen and carbon dioxide remain in the outlet stream of the reactor, which results in a simpler separation task for the membrane. Also less methane is permeating through the smaller membrane area, hence a purer and smaller recycle stream is obtained. Costs can be saved due to the decreased recycle flow rates and a smaller required membrane area for an increased process pressure. With a smaller and less CO_2 containing recycle flow, the volume of the reactor can be decreased as well, and with that, savings for catalyst material is possible. Nevertheless, compression costs of the two compressors have a minimum at 6 to 8 bara; for higher pressures, the recycle flow is not decreasing significantly, so that the bigger effort of compression due to higher pressures cannot be compensated any more by a decreased recycle flow rate. Also for this process, heat revenues are increasing with higher pressures due to the temperature increase caused by the increased compression of the input gas flow. Less heat is needed to pre-heat the gas and more process heat remains for selling. The lowest total delta-costs for the PPO membrane are obtained at 9 bara, if heat revenues are considered.

In diagram (b), the membrane Matrimid is evaluated. Here, a similar behaviour for increased process pressure can be observed. Total delta-costs are decreasing with the pressure. Like already shown in chapter 3, the Matrimid membrane requires a larger

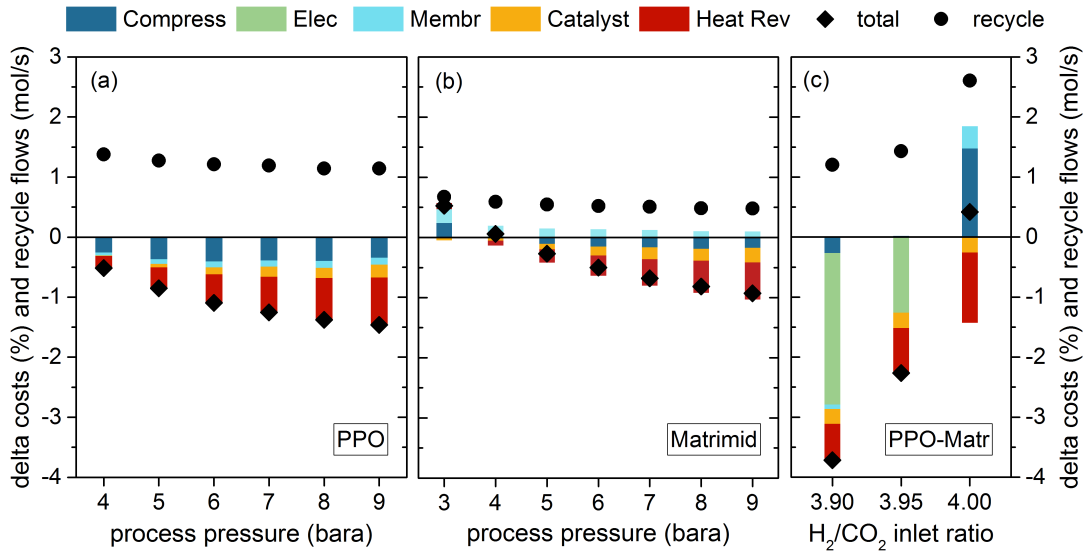

Figure 4.4: Delta Costs and recycle flow rates of the BFB-Mem process with different membrane types as a function of the process pressure or the inlet ratio $H_2/CO_{2,input}$. The membrane pressure is fixed for PPO and PPO-Matr of 19 bara and for Matrimid of 40 bara. The base case is at 3 bara process pressure, an input ratio $H_2/CO_{2,input}$ of 4.0 and a PPO membrane. (a) Delta-costs and recycle flow rates over the process pressure for the PPO membrane; (b) Delta costs and recycle flow rates over process pressure for the Matrimid membrane (c) Delta costs and recycle flow rates over the $H_2/CO_{2,input}$ ratio for the Matr-PPO membrane at 9 bara process pressure

membrane area for the same separation task than the PPO membrane. Since, the underlying costs of diagram (b) are also compared to the base case with a PPO membrane, delta costs of the Matrimid membrane can become even positive. Hence, for all pressure levels the Matrimid membrane is more expensive than the PPO membrane in the base case. The compression delta-costs are positive at 3 bara as well due to the higher operating pressure of the Matrimid membrane of 40 bara. A direct comparison of the delta costs of diagram (a) and (b) is possible, since the same base case is applied and the same components costs are considered. For the Matrimid membrane, the lowest costs are obtained at 9 bara process pressure with a costs difference compared to the base case of 1 %. The PPO membrane reaches process conditions at 9 bara, with which 1.5 % of the costs can be saved in comparison to the base case. Hence, the PPO membrane is economically more beneficial for the BFB-Mem process than the Matrimid membrane.

In the last diagram (c), delta-costs and recycle flow rates are shown for the usage of the hypothetical Matr-PPO membrane in process BFB-Mem, as a function of the ratio $H_2/CO_{2,input}$ at a process pressure of 9 bara. The membrane Matr-PPO allows hydrogen saving in contrast to the other discussed membrane types due to its separation

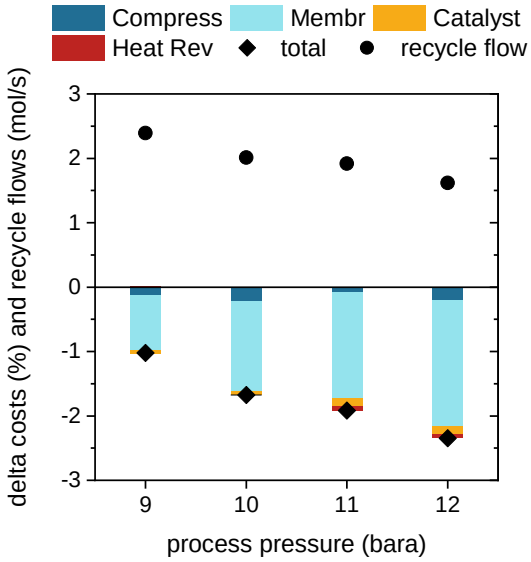

Figure 4.5: Delta-Costs and recycle flow rates for the BFB-MemS process with PPO membrane as function of the process pressure with a base case of 8 bara process pressure, an input ratio $H_2/CO_{2,input}$ of 4.0 and a PPO membrane

properties. Therefore, with the Matr-PPO membrane, $H_2/CO_{2,input}$ ratios below 4 are possible. Since the base case includes a $H_2/CO_{2,input}$ of 4.0, lower costs for the electrolysis are achieved with lower $H_2/CO_{2,input}$ ratios. The minimum technically achievable $H_2/CO_{2,input}$ ratio for the Matr-PPO membrane is 3.9 as explained in chapter 3. Heat revenues are decreasing with decreased $H_2/CO_{2,input}$ input ratios. Since less conversion of CO_2 in the reactor is achieved with less hydrogen addition less reaction heat is produced. The costs savings due to a decreased hydrogen production have the largest share and contribute significantly to the lowest total delta-costs at a $H_2/CO_{2,input} = 3.9$ in comparison to all three membranes (diagram (a) to (c)) with costs savings of -3.7 % compared to the base case. Hence, the membrane Matr-PPO would be economically most beneficial for the process, but since it is only hypothetical it is considered separately in an extra process called BFB-MemT for further evaluations. Regarding the process BFB-Mem, the optimal choice is the PPO membrane at a process pressure of 9 bara.

Process BFB-MemS

In the process BFB-MemS, the second compression after the BFB unit is omitted. In Figure 4.5, delta-costs and recycle flow rates of the process BFB-MemS are shown as a function of the process pressure. For this process, the pressure in the methanation part and the membrane pressure are the same for neglected pressure losses. Due to

the low maximum pressure of 12 bara (highest pressure possible in a fluidised bed, see chapter 3) for the process and therefore in the membrane, only the PPO membrane is appropriate for the actual separation task. This means also, that for this process no hydrogen saving is possible. Therefore, only hydrogen addition of $H_2/CO_{2,input}$ = 4.0 is considered. The corresponding costs are compared to a base case of this process with 8 bara process pressure, an inlet ratio of $H_2/CO_{2,input}$= 4.0 and the PPO type membrane. The following changing components are examined: capital and operating costs of compression, capital costs of the membrane, catalyst costs and heat revenues. With increasing pressure, almost no compression costs can be saved. On the one hand, with the pressure higher conversion rates in the reactor are obtained, on the other hand, the smaller pressure differences in the membrane than for the process BFB-Mem result in a larger recycle flow. Smaller pressure differences in the membrane require a larger membrane area to achieve the product gas quality. But the larger membrane area results in a higher permeation of methane, which is then present in the recycle and with that in the whole process loop. This additional methane in the loop must be compressed, too which compensates the cost-saving effect of higher conversion rates with higher pressures in this process. With increasing pressure differences in the membrane, the membrane area can be reduced. Therefore the membrane costs are decreasing for higher pressures. Catalyst savings and the change of heat revenues are marginal. The lowest total delta costs are obtained at 12 bara process pressure.

Process FB-Mem

The FB-Mem process is similar to the BFB-Mem process. The difference is the usage of a fixed bed as main reactor instead of a fluidised bed with corresponding changes for the heat exchange equipment. In Figure 4.6, delta-costs and recycle flow rates of the process FB-Mem are shown for different types of membranes as a function of the process pressure or the $H_2/CO_{2,input}$ ratio. The corresponding costs are compared to a base case of this process at 6 bara process pressure, an ratio $H_2/CO_{2,input}$ of 4.0 and a PPO membrane. The main FB reactor was fixed to a height of 3.5 m and 120 internal tubes of 2.5 cm diameter each. Inside those tubes, the catalyst is present. Like for the other membrane containing processes, the membrane area was adapted to reach gas grid quality in the retentate flow for every process pressure. The examined changing components are: capital and operating costs of both compressors and of electrolysis, capital costs of the membrane and heat revenues. The results are comparable with the BFB-Mem process. Again, in Figure 4.6 the diagrams (a) to (c) correspond to the membrane types PPO, Matrimid and Matr-PPO. In Figure 4.6 diagram (a) and (b), it is shown that with increasing process pressure, total delta costs decrease, due to smaller recycle flows. Smaller recycle flows result in decreased compression costs and membrane costs

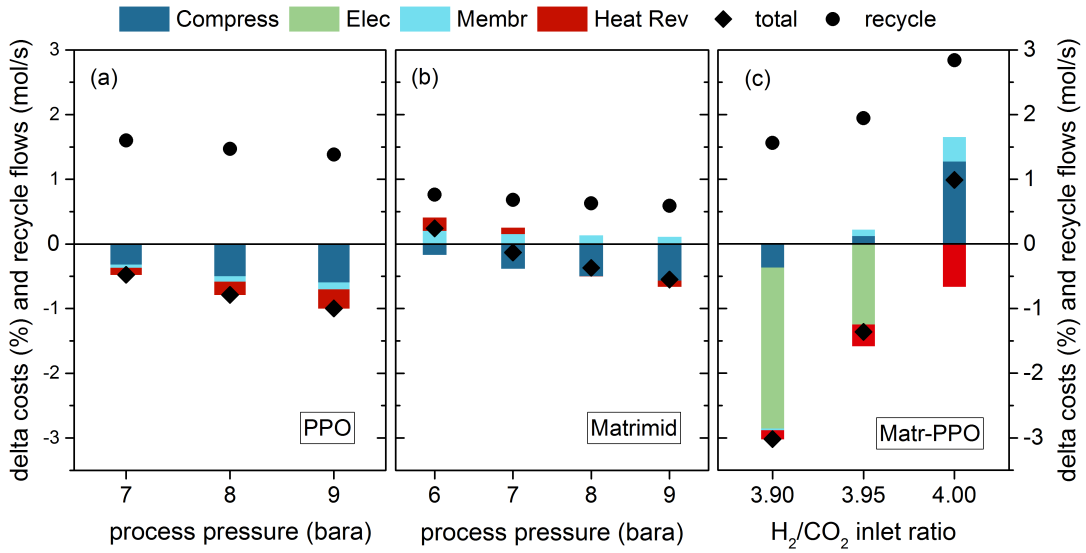

Figure 4.6: Delta-Costs and recycle flow rates for the FB-Mem process with different membrane types as a function of the process pressure or the inlet ratio $H_2/CO_{2,input}$. The membrane pressure is fixed for PPO and PPO-Matr of 19 bara and for Matrimid of 40 bara. The base case is at 6 bara process pressure, an ratio $H_2/CO_{2,input}$ of 4.0 and a PPO membrane. (a) Delta-costs and recycle flow rates over the process pressure for the PPO membrane; (b) Delta costs and recycle flow rates over process pressure for the Matrimid membrane (c) Delta costs and recycle flow rates over the $H_2/CO_{2,input}$ ratio for the Matr-PPO membrane at 9 bara process pressure

like explained for the BFB-Mem process. Compression costs are at minimum at 9 bara. Again, a PPO membrane is less expensive than a Matrimid membrane with two-times lower total delta-costs. Heat revenues are increasing with the pressure, due to the same fact as explained for the BFB-Mem process.

The effect of hydrogen-saving to the costs is illustrated in Figure 4.6 diagram (c) with the usage of the hypothetical membrane Matr-PPO for the FB-Mem process. For a $H_2/CO_{2,input}$ ratio smaller than four, Electrolysis costs can be saved in comparison to the base case. The membrane costs at $H_2/CO_{2,input} = 4.0$ are slightly higher than for the base case which corresponds with the technical results of chapter 3, where it was shown that the Matr-PPO membrane requires a larger membrane area and produces a larger recycle flow than the PPO membrane at stoichiometric inlet conditions. Larger recycle flow rates cause higher compression costs, which can be seen also in diagram (c). Only for sub-stoichiometric inlet conditions the hypothetical Matr-PPO membrane is economically more beneficial than the PPO membrane. For the ratio $H_2/CO_{2,input} = 3.9$, lower costs for compression and especially for the electrolysis result in the lowest total delta-costs for all three diagrams (a) - (c) with -3 %. The hydrogen-saving approach

requires less CO_2 conversion. Hence, less reaction heat is produced which is reflected in the decreasing amount of heat revenues in diagram (c). Also for this process, the membrane Matr-PPO would be most economically feasible. However, this membrane is hypothetical and will not be considered for the absolute economic assessment for this process. Besides the hypothetical membrane, the membrane PPO showed the best results at 9 bara process pressure, whose conditions will be considered as optimal and used in the absolute economic assessment.

Process FB-MemS

For this simplified process, the usage of a Matrimid or Matr-PPO membrane is possible, since the fixed bed reactor allows higher process pressures and with that higher membrane pressures. Due to higher pressure differences inside the membrane and therefore better separation performances, the hydrogen-saving approach is applicable. The cost development with the process pressure of this process behaves similar to the processes BFB-Mem and FB-Mem, but differs in regions with higher pressures. In Figure 4.7, delta-costs and recycle flow rates of the process FB-MemS are shown as a function of the process pressure or of the ratio of hydrogen and CO_2 at the inlet. Like for the FB-Mem process, the following changing components are considered: capital and operating costs of compression and electrolysis, capital costs of the membrane and heat revenues.

In diagram (a) of the course of the total delta-costs form a slight minimum between 20 and 25 bara. First, the total delta-costs can be reduced with the pressure, since higher conversion rates in the reactor create a simpler separation task for the membrane and therefore achieve smaller recycle flows. But with a further pressure increase, the decrease of the recycle flow rate cannot compensate any more the increased compression effort to reach higher pressures. Hence, the total delta-costs are increasing again, despite the lower costs for the membrane and higher heat revenues.

The same applies for diagram (b) of Figure 10. Here, the membrane Matrimid is examined. Again, a minimum of delta-costs with increasing pressures can be observed, but at a higher pressure range. Compression and membrane costs behave in the same way like for the PPO membrane. The PPO membrane achieves higher total-delta costs at its minimum than the Matrimid membrane.

In diagram (c), delta-costs and recycle flow rates of the FB-MemS process at 22 bara with the (hypothetical) Matr-PPO membrane are illustrated as a function of the inlet ratio of hydrogen and CO_2. In comparison to the base case at 9 bara, membrane costs can be reduced and decrease further with the decrease of hydrogen addition. The

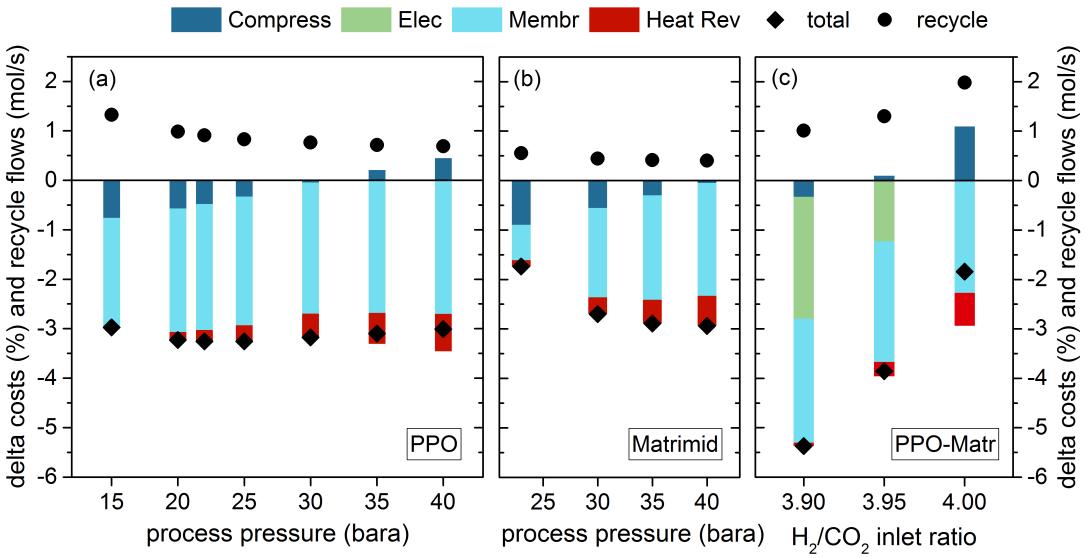

Figure 4.7: Delta-Costs and recycle flow rates for the FB-MemS process with different membrane types as a function of the process pressure or the inlet ratio $H_2/CO_{2,input}$. The membrane pressure is similar to the given process pressure. The base case is at 9 bara process pressure, an input ratio $H_2/CO_{2,input}$ of 4.0 and a PPO membrane. (a) Delta-costs and recycle flow rates over the process pressure for the PPO membrane; (b) Delta costs and recycle flow rates over process pressure for the Matrimid membrane (c) Delta costs and recycle flow rates over the $H_2/CO_{2,input}$ ratio for the Matr-PPO membrane at 22 bara process pressure

same applies for the electrolysis and compression costs. Again, heat revenues become smaller with the decreased hydrogen addition. The total delta-costs for the hypothetical membrane Matr-PPO are minimal with -5.4 % at $H_2/CO_{2,input} = 3.9$. Compared to the minimal total delta-costs with PPO membrane, this is 1.5 times lower. The hypothetical membrane Matr-PPO showed potential to reduce the costs of the direct methanation of biogas due to the ability of decreasing the hydrogen addition to the process. The combination of high permeabilities and medium selectivities of hydrogen and CO_2 over methane, as well as a lower permeability of CO_2 than of hydrogen is a promising concept for future gas separation membranes downstream of the direct methanation unit of biogas.

Key data of the optimised process configurations are listed in Table 4.3. With this database, the absolute economic analysis is conducted. Mostly, elevated pressures in reactors and in post processing units are more cost effective, because the therefore higher conversion rates result in a leaner process. High permeability rates, corresponding to the PPO membrane, are more cost-effective than high selectivity rates corresponding to the Matrimid membrane. The optimal case would be a combination of high selectiv-

	BFB-FB	BFB-Mem	BFB-MemS	BFB-MemT	FB-FB	FB-Mem	FB-MemS
p_{proc} (bara)	12	9	12	9	14	9	22
p_{mem} (bara)	-	19	12	19	-	19	22
$H_2/CO_{2,input}$ (-)	4.03	4.0	4.0	3.9	4.03	4.0	4.0
membrane type	-	PPO	PPO	Matr-PPO	-	PPO	PPO
Biomethane composition (vol-%)							
CH_4	97.86	97.49	97.50	96.41	97.90	97.55	97.59
H_2	1.97	1.98	1.95	1.96	1.94	1.94	1.91
CO_2	0.17	0.53	0.55	1.63	0.16	0.51	0.50

Table 4.3: Operating conditions and properties of optimal case for each process, considered in the absolute economic analysis for an inlet biogas stream of 200 Nm^3/h with 55 vol-% methane and 45 vol-% carbon dioxide

ity and permeability together. But research in literature showed that higher obtained permeability rates comes at the expense of selectivity properties [126, 127, 141]. The method to save hydrogen via hydrogen recycle with the Matr-PPO membrane creates the most economically feasible cases for processes with membranes. However, since the membrane Matr-PPO is theoretically constructed, a process with such a membrane is only considered for one reactor type (BFB) in the absolute economic analysis to give a comparison of conventional and potential membranes.

4.4.2 Absolute Economic Assessment

The technical data of each process, with which the absolute costs and revenues are calculated, can be found in Table A.1 in the appendix. The obtained technical data of the economically optimised processes are a result of the Delta-Costs evaluation. The optimised processes are also illustrated as Sankey diagrams, which are included in chapter 3 and in the appendix. Investment costs, operating costs and revenues are calculated for each process. The results are listed in Table 4.4. Different cost-categories for each process are applied in order to understand the cost impact of the single units to the process. The considered components for the methanation reactors are explained in the section 'methods'. The categories 'biogas compressor' and 'condensers' are self-explaining and does consider only the components of the category name. For the category 'electrolysis' the electrolysis unit and a hydrogen tank is considered. The category 'post-upgrading' comprises the different technologies after the main reactor for fulfilling the gas grid requirements in the product gas. That can be either a second fixed bed in combination with a drying unit or a gas separation membrane, where in some cases a second compressor is considered as well. The corresponding processes are illustrated in Figure 3.1 to Figure 3.3. The category 'supporting modules' includes the rest of the needed equipment in the processes, which are a biogas tank, the gas cleaning, the evaporator, additional heat exchangers for a fixed bed and injection costs of the gas grid. It is very important

Investment Costs, k€							
	Electrolysis	Main Reactor	Biogas Compressor	Post-Upgrading	Supporting Modules	Condensers	Total
BFB-FB	2 243.6	357.4	407.1	230.4	403.9	151.0	3 793.7
BFB-Mem	2 226.1	331.4	500.9	250.5	362.4	123.5	3 795.0
BFB-MemS	2 226.1	346.6	621.4	153.1	363.7	78.1	3 789.1
FB-FB	2 243.6	762.4	433.9	217.2	459.1	157.1	4 273.6
FB-Mem	2 226.1	700.3	527.7	222.0	418.4	126.5	4 221.4
FB-MemS	2 226.1	885.3	674.8	39.7	427.6	83.5	4 337.2
BFB-MemT	2 170.9	325.4	500.9	259.1	362.4	123.2	3 742.3
Operating Costs, k€/a							
	Electrolysis (Electricity)	Main Reactor	Biogas Compressor	Post-Upgrading	Supporting Modules	O&M	Total
BFB-FB	694.7	9.0	10.4	16.0	5.3	189.6	925.1
BFB-Mem	689.3	10.0	13.3	3.7	5.3	189.7	911.4
BFB-MemS	689.3	9.2	17.0	0	5.3	189.4	910.3
FB-FB	694.7	26.3	11.2	13.3	5.3	213.6	964.6
FB-Mem	689.3	26.3	14.1	4.4	5.3	211.0	950.6
FB-MemS	689.3	26.3	18.7	0	5.3	216.8	956.5
BFB-MemT	672.2	9.6	13.3	3.7	5.3	187.1	891.4
Revenues, k€/a							
	Bio-methane	Process Heat	Oxygen				Total
BFB-FB	2 019.4	63.8	137.3				2 220.5
BFB-Mem	2 011.9	64.5	136.3				2 212.8
BFB-MemS	2 011.9	67.4	136.3				2 215.7
FB-FB	2 020.0	63.8	137.3				2 221.2
FB-Mem	2 012.8	64.9	136.3				2 214.1
FB-MemS	2 013.5	69.8	136.3				2 219.6
BFB-MemT	1 989.6	63.4	132.9				2 185.9

Table 4.4: Investment costs, operating costs and revenues per category of the optimised processes. The sizing of the equipment can be found in table A.1 in the appendix

for the costs of a methanation unit that not only the reactor costs are considered but also costs of the necessary equipment up- and downstream the reactor, which is the biogas compressor, the evaporator and a condenser after the reactor. Furthermore, it turned out that it is not possible to reach the gas grid requirements for biomethane with one methanation unit. Therefore, the costs of biogas upgrading via methanation have to include not only the methanation unit but also costs of further upgrading technology (post-upgrading) like a gas separation membrane or a second methanation step. A comparison with data from literature showed that neglecting these additional costs result in an under-estimation of costs by a factor of 1.5 for the biogas upgrading via methanation excluding electrolysis and biogas costs. In order to give a clearer picture which costs have to be included, first the focus is put on the main reactor and the methanation unit. Secondly, the whole methanation unit in combination with additional post-upgrading after the main reactor is evaluated. In Figure 4.8, the investment costs of the main reactor (BFB or FB) and of the whole methanation unit (compressor, evaporator, reactor and condenser) are illustrated for each process. In general, the investment costs of the

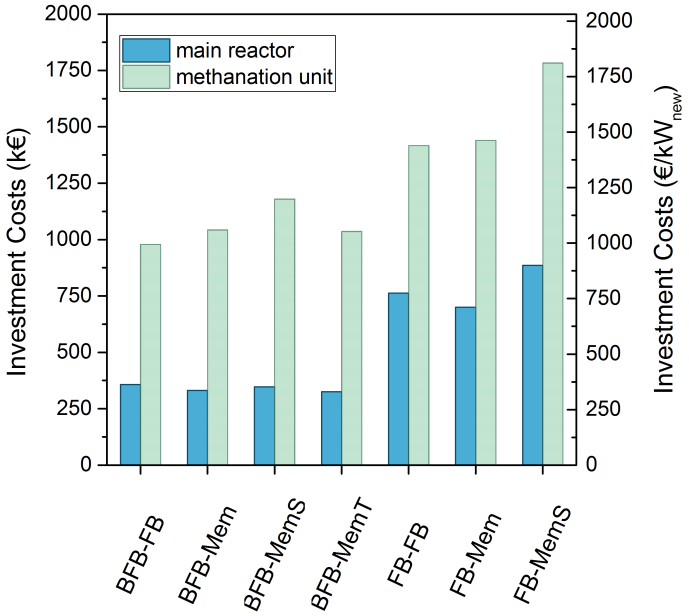

Figure 4.8: Absolute investment costs and specific investment costs per kW new produced methane for each process of the main reactor and the whole methanation unit (includes main reactor, subsequent condenser, biogas compressor and evaporator) regarding Table 4.4

methanation unit are two to three times higher than for the bare reactor. Besides the reactor, the investment costs of the biogas compressor contribute strongly to the overall investment costs of the unit. A fixed bed reactor is about two times more expensive than a fluidised bed reactor with investment costs per newly produced methane on average of 785 €/kW$_{new}$ in comparison to the average investment costs of a BFB reactor of 347 €/kW$_{new}$. Due to the improved heat transfer in a bubbling fluidised bed reactor, it is possible to run the reaction at optimum temperature over the whole height of the reactor. This reduces the necessary height of the BFB reactor in comparison to a fixed bed, where a temperature profile with a strong peak is formed (see results in chapter 3). For fixed beds, higher optimal pressures were obtained, which increase the investment costs as well expressed via higher pressure factors. Also the whole methanation unit with a fluidised bed is less expensive than with a fixed bed. However, the difference is not as large as between the bare reactors, since the compressor costs are more or less constant of the processes and reduce the overall costs difference. Therefore, the whole BFB methanation units are on average 30% less expensive with 1047 €/kW$_{new}$ than FB methanation units with 1446 €/kW$_{new}$. The investment costs differences between the BFB methanation units are caused by the different size of recycle flow rates of the processes, which cause higher compression costs in the biogas compressor. The process BFB-FB contains no recycle. For the processes BFB-Mem and BFB-MemS, the recycle

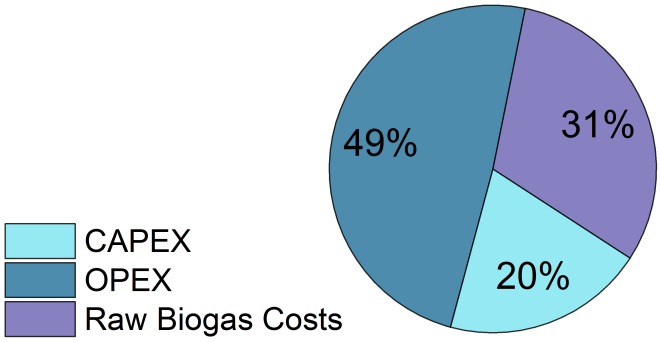

Figure 4.9: Average distribution of production costs for the methanation processes (capital expenditure (CAPEX), operating expenditure (OPEX) and biogas costs)

flow rates and with that the investment costs are increasing. For the FB methanation units, the total costs increase with the process pressure and with the recycle flow rate (for operating conditions see Table A.1) due to a higher compression effort.

In Figure 4.9, the average costs distribution of the processes is shown regarding the biogas costs, the capital and operating expenditures (CAPEX and OPEX). The biogas costs have a large share of 31 % of the total annualised costs, due to the high assumed biogas price. Like explained in the section 'methods', the biogas price is a result of the feed-in tariffs for electricity from biogas. These costs may be lower, if the policy for the feed-in tariffs is changing. Hence, for the further evaluation of annualised costs, the biogas costs are not illustrated. The 2.5 larger share of operating costs in comparison to the capital costs is characteristic for every shown process and is caused mainly by the significant electricity consumption needed for the hydrogen production. In order to explore the contribution of the different process units to the costs, in Figure 4.10 the shares of capital and operating costs for the different processes and different categories are illustrated. The values used in this diagram are corresponding with the values from Table 4.4. The sizing of the corresponding equipment can be found in table A.1. The average catalyst stress for the BFB main reactor and the FB main reactor both without recycle are 0.9 $Nm^3\ h^{-1}\ kg_{cat}^{-1}$ and 0.3 $Nm^3\ h^{-1}\ kg_{cat}^{-1}$ with a corresponding gas hourly space velocity (GHSV) defined in equation 3.25 of 3108 $Nm^3_{Feed}\ h^{-1}\ m_r^{-3}$ and 1948 $Nm^3_{Feed}\ h^{-1}\ m_r^{-3}$ considering the whole feed flow. The GHSV of the BFB reactor is not three times larger than of the FB reactor, as it is the case for the catalyst stress. Due to the fluidisation in the BFB reactor, the catalyst occupies more space per mass so that the difference in the GHSV of the reactor types is not as pronounced as for the catalyst

stress. The given values for GHSV and catalyst stress are slightly lower than the values given in the previous chapter. For the economic analysis, a safety margin of 50% was applied to the reactor height which decreases catalyst stress and GHSV.

The total annualised investment costs (CAPEX) are similar for processes containing a bubbling fluidised bed with about 365 k€/a. Hence, from an economic point of view, there is no difference between the application of a second fixed bed or a gas separation membrane for reaching the gas grid requirements. From an operating point of view, the processes with a membrane are more applicable, since these processes are more robust. The capital expenditures of the process with the theoretical membrane BFB-MemT, where hydrogen saving is possible, are 1.4 % lower than for the other processes with a bubbling fluidised bed. The processes containing a fixed bed as main reactor have higher capital expenditures with about 410 k€/a, due to the higher costs of a fixed bed in comparison to a bubbling fluidised bed. However, the difference of the total capital expenditures is only 10 % between processes with fixed bed and bubbling fluidised beds, since the electrolysis dominates the investment costs. The electrolysis costs are similar for every process. They vary in small ranges depending on the $H_2/CO_{2,\text{input}}$ ratio of 3.9 – 4.03 used in the different processes. Besides the electrolysis, the main reactor, the biogas compressor and supporting modules contribute pronouncedly to the total capital expenditures of the processes. The annual investment costs of the main reactor for the different processes correspond with Figure 4.8. Except for the process FB-FB, the biogas compressor is at minimum as expensive as the main reactor. For processes with larger recycle flows (BFB/FB-Mem and BFB/FB-MemS) the costs for the compressor are increasing. Also a higher pressure level like in process FB-MemS is reflected in the increased compressor costs. The capital costs in the category 'post-upgrading' for processes with a membrane or a second fixed bed are similar. Differences occur in the processes with a simplified membrane (no second compressor). For the processes BFB- and FB-MemS the capital costs for the membrane modules are smaller, because the membrane's compressor can be saved. However, a larger biogas compressor capacity is required with corresponding higher costs, due to the larger obtained recycle flows from a membrane operating at smaller pressure differences. This effect compensates the cost saving in the membrane module so that the application of only one compressor in the process does not result in less capital expenditure. For the process FB-MemS, the membrane costs are the smallest, since this process operates at a higher pressure level at which the membrane requires less membrane area for the separation task and the membrane's compressor can be saved.

Also the operating expenditures (OPEX) are dominated by the electrolyser due to its electricity consumption. About 75 % of the operating costs are assigned to the elec-

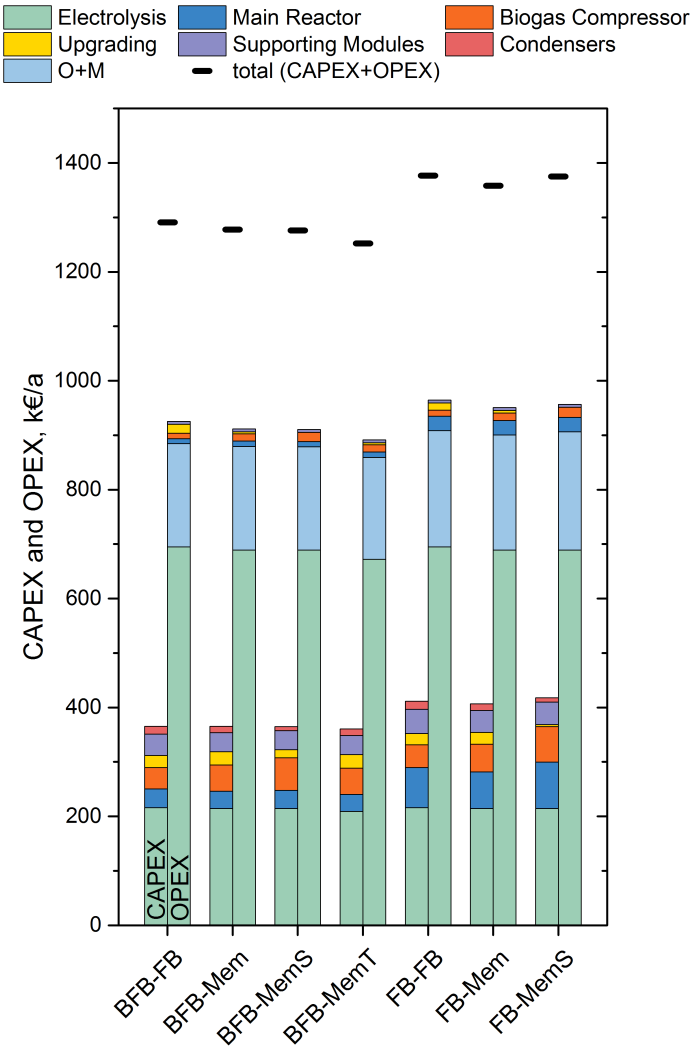

Figure 4.10: Capital and operating expenditures of the different processes. The biogas costs of 600 k€/a for each process are excluded. The category 'Post-Upgrading' includes a second fixed bed and drying or a membrane unit, 'supporting modules' include the biogas tank, the gas cleaning, the evaporator, second heat exchanger in front of a fixed bed and injection costs. Operating costs are calculated based on the values given in Table 4.1, the sizing of the equipment can be found in table A.1 in the appendix.

trolysis. Small differences between the processes are caused again by the $H_2/CO_{2,\text{input}}$ ratios. Besides the operating cost for operation and maintenance (O & M), the remaining operating costs like electricity costs for the biogas compressor or catalyst material are only marginal. For processes with a fixed bed as main reactor, the larger impact of catalyst costs due to the larger size of a fixed bed than a fluidised bed, can be seen in the category 'main reactor' for the operating costs. Considering capital and operating

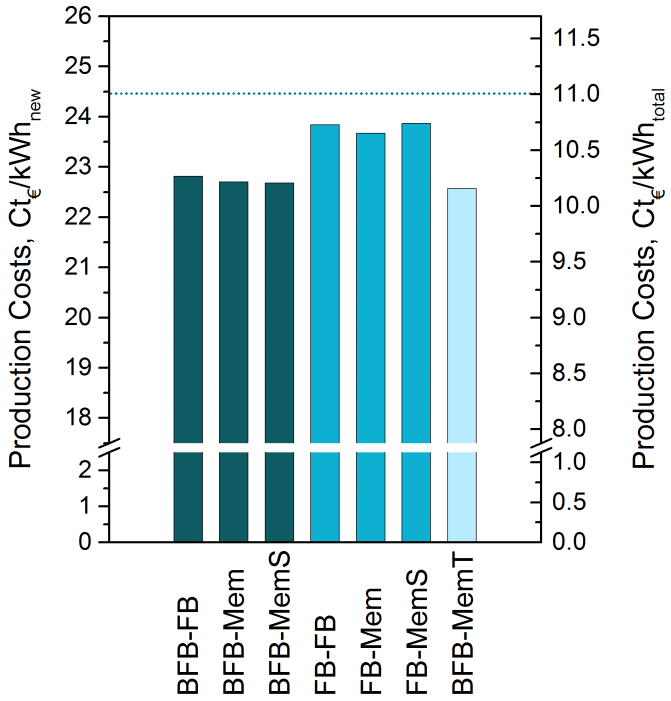

Figure 4.11: Production costs of the different processes per kWh of newly produced methane and per kWh of the total amount of methane for an electricity price of 5 $Ct_€/kWh_{el}$. No extra revenues (heat and oxygen) are considered. The dotted line shows the selling price of biomethane according to Table 4.1 and expresses the costs limit of profitability

expenditures together, processes with a fluidised bed are less expensive than those with a main fixed bed reactor. The process BFB-MemT shows the lowest costs, with 1.4 % decreased annualised costs compared to the processes BFB-Mem and BFB-MemS. Hence, the adapted membrane towards more beneficial selectivity values of hydrogen and carbon dioxide in process BFB-MemT shows an economic benefit for the previous separation task. Another possibility for the methanation of carbon dioxide in the biogas would be the prior separation of carbon dioxide via scrubbing or a gas separation membrane, so that only the carbon dioxide enters the methanation part. Here, the methanation process can be designed leaner than for the direct methanation due to the smaller feed stream. As a result, cost advantages for the methanation part are evident. However, to be equally profitable with the direct methanation processes, the costs of the CO_2 separation must be saved within the methanation part. Investment costs of an amine scrubber system for the CO2 separation are reported with 2.25 Mio € [29] for the given biogas flow rate of 200 Nm^3/h. The investment costs of the direct methanation processes are between 3.7 - 4.3 Mio € (Table 4.4). Therefore, 50 – 60 % of the investment costs have to be saved in the methanation part if a prior CO_2 separation is implemented

to be compatible with the direct methanation. However, already the electrolysis has a share in the investment cost of 50 - 60 %, where no savings can be made. Therefore, it is not possible to achieve the necessary costs reduction in the methanation part. As a result, the direct methanation of biogas is less expensive than a methanation with prior carbon dioxide separation.

The production costs of the processes are strongly sensitive to the electricity price, since the costs for electricity in the processes reach approximately the half of the capital and operating expenditures together. The production costs are defined as follows:

$$C_{prod} = C_{CAPEX} + C_{OPEX} + C_{biogas} - Rev_{extra} \tag{4.6}$$

For the production costs, capital and operating expenditures are considered as well as biogas costs and possible extra revenues, which can be earned by selling excess heat and oxygen from the electrolysis.

In Figure 4.11, the production costs of the methanation processes calculated with equation 4.6 are illustrated. Here, an electricity price of 5 $Ct_{€}/kWh_{el}$ is assumed and a biogas price of 6 $Ct_{€}/kWh_{biogas}$ according to Table 4.1. No extra revenues are considered. The production costs are standardised to the newly produced chemical energy output of methane (kWh_{new}) and to the total chemical energy output of methane (kWh_{total}) which includes the newly produced methane and the methane which is already present in the biogas after the digester. Again, the higher heating value is the base for the energy content determinations of the gases. In Figure 4.11, also the selling price of biomethane is illustrated as dotted line with 11 $Ct_{€}/kWh_{total}$.

The production costs of all methanation processes are below the selling price of biomethane. Hence, all presented processes are profitable with the assumed conditions. In general, the production costs for processes containing a fluidised bed are similar to each other. The same applies to processes containing a fixed bed, like already discussed earlier. The differences in production costs between the different post-upgrading technologies (membrane or second fixed bed) after one type of main reactor therefore are marginal. Production costs for processes containing a fluidised bed are on average 10.2 $Ct_{€}/kWh_{total}$ or respectively 22.7 $Ct_{€}/kWh_{new}$. The production costs of processes containing a fixed bed as main reactor are approximately 5 % higher with 10.8 $Ct_{€}/kWh_{total}$ or respectively 23.8 $Ct_{€}/kWh_{new}$. The process with the optimised membrane BFB-MemT shows no significant cost savings. The cost reduction for the electrolysis due to less hydrogen production is not sufficient to have a noticeable impact to the overall costs.

The increase of costs due to up-scaling is considered to be non-linear and can be determined by the cost-to-capacity method:

$$\frac{C_2}{C_1} = \left(\frac{Q_2}{Q_1}\right)^w \tag{4.7}$$

where the costs C of plant 2 are compared to the known costs of plant 1 via the capacities of the plants Q using a scale factor w. In this work, the upscaling behaviour of the electrolysis for the presented processes is considered to be linear, since the required size of the electrolyser modules are already in an industrial range with 1.3 MW_{HHV}. For a bigger electrolyser size, several modules would be installed in parallel. For the remaining part of the processes, a scaling factor of w = 0.62 can be applied [142]. As a consequence, a two times larger plant, electrolysis excluded, would cost 76 % of the doubled costs due to the economy of scale.

In Figure 4.12, the production costs for one of the least expensive process BFB-Mem (excluding process BFB-MemT) and for one of the most expensive process FB-FB are shown as a function of the electricity price. The production costs are normed to the energy content of the new produced methane (kWh_{new}) in the process or to the total amount of biomethane produced (kWh_{total}). The costs per total produced methane are 45% of the costs per new produced methane due to the carbon dioxide concentration of 45% in the biogas. For every process, three different production costs are considered: (1) without any extra revenues, (2) with heat revenues and (3) with heat and oxygen revenues (assumed oxygen selling price 0.09 €/Nm^3). A 'profitable area' is illustrated in the diagram, which is the area under the constant line at 24.5 $Ct_€/kWh_{new}$. This parameter is the selling price of biomethane normed to the energy of new-produced methane and corresponds to the assumed biomethane price in Table 1 of 0.11 €/kWh_{total}. Inside this area the processes are profitable. A linear relationship between electricity price and production costs is obtained, with the same gradient for the different processes due to the similar efficiencies. The highest possible electricity price so that the processes are still profitable is between 5.3 and 7.5 $Ct_€/kWh_{el}$, depending on the process and on the extra revenues. The difference of the maximum profitable electricity price is 0.7 $Ct_€/kWh_{el}$ between the two processes BFB-Mem and FB-FB, independent of the extra revenues as long as the same cases of extra revenues are compared with each other. Comparing the cases where no extra revenues are considered, the FB-FB process is profitable until an electricity price of 5.3 $Ct_€/kWh_{el}$ whereas for the BFB-Mem process, a maximum electricity price of 6.0 $Ct_€/kWh_{el}$ is obtained. If now heat revenues are considered, the maximum electricity price increases by 0.5 $Ct_€/kWh_{el}$ for both processes. Further, if heat and oxygen revenues are considered, the maximum price for electricity increases by 1.5 $Ct_€/kWh_{el}$ in comparison to processes with no extra revenues. Depending on the

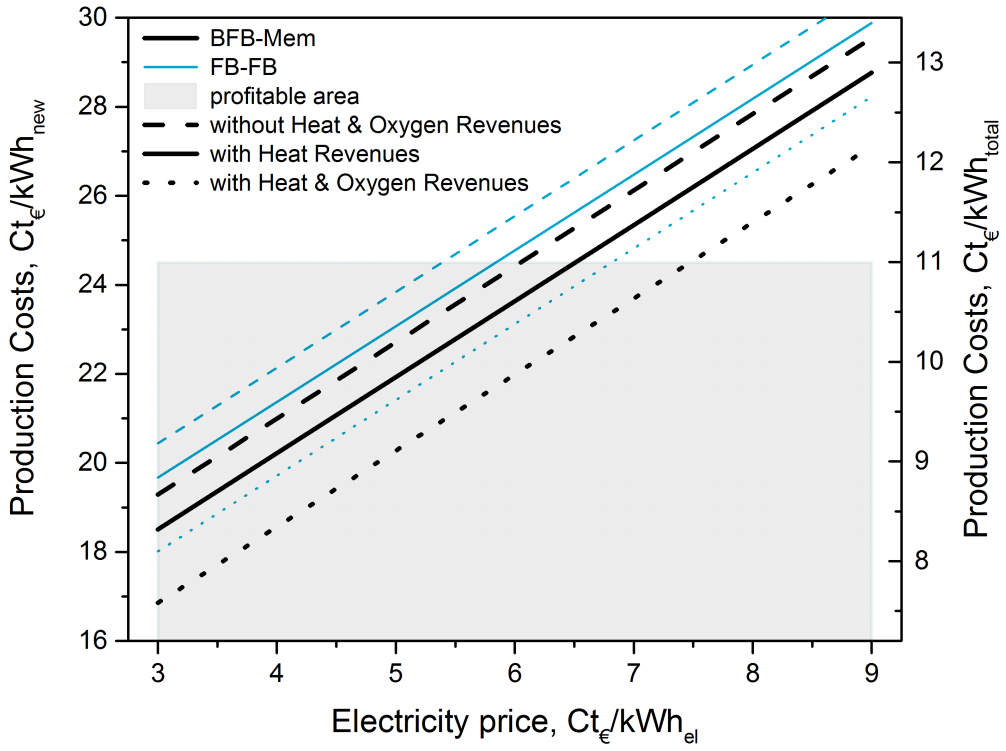

Figure 4.12: Production Costs per kWh of newly produced methane and per kWh of the total amount of methane of the processes BFB-Mem and FB-FB as a function of the electricity price. Extra revenues (heat and oxygen) are separately considered. The grey area represents the production costs, which are profitable as the selling price of biomethane of 24.5 $Ct_€/kWh_{new}$ correspond to 11 $Ct_€/kWh_{total\ methane}$

electricity markets in Switzerland or Germany, electricity prices of 5 to 7 $Ct_€/kWh_{el}$ may be available today if no further fees like grid-use fees have to be paid. Furthermore, the biogas prices may be decreasing, with the decrease of feed-in tariffs for electricity from biogas in Germany [143] and with the exclusion of biogas producer from sewage sludge and in landfill sites from feed-in tariffs in Switzerland as of 2018 [144]. A sensitivity analysis regarding the biogas price showed, that a 50 % reduction of the biogas price increases the maximum possible electricity price by 2 $Ct_€/kWh_{el}$.

Also the concentration of carbon dioxide in the biogas influences the economic performance of the processes significantly. In Figure 4.13, the profit of the processes BFB-Mem and FB-FB are illustrated as a function of the carbon dioxide concentration in the biogas. The profitability of the processes is decreasing clearly with the CO_2 concentration in the biogas. If the biogas would consist of 35 vol-% CO_2 instead of 45 vol-%, like assumed

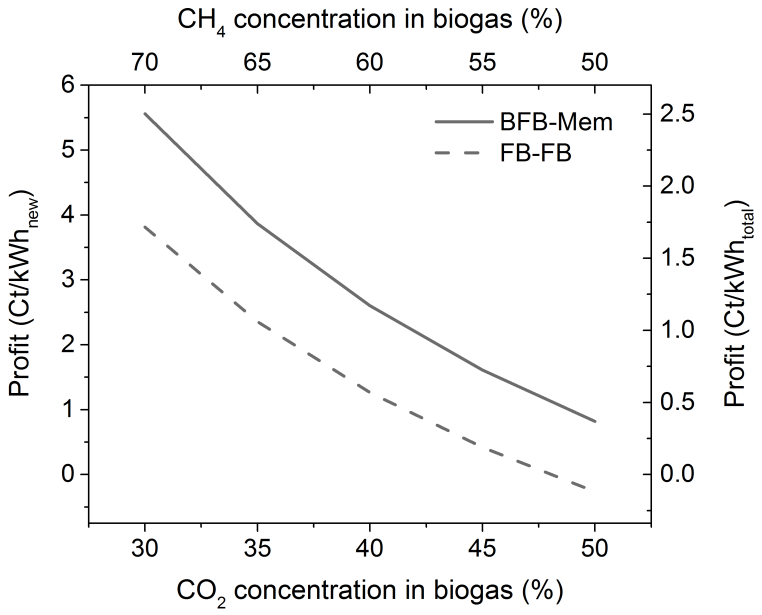

Figure 4.13: Profit of the processes BFB-Mem and FB-FB versus the carbon dioxide concentration in the biogas (C_{el} = 5 $Ct_{€}/kWh_{el}$, no extra revenues considered)

in this work, the profit would increase by 2.5 $Ct_{€}/kWh_{new}$ or respectively the maximum allowable electricity price would increase by 1.5 $Ct_{€}/kWh_{el}$. The less carbon dioxide the biogas contains, the less technical and economical effort is needed to purify it. Methane produced during fermentation in a digester is less expensive than methane produced in the presented upgrading processes via methanation. The selling price of biomethane at the end is constant. Hence, the costs of biomethane production via direct methanation decrease with decreasing CO_2 biogas concentration. Accordingly, the profit is increasing. The process BFB-Mem shows a higher profit than the process FB-FB according to the already presented economic results. The economically improving effect of a higher methane concentration in the biogas is comparable with a decreasing biogas price. A reduction of the biogas price by 1 $Ct_{€}/kWh_{biogas}$ has the same effect to the profit like an increase of the methane content in the biogas by approximately 6.5 %-points assuming linear behaviour of the profit.

4.5 Conclusions

Detailed process simulations for the direct methanation of biogas are crucial for a realistic process development, so that a more precise cost estimate is possible. The reactor types (fluidised and fixed bed) in this study are modelled with a rate-based approach (chapter 3), which considers not only the thermodynamic equilibrium but also the activity of the catalyst. Due to this more realistic approach, it turned out that one methanation step for the upgrading of biogas does not reach the gas grid requirements, whereas for a simple equilibrium model one methanation stage would be sufficient. Hence, a second post-upgrade step is needed, which is in this study either a second fixed bed methanation or a gas separation membrane. Also for the membrane a rigorous model was developed, since the accuracy of this model decides about the size and composition of the recycle flow, which influences again the size of the process inside the loop and is therefore an important aspect for the costs. The more precise cost estimates are supported by the detailed knowledge of the process units and their sizes and performances. The given costs for the methanation of biogas in literature are often under-estimated not only because the post-upgrading step is neglected, but also because the costs for the methanation unit are underrated.

The simulated processes were optimised regarding their annualised costs via the cost difference (dC-) method. With this method, the cost-optimal operation conditions of each process could be identified, while still fulfilling the gas quality demanded by the gas grid. With this information, the sizing of the equipment for each process was calculated, which again is used for the absolute economic analysis in the next step. It turned out that processes containing a fluidised bed are less expensive than processes with a fixed bed, due to a larger required size of a fixed bed. However, the electrolyser has the biggest impact to the production costs by far so that the lower costs of a fluidised bed result in 5 % less production costs in comparison to processes containing a fixed bed. The post-upgrading technologies, a second fixed bed or a membrane, differ economically only marginally and can be regarded as equally expensive. However, technically the processes with a membrane appeared to be more robust, since processes operating with a two-step methanation are highly sensitive to the ratio of hydrogen and carbon dioxide in the input which is fluctuating over time. Therefore, the application of a membrane for further gas upgrading seems to be more beneficial than a second methanation step. Comparing the processes containing a membrane, it turned out that the simplified membrane process with only one compressor does not result in cost benefits. Here, the costs simply are shifted from the removed second compressor to the first compressor. A membrane-process with two pressure levels seems technically more beneficial due to a wider operation window caused by the independently controllable pressures in the main

reactor and in the membrane. However, these results depend on the accuracy of the parameters in the membrane model, for which more precise information for the given separation task could be obtained by measurements with an industrial available membrane.

The processes BFB-Mem and BFB-MemS showed the highest profitability with production costs of 10.2 $Ct_{€}/kWh_{total}$ or 22.7 $Ct_{€}/kWh_{new}$ below the selling price of biomethane with 11 $Ct_{€}/kWh_{total}$ (without extra revenues, 6 $Ct_{€}/kWh_{biogas}$ and 5 $Ct_{€}/kWh_{el}$). Together with the argument of robustness, the processes BFB-Mem and BFB-MemS are technically and economically the most feasible processes for the direct methanation of biogas. The most expensive processes are FB-FB and FB-MemS with corresponding production costs of 10.8 $Ct_{€}/kWh_{total}$ or 23.9 $Ct_{€}/kWh_{new}$ (without extra revenues). With production costs of 22.6 $Ct_{€}/kWh_{new}$, the process with the hypothetical membrane BFB-MemT is more profitable than the BFB-Mem or BFB-MemS process, but less pronounced as expected. For all processes, the profitability can be increased up to 2.5 $Ct_{€}/kWh_{new}$ (corresponds to 1.1 $Ct_{€}/kWh_{total}$) by selling process heat and oxygen. The production costs of the processes are highly sensitive to the electricity price and the carbon dioxide content in the biogas. The presented processes are profitable with an originally assumed CO_2 content of 45 % in the biogas until electricity prices between 5.3 and 7.3 $Ct_{€}/kWh_{el}$ depending on the different processes and extra revenues. For the favourite processes BFB-Mem and BFB-MemS the maximum feasible electricity price is about 6 $Ct_{€}/kWh_{el}$ without considering extra revenues. Also a lower carbon dioxide content in the biogas increases the profitability of the processes significantly. The decrease of the CO_2 content in the biogas from 45 vol-%, which is a maximum amount, to a low content of 35 vol-%, increases the profitability again by 1.1 $Ct_{€}/kWh_{total}$.

Finally, a combination of technical and economic feasibility information provided the necessary knowledge for evaluating the presented processes and made it possible to give an answer to the question which is the most beneficial process for the direct catalytic methanation of biogas.

5 Long-Duration Methanation Experiments with Real Biogas[1]

5.1 Abstract

The catalytic direct methanation of biogas to produce biomethane was conducted in a pilot plant with real biogas from a biogas plant in Zurich. Stable operation of the methanation system including a bubbling fluidised bed could be demonstrated for over 1100 hours of regular operation with subsequent injection into the gas grid. An average methane yield of 96 % was reached. During the long-duration experiment, the slow deactivation process was monitored and found out to be only moderate. Organic sulphur compounds could be identified as the main source of deactivation. However, deactivation from coking cannot be fully excluded. A concentration of 1 ppm of sulphur compounds result in a yield reduction of about 1 % per 100 operation hours. With appropriate measures in the gas cleaning unit, so that no sulphur compounds were measured subsequently (limit of detection: 0.2 ppm), the yield reduction went close to zero. Additionally, experimental results were compared to simulation results from a rate-based model presented in chapter 3 and [110]. Model predictions and experimental results are in accordance. The rate-based model could be successfully evaluated by experimental results.

5.2 Introduction

The storage of excess energy from renewable sources is becoming more important with an increasing share of renewable energies in the energy system, which is targeted by countries like Germany or Switzerland [15, 143]. A widespread concept for the storage of fluctuating electric energy at large scale is the Power-to-Gas (PtG) method [95, 145–147]. For this, core technologies like electrolysers and methanation reactors connect the electricity grid with the gas grid, so that electricity is converted into storable gases

[1]This chapter is based on the following publication: J. Witte, A. Calbry-Muzyka, T. Wieseler, P. Hottinger, S.M.A. Biollaz, T.J. Schildhauer. "Demonstration of Technical Feasibility Performing Long-Term Direct Methanation of Real Biogas in a Bubbling Fluidised Bed Reactor". submitted (2018). Julia Witte supported the experiments with the specification of operation conditions, performed the experimental data evaluation, compared experimental results with simulation results, created all diagrams and wrote the text.

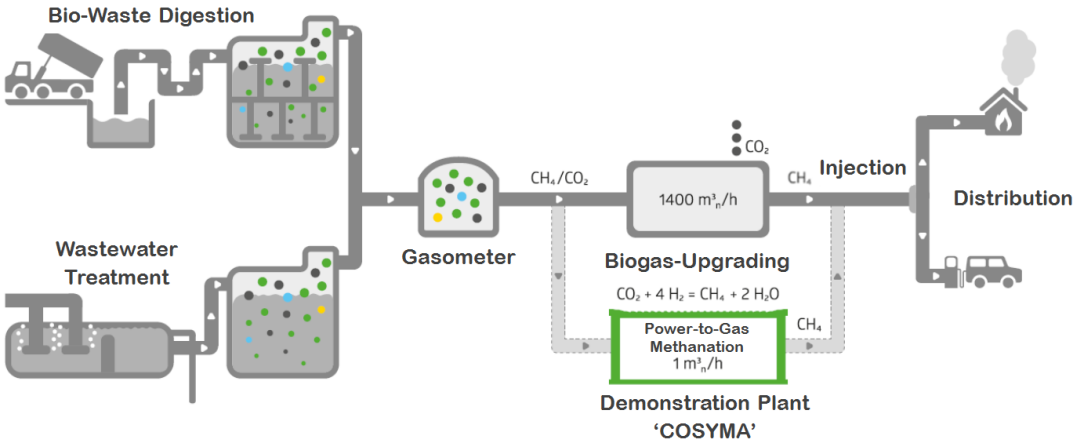

Figure 5.1: Overview of the biogas plant in Zürich, Werdhölzi (Biogas Zürich - energie360°) including the demonstration plant COSYMA

like methane to a large extent. However, those core technologies are often just at the beginning of being applied in industry due to their low maturity. For further application in industry, it must be shown that these technologies are feasible under real conditions for long-term operation, combined with knowledge transfer from research to industry.

This chapter focuses on one core technology of PtG processes, namely the methanation unit. A cooperation was started with the largest natural gas supplier *energie360°* in Switzerland so that the feasibility of the methanation unit could be demonstrated under real conditions with raw biogas from their biogas plant in Zurich, Werdhölzli. Biogas contains, besides trace components, mainly methane ($\sim$ 60 vol-%) and carbon dioxide ($\sim$ 40 vol-%). For unrestricted injection into the gas grid, the carbon dioxide must be removed to a minimum methane concentration of 96 vol-% to obtain biomethane [21, 100]. Conventionally, carbon dioxide is separated from methane via CO_2 scrubbing or by a gas separation membrane. After this, the carbon dioxide is released into the atmosphere as waste. A new way of biogas upgrading includes the application of a PtG system. Here, the biogas enters a methanation reactor where carbon dioxide is converted to further methane together with hydrogen from an electrolyser fuelled by renewable electricity. The corresponding chemical equations are can be found in chapter 3, equations 3.1 and 3.2. With this method, the biomethane production per unit of biomass can be increased by approximately 60 % and CO_2 emissions are avoided. A set-up for the methanation of biogas called COSYMA (COntainer-based SYstem for MethAnation) was built with a pilot-scale size of 10-20 kW chemical output. The Cosyma set-up was transported to a biogas plant of *energie360°* in Zurich-Werdhölzli where it was connected to its biogas flow. An overview of the biogas plant with the COSYMA set-up can be seen in Figure 5.1. The biogas is produced from two different sources: bio-waste and sewage sludge.

Then, the gases are directed into one gas tank (gasometer). About 1400 standard cubic meters per hour of biogas enters the conventional upgrading unit, where CO_2 is separated and released by amine scrubbing. Then the obtained biomethane (about 860 Nm^3/h, depending on the CO_2 content in the biogas) is injected into the gas grid. After the biogas tank, a slip stream (about 1 - 2 Nm^3/h) is directed to the COSYMA set-up where CO_2 is converted to methane together with hydrogen. Then, the product gas stream is mixed again with the main biomethane stream and is injected into the gas grid.

The scope of this work includes the demonstration of stable operation of the methanation set-up COSYMA with real biogas in a long-duration experiment of over 1000 hours. It will be shown here and in additional literature that several issues like cleaning of the gas from sulphur components [148], deactivation processes and attrition of particles in the fluidised bed [149] could be controlled and mastered.

5.3 Methods

5.3.1 Experimental Set-Up

A simplified version of the pilot-scale COSYMA set-up is illustrated in Figure 5.2. The set-up can be operated either by synthetic bottled gas or by real biogas coming from the digesters of the biogas plant in Zurich-Werdhölzli. Between 1.4 and 2.3 Nm^3/h of real or synthetic biogas entered the set-up. Starting from real biogas, the stream first is compressed to the desired system pressure and then directed through an orifice in order to determine the volumetric flow. After this, the biogas enters the gas cleaning unit, where harmful trace components like organic sulphur are removed. These contaminants lead to deactivation of the catalyst even in small amounts, therefore it is essential to remove them for stable operation of the methanation reactor. It was possible to measure these contaminents until a limit of detection of 0.2 ppm. A detailed description of the gas cleaning unit can be found in [148]. Subsequently biogas is mixed with hydrogen and helium from the bottled gas section. The mass flows of bottled gases are measured and controlled by mass flow controllers (MFC). The addition of a known amount of helium enables the determination of the flows of all components via concentration measurements. Next, a small volume flow of the gas mixture is continuously directed to a Micro Gas Chromatograph (mGC) to measure bulk gas concentrations including helium. Then the stream is preheated to reactor inlet temperature and mixed with steam. For this, water from a closed tank is heated to 360 °C. The decreasing mass of water in the tank is measured by scale I, which allows determining the inlet mass flow of water. Water addition is intended to prevent coking of the catalyst. Now the wet gas mixture enters the bubbling fluidised bed reactor, where the methanation reaction takes place with a nickel catalyst of Geldard particle type B. The reactor diameter is 5.2 cm and the

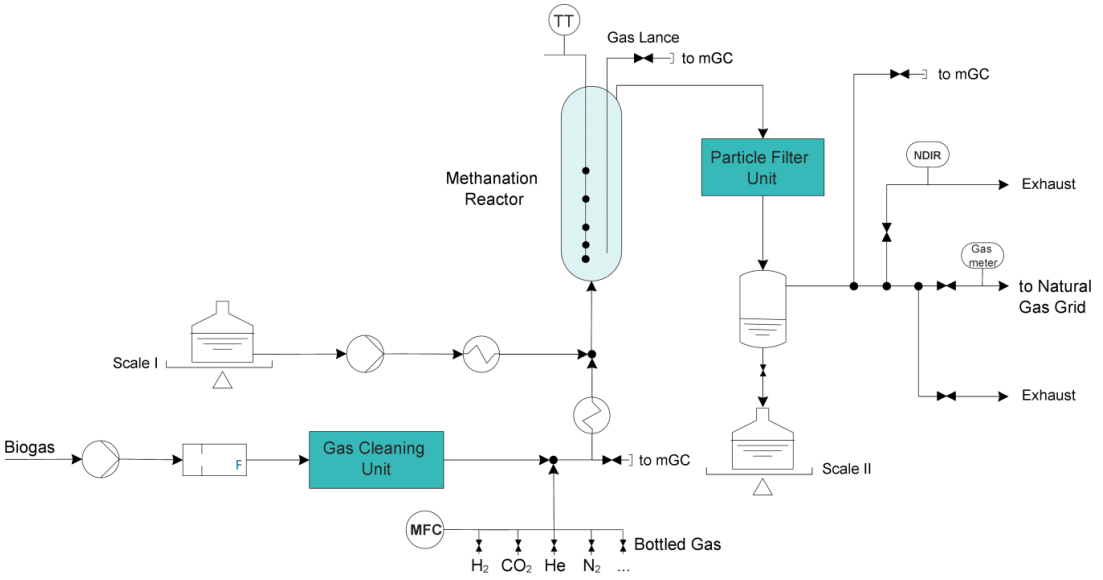

Figure 5.2: Simplified flowsheet of the Cosyma set-up

catalyst mass was 800 g at the beginning of operation. The corresponding non-fluidised bed height is 58 cm. Inside the reactor, two lances are present. One lance measures temperatures at different heights. The other lance discontinuously takes gas samples at 7 cm bed height, which are directed to a mGC to measure bulk gas concentration including helium. The reacted wet gas mixture leaves the reactor and enters the particle filter unit, where particles are removed from the gas and are analysed. A detailed description of the particle filter unit can be found in [149]. In a next step, the wet gas mixture is cooled, so that the water in the reacted gas condensates. The condensate is directed to a tank, which is weighed by scale II. With this procedure, it is possible to determine the water flow entering and leaving the reactor. The difference of those two streams is equal to the water produced during reaction, which contains information about the present conversion. The dry gas leaving the condenser is analysed again continuously via mGC and a non-dispersive infrared (NDIR) sensor. If the NDIR sensor displays permissible concentrations of methane ($CH_4 > 85$ %), the gas, which is now called 'biomethane', flows through a gas meter into the natural gas grid as a restricted injection. If the methane content was below the mentioned limit, the gas left the set-up as exhaust and the plant switches into stand-by mode.

5.3.2 Measurement System and Data Evaluation

Operational conditions which can be measured directly are recorded and visualised by a Intermodulation Analysis System (IAS), e.g. temperature, pressure, weights, concentrations by NDIR sensor etc. (155 measurement points in total). Calculations of operational

parameters with data from IAS or mGC are executed separately. During the whole operation a small flow of helium (0.4 Nl/min) was added to the biogas flow, which made it possible to obtain volume flows from the concentration measurements. A redundant measurement system was established, such that the same relevant operational condition could be measured or calculated in multiple ways independently from each other. This allows a direct verification of the redundantly obtained values for one operational condition. Also, an elemental mass balance was done for the whole set-up considering the elements carbon, hydrogen and oxygen. For this, a measurement data evaluation tool (MeDEa) programmed in Matlab© was established. First, the MeDEa tool merges the data from the different sources. For this, the same time stamp must be applied to every data source. In order to obtain a value within two measured data points, linear interpolation between those two data points was done. Second, non-directly measurable operational conditions (like inlet volume flow of biogas, fluidisation in BFB reactor, conversion of CO_2 etc.) were calculated via IAS and mGC data. Third, mass balances for C, H and O were executed for the whole set-up.

The explained procedure allowed an identification of reliable measurement values by which mass balances could be closed with an average error of +/- 5 %. Redundantly obtained values are in agreement with each other. A prompt tracking and detailed evaluation of the course of operation over 1130 h of operation became possible with the help of the automated MeDEa tool. Here, early insights could be obtained during operation which allowed the optimisation of operation parameters and the identification and rectification of irregularities during operation at an early stage.

5.3.3 Experiments

Regular Operation

Regular operation hours are defined as the time where real biogas from the plant in Werdhölzli was directed to the COSYMA set-up and biomethane produced by the reactor was injected into the gas grid. More than 1130 regular operation hours could be completed. The regular operation time can be divided into three phases.

In the first phase (0h – 429h), operational conditions were changed in order to find optimal conditions for maximum methane content in the reactor outlet gas. For this, the reactor temperature and the hydrogen feed were varied. The amount of hydrogen added to the system is expressed via the hydrogen-to-CO_2 ratio, where the hydrogen feed is put into relation to the carbon dioxide mole flow in the raw biogas. With this ratio, variations in the biogas feed are reflected although the hydrogen feed was constant. The pressure was set to 5.7 barg for the whole regular operation time. Steam was added to

the reactor in order to prevent deactivation of the catalyst from coke formation. Here, an overall molar ratio of water-to-CO_2 of 0.5 was chosen.

In the second phase (430h – 1035h), operational conditions were held constant within the range of the optimal conditions for temperature and hydrogen-to-CO_2 ratio identified in the first phase. Pressure and water-to-CO_2 ratio remained the same as in the first phase. The compressor for the biogas feed was not temperature-controlled. Hence, the temperature of the compressor was subject to ambient temperature variations from day to night, which resulted in changing output standard volume flows. In order to maintain a constant hydrogen-to-CO_2 ratio within a tolerated range, hydrogen had to be re-adjusted over time. However, fluctuations of the hydrogen-to-CO_2 ratio could not be fully avoided. Changes in the compressor flow affects various other operational conditions e.g. the fluidisation in the reactor and the water-to-CO_2 ratio.

During the last 96 operating hours, which represent the third phase, a stress test for the catalyst was executed. For this, the water addition was reduced stepwise until zero. Here, the deactivation of the catalyst caused by coking was investigated in order to evaluate which additional amount of water at the inlet is necessary to protect the catalyst.

Monitoring of Deactivation

With repeated reference experiments, it was possible to create exactly the same conditions in the reactor, such that the performance of the reactor could be compared over time regarding deactivation of the catalyst. Since the biogas concentrations from the biogas plant were subjected to fluctuations, only bottled gas was used for the reference experiments in order to achieve stable conditions. The reference experiments were distributed over the 1130 hours of regular operation and were repeated about every 100 operational hours (starting after 400 hours) or when there was a specific incident like catalyst addition etc. An average biogas composition of about 37 vol-% CO_2 and 63 vol-% methane was simulated with bottled gas as feed, in which methane was substituted with nitrogen for technical reasons. This procedure is valid, since methane in the feed gas passes the reactor as quasi-inert gas like nitrogen and the influence of the replacement of methane with nitrogen to the chemical equilibrium is minor. The experiments were carried out at two temperature levels. The predominant conditions of the reference experiments are listed in Table 5.1.

In addition, eight catalyst samples were taken over time from the bed material of the reactor in order to analyse the depositions on the catalyst surface. This analysis was done with the method of temperature programmed oxidation (TPO) in a thermo-gravimetric

H_2, Nl/min	CO_2, Nl/min	N_2, Nl/min	He, Nl/min	H_2/CO_2, -	H_2O/CO_2, -	p, barg	T_{reac}, °C
53.4	12.8	22.1	0.4	4.17	0.86	6.1	320; 350

Table 5.1: Operational conditions during reference experiments with bottled gas

analyser (TGA) at temperature levels between 150 °C and 900 °C. The gases formed during heating under diluted air were measured with a mass spectrometer (MS). With this method, it is possible to distinguish between carbon species and sulphur species which block the catalyst surface and are responsible for the catalyst deactivation.

5.3.4 Assessment of Rigorous Methanation Model

One additional target is the assessment of the existing rate-based model of a bubbling fluidised bed for methanation with the experimental data obtained during regular operation. The applied model is taken from [110] with the adaptations presented in chapter 3. Shortly explained, the model considers thermodynamic and kinetically driven effects for the reaction as well as the interplay of reaction and hydrodynamic influences caused by bubble forming and interphase mass transfer from the bubbles to the catalyst phase. A detailed description of the bubbling fluidised bed model can be found in chapter 3.

For the evaluation, the model is tested via variations in temperature and hydrogen addition to the biogas. With this, the kinetics of the model could be evaluated as well as the influence of the hydrodynamics on the reacting system. The experimental and rate based model results are compared to an equilibrium model for methanation based on minimising Gibbs enthalpy.

With the help of the rate based model, an optimal point of operation regarding temperature and hydrogen addition was found for maximising the methane content in the product gas and was applied during regular operation.

5.4 Results and Discussion

The pilot-scale methanation system COSYMA ran in total 1131 regular operating hours. In addition, eleven reference experiments were carried out and eight catalyst samples were taken from the reactor over time. The corresponding large amount of data was processed with the automated MeDEa tool with which inconsistent data could be identified immediately so that the causes of the inconsistencies could be removed directly.

5.4.1 Regular Operation

The operation of the COSYMA set-up was stable over the whole operating time with average concentrations in the outlet gas of 87 vol-% methane, 10.6 vol-% hydrogen, 1.4 vol-% carbon dioxide and 1 vol-% helium. Helium was only added for advanced measurements which are not necessary for an industrial operation. The average yield of methane was 95.8 %. In figure 5.3 and figure 5.4, operational conditions and the performance of the reactor are illustrated. More operating conditions during the regular operating hours can be found in the appendix (A.4 and A.5). The different ratios and the yield of methane used in the figures and elsewhere are defined as follows:

$$\frac{H_2}{CO_2} = \frac{\dot{n}_{H_{2,in}}}{\dot{n}_{CO_{2,biogas}}} \tag{5.1}$$

$$\frac{H_2O}{CO_2} = \frac{\dot{n}_{H_2O_{in}}}{\dot{n}_{CO_{2,biogas}}} \tag{5.2}$$

$$Y_{CH_4} = \frac{\dot{n}_{CH_{4,out}} - \dot{n}_{CH_{4,in}}}{\dot{n}_{CO_{2,in}}} \tag{5.3}$$

$$\text{catatlyst stress} = \frac{\dot{V}^{std}_{CO_{2,biogas}}}{m_{cat}} \tag{5.4}$$

In Figure 5.3, the dry molar fractions of the bulk components methane, hydrogen and carbon dioxide in the outlet gas are illustrated as a function of the regular operation time. Here, important incidents during operation are marked. In figure 5.4, the corresponding ratio of hydrogen-to-carbon dioxide at the inlet and the yield of methane are shown as a function of the regular operating hours. The values illustrated in both figures are averaged over one operating day.

During the first phase (0h – 429h), the reactor temperature was changed between 320 °C and 360 °C and for a short time to 380 °C. The system pressure was set constant. Especially during the first 200 hours, the temperature and the hydrogen-to-CO_2 ratio (Figure 5.4) in the inlet gas was varied strongly to identify optimal operation settings. A detailed description of the optimisation process can be found in section 5.4.3. Due to the pronounced changes of those parameters, the dry concentration of the bulk components in the outlet gas (Figure 5.3) and the methane yield (Figure 5.4) strongly vary during the first 200 operational hours. In the first phase, yields were reached between 94 vol-% and 99 vol-% with corresponding methane concentrations in the outlet stream

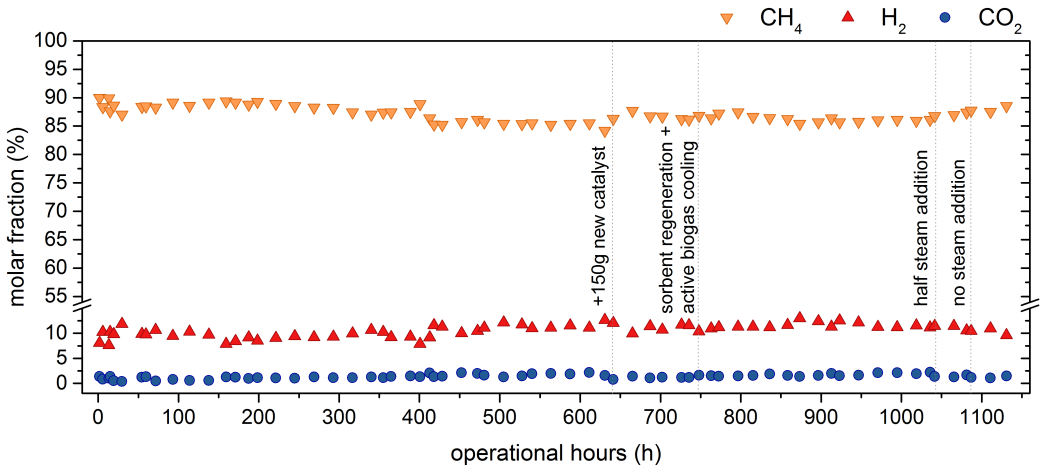

Figure 5.3: Molar fractions (dry) of bulk components after the methanation reactor as a function of regular operation hours

between 85 vol-% and 90 vol-%. Almost the whole amount of reacted carbon dioxide was converted to methane. Hence, a selectivity of almost 100 % can be assumed. After 200 regular operating hours, the first signs of deactivation occur with the start of a slow decrease in methane concentration at the outlet. However, the exact starting time of deactivation cannot be identified since the first measurements of non-H_2S sulphur compounds breaking through the gas cleaning unit was executed at 300 h and the first reference experiment with used catalyst was done at 400 h. Deactivation processes are described in more detail in section 5.4.2.

During the second phase (430h – 1035h), operational parameters were mainly set constant at optimum conditions within a certain range. Temperature and pressure were set to 355 °C and 5.7 barg. The optimum temperature increased due to deactivation issues. The average catalyst stress and the average H_2O/CO_2 ratio were 12 $Nl_{CO_2,\text{biogas}}/(\text{min kg}_{\text{cat}})$ and 0.55 respectively. Since it was not possible to hold the H_2/CO_2 ratio constant due to the changes of the compressor flow, the ratio varies between 3.85 and 4.15 (Figure 5.4). In the second phase, methane yields reached 93 vol-% to 98 vol-% with methane outlet gas concentrations between 84 % and 88 %. At 400 operating hours, an abrupt decrease of methane content of 2.2 vol-% - points in the biomethane stream can be observed (Figure 5.3). At this time, the operation was paused for about two weeks, and the system was purged with nitrogen during the shut-down. The nitrogen was passing the gas cleaning unit and then entered the methanation reactor, so that it is very likely that sulphur present on the adsorber in the gas cleaning unit desorbed to some extent and then could entered the reactor together with the nitrogen stream. The sulphur adsorbed on the catalyst, which led to the mentioned abrupt deactivation. From

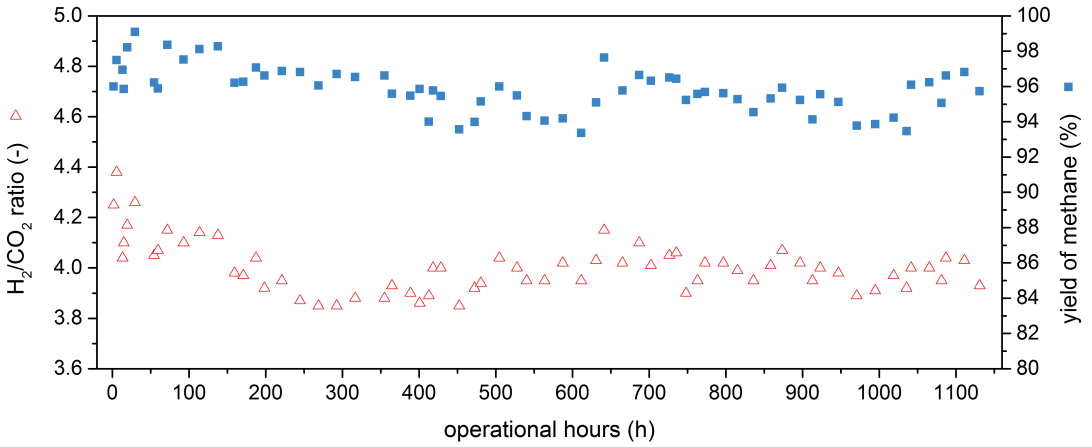

Figure 5.4: Inlet ratio of hydrogen to carbon dioxide from biogas and the yield of methane as a function of regular operation hours

400 to 600 hours, stable operation of the COSYMA set-up was obtained with an average level of 85.4 vol-% methane concentration in the biomethane flow. However, small decreases in the methane concentrations in the biomethane flow were observed over time. The reference experiments also showed signs of deactivation in the reactor (see section 5.4.2). Therefore, after 641 operating hours, 150 grams of fresh catalyst was added to the used catalyst (800 grams) in the reactor, which improved the yield of methane so that methane concentrations of 86.5 % were reached again. Over the next few 100 operation hours, measures were taken in the gas cleaning unit which improved the gas cleaning performance. Namely, the chosen sorbent materials were regenerated and the entering biogas flow was actively cooled to minimise competing adsorption between water and sulphur molecules [148]. These measures were successful, so that the methane concentration in the biomethane flow stayed constant at approximately 86 vol-% until the end of this second phase.

In the third phase (1036h - 1131h), the steam addition to the reactor was stepwise reduced to observe the effect of steam on the reaction mechanism. On the one hand, steam influences the thermodynamic equilibrium towards less methane production. On the other hand, steam is supposed to protect the catalyst against coking, since a higher ratio of elemental hydrogen in comparison to carbon is achieved in the reactor. With the reduction of steam addition, it can be evaluated if the steam addition is necessary for a stable operation. In Figure 5.3, the effect of steam reducing can be seen at the bulk concentrations. For about 50 hours, the steam was reduced by half and for the last 50 hours no steam was added to the reactor. Due to the improved thermodynamic equilibrium, the methane concentrations increased with the decreasing steam addition.

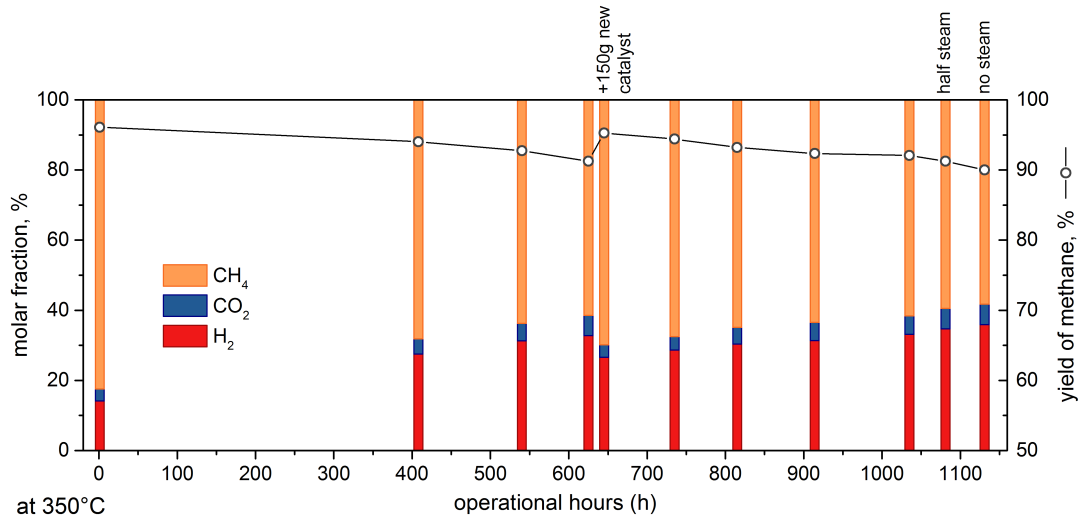

Figure 5.5: Normalised dry molar fraction of bulk components after the reactor and the yield of methane as a function of regular operation hours with a reference gas mixture at a reactor temperature of T = 350 °C

Hence, no severe deactivation occurred during this phase, so that the more beneficial thermodynamic equilibrium had its intended effect on the conversion.
In the following sections, however, it will be discussed that the methane content would have been higher, if no deactivation had occurred. In general, changes in catalyst stress within the given ranges have only minor influences on the reactor performance whereas variations of hydrogen addition and of temperature clearly impact the dry outlet concentration of the reactor. The yield of methane correlates directly with the predominant hydrogen-to-CO_2 ratio (Figure 5.4), besides deactivation effects.

However, operational conditions were continuously changing over the time, thus a clear comparison of the results over the operation hours regarding deactivation is not possible. In order to gain reliable information about the effects of deactivation, reference experiments were conducted.

5.4.2 Monitoring of Deactivation

For the reference experiments, dry molar concentrations of the components methane, hydrogen and carbon dioxide after the reactor are illustrated in Figure 5.5 at 350 °C reactor temperature. The concentrations of the mentioned components are normalised to 100 % so that nitrogen and helium are not illustrated in the graph. Also the yield of methane is shown for the corresponding experiment. At hour zero, a reference experiment was conducted before real biogas entered the COSYMA set-up. This point can be seen as the reference state for a non-deactivated catalyst with a yield of 96.1 vol-% and

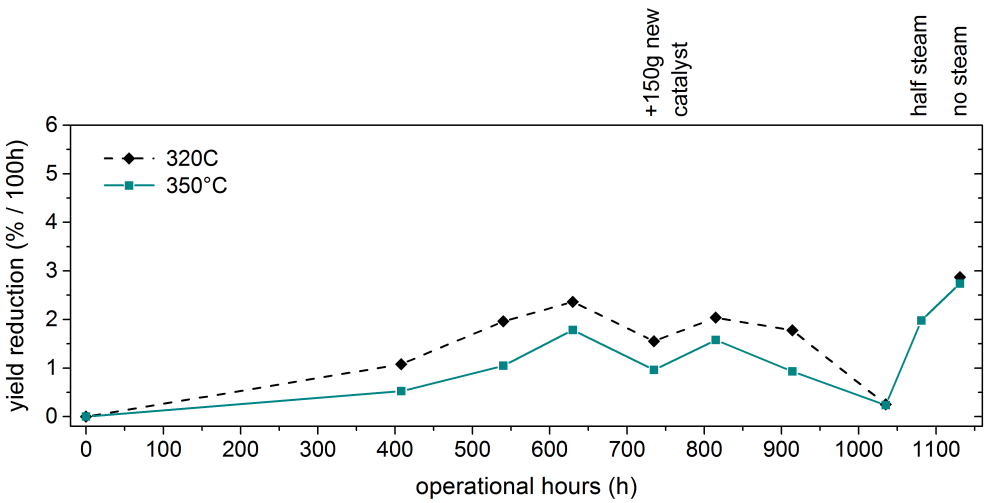

Figure 5.6: Yield reduction per hundred operation hours as a function of regular hours of operation at 320°C and 350°C reactor temperature measured during reference experiments

a normalised methane concentration after the reactor of 82.5 vol-% at corresponding conditions. The normalised concentration of methane is not directly comparable with the results of section 5.4.1 since only the produced methane is shown in Figure 5.5 and not the sum of methane from biogas and the produced methane like in Figure 5.3. Theoretically the methane content for this experiment would have been 91 vol-%, if methane had been added to the feed instead of nitrogen. In Figure 5.6, the corresponding yield reduction per 100 hours observed during the reference experiments is shown as a function of regular operating hours at 320 °C and 350 °C reactor temperature. The yield reduction per time step j is defined as follows:

$$Y_{red,j} = \left(1 - \frac{Y_j}{Y_{j-1}}\right) \cdot 100\ \% \tag{5.5}$$

$$\frac{Y_{red,j}}{100\ \text{h}} = \frac{Y_{red,j}}{t_j - t_{j-1}} \cdot \frac{100\ \text{h}}{100\ \text{h}} \tag{5.6}$$

This definition is equivalent to a deactivation gradient or deactivation rate over time. At about 400 hours of regular operation, the first reference experiment was conducted with used catalyst. A decreased yield can be observed together with a decreased normalised concentration of methane after the reactor, see figure 5.5. Corresponding to this, the hydrogen and carbon dioxide content is increasing due to the lower conversion rates. With further regular operation hours, deactivation progresses until a yield of 91.3 vol-%

at about 630 hours. Several breakthroughs of sulphur compounds in the gas cleaning unit could be identified as the source of the deactivation, as is shown in the next part. The gradient of deactivation increased during this period and formed a local maximum at 630 h with a value of 1.8 %/100 h at 350 °C and 2.4 %/100 h at 320 °C. The gradient of deactivation at 320 °C is always higher than at 350 °C, which is explained in the next section. As a countermeasure to the growing deactivation gradient, 150 g of new catalyst was added to the 800 g of catalyst already inside the reactor at about 640 operating hours. As a result, yield and methane concentration increased again to a level between the initial state and the reference experiment at 400 hours. Less than one fifth of the original catalyst amount was added to the reactor, but this resulted in almost in the same performance of the reactor as for the non-deactivated catalyst. Since the methanation reaction in a fluidised bed is not mainly restricted by kinetics, but among others by heat transfer at the given operational conditions, the main part of the catalyst bed is used to dissipate heat via heat exchangers, so that approximately isothermal conditions are reached. Now, the small amount of 150 g new catalyst is kinetically active enough to almost compensate the partly deactivation of the old catalyst. Nevertheless, the catalyst material inside the reactor slowly deactivated again as time progressed. As mentioned before, adaptations in the gas cleaning unit were made to improve the gas cleaning performance. In the period between 914 h and 1035 h of regular operation, the reference experiments show that almost no further deactivation occurred. Here, a combination of measures in the gas cleaning unit for improving performance was successful. The yield reduction for both temperature levels became almost zero with 0.25 %/100 h. With this deactivation rate, it is possible to run the methanation only with a yearly replacement of the catalyst assuming 8000 hours of operation per year.

In the last phase, the steam addition was reduced in two steps to zero. Although the methane content during regular operating hours was increasing during this last phase (Figure 5.3), a significant deactivation can be observed (figure 5.5 and figure 5.6). The positive effect of a more beneficial thermodynamic equilibrium could not totally be overruled by the deactivation process during the regular operation. However, whether the deactivation was caused by coking due to the lack of steam in the last phase or again by sulphur compounds cannot by identified only by comparing deactivation rates in full-steam and no-steam modes.

Normalised concentration profiles over the bed height were derived at different points in time via lance measurements in the reactor during reference experiments (Figure 5.7). Here, the dry molar fractions of the bulk components methane, hydrogen and carbon dioxide are illustrated. After 408 operational hours, the first lance measurement was conducted, where already a performance loss of the reactor occurred due to deactivation

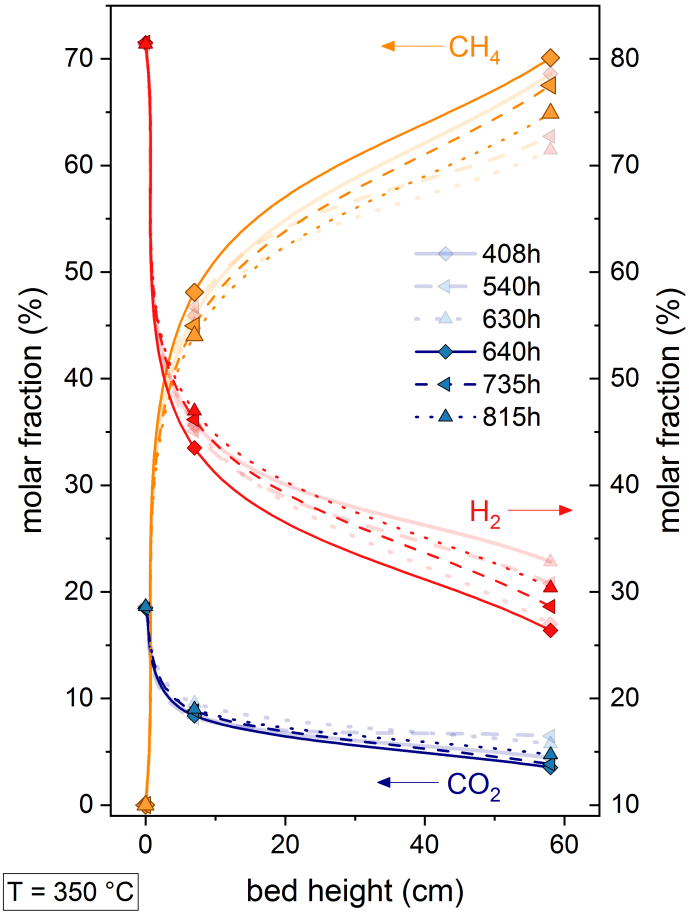

Figure 5.7: Normalised (dry) concentration profiles of bulk components over bed height at different points in time; measurement positions: inlet, lance height (7 cm) , outlet; reference experiments at 350 °C reactor temperature; the lines are for orientation only

as discussed earlier. Then, before (630 h) and after the catalyst addition (640 h), the corresponding profiles are shown. In general, approximately two thirds of the total methane production is completed after 7 cm of bed height, which is about 12 % of the total height. In the following 88 % of bed height, the remaining one third of total methane production is completed which is slowed down by mass transport limitations. Normalised concentration profiles changed over time due to deactivation. For the first three measurements in time (408 h, 540 h and 630 h), normalised concentration of methane decreases, hence hydrogen and carbon dioxide concentrations increase both at the lance height and at the end of bed. After the catalyst addition at 640 h, the methane content increases. Due to the previously discussed deactivation, the methane concentration over the bed height is decreasing again with the time.

It was expected that the difference of concentrations for one component at different points in time would be more pronounced at the lance height than at the total height. Therefore, this method was supposed to give an early warning of deactivation. However, the measurements show that this is hardly the case. Mass transfer limitations from bubble to dense phase may influence the reaction in a way that the reaction course is dampened, therefore deactivation of the catalyst cannot be seen so clearly at the lance height via different concentrations of each component. The catalyst particle movement in the reactor might also contribute to the similar concentration profiles. Deactivated particles are evenly distributed in the reactor volume due to the mixing properties of the fluidised bed. Therefore, the reaction rates are evenly slowed down over the bed height. As a result, the lance measurements are not fully reliable to give early warnings regarding catalyst deactivation.

Catalyst samples and breakthrough concentrations after the gas cleaning unit were analysed to identify the source of deactivation. The catalyst samples taken from the reactor over time were analysed with the TPO method to identify which compounds are bound to the catalyst surface and are responsible for the blockage of the active sites of the catalyst. In Figure 5.8 and Figure 5.9, the results of the TPO analysis are presented for the investigation of carbon and sulphur depositions. Catalyst samples were frequently taken over the operation time. Additionally, the fresh catalyst used in the COSYMA set-up and a sample from a former methanation experiment starting from wood gasifier gas in Güssing (AT) in 2007 [151, 152] were investigated.

In Figure 5.8 (b), the temperature profile applied for all TPO samples is illustrated. In Figure 5.8 (a), the corresponding relative mass change of the investigated catalyst samples are shown together with the MS signal for carbon dioxide normalised by the catalyst sample mass. From 20 °C to 150 °C, the mass decreases for every sample partly due to a drying process. A first peak in the CO_2 signal can also be seen, which corresponds to the combustion of adsorbed carbon (C_α). With further time, the Güssing sample from 2007 behaves different from the current ones. The mass of the Güssing sample further decreases with rising temperatures, whereas the mass of the other samples increases until a temperature of 360 °C. The mass increase can be explained by oxidation of the bulk nickel in the catalyst sample. This oxidation did not occur for the Güssing sample. At the same time, carbon dioxide is released from combusted polymeric carbon which is supposed to be the source of deactivation by coking. Hence, two effects co-existed where increasing mass due to oxidation of the bulk nickel and decreasing mass due to coke combustion are in competition. Here, the mass difference cannot give a precise result for the amount of carbon on the catalyst surface for the current samples due to the co-existing competing effects. However, the MS signals for carbon dioxide between 150 °C

and 500 °C, which corresponds to polymeric carbon (C_β), are not significant for the current samples in comparison to the Güssing sample. The catalyst of the methanation in Güssing, 2007 was subjected to a more challenging feed gas composition, since from the wood gasifier more tars were produced and therefore a bigger risk of coking existed. But even the state of the sample from 2007 did not lead to significant deactivation from coking in the former experiments. Therefore, deactivation of the catalyst due to coking is most likely not the main cause for deactivation even for the operating time where reduced or no steam was added to the reactor. Between 500 °C and 800 °C, a second peak of the MS signal for carbon dioxide can be observed (Figure 5.8 (a)). Here, graphite (C_C) from the catalyst structure itself is combusted. The structure of the current and the former catalyst (2007) is most likely different regarding the graphite composition,

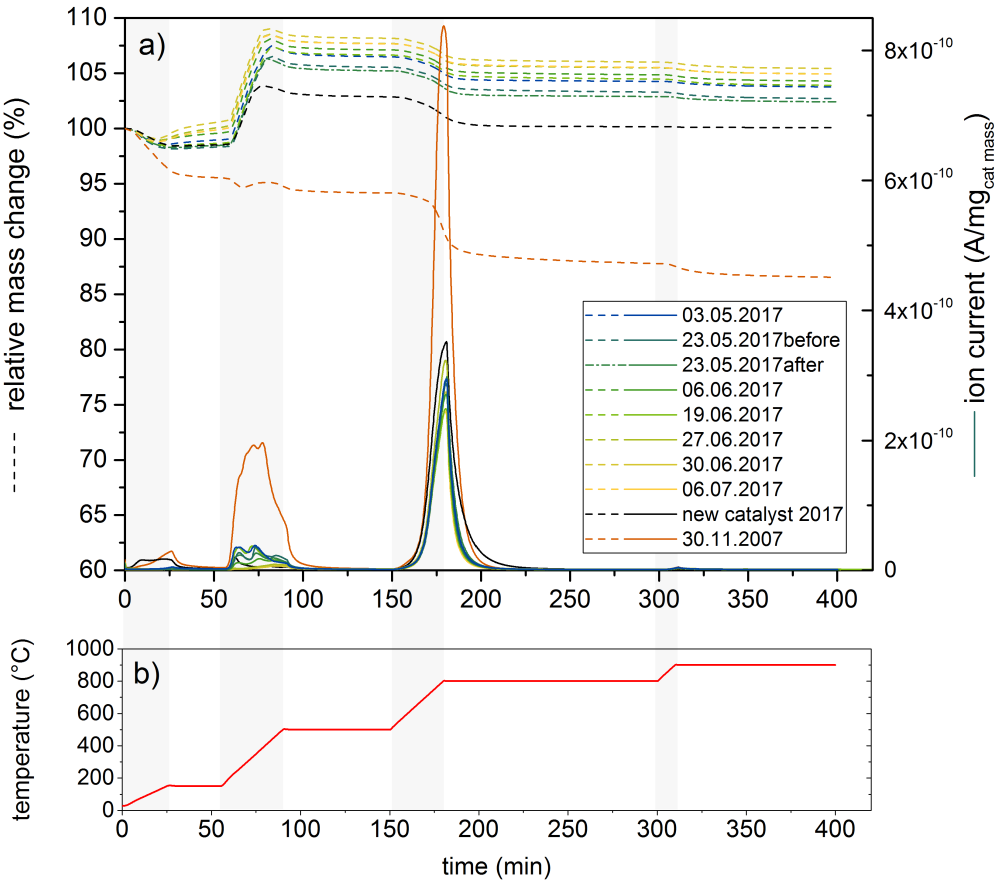

Figure 5.8: a) Relative mass change of catalyst samples and MS measurement signal of CO_2 during TPO analysis for used catalyst samples (03.05.2017 – 06.07.2017), fresh catalyst and for a catalyst sample taken from a methanation project from wood gasifier gas in 2007 [150]; b) corresponding temperature profile during TPO

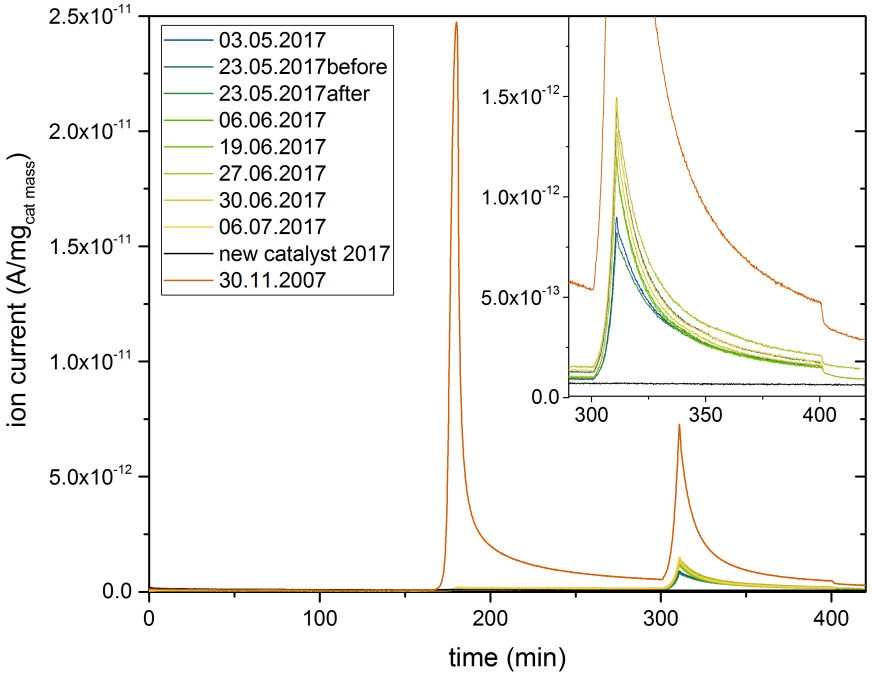

Figure 5.9: MS measurement signal of sulphur dioxide during TPO analysis for used catalyst samples (03.05.2017 – 06.07.2017), fresh catalyst and for a catalyst sample taken from a methanation project from wood gasifier gas in 2007 [150]

therefore different peak intensities are obtained. The last mass change in Figure 5.8 (a) can be observed between 800 °C and 900 °C, which is due to sulphur combustion.

The corresponding normalised MS signal for sulphur dioxide can be seen in Figure 5.9. For the currently used catalyst samples, only one peak occurs between 800 °C and 900 °C which is directly related to sulphur on the catalyst surface. It can be seen that with progressing time, the formed peaks become higher with the same width. Hence, more sulphur was adsorbed at the catalyst surface over the operating time, which corresponds to the previous deactivation monitoring results. For the unused catalyst, no sulphur signal was obtained. The catalyst used in 2007 showed a higher deposition of sulphur than the samples from the biogas methanation. Here, also a second peak between 500 °C and 800 °C can be observed, where most likely the sulphur situated on the graphite was burned together with the graphite from the catalyst material [153] according to the carbon dioxide signal from Figure 5.8 (a) at the mentioned temperature level. The concentration of sulphur contaminants in the gasifier gas from wood was significantly higher than in the biogas [153], which explains the larger integral of the MS signals for SO_2 of the catalyst sample from 2007.

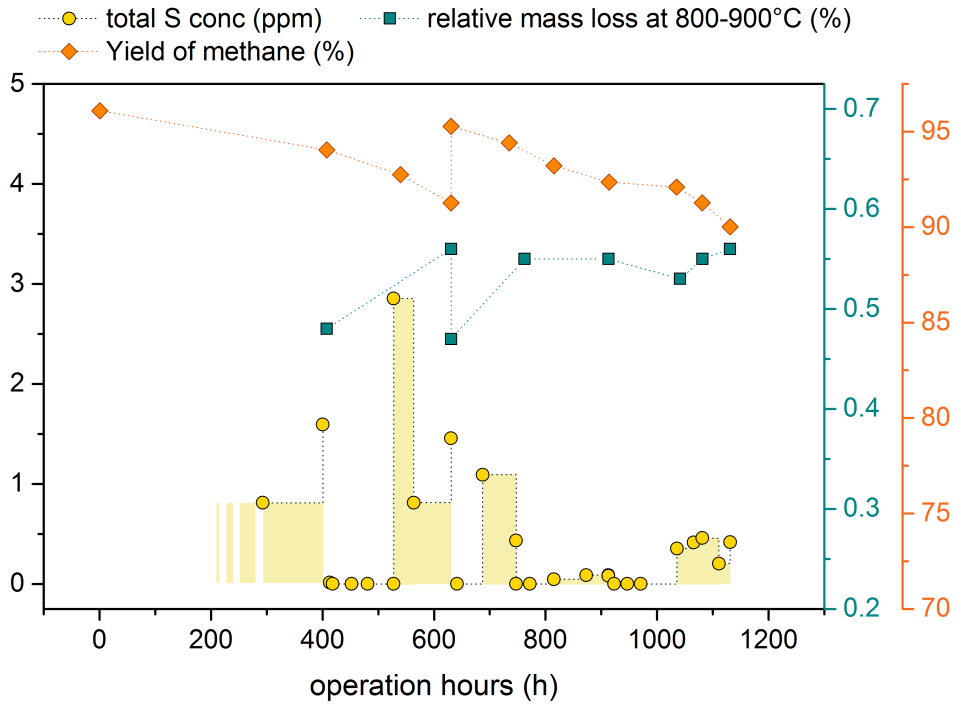

Figure 5.10: Breakthrough concentrations of total sulphur after the gas cleaning unit, relative mass loss of catalyst samples related to sulphur during TPO analysis and the methane yield at reference experiments as a function of regular operation hours, adapted from [148]

In Figure 5.10, results from different sources regarding sulphur poisoning of the catalyst during the biogas methanation are illustrated. Here, the breakthrough concentrations of total sulphur after the gas cleaning unit [148] as a function of the operating hours are compared first to the relative mass loss of the used catalyst samples during the TPO analysis at 800 °C - 900 °C, which is directly related to sulphur deposition on the catalyst surface as explained in the previous section. Secondly, the yield of methane during the reference experiments is shown again as a function of the operating hours. All three indicators correlate with each other. During a sulphur breakthrough, the concentrations of total sulphur were between 0.5 and 3 ppm. According to increased sulphur concentrations, the relative mass loss of the corresponding catalyst sample increased. With that the yield of methane decreased as a result of catalyst deactivation due to sulphur. At about 600 operating hours, new catalyst was added which produced the upper peak in the yield and the lower peak in the relative mass loss. Here, the used catalyst was diluted with fresh catalyst so that the specific sulphur deposition per catalyst mass decreased, which improved the yield temporarily. After that, a third breakthrough of sulphur can be observed, which is reflected again in the mass loss and the yield. During the oper-

ation hours between 750 h and 900 h, only small amounts of sulphur were entering the reactor, so that no change of mass loss can be seen. But these small amounts of sulphur seemed to be sufficient to cause deactivation, since the yield is decreasing further. Only at the operating hours between 900 h and 1050 h, where no sulphur was detected in the feed gas, the yield stayed approximately stable. The relative mass loss even decreased, which would mean that the desorbed sulphur on the catalyst was reduced which is unlikely. The decrease of relative mass loss at that time can be seen as the error of the method. One error cause can be the imperfectly mixed catalyst material inside the reactor, where a single catalyst sample might have a different amount of deposition than the average amount of deposition at the corresponding operating time. During the last 100 operating hours, the concentration of sulphur components increased again and with that the relative mass loss in the TPO analysis. The yield of the reference experiments is correspondingly reduced again. The addition of steam was reduced at this time, but significant deactivation due to carbon deposition can be excluded. The TPO analysis showed only minor effects of carbon deposition and the yield reduction can be explained directly by the sulphur poisoning. However, the yield reduction at the end of operation was globally at maximum (Figure 5.6) although only a medium amount of 0.5 ppm of total sulphur was entering the reactor. This is an indication that sulphur was not only cause of the deactivation, but carbon depositions were also present due to the lack of steam.

In general, the total sulphur concentration in the feed gas should be lower than 0.2 ppm in order to stop deactivation from sulphur. With a total sulphur concentration of 1 ppm in the feed gas, a yield reduction of about 1 % per 100 operation hours is obtained. For industrial plants, a compromise between the amount of adsorption material and catalyst material has to be found.

5.4.3 Model Evaluation

The model evaluation was carried out in order to optimise the operating conditions of the methanation reactor for a maximum methane content in the product gas biomethane. For this, the ratio of hydrogen and carbon dioxide in the feed and the reactor temperature were varied in the model and during the experiments (regular operation – first phase) considering the same operating conditions in the model as in the experiments. In the following section, the results of this procedure are compared with each other.

The other parameters during experiment which influence the methanation reaction (H_2O/CO_2, catalyst stress and reactor pressure) were kept constant within a certain range. The water-to-CO_2 ratio and the catalyst stress vary in a range from 0.51 to 0.67 and from 13.3 Nl/(min kg) to 17.1 Nl/(min kg) respectively due to different ambient

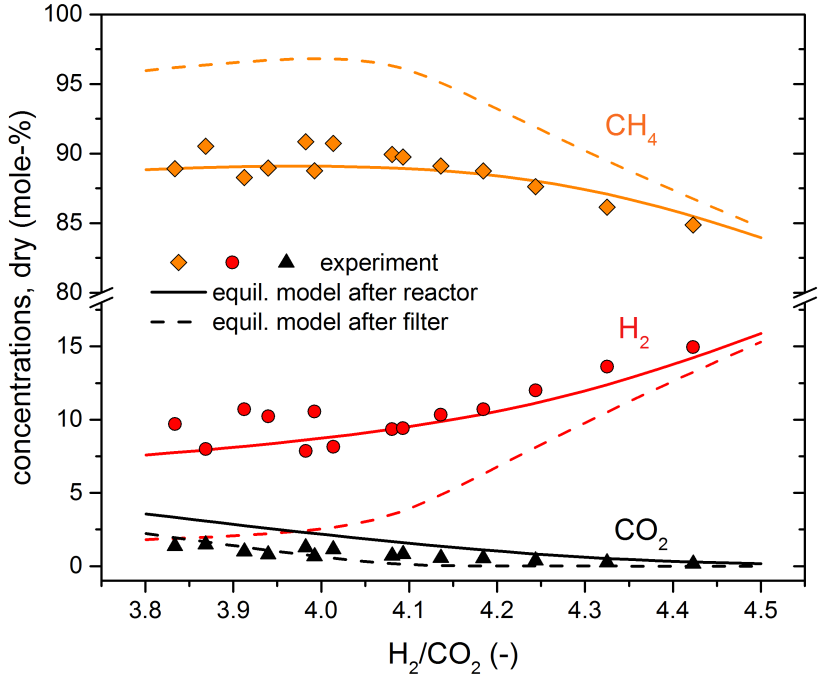

Figure 5.11: Dry molar fractions of bulk components after the reactor over different hydrogen-to-CO_2 inlet ratios derived via experiment and equilibrium model for the methanation at T=340°C and for the filter at 243 °C; average H_2O/CO_2 = 0.55, average cat stress =16.4 Nl/(min kg), biogas concentrations of 63.8 % methane and 36.2 % CO2 and p = 5.7 barg, experimental results taken from the first 300 regular operating hours

conditions, whereas the reactor pressure was constant at 5.7 barg. The experimental data for the analysis were taken during the regular operation hours. The experimental data are compared to the results of the methanation model, for which the equilibrium model and the rate-based model is used.

The result of the variation of the parameter H_2/CO_2 of the feed is shown in Figure 5.11. Experimental data first are compared with results from the equilibrium model. Dry molar fractions of the bulk components methane, hydrogen and carbon dioxide downstream of the reactor are illustrated as a function of the inlet ratio H_2/CO_2. After the reactor, a particle filter system was placed (Figure 5.2) running at temperatures between 215 °C and 243 °C. Here, catalyst material was present due to attrition in the reactor. The temperatures and the presence of the catalyst particles in the filter were most likely the cause for further reaction in the filter, since it is known that the present nickel catalyst is still active at 200 °C [154]. In order to reflect this situation, the bulk

concentrations after the filter are also illustrated assuming equilibrium conditions for the reaction in the filter. For high H_2/CO_2 inlet ratios, larger amounts of hydrogen remain in the outlet stream of the reactor, hence the outlet hydrogen fraction is at a maximum at high ratios and decreases with the H_2/CO_2 ratio. Vice versa, the fraction of carbon dioxide decreases with the H_2/CO_2 ratio. For high hydrogen additions, the outlet carbon dioxide fraction is at a minimum, because larger amounts of hydrogen enhance the reaction and therefore the conversion of CO_2. With decreasing hydrogen addition, the reaction becomes more restricted by the lack of hydrogen and less carbon dioxide converts, so more CO_2 remains in the outlet stream of the reactor. The methane fraction behaves differently since a maximum is formed. For increased hydrogen addition, high conversion rates to methane are obtained, but more hydrogen also remains in the outlet flow. For decreased hydrogen addition, less hydrogen remains in the outlet flow, but the conversion to methane is inhibited. The interplay of these factors results in an optimum value of H_2/CO_2-ratio where the conversion rates to methane and low hydrogen addition are balanced. This optimum can be found at an H_2/CO_2-ratio of 3.9 in the model as well as from experimental results. However, sub-stoichiometric hydrogen addition may increase the risk of catalyst deactivation due to coking.

For lower H_2/CO_2–ratios, the conversion rates in the experiments are even higher than the equilibrium model of the reactor predicts. Theoretically it is not possible to go beyond the thermodynamic limit shown by the equilibrium model but during the experiment conditions occurred, which are not considered in the model. First, as already discussed, it is very likely that further conversion of carbon dioxide took place in the subsequent filter. The theoretical maximum of this conversion is illustrated in Figure 5.11 with the bulk concentrations after the filter with the assumption that thermodynamic equilibrium was reached. However, low temperatures and the small amount of catalyst material in the filter could not convert the reactants fast enough, so that the thermodynamic limit in the filter was clearly not reached but still had an influence on the bulk concentrations. Second, a temperature profile was established in the reactor during experiments which is illustrated in Figure 5.12. In contrast, the equilibrium model and the rate-based model assume isothermal conditions. Hence, temperature changes over the reactor height and the corresponding impact on the reaction cannot be simulated, although appropriate temperature profiles can help to obtain a higher overall conversion than at isothermal conditions. Higher temperatures at the beginning of the reactor bed result in a higher activity of the catalyst, which leads to faster conversion. If then in a next step, the reactor temperature decreases, thermodynamically more beneficial conditions are obtained, which results in further but also slower conversion of the remaining carbon dioxide due to the decreased activity at lower temperatures. However, further research regarding the effect of medium temperature profiles in bubbling fluidised beds are

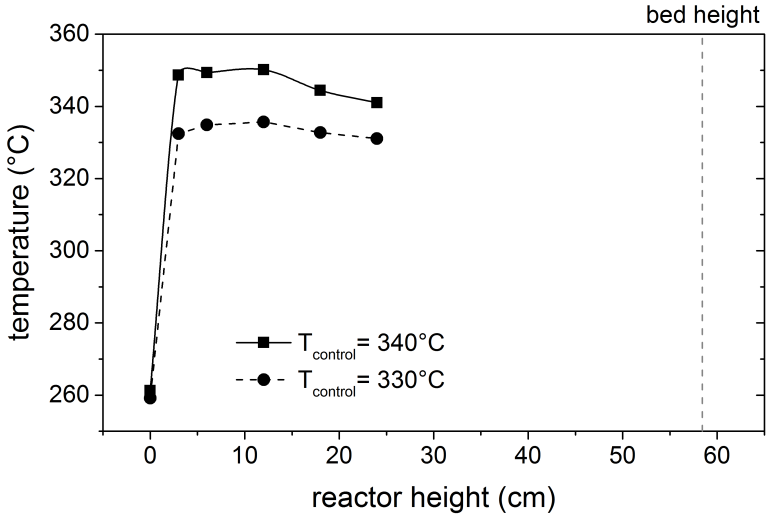

Figure 5.12: Temperature profile over the COSYMA reactor height for different control temperatures

required to understand the impact in more detail. In addition, the outlet temperature of the reactor is unknown. The temperature at the end of the bed might be even lower than the last known temperature located in the middle of the bed, so that further conversion might have been possible. In the models, $T_{control}$ was assumed as the isothermal reactor temperature. Therefore, the unknown conditions at the end of the reactor bed also could have caused the bulk concentrations exceeding the thermodynamic limit of $T_{control}$.

In Figure 5.13, the same experimentally obtained methane concentrations are shown as in Figure 5.11. In addition, besides the results of the equilibrium model the results of the rate-based model are also illustrated as a function of the H_2/CO_2 inlet ratio. The influence of the filter is also shown via experimental results and via equilibrium simulations, but at two different temperatures. The lower filter temperature (215 °C) results experimentally in slightly higher conversion rates, so that the methane concentrations are slightly increased in comparison to the methane concentrations at a filter temperature of 243 °C. This indicates not only that more conversion than predicted by the thermodynamic equilibrium was reached in the reactor due to unknown temperature profiles, but also that further reaction occurred in the filter. The rate-based model and the equilibrium model show differences in their results for the reactor. For higher H_2/CO_2 inlet ratios, the equilibrium model predicts higher methane concentrations than the rate-based model. The rate-based model considers hydrodynamic effects. With the increasing hydrogen addition, the fluidisation of the reactor bed increases and with that the average bubble size. Larger bubbles worsen the interphase mass transfer from the bubbles to the catalyst phase so that the interphase mass transport of the reactants takes

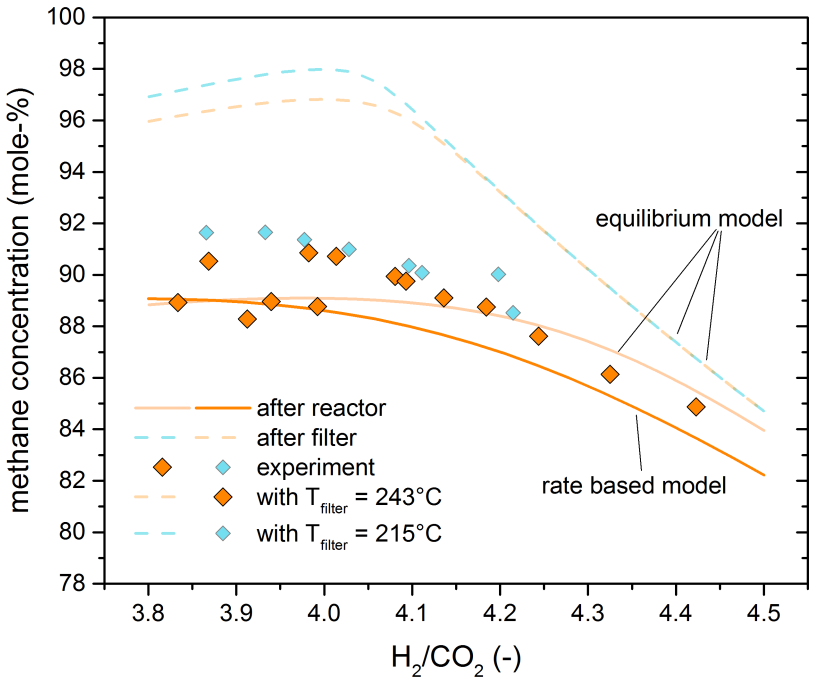

Figure 5.13: Dry molar fractions of methane after the reactor over different hydrogen-to-CO_2 inlet ratios derived via experiment, rate based model and equilibrium model for the methanation at T = 340 °C and for the filter at 243 °C or 215 °C; average H_2O/CO_2 = 0.6, average catalyst stress = 15.5 Nl/(min kg) and p = 5.7 barg, experimental results taken from the first 300 regular operating hours

more time, which reduces the reaction rates. This results in a steeper decrease of the methane concentration, which can be seen also in the experimentally obtained methane concentrations. In this case, the rate-based model provides more precise results than the equilibrium model because hydrodynamic effects are considered.

To validate the kinetics applied in the rate-based model, the temperature in the reactor during the regular operation was varied. The results of parameter variations regarding the reactor temperature are shown in Figure 5.14. Here, experimental results are compared with results of the rate-based model for bubbling fluidised bed methanation as a function of the reactor temperature. Dry molar fractions of methane at the reactor outlet are shown, experimentally obtained for different H_2/CO_2 inlet ratios. Model results are illustrated with a normal and a dashed line as a maximum and minimum case. Since during the experiment, the water-to-CO_2 inlet ratio and the catalyst stress varied in a certain range, experimental results are not directly comparable with the model results. Therefore, the model results are divided into a case where maximum methane concentra-

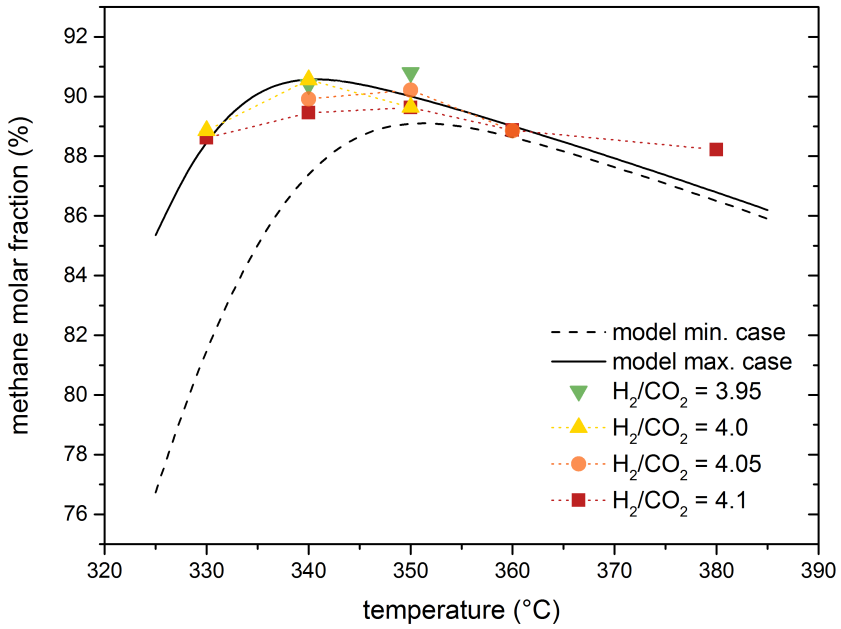

Figure 5.14: Dry molar fractions of methane after the reactor as a function of the temperature, experimentally obtained at different H_2/CO_2 ratios and simulated with the rate-based model for a minimum and maximum case

tions were established after the reactor within the given experimental ranges of the two varying parameters and into a case for minimum methane concentrations. The experimental results should be situated within the range given by the maximum and minimum case of the rate-based model. The input parameters of the two cases are listed in Table 5.2. For the case with maximum methane concentration at the outlet, within the given experimental operational conditions a low H_2/CO_2 inlet ratio was chosen together with a low steam addition and a low catalyst stress of 0.7 $Nm^3\ h^{-1}\ kg_{cat}^{-1}$. At the beginning of this section, it was already shown that sub-stoichiometric H_2/CO_2 inlet ratios at 3.9 cause higher methane contents at the outlet than stoichiometric or hyper-stoichiometric hydrogen addition. Lower water addition also influences the thermodynamic equilib-

Case	H_2/CO_2 (inlet)	H_2O/CO_2 (inlet)	$V_{CH4,in}$, Nl/min	$V_{CO2,in}$, Nl/min	pressure, barg
Max	3.95	0.47	17.36	9.85	5.71
Min	4.10	0.51	24.94	14.15	5.71

Table 5.2: Input parameters corresponding to experimental conditions of the maximum and minimum methane output concentrations cases for the rated-based methanation model

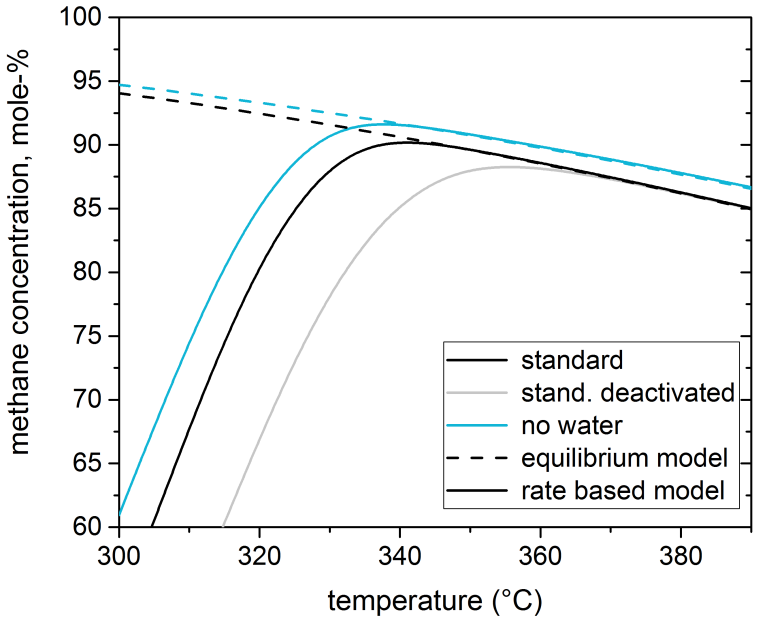

Figure 5.15: Theoretical dry molar fraction of methane after the reactor as a function of the temperature for a standard inlet gas composition with simulated fresh catalyst and deactivated catalyst and without water addition and fresh catalyst; the results are obtained by the rate-based model and the equilibrium model

rium beneficially towards higher methane concentration as shown in section 5.4.1. A lower catalyst stress and in general a smaller inlet volume flow results in higher reaction performance and less mass transfer limitations. For the case with minimum methane concentrations at the outlet, by contrast a hyper-stoichiometric hydrogen addition was chosen, high steam addition and a high catalyst stress value (1.1 $Nm^3\ h^{-1}\ kg_{cat}^{-1}$). All parameters chosen in Table 5.2 were actual experimental conditions with corresponding experimental results shown in Figure 5.14. The experimental results illustrated in Figure 5.14 form a characteristic curve with a maximum for the methane concentration at a certain temperature. At lower temperatures the catalyst is less active and low methane concentrations are obtained. The reaction does not reach the thermodynamic limit due to kinetic limitations.

At higher temperatures, the thermodynamic limit for the methane concentration is reached but the limit also decreases with the temperature due to exothermic properties of the reaction. Hence, a maximum of methane concentration is formed, where the reaction course limited by the kinetics reaches the thermodynamic limit. In general, the kinetics of the rate-based model can predict the activity of the catalyst. The experimen-

tal results are mostly in between the two simulated cases. There is a small tendency of higher experimental values than predicted values. This can be caused by the influence of the filter after the reactor, which results in slightly higher methane concentrations like explained earlier in this section. Especially the experimental value at 380 °C was produced at a lower filter temperature than the other values. We have already seen that a low filter temperature can increase the methane content up to 1 vol-% at the present conditions. The influence of the H_2/CO_2 inlet ratio on the methane outlet concentration experimentally obtained is not as clear as expected. Here, changing conditions in the reactor due to fluctuating catalyst stress and with that, changing H_2O/CO_2 inlet ratios, temperature profiles with a spread of 5 K in average, as well as starting deactivation of the catalyst made it difficult to obtain comparable results. However, trends for the position of the optimal temperature can be derived. Like in the model, the optimal temperature increases with the H_2/CO_2 ratio. Like expected, the data points from experiments have the tendency to be closer to the model results of the maximum case for low H_2/CO_2 ratios and with increasing H_2/CO_2 ratio, experimental data points evolve more towards the minimum case which corresponds with the H_2/CO_2 input values for the cases. More detailed investigations are only possible in a more controlled environment, which cannot be achieved during operation with real biogas. The kinetics used in the model were derived from experiments where CO methanation was investigated and at operational conditions far away from this work (H_2/CO = 5 to 6, p = 1 barg) [155]. Nevertheless, experimental data are in good agreement with the rate-based model presuming that the water-gas-shift reaction and CO methanation allow to describe CO_2 methanation. The optimal temperature was identified to be between 340 °C and 350 °C for the given range of operating conditions both from experimental and simulation results.

After 430 regular operating hours, the optimal temperature was readjusted from 340 °C to 355 °C in order to obtain again a higher conversion rate. Here, the effect of deactivation on the optimal temperature could be observed. This effect is described in Figure 5.15 via simulation results from the rate-based model and the equilibrium model. Here, dry concentrations of methane after the reactor are shown as a function of the temperature for a standard case (H_2/CO_2 = 4.0, H_2O/CO_2 = 0.5), a deactivated standard case, and a case with no steam addition (H_2/CO_2 = 4.0, H_2O/CO_2 = 0). The case with partly deactivated catalyst shows a reduction in activity in comparison to the standard case, so that only at higher temperatures the kinetics reach the thermodynamic limit where the optimum is. It also shows, why the yield reduction illustrated in Figure 5.6 is more pronounced at 320 °C than at 350 °C. The concentration difference between the standard case and the deactivated case becomes less with increasing temperatures until both cases reach the thermodynamic equilibrium. For the case of no steam addition,

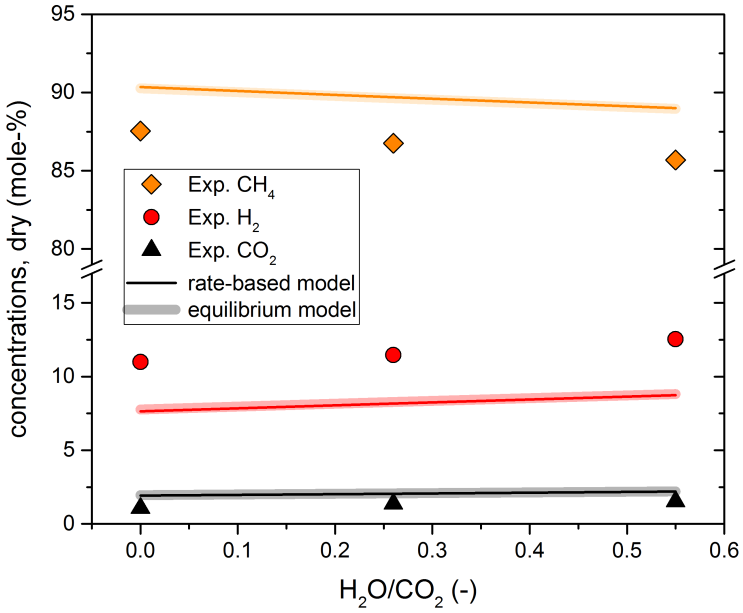

Figure 5.16: Dry molar fractions of bulk components after the reactor as a function of the water addition, experimentally obtained (last 200 regular operating hours) and simulated with the rate-based model and the equilibrium model

a new equilibrium is established above the standard case. As a result, a lower optimal temperature is achieved and a higher maximum methane concentration.

During the last phase of regular operation, the steam addition was stepwise reduced from $H_2O/CO_2 = 0.5$ until zero. In Figure 5.16, the dry bulk concentrations after the reactor are illustrated as a function of the H_2O/CO_2 ratio at the inlet via experimental data points and again the rate-based and the equilibrium model. The lack of steam addition results in higher methane contents as consequence of a more beneficial equilibrium. The equilibrium model shows the same result as the rate-based model. This means that the reaction was limited neither by mass transfer nor by insufficient catalyst activity due to low temperatures and could reach the maximum conversion rate, which is then only restricted by thermodynamics. The experimental results are consequently below the model results, which can be explained by the deactivation of the catalyst over time. However, the gradient of the methane concentrations are approximately the same for the model and experimental results.

5.5 Conclusions

The direct methanation of biogas was tested with a set-up operating on-site with real biogas from a biogas plant in Zurich. The methanation reactor used was a bubbling fluidised bed, which is supposed to be less sensitive towards deactivation due to carbon depositions than a fixed bed reactor. A stable operation of over 1100 hours could be demonstrated with an average yield of 96 % and average bulk concentrations of 88 vol-% CH_4, 11 vol-% H_2 and 1 vol-% CO_2 in the product gas, which is close to equilibrium. The obtained product gas quality is in accordance with the model predictions done in this work. However, for an unrestricted injection into the gas grid, the remaining hydrogen in the product gas must be separated in a next step, which can be done via a gas separation membrane or a second methanation reactor (see chapter 3). Optimised operating conditions for the COSYMA set-up could be found to be supported by model simulations. During the last 100 operating hours, a stress test was carried out with the stepwise reduction of steam addition. Additional steam is supposed to protect the catalyst from coking in order to inhibit deactivation processes. Even without any steam addition during 50 hours, no significant carbon depositions were found on the catalyst surface.

Deactivation processes could be monitored via reference experiments and catalyst samples taken frequently over the operating time. The main source for deactivation of the catalyst were sulphur compounds, which broke through the gas cleaning unit and entered the reactor with concentrations between 0.5 and 3 ppm. A direct relation could be shown between breakthrough concentrations of total sulphur, the relative mass of sulphur from the catalyst samples (TPO method) and the progression of the decreasing yield during reference experiments. It turned out that approximately 1 ppm of sulphur in the feed stream to the reactor results in a yield reduction of 1 % per 100 operation hours. Carbon depositions contributed to the deactivation processes only marginally.

Two different methanation models were compared with experimental data from the COSYMA set-up. Here, the main target was the verification of the applied kinetics in the rate based model. A comparison with results from a simple equilibrium model was consistent regarding conditions in the reactor where equilibrium can be reached. Also predictions from the rate-based model in regions which are kinetically limited are in accordance with experimental data within the accuracy of the experiment. In addition, the rate based model could reflect the consequences of changing fluidisation in the reactor.

In summary, the demonstration of the direct methanation of real biogas in a long-term experiment was successful. Product concentrations close to equilibrium were reached.

With an appropriately adjusted gas cleaning unit, the deactivation of the catalyst is minor, which would allow an exchange of the whole catalyst material only once per year. The attrition rates of the catalyst particles due to fluidisation were small, so that in total only 70 g of the catalyst material was lost in the particle filter [149]. All three aspects are beneficial not only for the operation but also for economic reasons.

6 Investigations of Gas Separation Membrane Properties for Technical Applications[1]

6.1 Introduction

Purification processes in chemical industry are one major part of the whole production routes. Unfortunately, they are mostly thermal processes like distillation and with that they are energy intensive to a large extent. Half of the energy consumption from the industrial sector in the USA accounts for purification processes [156] and on a global view they consume 10–15 % of the world's energy consumption [157, 158]. Other purification technologies, which are non-thermal and instead separate molecules by their chemical properties or by their size like membrane units could be an interesting alternative to conventional separation technologies in order to save energy and reduce the carbon footprint. In literature, it is stated that membrane based processes would use 90% less energy than distillation [156]. However, the materials of a membrane unit have to be exchanged frequently over its lifetime and some membranes contain metal ions such as Co^{2+}, Ni^{2+}, Cu^{2+}, Zn^{2+}, Cd^{2+}, and Pb^{2+} [159, 160], which can be problematic in terms of metal production and their disposal as waste. Additionally, the costs of membrane based separation technologies must be competitive to the thermal technologies, which at large scale is a challange until today [156]. Evaluations of advantages regarding membrane technologies must be executed under a holistic view containing techno-economic analysis as well as life cycle assessments [161, 162].

In this work, the focus is put on polymeric gas separation membranes, which have reached industrial maturity over the last decades. They are commercially applied for air separation, carbon dioxide removal from natural gas or removing hydrogen from nitrogen or hydrocarbons [163]. Those membrane types are applicable for the separation of hydrogen from methane and carbon dioxide after a direct methanation of biogas or

[1] This chapter is based on the following publication: J. Witte, A. Gantenbein, S.M.A. Biollaz, T.J. Schildhauer. "Investigation of Gas Separation Membrane Properties for Technical Applications ". in preparation. Julia Witte prepared the specification of operation conditions for the experiments and contributed to the operation of experiments. She performed the data evaluation and the comparison of experimental and model results, created all diagrams and wrote the text.

of pure carbon dioxide. The membrane separation properties can be described by the permeability and the selectivity. Ideally, membranes have both high permeability rates and high selectivities. However, there is a general restriction observed so that a trade-off exists between the two properties [90]: more permeable membranes are less selective and vice versa. High permeation rates result in a smaller required membrane area for the separation, and high selectivities result in higher degrees of purities in the permeate. Previous investigations (chapter 4) have shown that the most beneficial membrane properties for the given separation task are a combination of high permeability rates and medium selectivities (see chapter 4). Those membranes still reach the required product gas quality (selectivity) and are economically more feasible due to the smaller size of membrane area required (permeability).

There are several approaches of modelling whole gas membrane modules [53, 124, 164–166] in co-current and counter-current operation either based on diffusion by Fick's Law [164–166] or on resistance by Ohm's Law [53]. In both cases, permeability factors are used and set constant for each gas component. However, permeabilities strongly depend on the pressure, the temperature and the multi-component gas mixture in the membrane $C_i = f(x_i, \Delta p, T)$. In literature which concentrates on transport processes in the membrane, there are several approaches of calculating permeabilities depending on pressure and concentrations. Most prevalent is the 'dual-mode sorption, partial immobilisation model [167]. Here, the permeability C_i is separated into two steps: first solubility, second diffusivity. Like gas dissolution in liquids, the permeating gases dissolve first on the polymer surface and then diffuse across the membrane driven by partial pressure differences between the high and low pressure side of the membrane. The 'dual-mode' model first was proposed by Barrer [168] and has been modified by many others inter alia of [169–171] for single component permeation. Later the model was extended to multi-component gas mixtures by [172].

The aim of this chapter is the experimental investigation of the technical performance of a commercially available membrane module using fibres produced by *Evonik AG*. For this, the separation performance of hydrogen and carbon dioxide from methane is tested corresponding to the post-upgrade after a methanation reactor like presented in chapter 3 and chapter 4. In addition, the behaviour of the specific permeability is investigated regarding pressure changes and different concentrations in the feed of the gas components methane, hydrogen, carbon dioxide and nitrogen. In a last step, the permeability is described mathematically with which the proposed membrane model from chapter 3 is evaluated.

6.2 Methods

The investigations of the gas separation membrane are conducted from the perspective of carbon dioxide methanation and necessary post-upgrading for reaching high contents of methane after the membrane unit (see gas grid requirements in table 3.1). The methanation of carbon dioxide is similar to the direct methanation of biogas which is discussed in chapter 3. For some experiments, the feed stream to the membrane module was a gas mixture which was passing upstream a methanation reactor (bubbling fluidised bed), where carbon dioxide reacted together with hydrogen to methane and water (see equation 3.1 and 3.2). Upgrading of methanation gas from carbon dixode is more challenging than from biogas, since the methanation gas is not diluted by methane from the biogas. These experiments were conducted to show the technical feasibility of a membrane separation as post-upgrade unit for CO_2 methanation so that general gas grid requirements for Germany or Switzerland can be reached [21, 100]. In other experiments, the reactor in the methanation unit contained no catalyst material, so that the gases can pass the reactor without reaction.

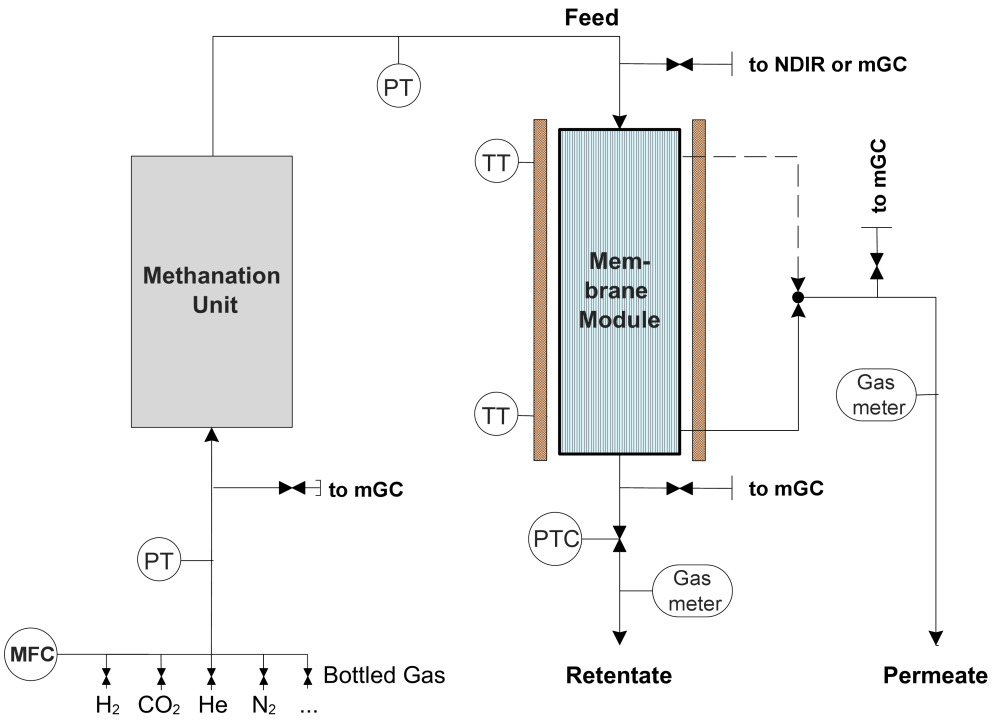

Figure 6.1: Flowsheet of the experimental set-up for the gas separation membrane

6.2.1 Set-Up and Experiments

The experimental set-up *COSYMA* is illustrated in Figure 6.1. The bottled gas flows enter first the methanation unit described in chapter 5. Here for the experiments with prior methanation, catalyst was present inside the methanation reactor so that carbon dioxide and hydrogen was converted to methane and water. For the other experiments, the inlet gases pass the empty reactor without reacting and enter the membrane module unchanged. The inlet gases were adjusted via volume flows (mass flow controllers, MFC) and controlled via concentration (micro gas chromatography, mGC), pressures and temperature measurements. After the methanation unit, the gases are pre-heated and enter the membrane module on the tube side (inside the fibres). The gases which do not permeate leave the membrane module on the retentate side. This side is assigned to contain the product stream in case of biogas methanation. On the shell side, two connections are installed which allows to operate the membrane module either in co-current or counter-current flow. The shell side contains the permeate, which is supposed to be recycled back to the methanation reactor as discussed in chapter 3 where whole processes are assessed. The inlet and outlet flows of the membrane module are monitored regarding their concentrations (mGC or NDIR), volume flows (gas meters), pressure and temperature. In addition, the temperature of the membrane is controlled via a water bath. This is necessary, since the performance of the membrane clearly depends on the temperature. The pressure in the system p is monitored and controlled at the retentate side of the membrane. The permeate is released at ambient pressure p_0. Due to the

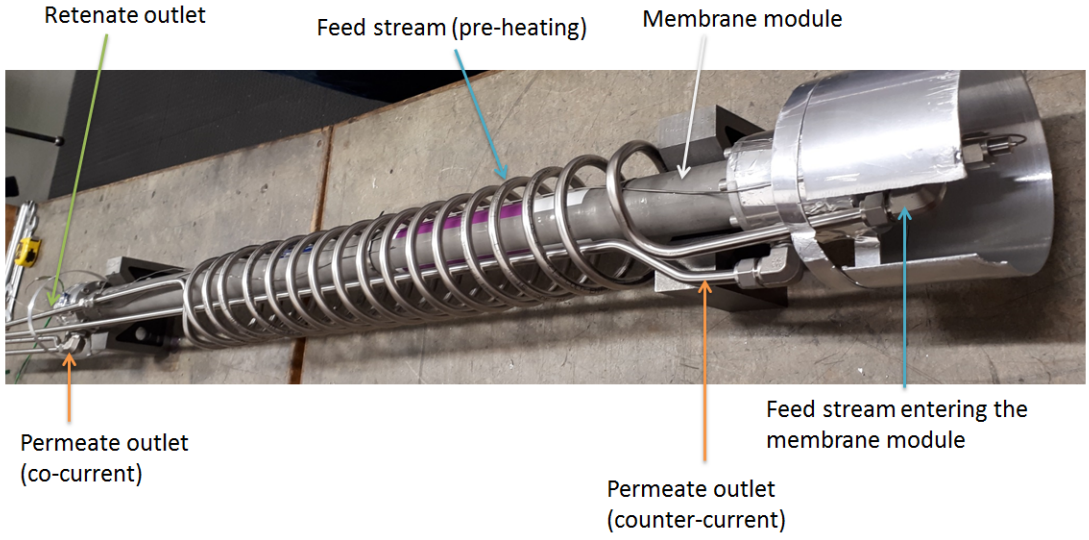

Figure 6.2: Adapted membrane module from *Evonik* used for experiments

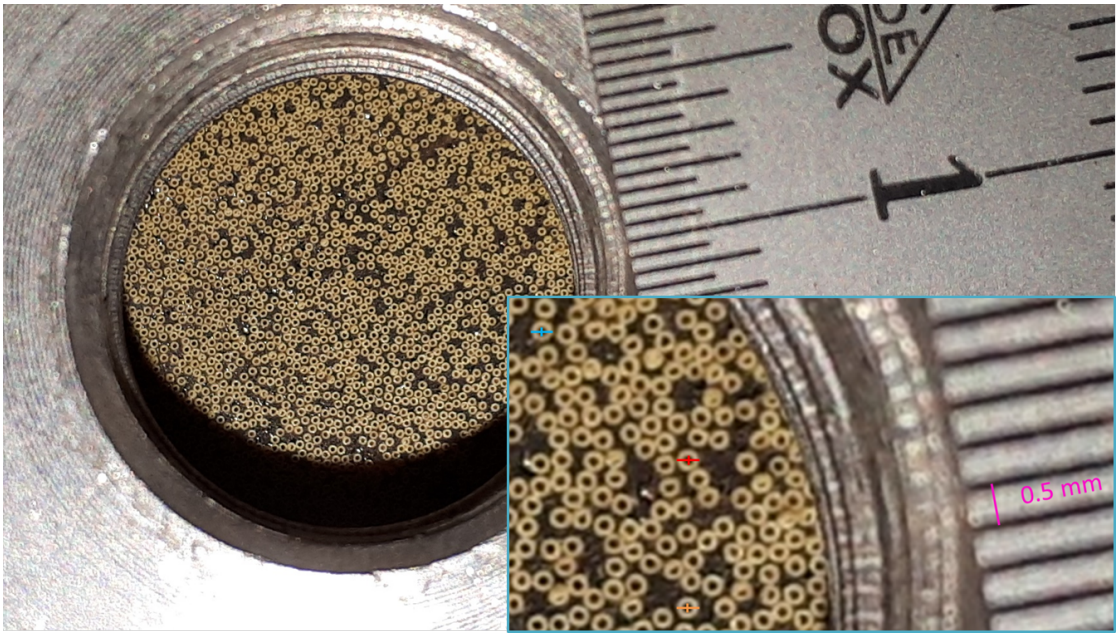

Figure 6.3: View on hollow fibres from the membrane module (*Evonik*)

multiple measurements on several points in the set-up, mass balances of the components could be validated.

The adapted membrane module with fibres from *Evonik AG* used for the experiments is shown in Figure 6.2. Here, the gas pipe of the feed stream is a helical coil around the outer vessel of the module. Since the whole module is placed in a heating bath, the coil serves as heat exchanger for pre-heating the gas feed. Three outlet pipes are present, from which one outlet is for the retentate and two outlets are for the permeate (co-current pipe and counter-current pipe). The whole vessel where the separation takes place has a length of 1.18 m and and a diameter of 4.3 cm. More information regarding the size of the module can be found in in Table 6.1. In Figure 6.3, the hollow fibres from a top view into the module are illustrated. In order to determine the membrane area, the number of hollow fibres has to be determined. For this, the arrangement of the fibres are assumed to be in a hexagonal circle packing, which has in general the smallest void fraction of circle packings for uniform diameters [173]. In the picture of Figure 6.3, the fibres at the end of the vessel are already spread more open, which does not correspond to a hexagonal circle packing. However, inside the vessel where the separation takes place, the fibres are hold together closely so that the packing is at maximum density. The void fraction η of a circle packing with uniform diameters is defined as follows:

$$\eta = \frac{A_{circles}}{A_{circles} + A_{void,tot}} = \frac{\pi}{2\sqrt{3}} \quad \text{for } N_{circle} \gg 1 \tag{6.1}$$

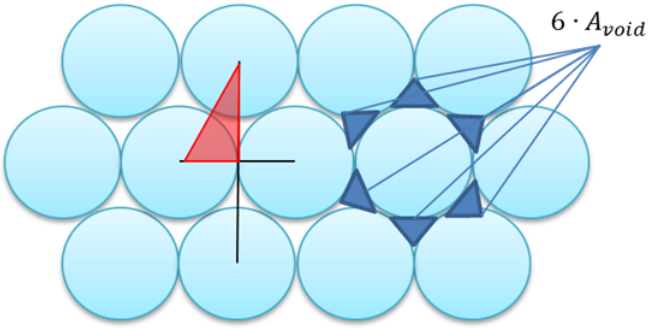

Figure 6.4: Scheme of a hexagonal circle packing with uniform diameters and void fractions

In Figure 6.4, the hexagonal packing with corresponding void fractions is illustrated. This void fraction is valid for an infinite number of circles, which assumes that no border is present which would change the relation of circles to the surrounding void areas A_{void}. Hence, for a valid assumption the number of circles must be considerably larger than one. Since the number of circles correspond to the number of fibres in the membrane module, the requirement of a large number is fulfilled. With the void fraction, the numbers of fibres N_{fiber} and the memberane area A_{mem} can be determined:

$$N_{fiber} = \eta \frac{D_{vessel}^2}{D_{fiber}^2} \tag{6.2}$$

$$A_{mem} = N_{fiber}\ \pi\ d_{fiber}\ L_{vessel} \tag{6.3}$$

The complete informations about the dimensions of the membrane can be found in Table 6.1.

For the experiments without reaction, the components methane, hydrogen, nitrogen and carbon dioxide are investigated. First, the pure components are evaluated regarding their permeability properties as a function of the pressure (pressure range: 2 - 10 bara).

parameter	**name**	**unit**	**value**
length of vessel	L_{vessel}	cm	118.0
diameter of vessel	D_{vessel}	cm	4.31
outer diameter of fibre	D_{fiber}	mm	0.27
average diameter of fibre	d_{fiber}	mm	0.19
number of fibres	N_{fiber}	-	23 109
membrane area	A_{mem}	m^2	16.28

Table 6.1: Dimensions of the membrane module

Second, experiments for binary mixtures are carried out for concentrations of 3 %, 6 %, 12 % and 30 % of the component hydrogen, nitrogen and carbon dioxide in methane. For every binary gas mixture, the pressure was varied in steps from 4 bara over 7 bara to 10 bara. The membrane module was switched between co-current and counter-current flow for all mentioned measurements points. With this procedure, the influence of the pressure, the inlet concentrations and the flow conditions on the permeability can be investigated.

In addition, experiments were carried out with carbon dioxide and hydrogen, which were first directed into the methanation unit in a H_2/CO_2 ratio, which is slightly hyper-stoichiometric. Here, the reaction of carbon dioxide to methane took place. The outlet gases of the reactor passed first a condenser to remove the largest part of the water produced during reaction. Then the gas mixture entered the membrane module, where hydrogen is supposed to be separated from the produced methane. The experiments were carried out for different pressures between 3 and 7 bara and for co-current and counter-current operation.

The volume flow through the membrane is driven by the partial pressure differences of the components i between the membrane sides and can be described by Fick's law with the corresponding SI units (SI units for 1 Barrer are given in equation 2.18):

$$\dot{V}_i = A_{mem} \cdot \frac{C_i}{s} \cdot \Delta p_i \tag{6.4}$$

$$\frac{Nm^3}{s} = m^2 \cdot \frac{Nm^3\ m}{s\ m^2\ bar \cdot m} \cdot bar \tag{6.5}$$

The term $\frac{C_i}{s}$ represents the permeability C of component i divided by the effective membrane thickness s. The effective thickness is only the part of the membrane layers, which represents a resistance to the permeating components. Since their are no accurate data about the effective thickness, the combined term $\frac{C_i}{s}$ will be determined in experiments and is called specific permeability or permeance. Fick's Law shows similarities to the well known heat transfer equation:

$$\dot{Q} = A_{HX} \cdot U \cdot \Delta T_{ln} \tag{6.6}$$

where ΔT_{ln} is the logarithmic temperature difference. Similar to ΔT_{ln} the partial pressure difference in Equation 6.4 can be determined with the same approach [124] by

an integral over the membrane length:

$$\Delta p_{i,ln} = \frac{\Delta p_{i,max} - \Delta p_{i,min}}{ln\left(\frac{\Delta p_{i,max}}{\Delta p_{i,min}}\right)} \tag{6.7}$$

Here, the maximum and minimum partial pressure differences refer to the differences between the permeate and retentate side of the membrane. Using the logarithmic partial pressure difference together with Equation 6.4, the specific permeability can be determined via experiment with the measured data from the in- and outlet flows of the membrane.

6.2.2 Model of Gas Separation Membrane

The model for the gas permeation $\dot{n}$ through the membrane is described into detail in section 3.3.2. A general expression of the model for the components i is given by:

$$\frac{d\dot{n}}{dA_{mem}} = \sum_i \frac{C_i}{V_m s} \cdot (x_{i,ret}\ p_{ret} - x_{i,per}\ p_{per}) \tag{6.8}$$

$$\frac{mol}{s \cdot m^2} = \frac{Nm^3\ m}{s\ m^2\ bar} \cdot \frac{1}{m} \cdot \frac{mol}{Nm^3} \cdot\ bar \tag{6.9}$$

for i = H_2, CO_2, CH_4 and N_2.
The overall material balances are given by:

$$\dot{n}_{feed} = \dot{n}_{per} + \dot{n}_{ret} \tag{6.10}$$

$$x_i\ \dot{n}_{feed} = x_i\ \dot{n}_{per} + x_i\ \dot{n}_{ret} \tag{6.11}$$

The pressure drop on the retentate and permeate side was neglected. The permeability C_i is described by the mechanisms of solubility S_i and diffusivity D_i of the component i.

$$C_i = S_i \cdot D_i \tag{6.12}$$

Driven by partial pressure differences between the high and low pressure sides of a membrane, the gas components first dissolve (S_i) on the surface of the membrane at the high pressure side. Second, the gas components diffuse (D_i) across the membrane to the low pressure side and desorb from the membrane surface into the gas phase. The diffusion can be described by an Arrhenius type approach [174]

$$D_i = D_{i,0}\ exp\left(-\frac{E_{A,D_i}}{RT}\right) \tag{6.13}$$

where the temperature-driven diffusion process is characterized by the activation energy E_{A,D_i} and a pre-exponential factor $D_{i,0}$. The gas sorption is basically described by Henry's Law (H_i), but needs to be extended with a Langmuir adsorption term (L_{cap}-capacity factor and B affinity factor) [171] which has the form of:

$$S_i = H_i \cdot p + \frac{L_{cap,i} \cdot B_i \cdot p}{1 + B_i \cdot p} \tag{6.14}$$

for a sinlge mixture and

$$S_i = H_i \cdot p_i + \frac{L_{cap,i} \cdot B_i \cdot p_i}{1 + \sum_{i=1}^{n} B_i \cdot p_i} \tag{6.15}$$

for a n multi-component mixture [172]. In a gas mixture, the different components compete with each other in terms of solution and diffusion. This results in decreasing permeabilities and selectivities for each component [172]. Various attempts have been made to model permeabilities as a function of feed pressure [168–171] and concentrations [172, 175]. However, a large number of coefficients for each component-permeability has to be fitted with experimental data in these approaches. In order to simplify the approach, the permeability C in this chapter is described in a polynomial form including corresponding parameters K_{ab}:

$$C(x,p) = \begin{pmatrix} 1 & p \end{pmatrix} \begin{pmatrix} K_{11} & K_{12} & K_{13} \\ K_{21} & K_{22} & K_{23} \end{pmatrix} \begin{pmatrix} 1 \\ x \\ x^2 \end{pmatrix}$$

The parameters K_{ab} are fitted for every component i. This approach is similar to the method used in [175], where permeabilities are described via the fugacity of the gases and individual parameters. In this case, ideal gas behaviour is assumed so that the fugacity reduces to partial pressures, which are again dependent on mole fractions and total pressure like in the present approach. Neglecting real behaviour of the gases is valid in this case, since for the investigated application, only moderate pressures are present (up to 10 bara), which are in the most cases clearly below critical pressures of the components and result in activity coefficients close to one (ideal gas) [176]. However, for higher pressures, the application of partial fugacities instead of partial pressures is recommended [172].

6.3 Results and Discussion

6.3.1 Performance of the Gas Separation Membrane as Upgrade Unit after CO_2 Methanation

In this section, the experiments include CO_2 methanation with a hydrogen addition to the reactor at $H_2/CO_2 \approx 4.2$. Subsequently, the product gas stream entered the membrane module for the separation of non-reacted hydrogen and carbon dioxide from methane. The focus here is put on the influence of different operation modes on the membrane performance in case of CO_2 methanation. The operation conditions investigated for the membrane module include varying temperatures, pressures, as well as co-current and counter-current operation. The purification of methanation gas from biogas is less demanding, since the inlet flow to the reactor is already diluted with methane so that hydrogen and carbon dioxide concentrations in the outlet flow is lower.

The methantion reactor needs specific volume flows for every investigated reactor pressure to reach appropriate fluidisation states (see chapter 3), therefore the choice of the total volume flow to the membrane module was restricted. The given total volume flow by the reactor appeared to be too small for the membrane module so that only for small pressure differences between permeate and retentate side, evaluations were possible. In figure 6.5, the standard volume flows of the reactants hydrogen and carbon dioxide and the product methane are illustrated as a function of the membrane temperature. The feed pressure of the membrane is 2.15 barg and the permeate pressure is atmospheric. The conversion of carbon dioxide to methane was 96.7 % and resulted in a membrane-inlet concentration of 79.3 vol-% CH_4, 2.7 vol-% CO_2, 18 vol-% H_2. The membrane operates in counter-current mode. The influence of the temperature is significant as the total permeation flow almost doubles between 15 °C and 45 °C. With increasing temperatures, the diffusion coefficient D_i increases (equation 6.13) [168] as does the permeability factor (see equation 6.12), since the solubility coefficient is supposed to stay constant for changing temperatures (see equation 6.2.2). The shares of components in the permeate and retentate are also influenced by the temperature. The methane concentration in the retentate increases with the temperatures due to enhanced permeation of all components. However in the permeate, the methane concentration increases also. At 15 °C, the permeating volume flows of methane and hydrogen are about equal. At 45 °C the shares of methane and hydrogen in the permeate shift towards two thirds and one third. Due to the larger permeation rates, it is likely that the membrane behaves less selective at higher temperatures, which is the case for the selectivity of hydrogen to nitrogen in literature [175]. Nitrogen and methane have similar properties regarding their permeabilities and are comparable in this case. The changing behaviour of the membrane for different temperatures is expressed within the permeability factor. How-

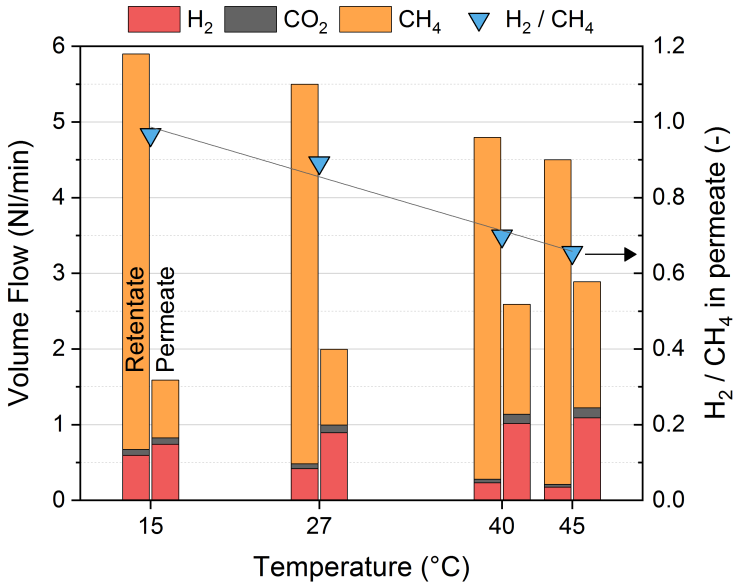

Figure 6.5: Standard volume flows of bulk components in the retentate and permeate and the ratio of hydrogen to methane in the permeate as a function of the temperature with a feed stream from the CO_2 methanation unit: $p_{feed,mem}$ = 2.15 barg $V_{feed,mem}$= 7.45 Nl/min with 79.3 vol-% CH_4, 2.7 vol-% CO_2, 18 vol-% H_2, counter-current

ever, this effect is not considered in various membrane unit models in literature [53, 124, 164–166]. Considering the whole process of the CO_2 methanation including the membrane, the retentate flow is the product flow and the permeate flow is assigned to be a recycle flow directed back to the methanation reactor so that the reactants and the product methane are not lost. Increasing the temperature of the membrane helps to purify the retentate flow, on the other hand it produces a large recycle flow with a significant share of methane. This recycle must be compressed again before it enters the reactor, therefore a large recycle flow enlarges the whole process and particularly results in increased compression and reactor costs.

The low feed pressure of 2.15 barg in figure 6.5 prevents further separation of hydrogen so that at 45 °C still a hydrogen concentration of about 4 vol-% in the retentate is present. In the following, the effect of the membrane feed pressure to the separation performance is discussed. In figure 6.6 and 6.7, the influence of the feed pressure on the membrane performance is illustrated. Here, no prior methanation was done, so that the feed volume flow could be chosen appropriate to the membrane size and pressure. No carbon dioxide was added to the feed, since the separation task in general corresponds to the separation of hydrogen from methane due to the low carbon dioxide contents after the methanation. In the diagrams, the standard volume flows of methane and hydrogen

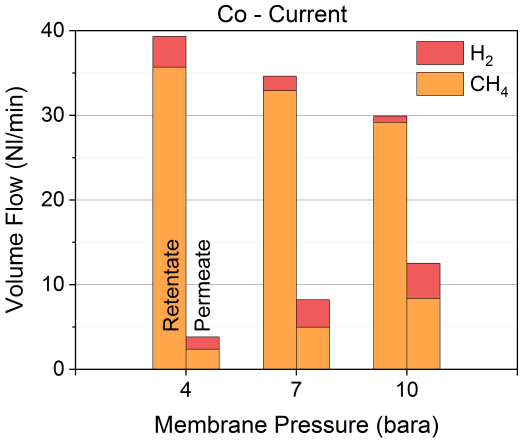

Figure 6.6: Standard volume flows of methane and hydrogen in the retentate and permeate as a function of the feed pressure; operation mode: co-current; feed flow: 37 Nl/min methane, 5 Nl/min hydrogen

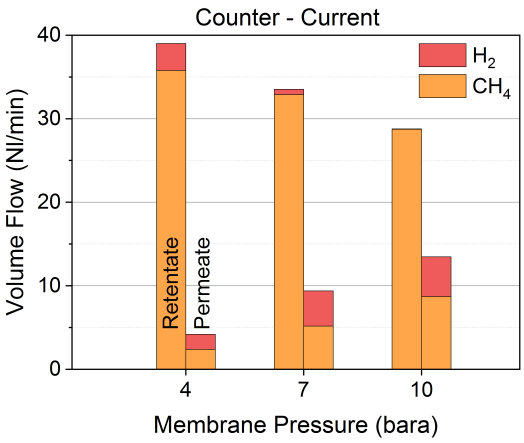

Figure 6.7: Standard volume flows of methane and hydrogen in the retentate and permeate as a function of the feed pressure; operation mode: counter-current; feed flow: 37 Nl/min methane, 5 Nl/min hydrogen

in the retentate and permeate are shown for co-current (figure 6.6) and counter-current (figure 6.7) operation as a function of the feed pressure. Like for the temperature, the permeation flow through the membrane increases with the feed pressure for both operation modes (co-/ and counter-current), inter-alia, due to the increasing partial pressure differences. Both operation modes reach in the retentate a hydrogen fraction smaller than 2 vol-% at sufficiently high pressures, which is required for an unrestricted injection into the gas grid. However, the counter-current mode is more beneficial for the given separation task, since additionally to the 2 % limit of hydrogen in the retentate, the concentration of methane in the recycle is lower which results in a smaller recycle flow and with that in a leaner process with lower costs. Hence, the counter-current mode and increased pressure result in a beneficial combination for the upgrade to SNG after a methanation unit, so that gas grid requirements can be fulfilled. The favourable influence of the pressure becomes clearer with the illustration of the volume flows as a function of the membrane area as it is shown in figure 6.8 with the results from a simulation using the membrane model presented in section 3.3.2 and 6.2.2. Here, the permeate and retentate side is illustrated for the components hydrogen and methane for 10 bara and 20 bara feed pressure (permeate pressure is atmospheric). The course of the methane flows is linear on the permeate and retentate side, whereas the hydrogen flows first strongly increase due to the significant higher permeability of hydrogen in comparison to methane until the hydrogen reaches a partial pressure equilibrium between permeate and retentate side. Then the hydrogen flow increases only slightly. At this point, the hydrogen transport through the membrane is driven by the dilution of the permeate

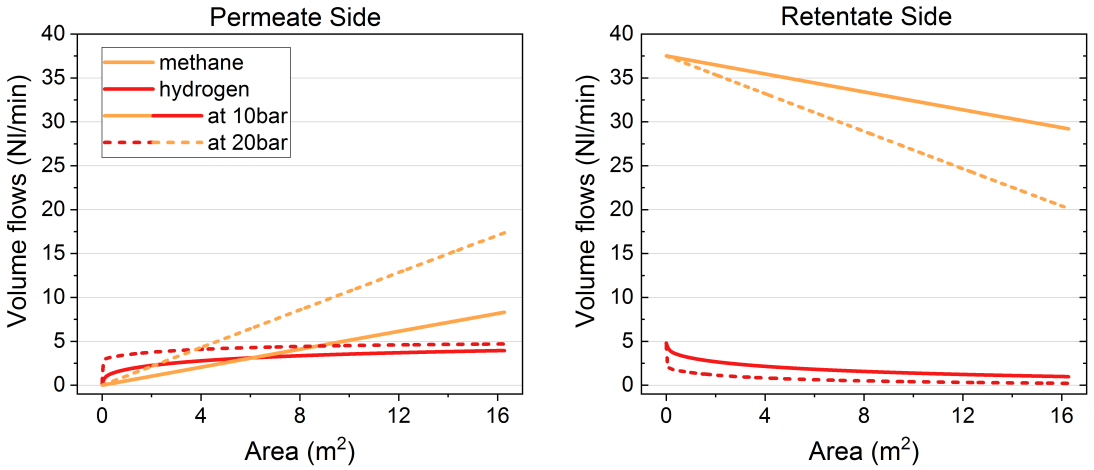

Figure 6.8: Simulated course of the methane and hydrogen flows as a function of the membrane area for different pressures; feed flows: 37.5 Nl/min methane, 4.9 Nl/min hydrogen

with methane which is permeating constantly through the membrane. In this region, an increasing membrane area results in higher methane concentrations in the permeate (recycle), which is not favourable. Therefore, the size of the membrane area should be chosen in way that the partial pressure of hydrogen just reaches equilibrium. In the case of 20 bara, the area should not be bigger than 1 m^2. In order to reach the specified purification target with the restricted area size, the total pressure difference must be adapted. This procedure results in smaller recycle flows with a high hydrogen content for increased pressures. However, for a final statement which operation conditions are optimal, also economic considerations must be taken into account as discussed in chapter 4.

6.3.2 Permeabilities of Pure Gases and Binary Mixtures

In this section, results without prior reaction in the methanation unit are presented. The specific permeability $C_{i,spec}$ of each component is determined from experimental data obtained from membrane experiments in counter-current operation with:

$$C_{i,spec} = \frac{C_i}{s} = \frac{V_i}{A\ \Delta p_{i,ln}} \tag{6.16}$$

corresponding to equation 6.4. The effective thickness s of the investigated membrane is unknown, therefore only specific permeability rates are considered.

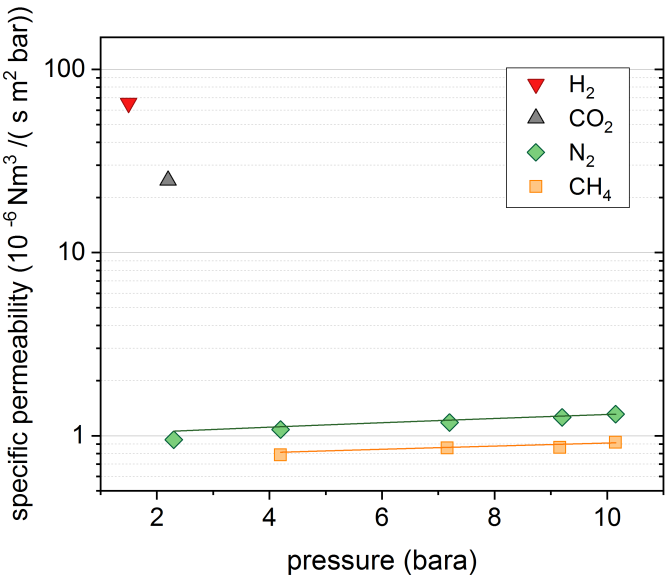

Figure 6.9: Specific permeability of pure components as a function of the pressure

Pure gases

In figure 6.9, the specific permeability factors are illustrated as a function of the feed pressure for the pure components hydrogen, carbon dioxide nitrogen and methane. Hydrogen shows the highest specific permeability followed by carbon dioxide. These components are highly permeable and are referred to as penetrants. Nitrogen and methane have small specific permeability rates, hence they are likely to stay in the retentate. This permeability-sequence of the mentioned components is typical for commercially available polymer-based membranes [58]. For hydrogen and carbon dioxide, it was not possible to reach increased pressures on the retentate side. The permeation flow of these components through the membrane was correspondingly high so that the pressure on the retentate side could not be further elevated. Significantly higher feed volume flows would allow higher pressures for high permeable components. However, with the present set-up, those volume flows were not possible. For methane and nitrogen, a small increase of the specific permeability with the pressure is discernible. The gradient is constant and similar for both components. Hence, the selectivity of methane against nitrogen is not changing with the pressure. No differences for the specific permeability regarding changing volume flows (20 and 30 Nl/min) have been identified for methane and nitrogen. It is likely, that the specific permeability rates for pure hydrogen and carbon dioxide increase more strongly with the pressure than for pure methane and nitrogen like it is the case for the binary mixtures discussed in the next section.

	Evonik	Matrimid®	PSF[2]	CA-2.45[3]	PPO[4]
H_2/CO_2	2.6	2.4	2.5	2.5	1.0
H_2/CH_4	89.8	83.3	56.0	80.0	14.2
H_2/N_2	68.8	79.5	56.0	80.0	14.9
literature	this work	[126]	[177]	[178]	[179]

Table 6.2: Ideal selectivity data for different polymeric membranes, at operation conditions between 1 and 4 bar and 35 °C - 40 °C

In order to compare these results with data from literature, ideal selectivities are used. Specific permeability data are rarely found in literature and depend strongly on operation conditions. The selectivity data of this work and from literature can be found in table 6.2 at comparable operation conditions. The selectivity of hydrogen against carbon dioxide is similar for almost all listed membrane types. For the selectivities of hydrogen against methane and nitrogen, the most similar membrane in comparison to this work is the Matrimid membrane followed by the CA-2.45 membrane. The Matrimid membrane shows the same sequence as the *Evonik* membrane from low to highly permeable components in the order of methane, nitrogen carbon dioxide and hydrogen together with similar selectivity values.

Binary Gas Mixtures

All considered binary gas mixtures contain methane as base component and one of the components hydrogen, carbon dioxide or nitrogen as additional component. For each gas mixture, the specific permeability factors are investigated for different feed pressures and for co-current and counter-current flow. The permeability factors for the different components are illustrated in figure 6.10 to 6.13 as a function of the concentration. The permeability factors of all components depend clearly on the pressure and on the concentration of the gas mixture. The permeability is described by the product of sorption and diffusion (equation 6.12). In the presented theory, only the sorption term is pressure dependent and consist of the Henry's law mechanism and the Langmuir sorption mechanism. The permeability factors increase linearly with the pressure. This is an indicator that corresponding to equation 6.2.2, the 'Henry's Law' -term $H_i \cdot p_i$ is dominant for the gas sorption at these operating conditions. Increasing feed pressure has a larger effect on the permeability factors (and with that on the sorption factor) of the highly permeating components hydrogen and carbon dioxide than on the low permeating components nitrogen and methane. Since, the permeability is driven by Henry's Law

[2]Polysulfone
[3]Cellulose acetate (2.45 degree of acetylation)
[4]Poly(2,6-dimethylphenylene oxide)

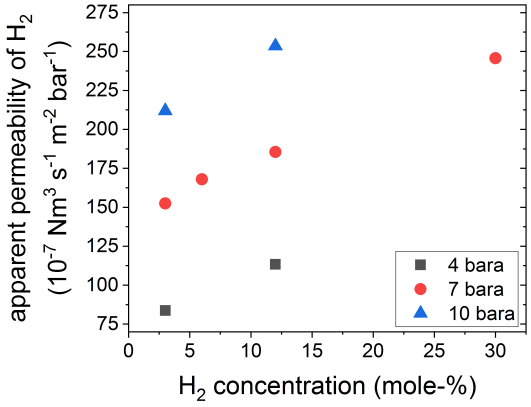

Figure 6.10: Apparent specific permeabilities of hydrogen in a binary mixture with methane for different pressures, T = 40 °C

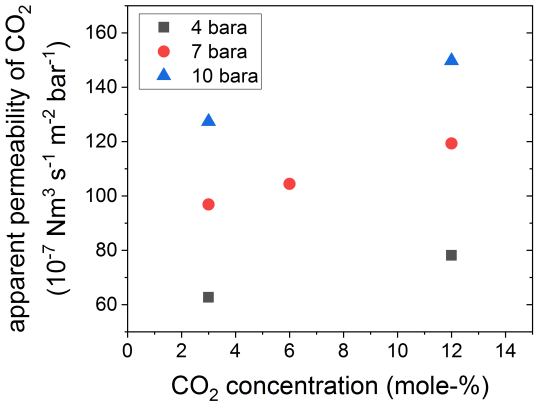

Figure 6.11: Apparent specific permeabilities of CO_2 in a binary mixture with methane for different pressures, T = 40 °C

and the Henry coefficient H_i expresses the affinity of sorption for each component. The pressure effect on the permeability of highly permeating components must be stronger since the corresponding higher Henry coefficient H_i serves as gradient.

For hydrogen and carbon dioxide, the specific permeability is decreasing strongly with their concentrations in methane (figure 6.10 and 6.11). That means, that the separation performance of the membrane becomes worse with high contents of methane in the retentate. The decreased permeabilities can be caused by competitive sorption effects on the membrane surface between the penetrant and methane, as well as interactions between the gas molecule resulting in non-ideal thermodynamics. Competitive sorption reduces the ability of hydrogen and carbon dioxide to pass the membrane which also decreases the selectivity of hydrogen or carbon dioxide against methane. The course of the specific permeability over the corresponding concentrations is linear for low concentrations. However, it is assumed that the gradient may decrease for further increased concentrations above 30 mole-%.

The concentration effect for nitrogen is not as dominant as for the highly permeating components (figure 6.12). The low affinity of nitrogen to pass the membrane has a bigger influence on the transport behaviour than the presence of methane so that the 'blocking' effect of methane is less prevalent. This results only in a very small increase of nitrogen-permeability with decreasing methane concentrations. In figure 6.13, the specific permeability of methane is illustrated as a function of the methane concentration for different additional components and pressures. The permeability of methane in a binatry mixture increases with the pressure as was the case for pure methane. For the permeability of methane, it seems to make no difference, with which additional

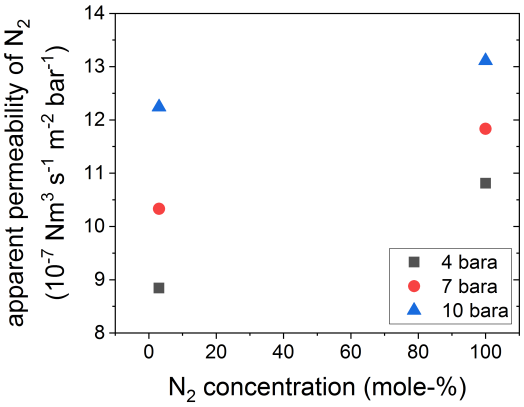

Figure 6.12: Apparent specific permeabilities of nitrogen in a binary mixture with methane and for pure nitrogen for different pressures, T = 40 °C

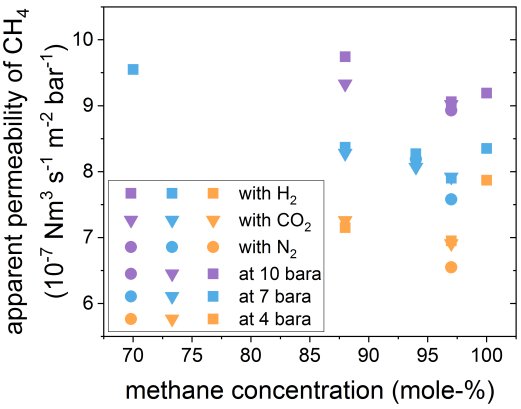

Figure 6.13: Apparent specific permeabilities of methane in a binary mixture with hydrogen or nitrogen and of pure methane for different pressures, T = 40 °C

component methane was mixed. Also, for high methane concentrations above 85 vol-%, the methane-permeability stays about constant and seems to be free from the influence of the additional components. However, below 85 vol-% the permeability of methane is increasing. This can be explained by the influence of a bulk flow [172] caused by an increased concentration of a highly permeating compound (penetrant). Due to the penetrant flow through the membrane, methane is transported more easily with that flow through the membrane. The influence of the bulk flow decreases the selectivity H_2/CH_4 of the membrane further, beside the effects of competitive sorption and non-ideal thermodynamics as discussed earlier.

6.3.3 Model Evaluation

For the model evaluation, the specific permeability is described with the equation:

$$C(x_i, p)_{feed} = K_{11} + K_{12}x_i + K_{13}x_i^2 + K_{21}p + K_{22}px_i + K_{23}px_i^2 \tag{6.17}$$

according to the polynomial form in section 6.2.2. The variables x_i and p are assigned to the feed flow. Hence, the determined permeability factors are an average value over the whole membrane module. The parameters K_{mn} were fitted for every component with experimental data obtained at counter-current operation. With this operation mode, the partial pressures of the components do not reach as fast equilibrium conditions as for the co-current operation which is beneficial for the permeability determination. The specific permeability factors are listed in table 6.3. These parameters are applied to the co-current model. The illustrated surface areas of the calculated specific permeability factors for each component can be found in the appendix (figure A.6 - A.8). In figure

	K_{11}	K_{12}	K_{13}	K_{21}	K_{22}	K_{23}
H_2	-7.072	2.375	-0.006	20.889	0.206	-0.001
CO_2	15.424	1.659	-0.022	10.395	0.128	0.002
CH_4	5.482	0.0	0.0	0.352	0.0	0.0
N_2	6.113	0.026	0.0	0.594	-0.001	0.0

Table 6.3: Fitted parameters K_{mn} for the different components, obtained from experiments in counter-current mode

6.14 - 6.16, the comparison of the model results with experimental data is illustrated for the components hydrogen, carbon dioxide and nitrogen which each are in a binary mixture with methane. In figure 6.14 on the left side, the hydrogen concentration in the permeate and retentate outlet is shown as a function of the feed pressure for different hydrogen inlet concentrations. The lines reflect the modelling results, the markers show experimental results. The hydrogen concentrations in the retentate decrease with the feed pressure due to the larger pressure difference and increased permeation flows through the membrane. The hydrogen concentrations in the permeate show a different course. Here, with increasing pressure, hydrogen concentrations form a maximum, which shifts towards higher pressures for lower hydrogen feed concentrations and which are less pronounced. First, a higher feed pressure results in higher permeation rates of hydrogen, so that the permeate concentration of hydrogen is increasing. However, with further increasing feed pressure, more methane is permeating in comparison to hydrogen, so that the hydrogen concentration on the permeate side decreases again. In this region, the permeation flow of hydrogen is driven by the dilution of the permeate side with methane, as described in section 6.3.1. The experimental results show the same trend like the simulation. For the case of 12 % and 3 % hydrogen concentration in the feed, experimental data allow the verification of the approximate position of the maximum given by the simulation which is about at 7 bara and 9 bara. The shift of the maximum towards higher pressures for lower feed concentrations of hydrogen is caused by the slower permeation of hydrogen due to the lower partial pressure. On the right side of figure 6.14, the specific permeability factors are shown which are applied in the simulation. The specific permeabilities are calculated with equation 6.17 and the corresponding parameters K_{mn} from table 6.3. The permeability factors increase linearly with the pressure but with different gradients due to the non-linear relationship of the permeability factors for increasing concentrations of penetrants mixed with methane.

In figure 6.15, the same model evaluation procedure was applied as for hydrogen (figure 6.14), but in this case with carbon dioxide. Basically, the same trends as for hydrogen can be observed regarding the behaviour of the permeate and retentate concentrations

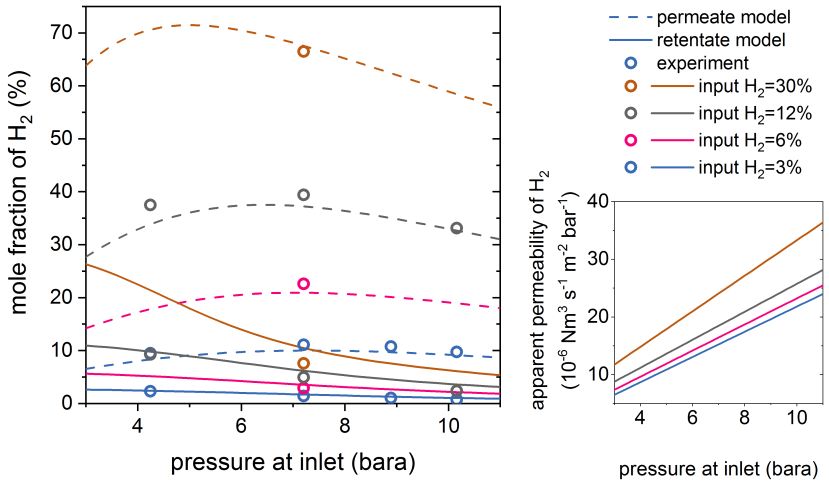

Figure 6.14: (left) hydrogen concentrations of the membrane outlet flows as a function of the feed pressure for different hydrogen feed concentrations diluted in methane ($V_{feed} \approx 42\ Nl/min$); (right) corresponding apparent permeabilities in the simulation calculated with equation 6.17 and parameters from table 6.3

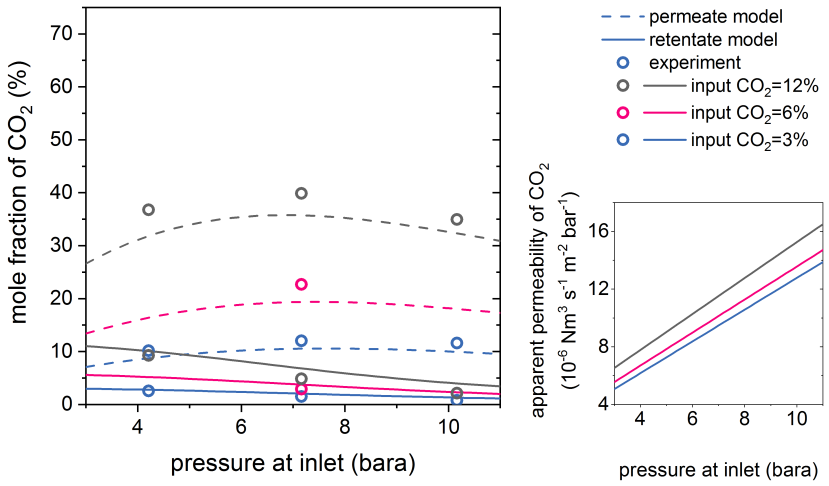

Figure 6.15: (left) carbon dioxide concentrations of the membrane outlet flows as a function of the feed pressure for different carbon dioxide feed concentrations diluted in methane ($V_{feed} \approx 42\ Nl/min$); (right) corresponding apparent permeabilities in the simulation calculated with equation 6.17 and parameters from table 6.3

with increasing pressure. Carbon dioxide concentrations in the retentate are decreasing and in the permeate flow, a maximum is formed. The corresponding specific permeability factors applied in the simulation are illustrated in the right diagram. For carbon

dioxide, the model predictions are not as accurate as for hydrogen. Simulated concentrations can differ from the experimental results up to 4 vol-%-points. In all cases, the permeability is underestimated. As mentioned earlier, the inaccuracies might result from the determination of permeability factors from counter-current mode and applying them to the co-current model, which is then compared to experimental data from co-current operation. However, the general trend of the concentrations in permeate and retentate can be expressed by the model. The simulation results of the less permeable component nitrogen is presented in figure 6.16. In the left diagram again, nitrogen concentrations for the permeate and retentate flow are illustrated as a function of the feed pressure. For nitrogen only inlet concentrations of 3 vol-% and 6 vol-% were evaluated experimentally, since the amount of nitrogen for biogas or carbon dioxide methanation is usually low. The corresponding specific permeability factors calculated of the model are shown in the right diagram. The change of permeability for different nitrogen concentration is very low, hence the graphs of the specific permeability in the right diagram for 3 vol-% and 6 vol-% are similar. Due to the low permeation rates of nitrogen, effects to the nitrogen concentrations in the permeate and retentate with increasing pressure are not as pronounced as for the highly permeable components. In the retentate, the nitrogen concentrations are sightly decreasing and vice versa in the permeate.

Since there are indications that the permeability factors might be different for co-current and counter-current operation, due to the different flow conditions which effects

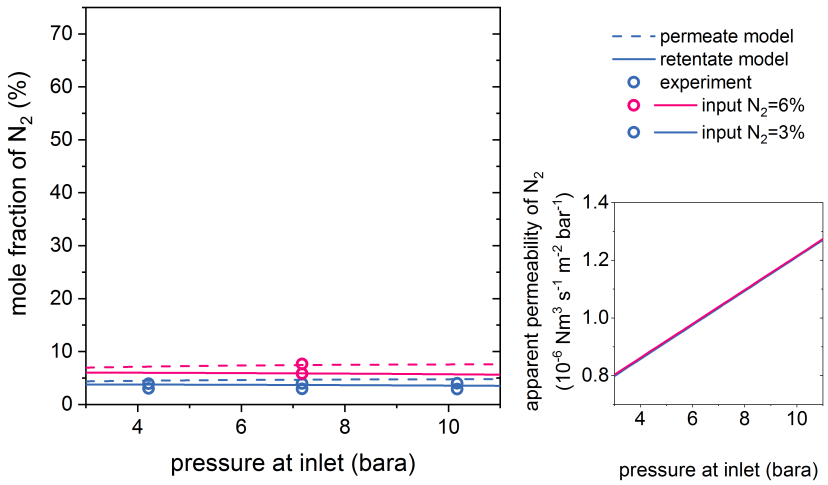

Figure 6.16: (left) nitrogen concentrations of the membrane outlet flows as a function of the feed pressure for different nitrogen feed concentrations diluted in methane ($V_{feed} \approx 42\ Nl/min$); (right) corresponding permeabilities in the simulation calculated with equation 6.17 and parameters from table 6.3

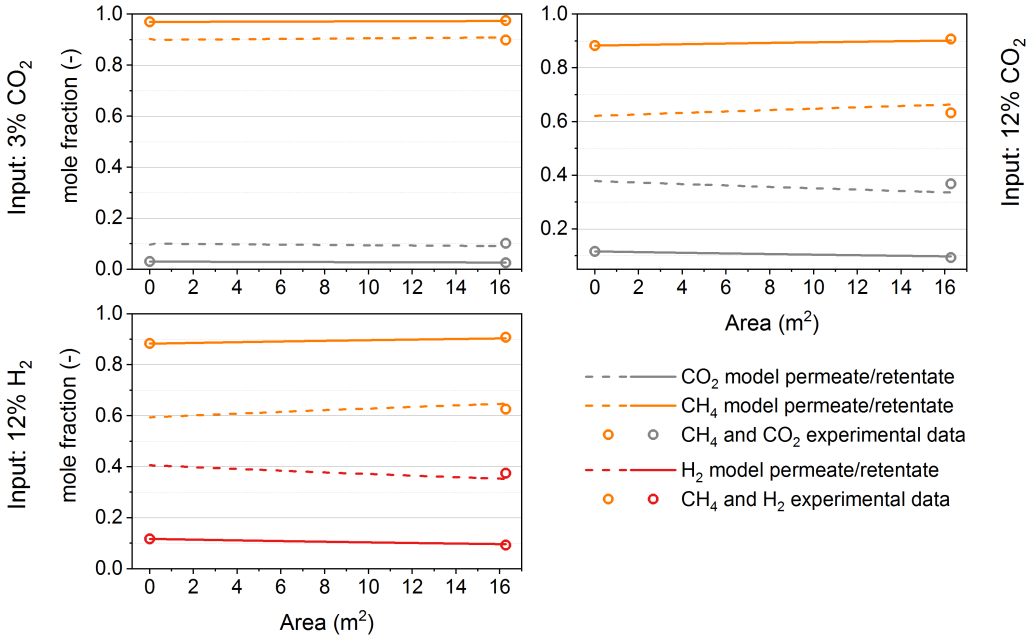

Figure 6.17: Simulated concentrations of bulk components as a function of the membrane area and corresponding experimental data for the inlet and outlet flows at 4.2 bara feed pressure, T=40 °C (co-current mode) for different binary feed concentrations: 3 % CO_2 (top left), 12 % CO_2 (top right) and 12 % H_2 (bottom left) diluted with methane

the mass transport through the membrane, in figure 6.17, simulation results are presented where permeability factors are applied directly from the corresponding experiments in co-current mode (see table 6.4). Hence, in this case permeability factors from co-current experiments are used for the co-current model. In the three diagrams of figure 6.17, the simulated concentrations of carbon dioxide, hydrogen and methane in permeate and retentate are illustrated as a function of the membrane area. For the inlet and outlet flows, experimental data is shown. For an inlet flow of 3 % carbon dioxide and 97 % methane, the concentration changes are small over the area and experimental data are in good agreement with the model results. For higher penetrant concentrations (H_2

penetrant concentration in feed	specific permeability CH_4 $10^{-7}Nm^3/(s\ m^2\ bar)$	specific permeability penetrant $10^{-7}Nm^3/(s\ m^2\ bar)$
CO_2: 3 vol-%	6.92	85.26
CO_2: vol-12%	7.31	113.92
H_2: vol-12%	7.30	155.48

Table 6.4: Specific permeability factors from co-current experiments with binary mixtures (penetrant and methane) determined with equation 6.16 at 4.2 bara and T=40°C

or CO_2: 12 vol-%), the deviation between the model results and the experimental data becomes larger in the permeate. The differences can be explained by the application of an overall permeability factor instead of local factors over the membrane area in the model. However, the specific permeability factors determined from co-current operation show better results in the co-current model than the specific permeability factors obtained from counter-current mode. The presumption seems to be valid that the permeability factors also depend on the flow conditions in the membrane. In experiments, the specific permeability factors for co-current flow conditions were generally higher than for counter-current conditions. This explains the underestimation of permeation in the co-current model using counter-current permeability factors. However, only for a few experiments in co-current mode, specific permeability factors could be determined. The influence of the operation at different flow conditions needs to be investigated further.

6.4 Conclusions

A commercially available membrane (based on fibres from *Evonik*) has been investigated regarding its technical feasibility serving as upgrade unit of methanation gas. Additionally, several influences on the permeability factor have been studied and expressed mathematically. This expression has been included into a membrane unit model in order to compare the model with experimental data.

The technical feasibility of the gas separation membrane as upgrade unit of methanation gas could be demonstrated with the sufficient separation of hydrogen from methane. The obtained product gas reaches gas grid requirements of Germany or Switzerland (table 3.1). Not only the pressure, but also the temperature appeared to have significant influence on the separation performance of the membrane. Increased temperatures or pressures result in increased permeation rates of all components, which increase the methane content in the retentate but also in the permeate if no further adjustments are done. However, with the appropriate choices of temperature, pressure and membrane size, the permeate flow can be minimised while still the sufficient amount of hydrogen is separated from methane. For this, the counter-current operation of the membrane unit appeared to be more beneficial than the co-current operation.

In literature, there are various modelling approaches of membrane modules for gas separation [53, 124, 164–166]. However, permeability factors have been stated constant in literature although various influences in a membrane module exist which affects the permeability factor. In our own experiments, the effect of temperature, pressure, binary mixtures and flow conditions to the specific permeability factor appeared to be strongly pronounced. Different binary gas mixtures which contained hydrogen, carbon dioxide or nitrogen each mixed with methane were investigated. For highly permeable components, permeabilities and selectivities decrease with their decreasing share in the mixture, whereas for low-permeable components, permeability factors increase with a decreasing share. This behaviour is caused by competitive sorption on the membrane surface and bulk flow effects. Both effects worsen the selectivity factors of the membrane. In general, the investigated membrane showed separation properties comparable with data from literature and belongs to a membrane type with elevated selectivities regarding hydrogen against methane. With experimental data, the influence of the pressure and the inlet gas composition to the specific permeability could be mathematically described.

The membrane model with permeability calculations as a function of pressure and feed gas concentrations can predict concentration trends in the permeate and retentate properly for different operating conditions. It turned out that permeability factors ob-

tained in counter-current operation tend to underestimate the permeation flow through the membrane in the co-current model. The application of permeability factors from co-current operation improved the predictions with a maximum error of 3 %-points for concentrations in the outlet flows. The remaining error can be explained by the application of overall permeability factors instead of local factors changing over the membrane area due to changing gas concentrations.

7 General Conclusions

In the introduction, the objectives of establishing a technically and economically feasible process were defined for the direct methanation of biogas. The technical feasibility of the bubbling fluidised bed reactor and the gas separation membrane could be demonstrated in experiments at pilot-scale with an chemical output of 10 - 20 kW. The data from these experiments were also used to compare the forecasts of the rigorous models with the experimental results. Complete process chains could be simulated which were able to produce biomethane so that general gas grid requirements for unrestricted injection could be fulfilled. Finally, the necessary specific site conditions could be identified for economic feasibility of the optimised processes.

In the process simulations, a cooled fixed bed and a bubbling fluidised bed were investigated, both serving as the main reactor for the methanation. Both types of reactor showed the same performance which is restricted by kinetic and thermodynamic effects, so that the mentioned gas grid requirements cannot be fulfilled by a single reactor. However, the cooled fixed bed requires about three times more catalyst material than the fluidised bed. A further upgrade of the methanation gas is needed to remove the excess hydrogen in the gas, which is often not considered in literature. For this, a gas separation membrane or a second stage fixed bed was investigated. Both options were able to reach the demanded gas quality. However, the second fixed bed required a strictly controlled H_2/CO_2 ratio of 4.03 upstream the main reactor so that the gas separation membrane showed more beneficial properties regarding the process robustness. The electrolysis, which provides the process with hydrogen, consumes by far the most energy of the process in the form of electricity.

Economically optimised operation conditions were used for the absolute economic assessment of the simulated processes. The process with a bubbling fluidised bed and a gas separation membrane appeared to be the most economical one. A fluidised bed is half as expensive as a fixed bed due to its smaller size. For the further upgrading, the gas separation membrane and the second-stage fixed bed are equally expensive. However as already mentioned, the membrane module has technically more beneficial properties. For an electricity price of 6 $Ct_{€}/kWh_{el}$ and an assumed biogas price of 6 $Ct_{€}/kWh_{biogas}$, the production costs of the optimum process are 11 $Ct_{€}/kWh_{SNG}$, which is the limit of

profitability. Cost data given in literature are often under-estimated because additional equipment is not considered such as the upgrade of the methanation gas. As expected, the electrolysis clearly dominates the total costs of the processes due to the high electricity consumption but also due to the elevated capital costs. As a consequence, the profitability of the processes strongly depends on the electricity price, which must be in the range of 5 to 6 $Ct_€/kWh_{el}$ to be economically feasible for the corresponding production costs of biomethane. Electricity at this price might be purchased if no grid use fees have to be paid. Hence, it depends on whether the site has direct access to electricity or has to obtain it from the electricity grid. Other site factors also influence the profitability of the processes (e.g. the possibility of selling side products and the methane content in the biogas) so that a feasible electricity price could increase up to 9 $Ct_€/kWh$.

The bubbling fluidised bed reactor for the biogas methanation could be successfully tested in a long-duration experiment with real biogas as the feed stream. The pilot-scale reactor was directly connected between the digester and the gas grid injection of the biogas plant in Zürich-Werdhölzli. Stable operation of over 1100 hours could be demonstrated with an average methane-yield of 96 %. The progress of deactivation was monitored over the operation hours and found out to be between medium and low, depending on the sulphur concentrations in the gas flow to the reactor between 3 ppm and < 0.2 ppm. Sulphur compounds could be identified as the main source of deactivation. Finally, the sulphur species could be removed almost completely by a gas cleaning unit upstream of the reactor, so that almost no further deactivation was observed. If carbon deposition contributed to the deactivation process, then it was only to a minor extent. The applied kinetics of the rigorous bubbling fluidised bed model could be validated.

The experimentally tested performance of the membrane module is sufficient to remove excess hydrogen from the methanation gas to fulfil the gas grid requirements. For this, high pressures and temperatures in the membrane module are beneficial. The counter-current operation mode is more efficient than the co-current mode for the given separation task. The effect of the pressure and the feed gas concentrations on the permeability factors has been studied. The permeability factors increase with the feed pressure. The permeability factors of the penetrants (hydrogen and carbon dioxide) decrease significantly, if they are mixed with less permeable gases (methane, nitrogen) due to competitive adsorption. Additionally, the selectivities decrease due to bulk flow effects. Hence, the performance of the membrane module is significantly lower for realistic gas mixtures in the feed than for a pure feed gases. However, often only pure gases are investigated in literature regarding their separation properties in a membrane. As a result, permeabilities of the gas species are often set constant in literature, although various operation conditions influence the permeability strongly. In this work, perme-

ability factors influenced by the feed pressure and the feed gas concentration could be described mathematically and were compared to experimental data.

With the demonstration of the technical and economic feasibility of the direct methanation of biogas at process level, one step further was achieved towards the implementation of this technology into industry. If implemented, not only a feasible conversion process from electricity to fuel for the storage of renewable electricity would be established in industry. Also, a more efficient route for the biomethane production would be available, allowing an increase of the biomethane production of about 60 % with the same consumption of biomass. This is an important aspect, since biomass generally is only restrictedly available due to the slow production of biomass by nature and its transport to biogas plants.

8 Outlook

Future research topics can be based on the following summarised suggestions regarding the methanation and gas separation membrane.

8.1 Methanation

In this work, catalytic methanation technologies were investigated regarding their technical and economic feasibility. As indicated in the introduction's section 2.2.5, there is also a biological route to produce biomethane via the micro organisms methanogenic archaea. This alternative technology operates at about 60 °C so that thermodynamic restrictions are minimum and higher conversion rates are possible than for the catalytic approach. However, significantly larger reactors are required due to the lower reaction rates. The biological methanation should be assessed also regarding their technical and economic feasibility to obtain comparable results for all mentioned methanation technologies.

Regarding the bubbling fluidised bed model, the following improvements are recommended: (1) The implementation of improved bubble size correlations and (2) the determination of local heat transfer coefficients. For a precise modelling of the hydrodynamic behaviour and especially of the mass transfer between the bubble and the dense phase, bubble size correlations are essential which consider the special conditions in the fluidised bed reactor like the volume reducing reaction at high pressures and temperatures as well as the presence of internal heat exchanger tubes. The existing bubble size correlations in literature do not reflect the conditions in the bubbling fluidised bed reactor sufficiently.

No energy balance is implemented in the bubbling fluidised bed model so far due to its close to isothermal behaviour. However, experiments indicated that slightly pronounced temperature profiles might achieve higher conversion rates than a reactor under isothermal conditions. In order to improve the performance of the reactor, the influence of temperature profiles should be simulated. For this, local heat transfer coefficients have to be determined via experiments and introduced in a model which considers also general particle movements in the reactor vessel. With this information, an energy balance can be added to the existing pseudo-homogeneous model considering axial dispersion or for

a higher degree of complexity a heterogeneous model can be established which contains an energy balance.

8.2 Gas Separation Membrane

During the recent years, new membrane materials are emerging such as polymeric metal organic framework (MOF) composite membranes. These materials can be produced tailor-made corresponding to the required properties. They show high permeability with medium selectivity factors. However, the application of those materials is currently restricted by the lack of mechanical stability and and scalability. Evaluations of those materials would be interesting, since the mentioned properties regarding the permeability and selectivity are beneficial for the purification of catalytic methanation gas.

Further research is recommended for the development of the membrane model. For this, a physical description of the permeability by the sorption-diffusion approach is suggested expressed via the equations 6.13 and 6.15. This approach considers the influence of temperature, pressure and gas concentration on the permeability for each component. In a next step, non-ideal behaviour of the gas components can be considered by applying fugacities instead of partial pressures to the mentioned equation for the gas sorption. Additionally, it is recommended to include the pressure-loss into the model, since the pressure drop during experiments on the tube side was not negligible small. The pressure-loss Δp over the length of the membrane fibre L can be implemented with the Hagen-Poiseuille equation given by:

$$\Delta p = \dot{V}_{mix}(T,p) \cdot \frac{8\ \eta_{mix}}{\pi r^4} \cdot L \tag{8.1}$$

where $\dot{V}_{mix}(T,p)$ is the volume flow of the gas mixture at the current temperature and pressure, η_{mix} represents the dynamic viscosity of the gas mixture and r is the inner radius of the fibre tube.

Also, further experiments in co-current mode are recommended under non-equilibrium conditions with a sufficient gas flow to determine the permeabilities. Preliminary results indicated that there might be differences for multi-component mixtures between the permeabilities derived in co-current and counter-current mode under conditions that are otherwise identical. If the permeabilities are not equal, flow conditions in the fibre and the surrounding vessel influence the permeability as well which can be also considered in a mathematical expression. Another task is the transformation of the co-current model into a counter-current model which can be applied in process simulations.

Bibliography

[1] P. Mann, L. Gahagan, and M. B. Gordon. *Giant Oil and Gas Fields of the Decade 1978-1988: Tectonic setting of the world's giant oil and gas fields*. Ed. by M. T. Halbouty. American Association of Petroleum Geologists, 2009.

[2] M. Sato. "Thermochemistry of the formation of fossil fuels". In: *The Geochemical Society* 2 (1990), pp. 271–283.

[3] A. Bradfort and S. Pappas. *Effects of Global Warming*. Tech. rep. Live Science, 2017.

[4] S. Fuss, J. G. Canadell, G. P. Peters, M. Tavoni, R. M. Andrew, P. Ciais, R. B. Jackson, C. D. Jones, F. Kraxner, N. Nakicenovic, C. Le Quéré, M. R. Raupach, A. Sharifi, P. Smith, and Y. Yamagata. "COMMENTARY: Betting on negative emissions". In: *Nature Climate Change* 4.10 (2014), pp. 850–853. DOI: 10.1038/nclimate2392.

[5] C. Welch. "Carbon Emissions Had Leveled Off. Now They're Rising Again". In: *National Geographic Partners* (2017).

[6] Global Monitoring Devision. *Recent Monthly Average Mauna Loa CO2*. Tech. rep. National Oceanic and Atmospheric Administration - Earth System Research Laboratory, 2018.

[7] J. Rogelj, M. Den Elzen, N. Höhne, T. Fransen, H. Fekete, H. Winkler, R. Schaeffer, F. Sha, K. Riahi, and M. Meinshausen. "Paris Agreement climate proposals need a boost to keep warming well below 2 °c". In: *Nature* 534.7609 (2016), pp. 631–639. DOI: 10.1038/nature18307. arXiv: NIHMS150003.

[8] M. Holt, R. J. Campbell, and M. B. Nikitin. *Fukushima Nuclear Disaster*. Tech. rep. 2012. DOI: 10.1016/B978-0-12-416727-8.00009-6.

[9] S. Vogel-Misicka. "Europe's Nuclear Waste Storage Problems". In: *Oilprice* (2010).

[10] Institute for Energy Research - Web Page. *Electricity Generation*. (Visited on 05/03/2018).

[11] J. L. Sawin. *Advancing the global renewable energy transition*. Tech. rep. Renewable energy policy network for the 21st century, 2017.

[12] Erneuerbare Energien-Statistik. *Erneuebare Energien in Deutschland: Daten zur Entwicklung im Jahr 2017*. Tech. rep. Umweltbundesamt, Germany, 2018.

[13] Bundesamt für Energie. *Elektrizitätsstatistik 2016*. Tech. rep. Schweizer Eidgenossenschaft, 2017.

[14] U. Kaufmann, S. Muff, and M. Kost. *Schweizerische Statistik der erneuerbaren Energien. Ausgabe 2016*. Tech. rep. Bundesamt für Energie (BFE), 2017.

[15] M. Piot. "Energiestrategie 2050 der Schweiz". In: *13. Symposium Energieinnovation*. Kapitel 5. 2014, pp. 21–23.

[16] A. Zervos, C. Lins, and L. Tesnière. "Mapping Renewable Energy Pathways towards 2020". In: *European Renewable Energy Council* (2011), p. 28.

[17] Bundesamt für Energie. "Schweizerische Gesamtenergiestatistik 2014 Statistique globale suisse de l ' énergie 2014". In: (2015).

[18] Bundesnetzagentur Deutschland. *Entwicklung der Ausfallarbeit durch Abregelung der EE-Stromeinspeisung in Deutschland in den Jahren 2009 bis 2016 (in Gigawattstunden)*. Tech. rep. 2017.

[19] B. Aust and C. Morscher. "Negative Strompreise in Deutschland". In: *Wirtschaftsdienst* 4 (2017), pp. 304–306.

[20] P. Karka, S. Papadokonstantakis, K. Hungerbühler, and A. Kokossis. "Environmental Impact Assessment of Biorefinery Products Using Life Cycle Analysis". In: *Computer Aided Chemical Engineering*. Vol. 34. Elsevier, Jan. 2014, pp. 543–548. ISBN: 9780444634337. DOI: 10.1016/B978-0-444-63433-7.50075-4.

[21] Deutscher Verein des Gas und Wasserfaches. *Technische Regel Arbeitsblatt G262*. Tech. rep. 2011, p. 22.

[22] J. Cheng. *Biomass to Renewable Energy Processes*. CRC Press, 2009. ISBN: 1439882495.

[23] BioRefinex Canada Inc. *Biogas Production*. 2018. (Visited on 04/23/2018).

[24] EurObserv'ER. *The State of Renewable Energies in Europe*. Tech. rep. Edition 2016. 2016.

[25] F. Bauer, C. Hulteberg, T. Persson, and D. Tamm. "Biogas upgrading-Review of commercial technologies". In: *SGC Rapport* (2013), p. 83. DOI: SGCRapport2013:270.

[26] S. Sutanto, J. W. Dijkstra, J. A. Pieterse, J. Boon, P. Hauwert, and D. W. Brilman. "CO2removal from biogas with supported amine sorbents: First technical evaluation based on experimental data". In: *Separation and Purification Technology* 184 (2017), pp. 12–25. DOI: 10.1016/j.seppur.2017.04.030.

[27] "Anthropogenic and Natural Radiative Forcing". In: *Climate Change 2013 - The Physical Science Basis*. Ed. by Intergovernmental Panel on Climate Change. Cambridge: Cambridge University Press, pp. 659–740. DOI: 10.1017/CBO9781107415324.018.

[28] Verband der Schweizerischen Gasindustrie (VSG). *Positionspapier: Energieversorgung der Zukunft*. Tech. rep. 2017.

[29] S. Biollaz, A. Calbry-Muzyka, T. Schildhauer, J. Witte, and A. Kunz. *Direct Methanation of Biogas*. Tech. rep. Paul Scherrer Institute, Energie360°, Bundesamt für Energie - Schweiz, 2017, p. 78.

[30] M. Andersson, T. Bligaard, A. Kustov, K. Larsen, J. Greeley, T. Johannessen, C. Christensen, and J. Norskov. "Toward computational screening in heterogeneous catalysis: Pareto-optimal methanation catalysts". In: *Journal of Catalysis* 239.2 (Apr. 2006), pp. 501–506. DOI: 10.1016/j.jcat.2006.02.016.

[31] J. Sehested, K. E. Larsen, A. L. Kustov, A. M. Frey, T. Johannessen, T. Bligaard, M. P. Andersson, J. K. Nørskov, and C. H. Christensen. "Discovery of technical methanation catalysts based on computational screening". In: *Topics in Catalysis* 45.1-4 (Aug. 2007), pp. 9–13. DOI: 10.1007/s11244-007-0232-9.

[32] P. De Groot, M. Coulon, and K. Dransfeld. “Ni(CO)4 formation on single Ni crystals: Reaction kinetics and observation of surface facetting induced by the reaction”. In: *Surface Science* 94.1 (Apr. 1980), pp. 204–220. DOI: 10.1016/0039-6028(80)90164-8.

[33] Committee on Acute Exposure Guideline Levels, Committee on Toxicology, and Board on Environmental Studies and Toxicology. “Nickel Carbonyl Acute Exposure Guideline Levels”. In: *Acute Exposure Guideline Levels for Selected Airborne Chemicals: Volume 6*. National Academies Press (US), 2008.

[34] H. Harms, B. Höhlein, and A. Skov. “Methanisierung kohlenmonoxidreicher Gase beim Energie-Transport”. In: *Chemie Ingenieur Technik* 52.6 (1980), pp. 504–515. DOI: 10.1002/cite.330520605.

[35] R. G. Reddy. “Molten salts: Thermal energy storage and heat transfer media”. In: *Journal of Phase Equilibria and Diffusion* 32.4 (2011), pp. 269–270. DOI: 10.1007/s11669-011-9904-z.

[36] J. Werther. “Hydrodynamics and Mass Transfer between the Bubble and Emulsion Phases in Fluidized Beds of Sand and Cracking Catalyst”. In: *Proceedings of the Fourth International Conference on Fluidization, Kashikojima, Japan* (1984).

[37] F. Schillinger, S. Maurer, M. Künstle, T. J. Schildhauer, and A. Wokaun. “Hydrodynamic investigations by a local optical measurement technique designed for high-temperature applications - First measurements at a fluidized bed immersed by vertical internals at cold conditions”. In: *in preparation* (2018).

[38] J. Lefebvre, M. Götz, S. Bajohr, R. Reimert, and T. Kolb. “Improvement of three-phase methanation reactor performance for steady-state and transient operation”. In: *Fuel Processing Technology* 132 (Apr. 2015), pp. 83–90. DOI: 10.1016/J.FUPROC.2014.10.040.

[39] K. P. Brooks, J. Hu, H. Zhu, and R. J. Kee. “Methanation of carbon dioxide by hydrogen reduction using the Sabatier process in microchannel reactors”. In: *Chemical Engineering Science* 62.4 (Feb. 2007), pp. 1161–1170. DOI: 10.1016/J.CES.2006.11.020.

[40] M. Götz, S. Bajohr, F. Graf, R. Reimert, and T. Kolb. “Einsatz eines Blasensäulenreaktors zur Methansynthese”. In: *Chemie Ingenieur Technik* 85.7 (July 2013), pp. 1146–1151. DOI: 10.1002/cite.201200212.

[41] L. Giani, G. Groppi, and E. Tronconi. “Heat Transfer Characterization of Metallic Foams”. In: *Industrial & Engineering Chemistry Research* 44.24 (Nov. 2005), pp. 9078–9085. DOI: 10.1021/ie050598p.

[42] S. T. Kolaczkowski, S. Awdry, T. Smith, D. Thomas, L. Torkuhl, and R. Kolvenbach. “Potential for metal foams to act as structured catalyst supports in fixed-bed reactors”. In: *Catalysis Today* 273 (Sept. 2016), pp. 221–233. DOI: 10.1016/j.cattod.2016.03.047.

[43] Y. Li, S. Chen, X. Cai, J. Hong, X. Wu, Y. Xu, J. Zou, and B. H. Chen. “Rational design and preparation of hierarchical monoliths through 3D printing for syngas methanation”. In: *Journal of Materials Chemistry A* 6.14 (Apr. 2018), pp. 5695–5702. DOI: 10.1039/C8TA01597J.

[44] L. Campbell. "Comparison of monolithic versus particulate reactor designs for the cracking of cumene and the dehydration of ethanol". In: *Spring Symposium of the Philadelphia Catalysis Club* (1974).

[45] G. Jarvi, K. Mayo, and C. Bartholomew. "Monolithic-Supported Nickel Catalysts: I. Methanation Activity Relative to Pellet Catalysts". In: *Chemical Engineering Communications* 4.1-3 (Jan. 1980), pp. 325–341. DOI: 10.1080/00986448008935913.

[46] G. Luo and I. Angelidaki. "Integrated biogas upgrading and hydrogen utilization in an anaerobic reactor containing enriched hydrogenotrophic methanogenic culture". In: *Biotechnology and Bioengineering* 109.11 (Nov. 2012), pp. 2729–2736. DOI: 10.1002/bit.24557.

[47] S. Kim, K. Choi, and J. Chung. "Reduction in carbon dioxide and production of methane by biological reaction in the electronics industry". In: *International Journal of Hydrogen Energy* 38.8 (Mar. 2013), pp. 3488–3496. DOI: 10.1016/J.IJHYDENE.2012.12.007.

[48] F. Graf, A. Krajete, and U. Schmack. *Techno-ökonomische Studie zur biologischen Methanisierung bei Power-to-Gas-Konzepten.* Tech. rep. Deutscher Verein des Gas- und Wasserfaches (DVGW), 2014. DOI: 10.13140/RG.2.1.2001.9366.

[49] H. C. Shin, D.-H. Ju, B. S. Jeon, O. Choi, H. W. Kim, Y. Um, D.-H. Lee, and B.-I. Sang. "Analysis of the Microbial Community in an Acidic Hollow-Fiber Membrane Biofilm Reactor (Hf-MBfR) Used for the Biological Conversion of Carbon Dioxide to Methane". In: *PLOS ONE* 10.12 (Dec. 2015). Ed. by C. Moissl-Eichinger. DOI: 10.1371/journal.pone.0144999.

[50] A. J. Guneratnam, E. Ahern, J. A. FitzGerald, S. A. Jackson, A. Xia, A. D. Dobson, and J. D. Murphy. "Study of the performance of a thermophilic biological methanation system". In: *Bioresource Technology* 225 (Feb. 2017), pp. 308–315. DOI: 10.1016/J.BIORTECH.2016.11.066.

[51] M. Burkhardt and G. Busch. "Methanation of hydrogen and carbon dioxide". In: *Applied Energy* 111 (Nov. 2013), pp. 74–79. DOI: 10.1016/J.APENERGY.2013.04.080.

[52] J. Lai, K. Tung, D. Lee, D. Wang, D. Ju, J. Shin, H. Lee, S. Kong, J. Kim, and B. Sang. "The Fourth Conference of Aseanian Membrane Society: Part 2-Effects of pH conditions on the biological conversion of carbon dioxide to methane in a hollow-fiber membrane biofilm reactor (Hf–MBfR)". In: *Desalination* 234 (2008), pp. 409–415.

[53] J. M. S. Henis and M. K. Tripodi. "Composite hollow fiber membranes for gas separation: The resistance model approach". In: *Journal of Membrane Science* 8 (1981), pp. 233–246.

[54] W. J. Moore. *Grundlagen der physikalischen Chemie.* Walter de Gruyter, 1990, p. 819. ISBN: 9783110099416.

[55] A. Brunetti, P. Bernardo, E. Drioli, and G. Barbieri. "Membrane Engineering: Progress and Potentialities in Gas Separation". In: *Membrane Gas Separation.* 2010. Chap. 14, pp. 281–313.

[56] R. Guo and J. McGrath. “Aromatic Polyethers, Polyetherketones, Polysulfides, and Polysulfones”. In: *Polymer Science: A Comprehensive Reference*. Elsevier, 2012, pp. 377–430. ISBN: 9780080878621. DOI: 10.1016/B978-0-444-53349-4.00153-9.

[57] R. W. Baker. “Future Directions of Membrane Gas Separation Technology”. In: (2002), pp. 1393–1411.

[58] D. F. Sanders, Z. P. Smith, R. Guo, L. M. Robeson, J. E. McGrath, D. R. Paul, and B. D. Freeman. “Energy-efficient polymeric gas separation membranes for a sustainable future: A review”. In: *Polymer (United Kingdom)* 54.18 (2013), pp. 4729–4761. DOI: 10.1016/j.polymer.2013.05.075.

[59] D. R. Paul and Y. P. Yampol’skii. *Polymeric gas separation membranes*. Boca Raton, FL: CRC Press, 1994, p. 623. ISBN: 0849344158.

[60] C. L. Aitken, W. J. Koros, and D. R. Paul. “Effect of structural symmetry on gas transport properties of polysulfones”. In: *Macromolecules* 25.13 (June 1992), pp. 3424–3434. DOI: 10.1021/ma00039a018.

[61] C. L. Aitken, W. J. Koros, and D. R. Paul. “Gas transport properties of biphenol polysulfones”. In: *Macromolecules* 25.14 (July 1992), pp. 3651–3658. DOI: 10.1021/ma00040a008.

[62] A. Erb and D. Paul. “Gas sorption and transport in polysulfone”. In: *Journal of Membrane Science* 8.1 (Jan. 1981), pp. 11–22. DOI: 10.1016/S0376-7388(00)82135-3.

[63] K. Ghosal, R. T. Chern, and B. D. Freeman. “Gas permeability of radel a polysulfone”. In: *Journal of Polymer Science Part B: Polymer Physics* 31.7 (June 1993), pp. 891–893. DOI: 10.1002/polb.1993.090310718.

[64] J. McHattie, W. Koros, and D. Paul. “Gas transport properties of polysulphones: 2. Effect of bisphenol connector groups”. In: *Polymer* 32.14 (Jan. 1991), pp. 2618–2625. DOI: 10.1016/0032-3861(91)90343-H.

[65] K. Ghosal and R. Chern. “Aryl-nitration of poly(phenylene oxide) and polysulfone.” In: *Journal of Membrane Science* 72.1 (Aug. 1992), pp. 91–97. DOI: 10.1016/0376-7388(92)80058-R.

[66] K. Ghosal, R. T. Chern, B. D. Freeman, W. H. Daly, and I. I. Negulescu. “Effect of Basic Substituents on Gas Sorption and Permeation in Polysulfone”. In: *Macromolecules* 29.12 (Jan. 1996), pp. 4360–4369. DOI: 10.1021/ma951310i.

[67] J. McHattie, W. Koros, and D. Paul. “Gas transport properties of polysulphones: 3. Comparison of tetramethyl-substituted bisphenols”. In: *Polymer* 33.8 (Jan. 1992), pp. 1701–1711. DOI: 10.1016/0032-3861(92)91070-I.

[68] J. McHattie, W. Koros, and D. Paul. “Gas transport properties of polysulphones: 1. Role of symmetry of methyl group placement on bisphenol rings”. In: *Polymer* 32.5 (Jan. 1991), pp. 840–850. DOI: 10.1016/0032-3861(91)90508-G.

[69] J. HAGGIN. “New Generation of Membranes Developed for Industrial Separations”. In: *Chemical & Engineering News* 66.23 (June 1988), pp. 7–16. DOI: 10.1021/cen-v066n023.p007.

[70] W. Schell, C. Wensley, M. Chen, K. Venugopal, B. Miller, and J. Stuart. "Recent advances in cellulosic membranes for gas separation and pervaporation". In: *Gas Separation & Purification* 3.4 (Dec. 1989), pp. 162–169. DOI: 10.1016/0950-4214(89)80001-5.

[71] L. S. White. "Evolution of natural gas treatment with membrane systems". In: *Membrane Gas Separation*. Wiley, 2010. Chap. 15, pp. 313–332. ISBN: 9780470746219.

[72] S. LOEB and S. SOURIRAJAN. "Sea Water Demineralization by Means of an Osmotic Membrane". In: Jan. 1963, pp. 117–132. DOI: 10.1021/ba-1963-0038.ch009.

[73] K. J. Edgar, C. M. Buchanan, J. S. Debenham, P. A. Rundquist, B. D. Seiler, M. C. Shelton, and D. Tindall. "Advances in cellulose ester performance and application". In: *Progress in Polymer Science* 26.9 (Nov. 2001), pp. 1605–1688. DOI: 10.1016/S0079-6700(01)00027-2.

[74] M. Donohue, B. Minhas, and S. Lee. "Permeation behavior of carbon dioxide-methane mixtures in cellulose acetate membranes". In: *Journal of Membrane Science* 42.3 (Mar. 1989), pp. 197–214. DOI: 10.1016/S0376-7388(00)82376-5.

[75] A. S. Hay. *Oxidation of phenols and resulting products (Patent number: US3306875A)*. July 1962.

[76] K. Toi, G. Morel, and D. R. Paul. "Gas sorption and transport in poly(phenylene oxide) and comparisons with other glassy polymers". In: *Journal of Applied Polymer Science* 27.8 (Aug. 1982), pp. 2997–3005. DOI: 10.1002/app.1982.070270823.

[77] M. Aguilar-Vega and D. R. Paul. "Gas transport properties of polyphenylene ethers". In: *Journal of Polymer Science Part B: Polymer Physics* 31.11 (Oct. 1993), pp. 1577–1589. DOI: 10.1002/polb.1993.090311114.

[78] F. Hamad, K. Khulbe, and T. Matsuura. "Characterization of gas separation membranes prepared from brominated poly (phenylene oxide) by infrared spectroscopy". In: *Desalination* 148.1-3 (Sept. 2002), pp. 369–375. DOI: 10.1016/S0011-9164(02)00732-4.

[79] S. Sridhar, B. Smitha, M. Ramakrishna, and T. M. Aminabhavi. "Modified poly(phenylene oxide) membranes for the separation of carbon dioxide from methane". In: *Journal of Membrane Science* 280.1-2 (Sept. 2006), pp. 202–209. DOI: 10.1016/j.memsci.2006.01.019.

[80] B. J. Story and W. J. Koros. "Sorption of CO2/CH4 mixtures in poly(phenylene oxide) and a carboxylated derivative". In: *Journal of Applied Polymer Science* 42.9 (May 1991), pp. 2613–2626. DOI: 10.1002/app.1991.070420926.

[81] B. J. Story and W. Koros. "Sorption and transport of CO2 and CH4 in chemically modified poly(phenylene oxide)". In: *Journal of Membrane Science* 67.2-3 (Mar. 1992), pp. 191–210. DOI: 10.1016/0376-7388(92)80025-F.

[82] A. Zampini and R. F. Malon. "Cross-Linked Polyphenylene Oxide Gas Separation Membranes". In: vol. 52. ACS, 1985, pp. 345–349. ISBN: 0841208824.

[83] R. Chern, F. Sheu, L. Jia, V. Stannett, and H. Hopfenberg. “Transport of gases in unmodified and arylbrominated 2,6-dimethyl- 1,4-poly (phenylene oxide)”. In: *Journal of Membrane Science* 35.1 (Dec. 1987), pp. 103–115. DOI: 10.1016/S0376-7388(00)80925-4.

[84] R. Chern, L. Jia, S. Shimoda, and H. Hopfenberg. “A note on the effects of mono- and di-bromination on the transport properties of poly(2,6-dimethylphenylene oxide)”. In: *Journal of Membrane Science* 48.2-3 (Feb. 1990), pp. 333–341. DOI: 10.1016/0376-7388(90)85014-C.

[85] P. Falcigno, M. Masola, D. Williams, and S. Jasne. “Comparison of properties of polyimides containing DAPI isomers and various dianhydrides”. In: *Polyimides: Materials, Chemistry and Characterization*. 1989, pp. 497–512.

[86] I. V. Farr, D. Kratzner, T. E. Glass, D. Dunson, Q. Ji, and J. E. Mcgrath. “The synthesis and characterization of polyimide homopolymers based on 5(6)-amino-1-(4-aminophenyl)-1,3,3-trimethylindane”. In: *Journal of Polymer Science Part A: Polymer Chemistry* 38.15 (Aug. 2000), pp. 2840–2854. DOI: 10.1002/1099-0518(20000801)38:15<2840::AID-POLA240>3.0.CO;2-N.

[87] Y. Zhang, I. H. Musselman, J. P. Ferraris, and K. J. Balkus. “Gas permeability properties of Matrimid® membranes containing the metal-organic framework Cu–BPY–HFS”. In: *Journal of Membrane Science* 313.1-2 (Apr. 2008), pp. 170–181. DOI: 10.1016/j.memsci.2008.01.005.

[88] A. Puleo, D. Paul, and S. Kelley. “The effect of degree of acetylation on gas sorption and transport behavior in cellulose acetate”. In: *Journal of Membrane Science* 47.3 (Dec. 1989), pp. 301–332. DOI: 10.1016/S0376-7388(00)83083-5.

[89] W. Koros, G. Fleming, S. Jordan, T. Kim, and H. Hoehn. “Polymeric membrane materials for solution-diffusion based permeation separations”. In: *Progress in Polymer Science* 13.4 (Jan. 1988), pp. 339–401. DOI: 10.1016/0079-6700(88)90002-0.

[90] L. M. Robeson. “Correlation of separation factor versus permeability for polymeric membranes”. In: *Journal of Membrane Science* 62.2 (1991), pp. 165–185. DOI: 10.1016/0376-7388(91)80060-J.

[91] Synder Filtration. *Hollow Fiber Membranes*. 2018. (Visited on 05/03/2018).

[92] Koch Membrane Systems. *About Spiral Membranes - Koch Membrane Systems*. 2018. (Visited on 05/03/2018).

[93] R. W. Baker. “Membrane Gas-Separation: Applications”. In: *Membrane Operations*. Weinheim, Germany: Wiley-VCH Verlag GmbH & Co. KGaA, 2009, pp. 167–194. DOI: 10.1002/9783527626779.ch8.

[94] Evonik. *Factsheet: Sepuran Green - Membrane Technology for Efficient Biogas Upgrading*. Tech. rep. 2018.

[95] M. Götz, J. Lefebvre, F. Mörs, A. Mc Daniel Koch, F. Graf, S. Bajohr, R. Reimert, and T. Kolb. “Renewable Power-to-Gas : A technological and economic review”. In: *Renewable Energy* 85 (2016), pp. 1371–1390. DOI: 10.1016/j.renene.2015.07.066.

[96] P. Collet, E. Flottes, A. Favre, L. Raynal, H. Pierre, S. Capela, and C. Peregrina. "Techno-economic and Life Cycle Assessment of methane production via biogas upgrading and power to gas technology". In: *Applied Energy* 192 (Apr. 2017), pp. 282–295. DOI: 10.1016/j.apenergy.2016.08.181.

[97] L. Jürgensen, E. A. Ehimen, J. Born, and J. B. Holm-Nielsen. "Utilization of surplus electricity from wind power for dynamic biogas upgrading: Northern Germany case study". In: *Biomass and Bioenergy* 66 (2014), pp. 126–132. DOI: 10.1016/j.biombioe.2014.02.032.

[98] B. Müller, K. Müller, D. Teichmann, and W. Arlt. "Energiespeicherung mittels Methan und energietragenden Stoffen ein thermodynamischer Vergleich". In: *Chemie-Ingenieur-Technik* 83.11 (2011), pp. 2002–2013. DOI: 10.1002/cite.201100113.

[99] I. Dzene and F. Romagnoli. "Assessment of the Potential for Balancing Wind Power Supply with Biogas Plants in Latvia". In: *Energy Procedia* 72 (2015), pp. 250–255. DOI: 10.1016/j.egypro.2015.06.036.

[100] Schweizerischer Verein des Gas- und Wasserfaches (SVGW). *Richtlinie für die Einspeisung von erneuerbaren Gasen - G13/G18*. Tech. rep. 2016.

[101] Deutscher Verein des Gas und Wasserfaches. *Technische Regel Arbeitsblatt G260*. Tech. rep. 2013, p. 26.

[102] S. L. Teske. "Integrating Rate Based Models into a Multi-Objective Process Design & Optimisation Framework using Surrogate Models". In: 6302 (2014). DOI: http://dx.doi.org/10.5075/epfl-thesis-6302.

[103] N. R. Parlikkad, S. Chambrey, P. Fongarland, N. Fatah, A. Khodakov, S. Capela, and O. Guerrini. "Modeling of fixed bed methanation reactor for syngas production: Operating window and performance characteristics". In: *Fuel* 107 (2013), pp. 254–260. DOI: 10.1016/j.fuel.2013.01.024.

[104] J. Xu and G. F. Froment. "Methane Steam Reforming , Methanation and Water-Gas Shift : 1 . Intrinsic Kinetics". In: *AIChE Journal* 35.1 (1989), pp. 88–96.

[105] S. C. Tentarelli and S. J. Gibbon. *Adsorbent bed support (Patent number: WO 2011138612 A1)*. 2011.

[106] Verband der Schweizerischen Gasindustrie (VSG). *Gas in Zahlen 2015 Erdgas / Biogas*. Tech. rep. 2015.

[107] J. Kopyscinski, T. J. Schildhauer, and S. M. A. Biollaz. "Production of synthetic natural gas (SNG) from coal and dry biomass - A technology review from 1950 to 2009". In: *Fuel* 89.8 (2010), pp. 1763–1783. DOI: 10.1016/j.fuel.2010.01.027.

[108] Evonik. *Factsheet - SEPURAN® Noble - Membrantechnologie für Helium- und Wasserstoffaufbereitung*. Tech. rep. Evonik, 2016.

[109] J. Kopyscinski. "Production of synthetic natural gas in a fluidized bed reactor". Dissertation ETH NO. 18800. Eidegnössische Technische Hochschule Zürich (ETHZ), 2010. DOI: 10.3929/ethz-a-006031831.

[110] J. Kopyscinski, T. J. Schildhauer, and S. M. A. Biollaz. “Methanation in a fluidized bed reactor with high initial CO partial pressure: Part II- Modeling and sensitivity study”. In: *Chemical Engineering Science* 66.8 (2011), pp. 1612–1621. DOI: 10.1016/j.ces.2010.12.029.

[111] K. Hilligardt and J. Werther. “Lokaler Blasengasholdup und Expansionsverhalten von Gas/Feststoff-Wirbelschichten”. In: *Chemical Engineering and Technology* 57.7 (1985).

[112] J. Kopyscinski, T. J. Schildhauer, and S. M. A. Biollaz. “Methanation in a fluidized bed reactor with high initial CO partial pressure: Part I-Experimental investigation of hydrodynamics, mass transfer effects, and carbon deposition”. In: *Chemical Engineering Science* 66.5 (2011), pp. 924–934. DOI: 10.1016/j.ces.2010.11.042.

[113] J. Werther. “Die Bedeutung der Blasenkoaleszenz fur die Auslegung von GaslFeststoff-Wirbelschichten”. In: *Chemie Engenieur Technik* 48.4 (1976), p. 339.

[114] S. Mori and C. Y. Wen. “Estimation of bubble diameter in gaseous fluidized beds”. In: *AIChE Journal* 21.1 (1975), pp. 109–115. DOI: 10.1002/aic.690210114.

[115] R. C. Darton. “A bubble growth theory of fluidized bed reactors”. In: *Transactions of the American Institute of Chemical Engineers* 57 (1979), pp. 134–138.

[116] P. N. Rowe. “Prediction of bubble size in a gas fluidised bed”. In: *Chemical Engineering Science* 31.4 (1976), pp. 285–288. DOI: 10.1016/0009-2509(76)85073-7.

[117] K. Hilligardt and J. Werther. “Influence of Temperature and Properties of Solids on the Size and Growth of Bubbles in Gas Fluidized Beds”. In: *272 Chem. Eng. Techno].* 10 (1987), pp. 272–280.

[118] R. R. Cranfield and D. Geldart. “Large Particle Fluidisation”. In: *Chemical Engineering Science* 29 (1974), pp. 935–947.

[119] C. Fryer and O. E. Potter. “Experimental investigation of models for fluidized bed catalytic reactors”. In: *AIChE Journal* 22.1 (1976), pp. 38–47. DOI: 10.1002/aic.690220104.

[120] L. R. Glicksman, W. K. Lord, and M. Sakagami. “Bubble properties in large particle fluidized beds”. In: *Chem. Eng. Sci.* 42 (1987), pp. 479–491.

[121] S. Maurer, D. Gschwend, E. C. Wagner, T. J. Schildhauer, J. Ruud van Ommen, S. M. Biollaz, and R. F. Mudde. “Correlating bubble size and velocity distribution in bubbling fluidized bed based on X-ray tomography”. In: *Chemical Engineering Journal* 298 (2016), pp. 17–25. DOI: 10.1016/j.cej.2016.02.012.

[122] D. Schlereth and O. Hinrichsen. “Chemical Engineering Research and Design A fixed-bed reactor modeling study on the methanation of CO 2”. In: *Chemical Engineering Research and Design* 92.4 (2013), pp. 702–712. DOI: 10.1016/j.cherd.2013.11.014.

[123] T. Schildhauer. “Untersuchungen zur Verbesserung des Wärmeübergangs in katalytischen Festbettreaktoren für Energiespeicheranwendungen”. PhD thesis. 2001.

[124] T. Pettersen and K. M. Lien. "A new robust design model for gas separating membrane modules, based on analogy with counter-current heat exchangers". In: *Computers and Chemical Engineering* 18.5 (1994), pp. 427–439. DOI: 10.1016/0098-1354(94)88021-2.

[125] B. D. Freeman. "Basis of permeability/selectivity tradeoff relations in polymeric gas separation membranes". In: *Macromolecules* 32.2 (1999), pp. 375–380. DOI: 10.1021/ma9814548. arXiv: arXiv:1011.1669v3.

[126] Y. Zhang, I. H. Musselman, J. P. Ferraris, and K. J. Balkus. "Gas permeability properties of Matrimid membranes containing the metal-organic framework Cu-BPY-HFS". In: *Journal of Membrane Science* 313.1-2 (2008), pp. 170–181. DOI: 10.1016/j.memsci.2008.01.005.

[127] D. F. Sanders, Z. P. Smith, R. Guo, L. M. Robeson, J. E. McGrath, D. R. Paul, and B. D. Freeman. "Energy-efficient polymeric gas separation membranes for a sustainable future: A review". In: *Polymer (United Kingdom)* 54.18 (2013), pp. 4729–4761. DOI: 10.1016/j.polymer.2013.05.075.

[128] L. Bertuccioli, A. Chan, D. Hart, F. Lehner, B. Madden, and E. Standen. "Study on development of water electrolysis in the EU". 2014.

[129] Deltech. *Adsorption Drying Technology*. Tech. rep. Deltech - SPX Dehydration & Filtration, 2016, pp. 1–8.

[130] A. Kunz and Energie 360° Switzerland. *Personal Communication*. 2017.

[131] Bundesministerium für Umweltschutz, Naturschutz, and Bau und Reaktorsicherheit. *Vergütungssätze und Degressionsbeispiele nach dem neuen Erneuerbare-Energien-Gesetz (EEG) vom 31. Oktober 2008 mit Änderungen vom 11. August 2010*. Tech. rep. 2010, pp. 1–14.

[132] G. D. Ulrich and P. T. Vasudevan. *Chemical Engineering - Process Design and Economics, A practical Guide*. 2. Edition. Taylor & Francis Group, 2004. ISBN: 0-9708768-2-3.

[133] Alibaba Market Place. *Nickel Catalyst Costs*. (Visited on 11/02/2016).

[134] Silica Gel Products. *Silica Gel Costs*. (Visited on 11/04/2016).

[135] SulfaTrap. *Budgetary Offer for Gas Cleaning*. Tech. rep. 2016.

[136] W. A. Amos and National Renewable Energy Laboratory. *Costs of Storing and Transporting Hydrogen*. Tech. rep. 1998.

[137] C. Tricase and M. Lombardi. "State of the art and prospects of Italian biogas production from animal sewage: Technical-economic considerations". In: *Renewable Energy* 34.3 (2009), pp. 477–485. DOI: 10.1016/j.renene.2008.06.013.

[138] M. Gassner. "Process Design Methodology for Thermochemical Production of Fuels from Biomass . Application to the Production of Synthetic Natural Gas from Lignocellulosic Resources". PhD thesis. 2010, p. 245. DOI: 10.5075/epfl-thesis-4693.

[139] D. E. Garrett. *Chemical Engineering Economics*. Springer Netherlands, 1989. ISBN: 978-94-011-6546-4. DOI: 10.1007/978-94-011-6544-0.

[140] Process Systems Enterprise (PSE). *Case study: High Performance multitubular reactor design*. Tech. rep. 2017.

[141] T. S. Chung, S. S. Chan, R. Wang, Z. Lu, and C. He. "Characterization of permeability and sorption in Matrimid/C60 mixed matrix membranes". In: *Journal of Membrane Science* 211.1 (2003), pp. 91–99. DOI: 10.1016/S0376-7388(02)00385-X.

[142] H. Thunmann, A. Larsson, and M. Hedenskog. "Commissioning of the GoBiGas 20MW biomethane plant". In: *Presentation at TC Biomass Chicago*. 2015.

[143] Feredal Ministry for Economic Affairs and Energy of Germany. "Gesetz zur Einführung von Ausschreibungen für Strom aus Erneuerbaren Energien und zu weiteren Änderungen des Rechts der Erneuerbaren Energien". In: *Bundesgesetzblatt* 1.49 (2016), pp. 2258–2360.

[144] Federal Assembly of the Swiss Confederation. *Energiegesetz (EnG)*. Tech. rep. 2016, pp. 7683–7730.

[145] S. Schiebahn, T. Grube, M. Robinius, V. Tietze, B. Kumar, and D. Stolten. "Power to gas: Technological overview, systems analysis and economic assessment for a case study in Germany". In: *International Journal of Hydrogen Energy* 40.12 (2015), pp. 4285–4294. DOI: 10.1016/j.ijhydene.2015.01.123.

[146] H. S. de Boer, L. Grond, H. Moll, and R. Benders. "The application of power-to-gas, pumped hydro storage and compressed air energy storage in an electricity system at different wind power penetration levels". In: *Energy* 72 (2014), pp. 360–370. DOI: 10.1016/j.energy.2014.05.047.

[147] G. Gahleitner. "Hydrogen from renewable electricity: An international review of power-to-gas pilot plants for stationary applications". In: *International Journal of Hydrogen Energy* 38.5 (2013), pp. 2039–2061. DOI: 10.1016/j.ijhydene.2012.12.010.

[148] A. S. Calbry-Muzyka, A. Gantenbein, J. Schneebeli, A. Frei, T. J. Schildhauer, and S. M. A. Biollaz. "Deep removal of sulfur and trace organic compounds from biogas to protect a catalytic methanation reactor". In: *to be published* (2017).

[149] S. Rodriguez Duran, M. Künstle, S. M. Biollaz, and T. J. Schildhauer. "Predicting attrition and elutriation in bubbling fluidized beds through a mechanistic-based model based on brittle fracture". In: *in preparation* (2018).

[150] T. J. Schildhauer and S. M. A. Biollaz. *Synthetic Natural Gas from Coal, dry Biomass and Power-to-Gas Applications*. John Wiley & Sons, 2016.

[151] T. J. Schildhauer, M. Seemann, S. M. A. Biollaz, S. Stucki, D. Ulrich, and R. Rauch. *Successful demonstration of long term catalyst stability in the methane from wood process*. Tech. rep. Paul Scherrer Institute, Switzerland, 2008.

[152] M. C. Seemann, T. J. Schildhauer, and S. M. A. Biollaz. "Fluidized Bed Methanation of Wood-Derived Producer Gas for the Production of Synthetic Natural Gas". In: *Ind. Eng. Chem. Res.* 49 (2010), pp. 7034–7038. DOI: 10.1021/ie100510m.

[153] R. P. W. J. Struis, T. J. Schildhauer, I. Czekaj, M. Janousch, S. M. A. Biollaz, and C. Ludwig. "Sulphur poisoning of Ni catalysts in the SNG production from biomass: A TPO/XPS/XAS study". In: *Applied Catalysis A: General* 362.1-2 (2009), pp. 121–128. DOI: 10.1016/j.apcata.2009.04.030.

[154] J. Zarfl, D. Ferri, T. J. Schildhauer, J. Wambach, and A. Wokaun. "DRIFTS study of a commercial Ni/γ-Al2O3 CO methanation catalyst". In: *Applied Catalysis A: General* 495 (2015), pp. 104–114. DOI: 10.1016/j.apcata.2015.02.005.

[155] J. Kopyscinski, T. J. Schildhauer, F. Vogel, S. M. a. Biollaz, and A. Wokaun. "Applying spatially resolved concentration and temperature measurements in a catalytic plate reactor for the kinetic study of CO methanation". In: *Journal of Catalysis* 271.2 (2010), pp. 262–279. DOI: 10.1016/j.jcat.2010.02.008.

[156] D. S. Sholl and R. P. Lively. "Seven chemical separations to change the world". In: *Nature* 532 (2016), pp. 435–437.

[157] J. L. Humphrey. *Separation Process Technology*. McGraw-Hill (canada), 1997, p. 408. ISBN: 9780070311732.

[158] Oak Ridge National Lab. (ORNL). *Materials for Separation Technologies. Energy and Emission Reduction Opportunities*. Tech. rep. 2005. DOI: 10.2172/1218755.

[159] M. Palencia, B. L. Rivas, E. Pereira, A. Hernández, and P. Prádanos. "Study of polymer-metal ion-membrane interactions in liquid-phase polymer-based retention (LPR) by continuous diafiltration". In: *Journal of Membrane Science* 336.1-2 (2009), pp. 128–139. DOI: 10.1016/j.memsci.2009.03.016.

[160] Y. Li, F. Liang, H. Bux, A. Feldhoff, W. Yang, and J. Caro. "Molecular Sieve Membrane: Supported Metal–Organic Framework with High Hydrogen Selectivity". In: *Angewandte Chemie* 122.3 (2010), pp. 558–561.

[161] M. A. Huijbregts, S. Hellweg, R. Frischknecht, K. Hungerbühler, and A. J. Hendriks. "Ecological footprint accounting in the life cycle assessment of products". In: *Ecological Economics* 64.4 (Feb. 2008), pp. 798–807. DOI: 10.1016/j.ecolecon.2007.04.017.

[162] M. Morales, P. Y. Dapsens, I. Giovinazzo, J. Witte, C. Mondelli, S. Papadokonstantakis, K. Hungerbühler, and J. Pérez-Ramírez. "Environmental and economic assessment of lactic acid production from glycerol using cascade bio- and chemocatalysis". In: *Energy & Environmental Science* 8.2 (Feb. 2015), pp. 558–567. DOI: 10.1039/C4EE03352C.

[163] D. R. Paul. *Polymeric Gas Separation Membranes*. CRC Press: Boca Raton, 1994. ISBN: 0-8493-4415-8.

[164] C. Y. Pan. "Gas Separation by High-Flux , Asymmetric Hollow-Fiber Membrane". In: *AIChE Journal* 32.12 (1986), pp. 2020–2027.

[165] D. T. Coker, B. D. Freeman, and G. K. Fleming. "Modeling multicomponent gas separation using hollow-fiber membrane contactors". In: *AIChE Journal* 44.6 (1998), pp. 1289–1302. DOI: 10.1002/aic.690440607.

[166] M. H. Murad Chowdhury, X. Feng, P. Douglas, and E. Croiset. "A new numerical approach for a detailed multicomponent gas separation membrane model and AspenPlus simulation". In: *Chemical Engineering and Technology* 28.7 (2005), pp. 773–782. DOI: 10.1002/ceat.200500077.

[167] S. Matteucci, Y. Yampolskii, B. D. Freeman, and I. Pinnau. "Transport of gases and vapors in glassy and rubbery polymers". In: *Materials Science of Membranes for Gas and Vapor Separation*. John Wiley & Sons, 2006.

[168] R. M. Barrer, J. A. Barrie, and J. Slater. "Sorption and Diffusion in Ethyl Cellulose. Part 111. Comparison between Ethyl Cellulose and Rubber". In: *Journal of Polymer Science* 27 (1958), pp. 177–197.

[169] A. S. Michaels, W. R. Vieth, and J. A. Barrie. "Solution of gases in polyethylene terephthalate". In: *Journal of Applied Physics* 34.1 (1963), pp. 1–12. DOI: 10.1063/1.1729066.

[170] K. Toi, G. Morel, and D. Paul. "Gas Sorption and Transport in Poly(pheny1ene Oxide) and Comparisons with Other Glassy Polymers". In: *Journal of Applied Polymer Science* 27 (1982), pp. 2997–3005.

[171] W. J. Koros. "Sorption and Transport of Gases in Glassy Polymers". In: *Journal of Mem brane Science* 2 (1977), pp. 165–190.

[172] J. D. Wind. "Improving Polyimide Membrane Resistance to Carbon Dioxide Plasticization in Natural Gas Separations Improving Polyimide Membrane Resistance to Carbon Dioxide Plasticization in Natural Gas Separations". PhD thesis. University of Texas at Austin, 2002, p. 232.

[173] M. Alonso, E. Sainz, F. A. Lopez, and K. Shinohara. "Void-size probability distribution in random packings of equal-sized spheres". In: *Chemical Engineering Science* 50.12 (1995), pp. 1983–1988. DOI: 10.1016/0009-2509(95)00061-9.

[174] R. M. Barrer. "Permeation, diffusion and solution of gases in organic polymers". In: *Transactions of the Faraday Society* 628 (1939), pp. 628–643.

[175] O. C. David, D. Gorri, A. Urtiaga, and I. Ortiz. "Mixed gas separation study for the hydrogen recovery from H2/CO/N2/CO2 post combustion mixtures using a Matrimid membrane". In: *Journal of Membrane Science* 378.1-2 (2011), pp. 359–368. DOI: 10.1016/j.memsci.2011.05.029.

[176] R. H. Newton. "Activity Coefficients of Gases". In: *Ind. Eng. Chem.* 27 (1935), pp. 302–306. DOI: 10.1021/ie50303a014.

[177] C. L. Aitken, W. J. Koros, and D. R. Paul. "Effect of structural symmetry on gas transport properties of polysulfones". In: *Macromolecules* 25.13 (1992), pp. 3424–3434.

[178] A. Puleo, D. Paul, and S. Kelley. "The effect of degree of acetylation on gas sorption and transport behavior in cellulose acetate". In: *Journal of Membrane Science* 47.3 (Dec. 1989), pp. 301–332. DOI: 10.1016/S0376-7388(00)83083-5.

[179] W. Koros, G. Fleming, S. Jordan, T. Kim, and H. Hoehn. "Polymeric membrane materials for solution-diffusion based permeation separations". In: *Progress in Polymer Science* 13.4 (Jan. 1988), pp. 339–401. DOI: 10.1016/0079-6700(88)90002-0.

List of Figures

List of Tables

A Appendix

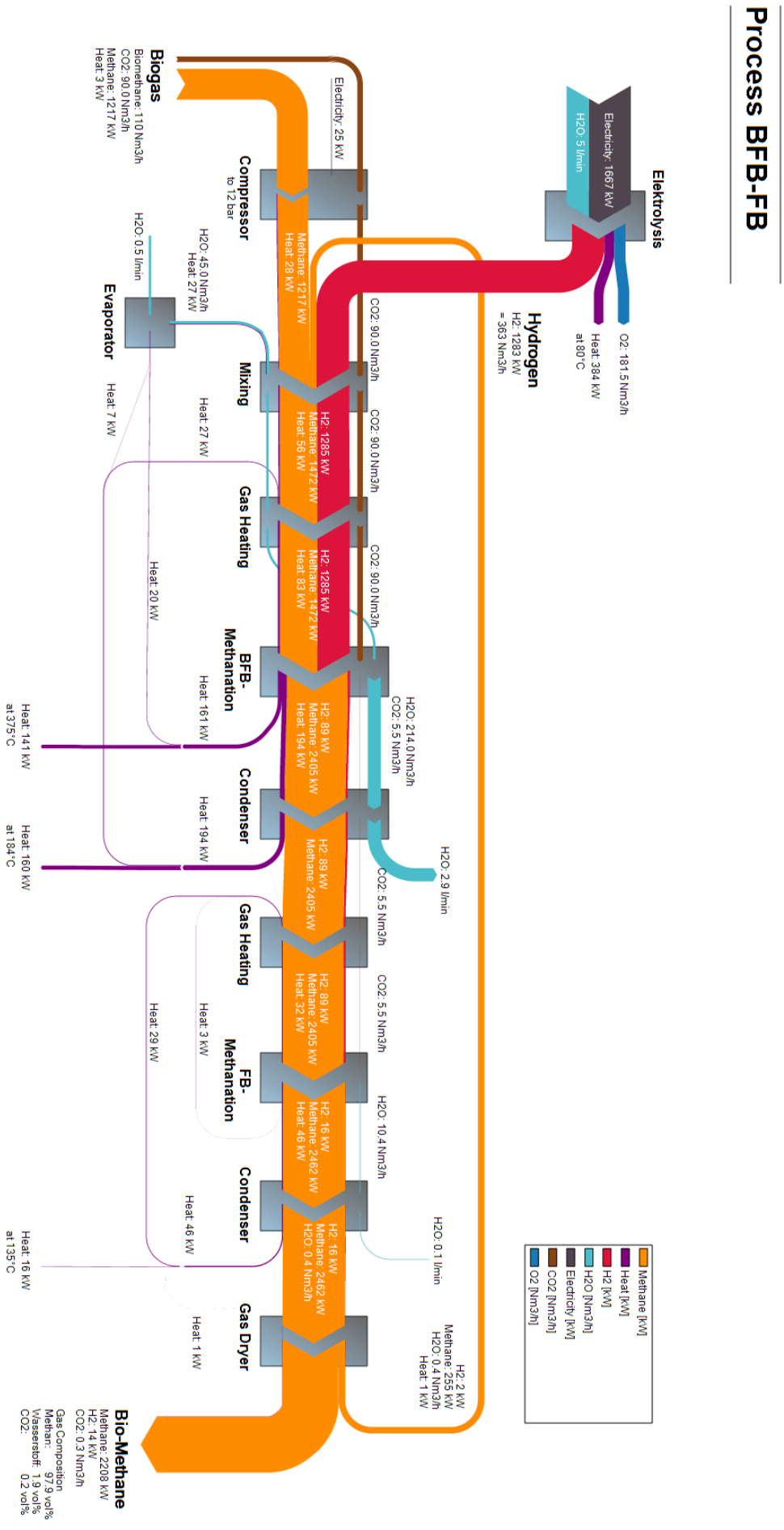

Figure A.1: Flow diagram of process BFB-FB ; p_{sys}=12 bara, $H_2/CO_{2,input}$= 4.03

Process FB-MemS

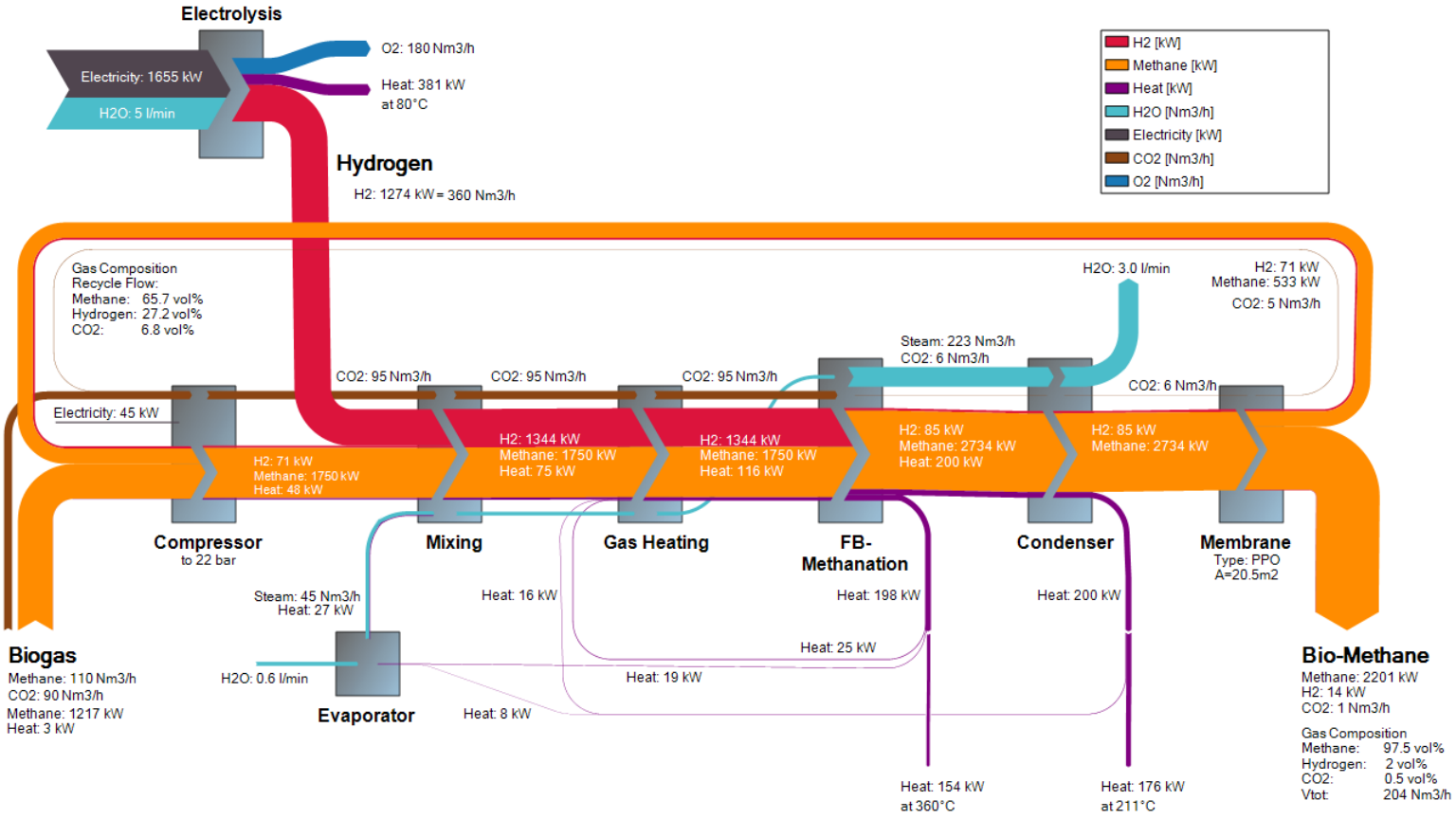

Figure A.2: Flow diagram of process FB-MemS ; p_{sys}=22 bara, $H_2/CO_{2,input}$= 4.0

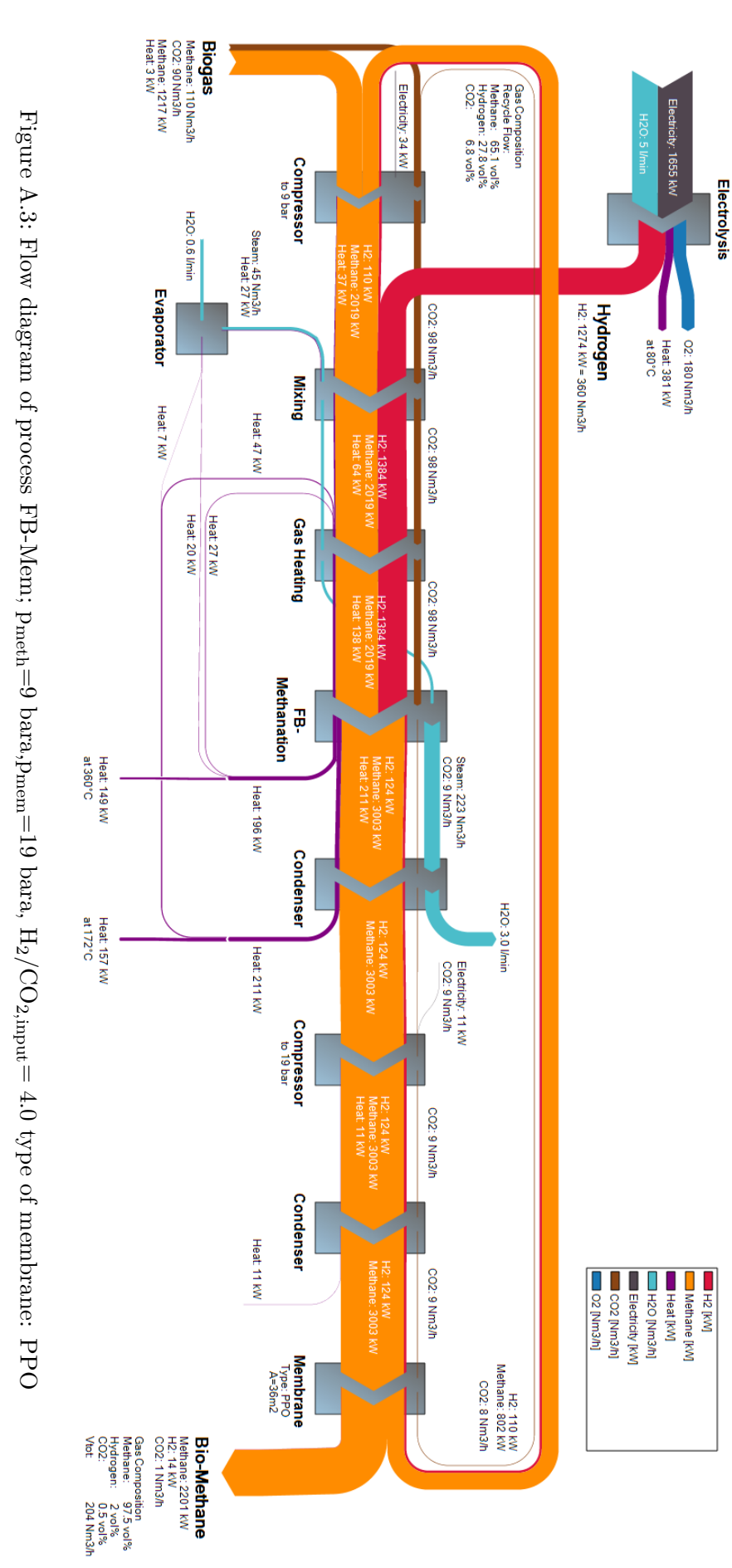

Figure A.3: Flow diagram of process FB-Mem; p_{meth}=9 bara,p_{mem}=19 bara, $H_2/CO_{2,input}$= 4.0 type of membrane: PPO

		BFB				FB		
Components/ Process	**Unit**	**BFB-FB**	**BFB-Mem**	**BFB-MemS**	**BFB-MemT**	**FB-FB**	**FB-Mem**	**FB-MemS**
Input flow biogas	Nm3/h	200	200	200	200	200	200	200
CO2 conc. biogas	%	45	45	45	45	45	45	45
Power of biomethane flow	kW	2 222	2 214	2 214	2 189	2 223	2 215	2 216
Biogas Tank	Nm3	350	350	350	350	350	350	350
Biogas Compressor	kW	25	32	41	32	27	34	45
Process pressure	bara	12	9	12	9	14	9	22
Evaporator area	m2	8.4	8.4	8.4	8.4	8.4	8.4	8.4
H2/CO2,feed	-	4.03	4.0	4.0	3.9	4.03	4.0	4.0
Electrolysis								
Electricity consumption	kW	1668	1655	1655	1614	1668	1655	1655
H2 Tank	Nm3	363	360	360	351	363	360	360
Main reactor								
Catalyst bed (diameter x height)	mxm	0.49x1.5	0.58x1.2	0.52x1.4	0.58x1.2	0.7x5.3	0.7x5.3	0.7x5.3
Catalyst mass	kg	99	110	101	106	289	289	289
Internal HX	m2	16	18	16	17	50	50	50
1. Condenser area	m2	25	24	23	23	27	24	24
2. Condenser area	m2	18	4	-	4	18	5	-
Post reactor								
Size (diameter x height)	mxm	0.5x1.8	-	-	-	0.5x1.5	-	-
Catalyst mass	kg	43	-	-	-	36	-	-
Membrane Module								
Type		-	PPO	PPO	Matr-PPO	-	PPO	PPO
Membrane area	m2	-	31	79	34	-	36	21
Compressor	kW	-	9.0	-	9.1	-	10.6	-
Gas Dryer (TSA)								
Size (diameter x height)	mxm	0.2x1.1	-	-	-	0.2x1.0	-	-
Adsorbent mass	kg	24	-	-	-	20	-	-
Excess Heat (without losses)								
Main reactor	kW	141	150	144	145	146	149	154
First condenser	kW	160	155	174	153	157	157	176

Table A.1: Technical data of economically optimised processes used in absolute economic analysis

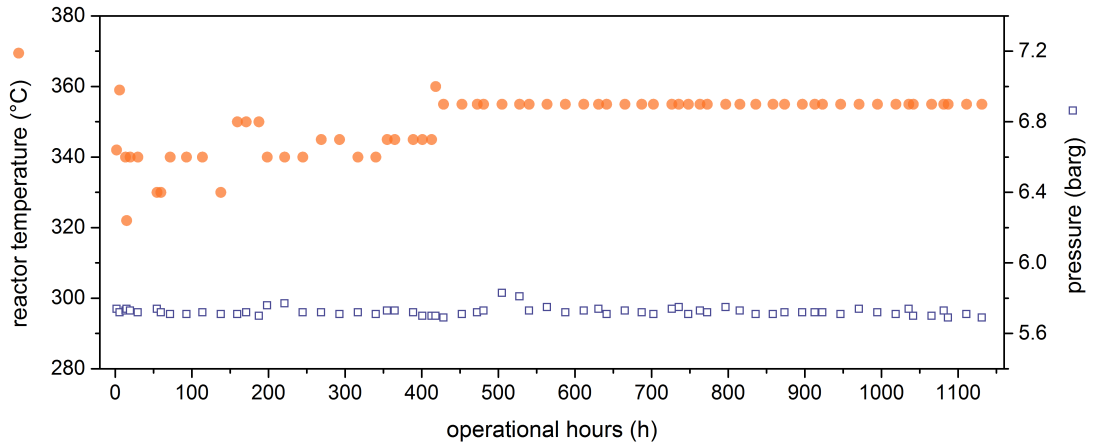

Figure A.4: Temperature and pressure in the methanation reactor (COSYMA) as a function of regular operation hours

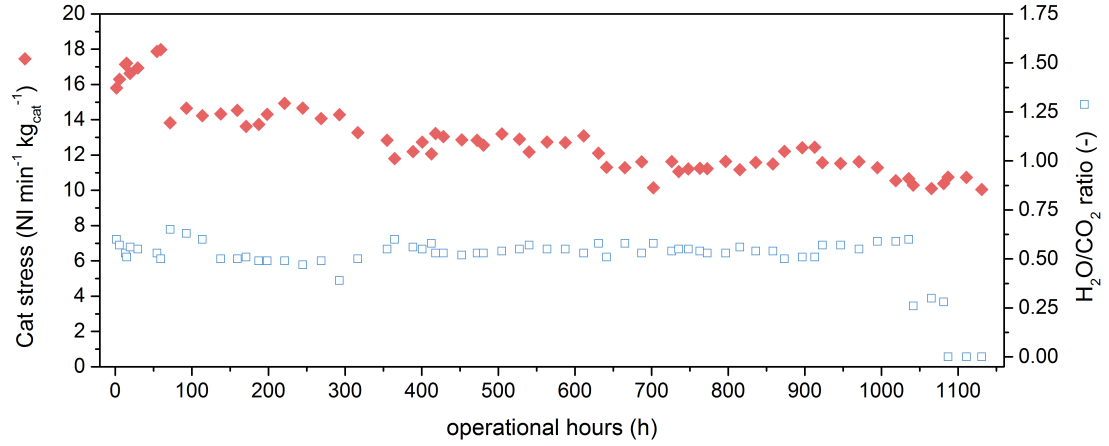

Figure A.5: Catalyst stress and the inlet ratio of water to carbon dioxide from biogas in the methanation reactor (COSYMA) as a function of the regular operation hours

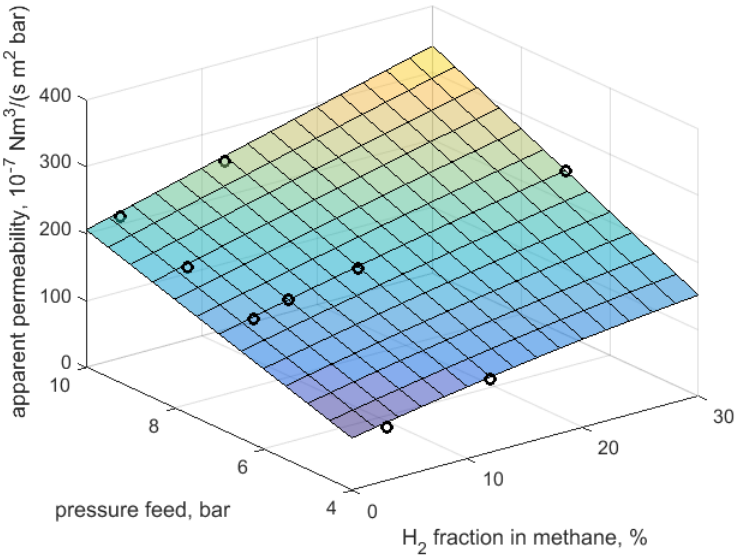

Figure A.6: Polynomial fit of permeability data from hydrogen in counter-current operation; surface area: simulation, markers: experimental data

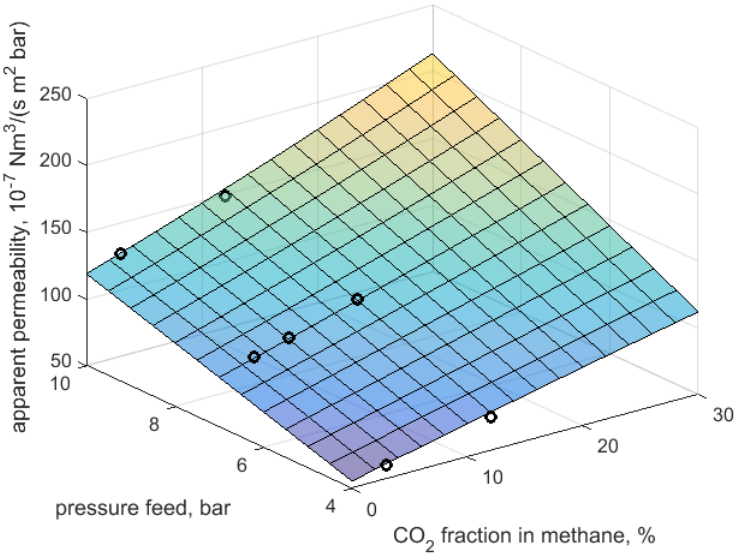

Figure A.7: Polynomial fit of permeability data from carbon dioxide in counter-current operation; surface area: simulation, markers: experimental data

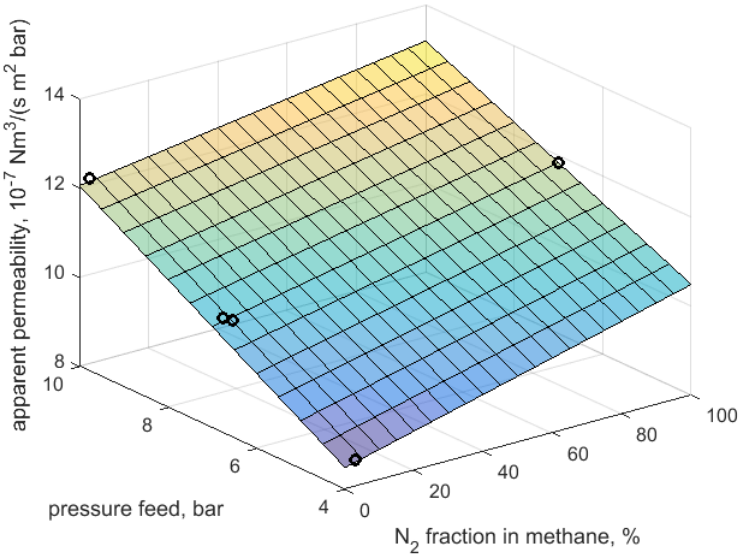

Figure A.8: Polynomial fit of permeability data from nitrogen in counter-current operation; surface area: simulation, markers: experimental data

List of Publications

1. M. Morales, P.Y. Dapsens, I. Giovinazzo, J. Witte, C. Mondelli, S. Papadokonstantakis, K. Hungerbühler, J. Pérez-Ramírez. "Environmental and economic assessment of lactic acid production from glycerol using cascade bio- and chemocatalysis". In: *Energy and Environmental Science* 8 (2015), pp. 558-567. DOI: 10.1039/ C4EE03352C.

2. J. Witte, J. Settino, S.M.A. Biollaz, T.J. Schildhauer. "Direct Catalytic Methanation of Biogas – Part I: New Insights into Biomethane Production using Rate-Based Modelling and Detailed Process Analysis". In: *Energy Conversion and Management* 171 (2018), pp. 750-768. DOI: 10.1016/j.enconman.2018.05.056

3. J. Witte , A. Kunz , S.M.A. Biollaz, T.J. Schildhauer. "Direct Catalytic Methanation of Biogas – Part II: Techno-Economic Process Assessment and Feasibility Reflections". In: *Energy Conversion and Management* 178 (2018), pp. 26-43. DOI: 10.1016/j.enconman.2018.09.079.